

Università degli Studi di Parma



Dottorato di Ricerca in
Sintesi e Progettazione di Composti Biologicamente Attivi
XVII ciclo (2012-2014)

*Design and synthesis of novel compounds interacting
with modulatory cysteines of MGL*

Coordinatore

Chiar.mo Prof. Marco Mor

Tutor

Chiar.mo Prof. Marco Mor

Dottorando

Mattia Anselmi

*Design and synthesis of novel compounds interacting
with modulatory cysteines of MGL*

Thesis by
Mattia Anselmi

In fulfillment of the requirements
for the degree of
Doctor of Philosophy



University of Parma
AD 2015

Alle wie duwe
duwe
fedele
fosa

Acknowledgments

I am deeply indebted to Professor Marco Mor for having given me the possibility of carrying out my doctoral studies at the Università degli Studi di Parma, under his strong and enthusiastic guidance. His mentorship helped me to grow both as a scientist and as a person. I am also grateful to him for the freedom I experienced in my scientific work, his never ending encouragement and the enlightening debates.

I express my gratitude to all the member of the research group where I spent these beautiful years: Professor Silvia Rivara, Professor Alessio Lodola, Professor Federica Vacondio and Professor Claudia Silva.

Part of the work presented in this dissertation would have not been possible without the help and the collaboration of enthusiastic scientific coworkers and friends I met: Dr. Daniele Pala, Dr. Caterina Carmi, Laura Scalvini, Michele Bassi and the undergraduate student who participate to the accomplishment of this PhD work, i.e. Vanessa Verardi and Marco Ravani.

I want to thank especially Dr. Riccardo Castelli, for having shared with me the laboratory and part of the daily life for more than two years, the launches and cigarettes-breaks. I am indebted for all he taught me about organic chemistry.

Table of contents

Summary	I
Sommario	IV
Chapter 1	
The endocannabinoid system	p.1
<hr/>	
1.1 Endocannabinoid system: the “early” view	p.2
1.2 Cannabinoid receptors	p.3
1.3 Endocannabinoids	p.6
1.3.1 Regulation of the endocannabinoid signal: formation	p.7
1.3.2 Regulation of the endocannabinoid signal: inactivation	p.9
1.4 The endocannabinoid system as therapeutic target	p.12
<i>References</i>	<i>p.15</i>

Chapter 2

The monoacylglycerol lipase (MGL) p.19

2.1 Characterization of MGL	p.19
2.1.1 Structure of MGL	p.19
2.1.2 Substrate selectivity	p.22
2.1.3 Tissue localization of MGL	p.23
2.2 <i>In vivo</i> relevance of MGL: biochemical and physiological roles	p.24
2.3 Regulatory cysteines of MGL	p.26
2.3.1 Sensitivity of MGL to oxidizing agents	p.28
2.4 MGL inhibition strategies	p.33
2.4.1 Targeting the catalytic serine	p.34
2.4.2 Targeting critical cysteines	p.39
2.4.3 Iso and benzisothiazolinones as MGL inhibitors	p.40
2.4.4 Triterpens as MGL inhibitors	p.43
2.5 Therapeutic potential of MGL inhibition	p.45
<i>References</i>	p.49

Chapter 3

MGL inhibitors: results and discussion p.55

3.1 BTZs as MGL inhibitors: results and discussion	p.56
3.1.1 Chemistry	p.60
3.1.2 Biological evaluation of BTZ derivatives on MGL	p.65
3.1.3 Reactivity studies on BTZ derivatives	p.76
3.2 Triterpenes as MGL inhibitors: results and discussion	p.85
3.2.1 Chemistry	p.87
3.2.2 Biological evaluation of celastrol derivatives on MGL	p.88
3.4 Conclusions	p.90
<i>References</i>	p.94

Chapter 4

Synthesis of NSC172285: a stereochemistry issue p.96

4.1 Introduction	p.96
4.2 Retrosynthetic approach and preliminary considerations	p.99
4.3 Results and discussion	p.102
4.3.1 Chemistry	p.102
4.3.2 Stereochemistry attribution	p.112
4.4 Conclusions	p.119
<i>References</i>	p.120

Chapter 5

Experimental section

p.122

5.1 Chapter 3	p.122
5.1.1 Chemistry	p.122
5.1.2 Pharmacology	p.135
5.1.3 Computational studies	p.137
5.1.4 Reactivity studies with glutathione	p.138
5.1.5 Kinetic studies by NMR spectroscopy	p.139
5.2 Chapter 4	p.140
5.2.1 Chemistry	p.139
5.2.2 Pharmacology	p.144
5.2.3 Computational studies	p.144
<i>References</i>	p.145

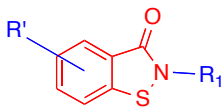
Summary

N-arachidonyletanolamine (AEA) and 2-arachidonoylglycerol (2-AG) are the most representative members of a class of endogenous ligands named endocannabinoid, which are able to activate cannabinoid receptors. The endocannabinoid neuromodulation plays important roles in various aspects of neural functions including learning and memory, anxiety, depression, appetite and feeding behavior, nociception, neuroprotection and movement control. Since 2-AG has been considered the true on-demand released endocannabinoid ligand for CB₁ receptor, a promising way to explore and promote its therapeutic potential could be the selective inhibition of the monoacylglycerol lipase (MGL), the enzyme responsible of 2-AG degradation. Three critical residues of cysteine have been identified as regulatory gates for the activity of the enzyme: Cys242, within the active site close to the catalytic triad, Cys201 and Cys208 located on the lid domain, a flexible solvent-exposed region that regulate the access of the substrate to the active site. Cys201 and Cys208 have been recently shown to be redox switches that regulate the activity of MGL by undergoing oxidation after oxidative stimulus induced by hydrogen peroxide.

Despite the potential of MGL as target for 2-AG signaling modulation, few potent and selective MGL inhibitors are available until now. Recently two class of partially-reversible MGL inhibitors has been reported: one is populated by covalent disulfide-bond forming compounds such as isothiazol-3(2*H*)-one (ITZ) and benzo[d]isothiazol-3(2*H*)-one (BTZ) derivatives, the second one is populated by triterpenes such as euphol and pristimerin. Both these classes of compounds interact with critical residues Cys201 and Cys208 of MGL thus preserving the catalytic activity of the enzyme. The modulation of MGL activity by interaction with these critical cysteine residues is a crucial point to fine tune the 2-AG signaling avoiding behavioral side-effects associated to the total disruption of the catalytic activity of MGL exerted by inhibitors addressing the catalytic site.

The research work reported in this PhD dissertation has been focused on the exploration of the structure-activity relationships (SAR) around the BTZ warhead in order to explore the pharmacophoric space around the targeted cysteines of MGL.

The structure of the driver portion (blue labeled) of compounds sharing an identical warhead (red labeled) has been broadly changed. I investigated the effect of substituent groups with different steric demand and electronic inductive effects on the nitrogen atom and the substituents on the phenyl ring of BTZ.



Benzo[4,5-d]isothiazol-3(2H)-one based derivatives

I performed the design and the synthesis of several compounds, applying different synthetic strategies.

The inhibitory potency of synthesized BTZs on MGL and was evaluated and SAR of this class were described. We identified promising compounds with inhibitory potency on MGL in the low nanomolar range. Moreover, the lead compound emerged from this screening was subjected to mechanistic studies that revealed a behavior similar to that of hydrogen peroxide in inactivating MGL supporting the theory that BTZs mimic the effect of an endogenous oxidation stimulus. To further elucidate the role of critical Cys201 and Cys208 in MGL activity, site-directed mutagenesis studies were performed identifying both cysteines as possible counterpart in the interaction with BTZs.

Moreover, in order to evaluate the stability and reactivity of these compounds towards biological thiols we investigated, through analytical methods the effect of substituent groups with different steric hindrance and electronic effects on the sulfenamidic reactive core of BTZ. I investigated by means of NMR experiments the reactivity of selected BTZs with a model biological thiol, *N*-acetyl cysteine (NAC). These studies allowed us to define a structure-reactivity relationship landscape that further validated our biological results.

To increase the knowledge in the field of the terpene-based inhibitors of MGL, I synthesized 3 new compounds starting from commercially available celastrol: these scaffold modifications led to less active compounds than reference compound pristimerin thus discouraging the development of triperpene-based MGL inhibitors.

Fibroblast growth factor-2 (FGF2) is a member of a large family of proteins that bind heparin and heparan sulfate and modulate the function of a wide range of cell types. FGF2 stimulates the growth and development of new blood vessels (angiogenesis) that contribute to the pathogenesis of several diseases (i.e. cancer, atherosclerosis), normal

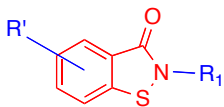
wound healing and tissue development. FGF2 exerts its activity on endothelial cells by interacting with high affinity tyrosine-kinase FGF receptors (FGFRs) and low affinity heparan sulphate proteoglycans (HSPGs), leading to the formation of productive HSPG/FGF2/FGFR ternary complexes. Presta and coworkers identified, from a virtual screening study of an NCI library, a promising molecule NSC172288 able to inhibit FGF2-FGFR interactions. During my PhD research I designed and performed the synthesis of this compound not described in literature. The major challenge associated was the necessity of planning the synthesis on the base of a poorly described structure. A synthetic pathway for NSC172285 was setup and an efficient method for using HFA trihydrate as electrophilic partner in an aldol reaction, with standard laboratory equipment was developed.

Sommario

N-arachidonoiletanolamina (AEA) e 2-arachidonoilglicerolo (2-AG) sono i membri più rappresentativi di una classe di ligandi endogeni chiamati endocannabinoidi in grado di attivare i recettori cannabinoidi. La neuromodulazione del sistema endocannabinoide regola numerose funzioni neurali che comprendono memoria e apprendimento, stati d'ansia, depressione, regolazione dell'appetito e di comportamenti legati alla nutrizione, nocicezione, neuroprotezione e controllo del movimento. Essendo il 2-AG il più abbondante tra i ligandi endocannabinoidi per il recettore CB₁, una promettente strategia per esplorare e promuovere il suo potenziale terapeutico risiede nell'inibizione selettiva dell'enzima monoacilglicerol lipasi (MGL) deputato alla degradazione metabolica del 2-AG. MGL presenta tre cisteine regolatorie fondamentali per la sua attività: Cys242, all'interno del sito attivo vicina alla triade catalitica, Cys201 e Cys208 posizionate sul lid domain, una regione flessibile ed esposta al solvente che regola l'accesso del substrato al sito attivo. Inoltre, queste due cisteine sono state recentemente identificate come sensori redox in grado di regolare l'attività di MGL ossidandosi in risposta allo stimolo ossidativo esercitato dal perossido d'idrogeno. Nonostante il grande potenziale di MGL come target per la modulazione del segnale stimolatorio del 2-AG sui recettori cannabinoidi, pochi inibitori selettivi per MGL sono attualmente disponibili. Recentemente due classi di inibitori parzialmente-reversibili sono state identificate: la prima classe è popolata da composti in grado di formare ponti disolfuro generando addotti covalenti come iso- (ITZ) e bezisotiazolinoni (BTZ), mentre la seconda classe è popolata da triterpeni come eufolo e pristimerina. Entrambe queste classi interagiscono con le cisteine critiche 201 e 208 dell'enzima preservando quindi l'attività catalitica di MGL. La modulazione dell'attività di MGL utilizzando composti in grado di interagire con queste cisteine regolatorie è un punto cruciale per ottenere una fine regolazione dei livelli di 2-AG evitando gli effetti collaterali a livello comportamentale che si manifestano in seguito alla totale inibizione dell'attività catalitica di MGL tipica degli inibitori che colpiscono il sito attivo.

Il lavoro di ricerca riportato in questa tesi di dottorato è stato focalizzato sull'esplorazione delle relazioni struttura-attività (SAR) intorno alla warhead a base benzisotiazolinonica in modo da esplorare lo spazio farmacoforico intorno alle cisteine

critiche di MGL. La struttura della driver portion (evidenziata in blu) è stata ampiamente modificata investigando l'effetto di sostituenti con diverse proprietà elettroniche e steriche sia sull'azoto sulfenamidico che sull'anello benzenico del nucleo benzisotiazolinonico.



Benzo[4,5-d]isothiazol-3(2H)-one based derivatives

Ho ideato e sintetizzato numerosi composti applicando diverse strategie sintetiche.

È stata quindi valutata la potenza inibitoria su MGL dei BTZs sintetizzati e sono state descritte le SAR per questa classe di composti. Abbiamo identificato composti promettenti in grado di inibire MGL con potenze nel range del basso nanomolare. Inoltre, il lead compound emerso da questo screening è stato sottoposto a dettagliati studi meccanicistici rivelando un comportamento inibitorio simile a quello esercitato dall'acqua ossigenata corroborando la teoria che questa classe di composti inibisca MGL mimando l'azione di uno stimolo ossidativo endogeno. Per chiarire meglio il ruolo delle cisteine critiche 201 e 208 sono stati eseguiti studi di mutagenesi sito-specifica che hanno mostrato come entrambe le cisteine siano coinvolte nel meccanismo di inibizione di questa classe di composti.

Inoltre, per valutare la stabilità e la reattività di questi composti verso tioli di rilevanza biologica, abbiamo investigato con metodi analitici gli effetti dei diversi sostituenti sulla reattività del nucleo sulfenamidico. Per mezzo di esperimenti condotti all'NMR ho studiato la reattività di alcuni BTZs selezionati verso un tiolo biologico modello, la N-acetilcisteina (NAC) permettendo di definire una scala di relazione struttura-reattività che ha ulteriormente validato i risultati biologici ottenuti.

Durante il mio periodo di dottorato ho investigato la possibilità di apportare modifiche strutturali allo scaffold della pristimerina sintetizzando tre nuovi composti partendo dal prodotto commerciale celastrolo, in modo esplorare le SAR per questa classe di inibitori di MGL. I derivati sintetizzati sono risultati essere meno attivi del composto di riferimento, scoraggiando lo sviluppo di nuovi inibitori a base triterpenica.

Il fattore di crescita 2 dei fibroblasti (FGF2) è un membro di una larga famiglia di proteine che legano l'eparina e l'eparan solfato e modulano le funzionalità di un ampio numero di cellule. FGF2 stimola la crescita e lo sviluppo di nuovi vasi sanguigni

(angiogenesi) che possono contribuire alla patogenesi di numerose disfunzioni (cancro, aterosclerosi), la normale guarigione delle ferite e lo sviluppo dei tessuti. FGF2 esercita la sua attività sulle cellule endoteliali interagendo con elevata affinità con recettori tirosin-chinasici (FGFRs) e con bassa affinità con proteoglicani formando dei produttivi complessi ternari HSPG/FGF2/FGFR. Il gruppo di ricerca del Prof. Presta ha individuato, da un virtual screening di una libreria di composti NCI, un promettente inibitore NSC172285 in grado di bloccare l'interazione tra FGF2 e FGFR. Durante il periodo di ricerca ho pianificato e portato a termine la sintesi di questo composto finora mai descritta in letteratura. La maggiore difficoltà incontrata è stata quella di intraprendere una campagna sintetica sulla base di una formula di struttura del composto di riferimento non propriamente chiara. Il prodotto desiderato è stato sintetizzato utilizzando l'esafuoroacetone (HFA) triidrato come partner elettrofilo in una reazione aldolica, sviluppando un metodo efficace per la sua disidratazione e la generazione *in situ* di HFA allo stato gassoso.

Chapter

1 The endocannabinoid system

Marijuana, or cannabis, is the most widely used illicit drug in Western societies and also the one with the longest recorded history of human use. The popularity of marijuana as a recreational drug is due to its ability to alter sensory perception and cause elation and euphoria, most vividly described by the 19th century French poet, Charles Baudelaire, in his book *Les Paradis Artificiels*¹. However, the ability of extracts of the hemp plant (*Cannabis sativa*) to cause a variety of medicinal effects unrelated to its psychoactive properties had been recognized as early as the third millennium BC, when Chinese texts described its usefulness in the relief of pain and cramps². In ancient India, the anxiety-relieving effect of bhang (the Indian term for marijuana ingested as food) had been recorded more than 3000 years ago. The use of cannabis or hashish as a psychoactive substance reached Europe and the Americas through the Arab world in the 19th century. During the same period, cannabis extracts had gained widespread use for medicinal purposes until 1937, when concern about the dangers of abuse led to the banning of marijuana for further medicinal use in the United States. The impediments to the development of cannabinoid medications has been the socially unacceptable psychoactive properties of plant-derived preparations and the, sometime misleading, information spread to block the diffusion of hemp for industrial applications. The rather turbulent history of marijuana and the recent resurgence of interest in its medicinal properties have been the subject of extensive researches. Added to this interest is the emergence of the endocannabinoid system (ECS), offering not only new insights into the mechanisms underlying the therapeutic actions of plant-derived phytocannabinoids but also novel molecular targets for pharmacotherapy.

This chapter will provide a brief overview on the current state of knowledge of the endocannabinoid system as a target of pharmacotherapy³.

1.1 Endocannabinoid system: the “early” view

Up until the last two decades, marijuana research was a rather esoteric field, of interest to a small number of scientists. A contributory factor was the highly lipophilic nature of the biologically active ingredients, which led to the notion that marijuana elicits its effects non-specifically by perturbing membrane lipids⁴. The first important breakthrough in the discovery of its actual mechanism of action was the identification in 1964 by Gaoni and Mechoulam⁵ of the correct chemical structure of the main psychoactive ingredient of marijuana, Δ^9 -tetrahydrocannabinol (THC), and the subsequent demonstration that bioactivity resides in the L-stereoisomer of this compound⁶, which is one of the approximately 60 cannabinoids present in the plant⁷. Cannabinoid compounds isolated from the plant *Cannabis sativa* comprise a family of tricyclic ring structures characterized by a phenol ring having a 5-carbon alkyl chain meta to the hydroxyl, a central pyran ring, and a mono-unsaturated cyclohexyl ring⁸ (Figure 1.1).

Δ^9 -tetrahydrocannabinol (Δ^9 -THC)		CB ₁ = CB ₂ agonist
Cannabivarin (Cannabivarol, CBV)		CB ₁ = CB ₂ antagonist
(-)-5'-(1,1-dimethylheptyl) cannabidiol (DMH-CBD)		CB ₂ = CB ₁ agonist inhibition of AEA uptake
(-)-Cannabidiol (CBD)		no activity at CB ₁ or CB ₂ antagonism of non-CB ₁ or non-CB ₂ modulator of α_1 -adrenoreceptor inhibition of AEA uptake and metabolism
Ajulemic acid (AJA, CT-3, IP-751)		CB ₁ = CB ₂ agonist

Figure 1.1 The chemical structure and pharmacological activity of selected plant derived cannabinoids

Studies of the biological effects of THC and its synthetic analogs^{9,10} revealed strict structural selectivity as well as stereoselectivity¹¹, telltale signs of drug-receptor interactions and turned out to be of key importance in the subsequent identification of an orphan G protein-coupled receptor (GPCR) as the brain receptor for cannabinoids later named CB₁ receptor. CB₁ receptor was cloned in Tom Bonner's laboratory in 1990¹² and 3 years later Sean Murno discovered CB₂ receptors¹³. These events were crucial steps for the definition of the ECS as a complex regulatory biochemical apparatus constituted by cannabinoid receptors, their endogenous ligands, and the catabolic and anabolic enzymes deputated to the regulation of endocannabinoids signaling.

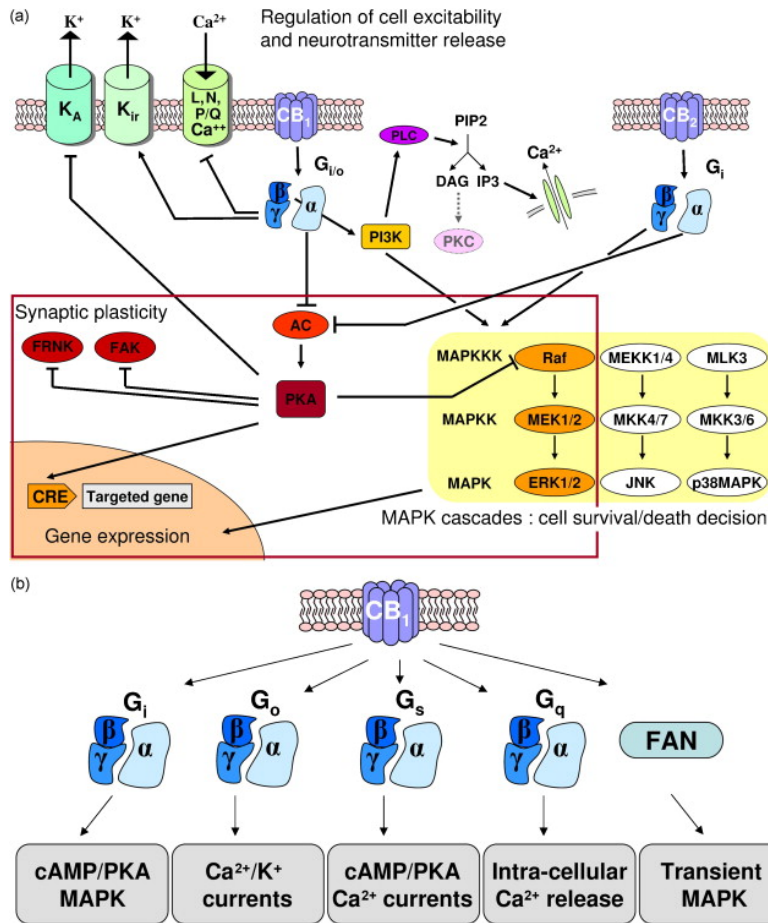
1.2 Cannabinoid receptors

The cannabinoid receptor subtypes characterized so far, CB₁ and CB₂, belong to the superfamily of G-protein-coupled membrane receptors (GPCRs). The two cannabinoid receptors exhibit 48% amino acid sequence identity at the protein level or 68% in the trans-membrane domains, which are thought to contain the binding sites for cannabinoids. Both receptor types are coupled through G proteins to adenylyl cyclase and mitogen-activated protein kinase (see below). It was originally believed that the CB₁ receptor was expressed mainly in the central nervous system (CNS), and hence it was considered a brain cannabinoid receptor. We are now aware that it is present in numerous peripheral organs, although in some of them the receptor levels are low. CB₁ receptors are among the most abundant GPCRs in the brain. The highest densities of CB₁ receptors, in the rodent brain, are noted in the basal ganglia, substantia nigra, globus pallidus, cerebellum, and hippocampus, but not in the brainstem. CB₁ receptors appear to be involved in γ -aminobutyric acid (GABA) and glutamate neurotransmission, as they are found on GABAergic and glutamatergic neurons. The CB₁ receptors are found primarily on central and peripheral neurons in the presynapse. These locations facilitate their inhibition of neurotransmitter release, which is one of the major functions of the endocannabinoid system.

The second cannabinoid GPCR, CB₂, is expressed primarily in cells of the immune and hematopoietic systems but recently were found to be present in the CNS¹⁴, though at

lower levels than those of the CB₁ receptors, in non-parenchymal cells of the cirrhotic liver¹⁵, in the endocrine pancreas¹⁶, and in bones¹⁷. Under some pathological conditions, CB₂ receptor expression is enhanced in the CNS as well as in other tissues. It seems possible that the CB₂ receptor is part of a general protective system (for a review, see Pacher & Mechoulam¹⁸).

Functional stimulation of CB₁/CB₂ by endogenous or exogenous cannabinoids triggers, *via* activation of heterotrimeric G_{i/o} proteins, those intracellular signaling events that are normally coupled to these two GPCRs¹⁹. As a consequence of this preferential coupling, activation of cannabinoid receptors primarily leads to the inhibition of adenylyl cyclase and reductions in cAMP accumulation in most tissues and models. In addition, both the CB₁ and CB₂ cannabinoid receptors regulate the phosphorylation and activation of different members of the family of mitogen-activated protein kinases (MAPKs), including extracellular signal-regulated kinase-1 and -2 (ERK1/2), p38 MAPK and c-Jun N-terminal kinase (JNK). In addition, CB₁ cannabinoid receptors can negatively couple to N- and P/Q-type voltage-operated Ca²⁺ channels and positively couple to A-type and inwardly rectifying K⁺ channels. The CB₁ cannabinoid receptor may also induce elevations in intracellular Ca²⁺ through G protein-dependent activation of phospholipase C- β (PLC- β)²⁰ (**Figure 1.2**). The implication of MAPK cascades in the regulation of cell survival/death and glucose metabolism by cannabinoids, or the involvement of cannabinoid-controlled ionic currents in the regulation of neurotransmitter release are typical examples revealing that biological activities modulated by cannabinoid receptors are supported by complex signaling cascades. While the classical view of GPCR signaling was initially to describe these receptors as simple on/off switches for the multiple intracellular cascades, recent studies have clearly indicated that they are extremely versatile signaling molecules governing complex intracellular responses. Indeed, research over the past decade has led to growing evidence for additional, unrelated mechanisms increasing the repertoire and the complexity of GPCR-associated signaling pathways. These include: (i) the ability of the receptor to couple with distinct G proteins, (ii) the interaction with GPCR-modifier proteins or with lipid raft domains to control receptor signaling or trafficking, (iii) the variety of desensitization mechanisms to limit signal duration/amplitude, (iv) or the oligomerisation of GPCRs into organized novel signaling unit.



Both CB_1 and CB_2 cannabinoid receptors are associated with $G_{\alpha_{i/o}}$ -dependent inhibition of adenylyl cyclase activity and $G_{\beta\gamma}$ -dependent activation of the different MAPK cascades (A). CB_1 cannabinoid receptor negatively regulates voltage-gated Ca^{2+} channels, positively regulates inwardly rectifying K^+ channels and induces elevation of intracellular free Ca^{2+} through $G_{\beta\gamma}$ -dependent activation of PLC. Cross-talks between signaling pathways are illustrated by the variety of responses requiring cannabinoid-mediated inhibition of PKA. Reduction of PKA activity is related to a reduction of gene expression through decreasing cAMP response element (CRE) activity. Reduction of PKA activity leads to a decrease in constitutive inhibitory phosphorylation of c-Raf and a consecutive activation of ERK1/2. Similarly, reduction of voltage-dependent K^+ A channel and focal-adhesion kinase (pp125 FAK and FRNK) phosphorylation through inhibition of PKA lead to activation of these different effectors. Besides, it is now demonstrated that activation of CB_1 cannabinoid receptors also leads to activation of G_s and G_q proteins (B). In addition the CB_1 cannabinoid receptor also signals through non-G protein partners such as the adaptor protein FAN. Preferential activation of different intracellular effectors by each G protein contributes to diversity and selectivity of responses regulated by cannabinoid receptors.

Figure 1.2 Complexity at cannabinoid receptor signaling

1.3 Endocannabinoids

The existence of specific receptors in mammalian cells that recognize a plant-derived substance rekindled the question raised two decades earlier, after brain receptors for morphine had been first described, i.e., is there an endogenous ligand? A positive answer was provided in 1992 by the report by Devane *et al.*²¹ describing the isolation from porcine brain of the lipid arachidonoyl ethanolamide, named anandamide (AEA) (**Figure 1.3**), which binds the brain cannabinoid receptor with reasonably high affinity and mimics the behavioral actions of THC when injected into rodents. Three years later a second endocannabinoid, 2-arachidonoylglycerol (2-AG), was discovered independently by Mechoulam *et al.*²² and Sugiura *et al.*²³. Since then, a number of related endogenous lipids with endocannabinoid-like activity have been reported (**Figure 1.3**), but follow-up studies about biosynthesis, cellular transport, metabolism, and biological function have focused on AEA and 2-AG, with much less information available about the other compounds with endocannabinoid-like properties.

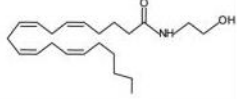
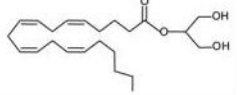
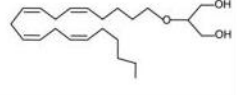
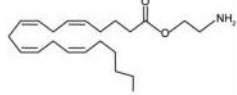
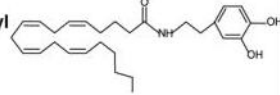
Anandamide (AEA)		CB ₁ >> CB ₂ agonist TRPV ₁ agonist
2-Arachidonoyl glycerol (2-AG)		CB ₁ ≈ CB ₂ agonist
2-Arachidonoyl glycerol ether		CB ₁ >> CB ₂ agonist
O-Arachidonoyl ethanolamine (virodhamine)		CB ₁ >> CB ₂ agonist
N-Arachidonoyl dopamine		CB ₁ >> CB ₂ agonist TRPV ₁ agonist

Figure 1.3 The chemical structure and pharmacological activity of endogenous cannabinoids

AEA is a partial or full agonist at CB₁ receptors, depending on the tissue and biological response measured. Although it also binds CB₂ receptors, it has very low efficacy and may act as an antagonist. 2-AG exert its action as full agonist both at CB₁ and CB₂

receptors. Any molecule acting as an endogenous mediator of physiological and pathological responses needs mechanisms for its biosynthesis and, following its action on specific molecular targets, for its inactivation. Based on original observations carried out with AEA²⁴, it was postulated that this endocannabinoid is not stored in resting cells but is, instead, synthesized and released “on demand” following physiological and pathological stimuli. This mechanism holds true also for 2-AG, which apart from being an endocannabinoid is also an intermediate in (phospho)glyceride metabolism. In general, pharmacological and electrophysiological data have shown that both Ca²⁺ influx and activation of some metabotropic receptors, either cooperatively or independently, can induce the formation of endocannabinoids acting as retrograde synaptic signals²⁵. After their biosynthesis, AEA and 2-AG are immediately released into the extracellular milieu *via* a mechanism still unknown, which could be dependent on the same putative membrane transporter, proposed to underlie endocannabinoid cellular uptake (see below). Endocannabinoids such as AEA may also act on intracellular sites of ion channels, such as those of vanilloid TRPV1 receptors and T-type Ca²⁺ channels.

The termination of the action of the endocannabinoids on extracellular targets is achieved through their reuptake by cells, a process that can be facilitated by yet-to-be-characterized membrane transporters, usually followed by one or more enzymatic reactions.

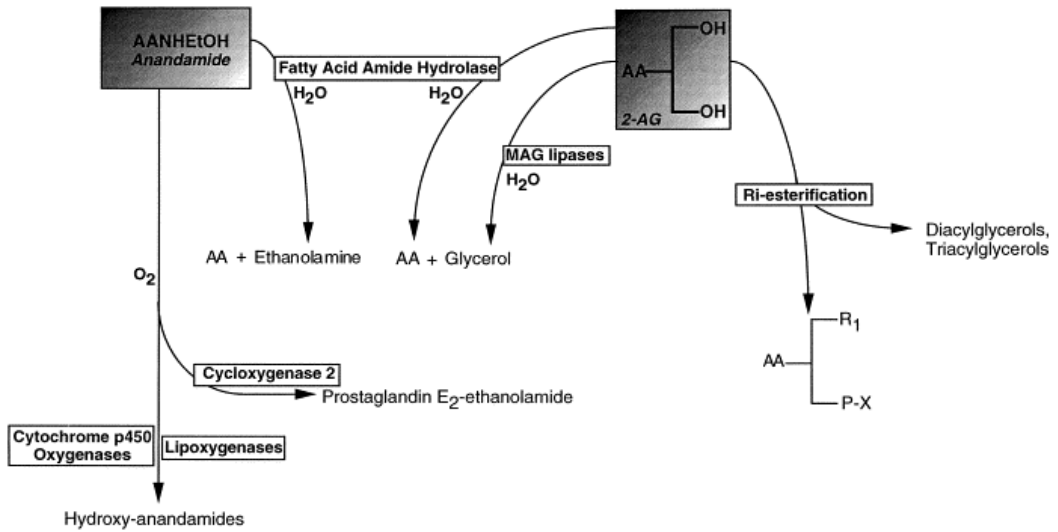
1.3.1 Regulation of the endocannabinoid signal: formation

The metabolic pathways of the class of lipids to which AEA belongs, the *N*-acylethanolamines, have been investigated since the 1960s. Work performed by Schmid's group²⁶ had shown that these compounds are biosynthesized *via* a phospholipid-dependent pathway (**Figure 1.4**), that is the enzymatic hydrolysis of the corresponding *N*-acyl-phosphatidylethanolamines (NAPEs). The enzyme catalyzing this reaction is a phospholipase D (PLD) selective for NAPEs (NAPE-PLD) with low affinity for other membrane phospholipids. NAPEs, in turn, are produced through the acyl transfer from the *sn*-1 position of phospholipids to the *N*-position of phosphatidylethanolamine (PE), catalyzed by a Ca²⁺-dependent *trans*-acylase. Neither

the PLD nor the *trans*-acylase appeared to exhibit any selectivity for a particular fatty acid moiety. However there may be parallel pathways for the generation of anandamide from NAPE. A secretory PLA2 that can catalyze the hydrolysis of N-acyl-PE to N-acyl-lysoPE, which is then acted on by a lysoPLD to generate N-acyl-ethanolamides, including anandamide, was recently identified in the stomach²⁷. Another route has been proposed for AEA biosynthesis, although only in cell-free systems, consisting of the ATP- and coenzyme A-independent condensation of free arachidonic acid and ethanolamine catalyzed by a “synthase”.

The levels of 2-AG in unstimulated tissues and cells are usually much higher than those of AEA, and are sufficient in principle to permanently activate both cannabinoid receptor subtypes^{23,28}. At any rate, the 2-AG found in cells and tissues is probably not uniquely used to stimulate cannabinoid receptors, as this compound is at the crossroads of several metabolic pathways, and is an important precursor and/or product of phospho-, di- and tri-glycerides, as well as of arachidonic acid. It is likely that a particular pool of 2-AG is produced *via* a special pathway only for the purpose of functioning as endocannabinoid. Of the several possible biosynthetic pathways known for 2-AG formation²⁹, those routes leading to the synthesis of an endocannabinoid should be Ca²⁺ dependent since the *de novo* formation of 2-AG, like for AEA, is induced in neurons by membrane depolarization³⁰. Several stimuli have been shown to lead to the formation of 2-AG in intact neuronal and non-neuronal cells³¹, but only seldom the pathways for 2-AG biosynthesis have been investigated. In most cases (**Figure 1.4**), 2-AG is produced from the hydrolysis of 2-arachidonate-containing diacylglycerols (DAGs) catalyzed by an *sn*-1-selective DAG lipase (*sn*-1 DAGL). DAGs serving as 2-AG precursors can be produced in turn from the hydrolysis of 2-arachidonate-containing phosphatidic acid (PA), catalyzed by a PA phosphohydrolase, or of phosphoinositides (PI), catalyzed by PI-selective phospholipase C (PI-PLC). Two *sn*-1 DAGL isozymes have been cloned and enzymatically characterized³². In summary, while a rather specific, albeit non-selective, pathway leads to AEA biosynthesis, several different mechanisms seem to underlie 2-AG formation in cells. It is possible that only a minor part of the 2-AG produced by stimulated cells is used to activate cannabinoid receptors.

rapidly reducing the intracellular concentration of the two compounds, or both (**Figure 1.5**). Indeed, AEA and 2-AG are taken up by cells via selective, saturable, temperature-dependent and Na⁺-independent “facilitated transport” mechanisms, known as the endocannabinoids membrane transporter(s) (EMT)³³. Once inside the cells, AEA and 2-AG are immediately degraded to arachidonic acid and ethanolamine or glycerol, respectively, through the enzymatic hydrolysis of their amide/ester bonds³⁴ (**Figure 1.5**). The enzyme responsible for AEA hydrolysis, originally named “anandamide amidohydrolase” or “amidase” has been discovered by Daniele Piomelli³⁵ and thoroughly studied by Cravatt *et al.*³⁶, who had purified and cloned the enzyme that was named “fatty acid amide hydrolase” (FAAH) in view of its ability to catalyze the hydrolysis of at least two distinct classes of bioactive fatty acid amides. FAAH has a molecular weight of ~ 65 kDa and a pH optimum of ~ 9 *in vitro*. Mutagenesis and chemical labeling studies, as well as the X-ray crystal structure have indicated that FAAH is a serine hydrolase with three catalytically essential amino acid residues Ser241/Ser217/Lys142³⁷. Immunocytochemical studies in rat brain have revealed that FAAH is expressed at high levels in several brain regions, especially in the neurons of the hippocampus, cerebellum, neocortex and olfactory bulb³⁸. These same brain regions are also enriched with CB₁ receptors. However, the CB₁ receptors are mainly pre-synaptic, whereas FAAH localizes to dendrites of postsynaptic neurons. The unique role of FAAH in terminating signaling by AEA was indicated by the phenotype of FAAH knockout mice, which displayed 10 to 15 times elevated levels of AEA across the brain. Anandamide is also sometimes metabolized by other intracellular enzymes such as palmitoylethanolamide-preferring acid amidase (PAA), *N*-acylethanolamine acid amidase³⁹ and type-2 fatty acid amide hydrolase⁴⁰. Other enzymes that can metabolize AEA are cyclooxygenase-2, lipoxygenases, and cytochrome P450⁴¹. To date, four enzymes responsible of 2-AG hydrolysis have been characterized at the molecular level: FAAH (responsible of 2% of total 2-AG hydrolysis),⁴² serine hydrolases ABHD12 and ABHD6 (responsible of 4% and 9% of total 2-AG hydrolysis, respectively)^{42,43} and monoacylglycerol lipase (MGL) considered as main actor in the degradation process of 2-AG⁴⁴.



Several pathways may contribute to the inactivation of the two endocannabinoids once they have diffused through the cell membrane. Both hydrolysis of the amide bond and oxidation catalyzed by enzymes of the AA cascade have been proposed for anandamide. As to 2-AG, hydrolysis of the ester bond and esterification into phosphoglycerides or neutral glycerolipids have been found to occur in intact cells. FAAH plays a key role in the inactivation of both metabolites. AA produced from the hydrolysis of endocannabinoids is immediately reincorporated into membrane phospholipids.

Figure 1.5 Catabolism of AEA and 2-AG.

MGL is a cytosolic serine hydrolase that cleaves medium- and long-chain monoacylglycerols into fatty acids and glycerol, with the highest rate for arachidonic acid.⁴⁵ MGL is 33 kDa protein belonging to α/β hydrolase family of enzymes⁴⁶ that exerts its hydrolyzing activity through a Ser122/His269/Asp239 catalytic triad. MGL is abundant in brain regions with high cannabinoid CB₁ receptor density, such as the hippocampus, but, unlike FAAH, it occurs in presynaptic neurons and is likely to be co-expressed with CB₁ receptors⁴⁷. MGL is the central topic of this PhD dissertation and will be exhaustively discussed in the next chapter (see Chapter 2).

1.4 The endocannabinoid system as therapeutic target

The ECS might serve important regulatory functions in physiological processes; thus, cannabinoid agents might prove useful in the treatment of pathological conditions that are associated with such processes.

The previous knowledge of THC pharmacology and, most importantly, recent studies carried out by using pharmacological, biochemical, analytical and genetic approaches are revealing several possible functions of endocannabinoid signaling under both physiological and pathological conditions. Modulating the activity of the ECS holds therapeutic promise for a broad range of diseases, including neurodegenerative, cardiovascular and inflammatory disorders, obesity/metabolic syndrome, cachexia, chemotherapy-induced nausea and vomiting and tissue injury and pain, amongst others (for reviews see ref. 3,48 and references therein).

Despite the ubiquitous expression of the various components of the ECS, their genetic ablation or pharmacological blockade in normal, healthy animals has minimal functional consequences. On the other hand, an increase or decrease in ECS tone is associated with various pathological states, as a result of the altered expression of CB receptors, endocannabinoid metabolizing enzymes and/or synthetic pathways, in a tissue-specific and time-dependent manner. In some cases, altered ECS activity is transient and forms part of the body's compensatory response to a particular insult, thus reducing symptoms and/or slowing progression of the disease (e.g. in neuropathic pain); in other cases, activation of the ECS may be pathogenic (e.g. in various forms of shock or diabetic complications) or may reflect a deficiency (e.g. in various tumors) of unknown significance.

Several pharmacological tools for the study of the endocannabinoid system have been developed⁴⁹. These tools can be grouped functionally into five super-families, i.e.: (i) "indirect" cannabinoid receptor agonists (i.e. inhibitors of endocannabinoid inactivation), (ii) "direct" cannabinoid receptor agonists, (iii) "indirect" antagonists of cannabinoid receptors (i.e. inhibitors of endocannabinoid biosynthesis), (iv) cannabinoid receptor inverse agonists and antagonists, and (v) cannabinoid receptor allosteric modulators.

Clinical trials with CB₁ antagonists in obesity/metabolic syndrome, and other studies with peripherally-restricted CB_{1/2} agonists and inhibitors of the endocannabinoid

metabolizing enzyme in pain, have introduced unexpected complexities, suggesting that a better understanding of the pathophysiological role of the endocannabinoid system is required to devise clinically successful treatment strategies.

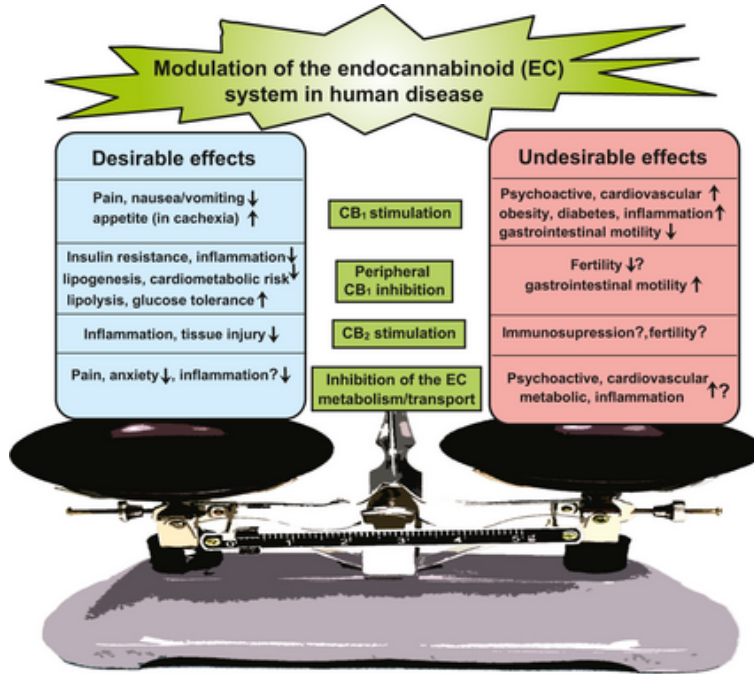


Figure 1.6 Cannabinoid therapeutics: finding the right balance

Among this complex scenario of modulating access points for the ECS, inhibitors of AEA and 2-AG degradation offer a potentially attractive alternative strategy compared to direct stimulation of cannabinoid receptors⁵⁰. Indeed, despite the structural similarity shared by AEA and 2-AG, distinct enzymes inactivate these lipids and thus serve as key points of control over specific endocannabinoid signaling events *in vivo*. Pharmacological studies have revealed that selective FAAH and MAGL inhibitors produce an intriguing subset of the behavioral effects observed with direct CB₁ agonists, including analgesia in multiple acute and chronic pain models⁵¹. Importantly, several findings indicate that selective blockade of FAAH or MAGL can disassociate some of the beneficial and undesirable effects of CB₁ activation.

The ECS is emerging as a key player in several physiological and pathological mechanisms, in both central and peripheral tissues. As such, this system is likely to lead in the future to the development of new therapeutic tools targeting disorders that

have been so far poorly managed in the clinical practice. Numerous examples exist of how “direct” or “indirect” activation of cannabinoid receptors can either counteract or contribute to the symptoms and/or progress of different pathologies. Furthermore, endocannabinoids seem sometimes to participate with opposing effects and, correspondingly, molecules that either reduce or enhance endocannabinoid tone both produce beneficial effects in different phases of the same disease.

Therefore, the most challenging task for medicinal chemists and the pharmacologists will be to devise ways to target this pleiotropic and “plastic” system in a selective, and hence, safe way, thus obtaining therapeutic drugs with more and more favorable benefit-to-risk profiles.

References

- ¹ Iversen, L.L. *The Science of Marijuana*. Oxford University Press; Oxford, UK: **2000**
- ² Mechoulam, R. *The pharmacohistory of cannabis sativa*. In: Mechoulam R, editor. *Cannabis as Therapeutic Agent*. CRC Press; Boca Raton, FL: **1986**. pp. 1-19
- ³ (a) Di Marzo, V.; Bifulco, M.; De Petrocellis, L. The endocannabinoid system and its therapeutic exploitation. *Nat. Rev. Drug. Discov.* **2004**, *3*, 771-784 (b) Howlett, A.C.; Breivogel, C.S.; Childers, S.R.; Deadwyler, S.A.; Hampson, R.E.; Porrino, L.J. Cannabinoid physiology and pharmacology: 30 years of progress. *Neuropharmacology*. **2004**, *47* (Suppl 1), 345-358 (c) Pertwee, R.G. The therapeutic potential of drugs that target cannabinoid receptors or modulate the tissue levels or actions of endocannabinoids. *AAPS J.* **2005**, *7*, E625-E654 (d) Di Marzo, V; Petrocellis, L.D. Plant, synthetic, and endogenous cannabinoids in medicine. *Annu. Rev. Med.* **2006**, *57*, 553-574 (e) Mackie, K. Cannabinoid receptors as therapeutic targets. *Annu. Rev. Pharmacol. Toxicol.* **2006**, *46*, 101-122 (f) Pagotto, U.; Marsicano, G.; Cota, D.; Lutz, B.; Pasquali, R. The emerging role of the endocannabinoid system in endocrine regulation and energy balance. *Endocr. Rev.* **2006**, *27*, 73-100 (h) Pacher, P.; Batkai, S.; Kunos, G. The Endocannabinoid System as an Emerging Target of Pharmacotherapy. *Pharmacol. Rev.* **2006**, *58*, 389-462. (i) Piomelli, D. The molecular logic of endocannabinoid signalling *Nat Rev Neurosci.* **2003** *4*(11), 873-84.
- ⁴ Lawrence, D.K.; Gill, E.W. The effects of Δ^1 -tetrahydrocannabinol and other cannabinoids on spin-labeled liposomes and their relationship to mechanisms of general anesthesia. *Mol. Pharmacol.* **1975**; *11*, 595-602
- ⁵ Gaoni, Y.; Mechoulam, R. Isolation, structure and partial synthesis of an active constituent of hashish. *J. Am. Chem. Soc.* **1964**, *86*, 1646-1647.
- ⁶ Mechoulam, R.; Gaoni, Y. The absolute configuration of Δ^1 -tetrahydrocannabinol, the major active constituent of hashish. *Tetrahedron Lett.* **1967**, *12*, 1109-1111.
- ⁷ Dewey, W.L. Cannabinoid pharmacology. *Pharmacol. Rev.* **1986**, *38*, 151-178.
- ⁸ (a) Mechoulam, R. Marijuana chemistry. *Science*, **1970**, *168*, 1159-1166. (b) Agurell, S.; Halldin, M.; Lindgren, J.E.; Ohlsson, A.; Widman, M.; Gillespie, H.; Hollister L. Pharmacokinetics and metabolism of Δ^1 -tetrahydrocannabinol and other cannabinoids with emphasis on man. *Pharmacol. Rev.* **1986**, *68*, 21-43.
- ⁹ Herkenham, M.; Lynn, A.B.; Johnson, M.R.; Melvin, L.S.; de Costa, B.R.; Rice, K.C. Characterization and localization of cannabinoid receptors in rat brain: a quantitative in vitro autoradiographic study. *J. Neurosci.* **1991**, *11*, 563-583.
- ¹⁰ Devane, W.A.; Dysarz, F.A. III; Johnson, M.R.; Melvin, L.S.; Howlett, A.C. Determination and characterization of a cannabinoid receptor in rat brain. *Mol. Pharmacol.* **1988**, *34*, 605-613.
- ¹¹ Jones, G.; Pertwee, R.G.; Gill, E.W.; Paton, W.D.; Nilsson, I.M.; Widman, M.; Agurell, S. Relative pharmacological potency in mice of optical isomers of Δ^1 -tetrahydrocannabinol. *Biochem. Pharmacol.* **1974**, *23*, 439-446.
- ¹² Matsuda, L.A.; Lolait, S.J.; Brownstein, M.J.; Young, C.A.; Bonner, T.I. Structure of a cannabinoid receptor and functional expression of the cloned cDNA. *Nature (Lond)* **1990**, *346*, 561-564.
- ¹³ Munro, S.; Thomas, K.L.; Abu-Shaar, M. Molecular characterization of a peripheral receptor for cannabinoids. *Nature*. **1993**, *365*, 61-65.

- ¹⁴ (a) Van Sickle, M.D.; Duncan, M.; Kingsley, P.J.; Mouihate, A.; Urbani P, Mackie, K.; Stella, N.; Makriyannis, A.; Piomelli, D.; Davison, J.S.; Marnett, L.J.; Di Marzo, V.; Pittman, Q.J.; Patel, K.D.; Sharkey, K.A.; Identification and functional characterization of brainstem cannabinoid CB₂ receptors. *Science*. **2005**, *310*(5746), 329-32. (b) Gong, J.P.; Onaivi, E.S.; Ishiguro, H.; Liu, Q.R.; Tagliaferro, P.A.; Brusco, A.; Uhl, G.R. Cannabinoid CB₂ receptors: immunohistochemical localization in rat brain. *Brain Res*. **2006**, *1071*(1), 10-23.
- ¹⁵ Julien, B.; Grenard, P.; Teixeira-Clerc, F.; Van Nhieu, J.T.; Li, L.; Karsak, M.; Zimmer, A.; Mallat, A.; Lotersztajn, S. Antifibrogenic role of the cannabinoid receptor CB₂ in the liver. *Gastroenterology*. **2005**, *128*(3), 742-55.
- ¹⁶ Cannabinoid receptors regulate Ca(2+) signals and insulin secretion in pancreatic beta-cell. Juan-Picó, P.; Fuentes, E.; Bermúdez-Silva, F.J.; Javier Díaz-Molina, F.; Ripoll, C.; Rodríguez de Fonseca, F.; Nadal, A. Cannabinoid receptors regulate Ca(2+) signals and insulin secretion in pancreatic beta-cell. *Cell Calcium*. **2006**; *39*(2), 155-62.
- ¹⁷ Karsak, M.; Ofek, O.; Fogel, M.; Wright, K.; Tam, J.; Gabet, Y.; Birenboim, R.; Attar-Namdar, M.; Müller, R.; Cohen-Solal, M. The cannabinoid CB₂ receptor: a potential target for the treatment of osteoporosis. *J. Bone Miner. Res*. **2004**, *19*, S383.
- ¹⁸ Pacher, P.; Mechoulam, R. Is lipid signaling through cannabinoid 2 receptors part of a protective system? *Prog. Lipid Res*. **2011**, *50*, 193-211.
- ¹⁹ Pertwee, R.G. Pharmacology of cannabinoid CB₁ and CB₂ receptors. *Pharmacol. Ther*. **1997**, *74*, 129-180.
- ²⁰ (a) Howlett, A.C. Cannabinoid receptor signaling *Handb. Exp. Pharmacol*. **2005**, 53-79. (b). Bosier, B.; Muccioli, G.G.; Hermans, E.; Lambert, D.M. Functionally selective cannabinoid receptor signalling: therapeutic implications and opportunities. *Biochem. Pharmacol*. **2010**, *80*(1), 1-12.
- ²¹ Devane, W.A.; Hanus, L.; Breuer, A.; Pertwee, R.G.; Stevenson, L.A.; Griffin, G.; Gibson, D.; Mandelbaum, A.; Etinger, A.; Mechoulam, R. Isolation and structure of a brain constituent that binds to the cannabinoid receptor. *Science*. **1992**, *258*(5090), 1946-9.
- ²² Mechoulam, R.; Ben-Shabat, S.; Hanus, L.; Ligumsky, M.; Kaminski, N.E.; Schatz, A.R.; Gopher, A.; Almog, S.; Martin, B.R.; Compton, D.R. Identification of an endogenous 2-monoglyceride, present in canine gut, that binds to cannabinoid receptors. *Biochem. Pharmacol*. **1995**, *50*(1), 83-90.
- ²³ Sugiura, T.; Kondo, S.; Sukagawa, A.; Nakane, S.; Shinoda, A.; Itoh, K.; Yamashita, A.; Waku, K. 2-Arachidonoylglycerol: a possible endogenous cannabinoid receptor ligand in brain. *Biochem. Biophys. Res. Commun*. **1995**, *215*(1), 89-97.
- ²⁴ Di Marzo, V.; Melk, D.; Bisogno, T.; De Petrocellis, L. Endocannabinoids: endogenous cannabinoid receptor ligands with neuromodulatory action. *Trends Neurosci*. **1998**, *21*, 521-528.
- ²⁵ Wilson, R.I.; Nicoll, R.A. Endocannabinoid signaling in the brain. *Science* **2002**, *296*, 678-682.
- ²⁶ Schmid, H.H.; Schmid, P.C.; Natarajan, V. The N-acylation-phosphodiesterase pathway and cell signalling. *Chem. Phys. Lipids* **1996**, *80*, 133-142.
- ²⁷ Sun, Y.X.; Tsuboi, K.; Okamoto, Y.; Tonai, T.; Murakami, M.; Kudo, I.; Ueda, N. Biosynthesis of anandamide and N-palmitoylethanolamine by sequential actions of phospholipase A₂ and lysophospholipase D. *Biochem. J*. **2004**, *380*(Pt 3), 749-56.
- ²⁸ Stella, N.; Schweitzer, P.; Piomelli, D. A second endogenous cannabinoid that modulates long-term potentiation. *Nature (Lond)* **1997**, *388*, 773-778.

- ²⁹ Sugiura, T.; Kondo, S.; Sukagawa, A.; Tonegawa, T.; Nakane, S.; Yamashita, A.; Ishima, Y.; Waku, K. Transacylase-mediated and phosphodiesterase-mediated synthesis of *N*-arachidonylethanolamine, an endogenous cannabinoid-receptor ligand, in rat brain microsomes. Comparison with synthesis from free arachidonic acid and ethanolamine. *Eur. J. Biochem.* **1999**, *240*, 53–62.
- ³⁰ Bisogno, T.; Sepe, N.; Melk, D.; Maurelli, S.; De Petrocellis, L.; Di Marzo, V. Biosynthesis, release and degradation of the novel endogenous cannabimimetic metabolite 2-arachidonoylglycerol in mouse neuroblastoma cells. *Biochem. J.* **1997**, *322*, 671–677.
- ³¹ Sugiura, T.; Kobayashi, Y.; Oka, S.; Waku, K. Biosynthesis and degradation of anandamide and 2-arachidonoylglycerol and their possible physiological significance. *Prostaglandins Leukot. Essent. Fatty Acids* **2002**, *66*, 173–192.
- ³² Bisogno, T.; Howell, F.; Williams, G.; Minassi, A.; Cascio, M.G.; Ligresti, A.; Matias, I.; Schiano-Moriello, A.; Paul, P.; Williams, E.J.; Gangadharan, U.; Hobbs, C.; Di Marzo, V.; Doherty, P. Cloning of the first sn1-DAG lipases points to the spatial and temporal regulation of endocannabinoid signaling in the brain. *J. Cell Biol.* **2003**, *163*(3), 463–8.
- ³³ (a) Beltramo, M.; Stella, N.; Calignano, A.; Lin, S.Y.; Makyiannis, A.; Piomelli, D. Functional role of high-affinity anandamide transport, as revealed by selective inhibition. *Science* **1997**, *277*, 1094–1097. (b) Oowler, C.J.; Jaconsson, S.O. Cellular transport of anandamide, 2-arachidonoylglycerol and palmitoylethanolamide – targets for drug development *Prostaglandins Leukot. Essent. Fatty Acids* **2002**, *66*, 193–200.
- ³⁴ Di Marzo, V.; Bisogno, T.; Sugiura, T.; Melck, D.; De Petrocellis L. The novel endogenous cannabinoid 2-arachidonoylglycerol is inactivated by neuronal- and basophil-like cells: connections with anandamide *Biochem. J.* **1998**, *331*, 15–19.
- ³⁵ Di Marzo, V.; Fontana, A.; Cadas, H.; Schinelli, S.; Cimino, G.; Schwartz, J.C.; Piomelli D. Formation and inactivation of endogenous cannabinoid anandamide in central neurons. *Nature*. **1994**, *372*(6507), 686–91.
- ³⁶ Cravatt, B.F.; Giang, D.K.; Mayfield, S.P.; Boger, D.L.; Lerner, R.A.; Gilula N.B. Molecular characterization of an enzyme that degrades neuromodulatory fatty-acid amides *Nature* **1996**, *384*, 83–87.
- ³⁷ Bracey, M.H.; Hanson, M.A.; Masuda, K.R.; Stevens, R.C.; Cravatt, B.F. Structural adaptations in a membrane enzyme that terminates endocannabinoid signaling. *Science* **2002**, *298*, 1793–6.
- ³⁸ Egertova, M.; Giang, D.K.; Cravatt, B.F.; Elphick, M.R. A new perspective on cannabinoid signalling: complementary localization of fatty acid amide hydrolase and the CB₁ receptor in rat brain. *Proc. Biol. Sci.* **1998**, *265*, 2081–5.
- ³⁹ Tsuboi, K.; Sun, Y.X.; Okamoto, Y.; Araki, N.; Tonai, T.; Ueda, N. Molecular characterization of *N*-acylethanolamine-hydrolysing acid amidase, a novel member of the cholesteryl-glycine hydrolase family with structural and functional similarity to acid ceramidase. *J. Biol. Chem.* **2005**, *280*, 11082–92.
- ⁴⁰ Wei, B.Q.; Mikkelsen, T.S.; McKinney, M.K.; Lander, E.S.; Cravatt, B.F. A second fatty acid amide hydrolase with variable distribution among placental mammals. *J Biol. Chem.* **2006**, *281*, 36569–78.
- ⁴¹ Kozak, K.R.; Marnett, L.J. Oxidative metabolism of endocannabinoids. *Prostaglandins Leukot. Essent. Fatty Acids* **2002**, *66*, 211 - 220.
- ⁴² Blankman, J. L.; Simon, G. M.; Cravatt, B. F. A comprehensive profile of brain enzymes that hydrolyze the endocannabinoid 2-arachidonoylglycerol. *Chem. Biol.* **2007**, *14*, 1347–1356.

- ⁴³ Tornquist, H; Belfrage, P. Purification and some properties of a monoacylglycerol-hydrolyzing enzyme of rat adipose tissue. *J. Biol. Chem.* **2006**, *281*, 36569-36578.
- ⁴⁴ Saario, S. M.; Laitinen, J. T. Monoglyceride lipase as an enzyme hydrolyzing 2-arachidonoylglycerol. *Chem. Biodiversity* **2007**, *4*, 1903-1013.
- ⁴⁵ Okazaki, T.; Sagawa, N.; Okita, J. R.; Bleasdale, J. E.; Macdonald, P. C.; Johnson, J. M. Diacylglycerol metabolism and arachidonic acid release in human fetal membranes and decidua vera. *J. Biol. Chem.* **1981**, *256*, 7316-7321.
- ⁴⁶ Ollis, D. L.; Cheah, E.; Cykler, M.; Dijkstra, B.; Frolow, F.; Franken, S. M. The α/β hydrolase fold. *Protein Eng.* **1992**, *5*, 197-211.
- ⁴⁷ Gulayas, A. I.; Cravatt, B. F.; Bracey, M. H.; Dinh, T. P.; Piomelli, D.; Boscia, F.; Freund, T. F.; Segregation of two endocannabinoid-hydrolyzing enzymes into pre- and postsynaptic compartments in the rat hippocampus, cerebellum and amygdala. *Eur. J. Neurosci.* **2004**, *20*, 441-458.
- ⁴⁸ (a) Pál, P.; Kunos, G. Modulating the endocannabinoid system in human health and disease: successes and failures *FEBS J.* **2013**, *280(9)*, 1918-1943. (b) Di Marzo, V. The endocannabinoid system: Its general strategy of action, tools for its pharmacological manipulation and potential therapeutic exploitation *Pharmacological Research* **2009**, *60(2)*, 77-84.
- ⁴⁹ (a) Di Marzo, V. Targeting the endocannabinoid system: to enhance or reduce? *Nat. Rev. Drug Discov.* **2008**, *7*, 438 - 455. (b) Fowler C.J. "The tools of the trade" –an overview of the pharmacology of the endocannabinoid system. *Curr. Pharm. Des.* **2008**, *14*, 2254-2265.
- ⁵⁰ (a) Cravatt, B.F.; Lichtman, A.H. Fatty acid amide hydrolase: An emerging therapeutic target in the endocannabinoid system. *Curr. Opin. Chem. Biol.* **2003**, *7*, 469-475. (b) Piomelli, D. The endocannabinoid system: A drug discovery perspective. *Curr. Opin. Investig. Drugs* **2005**, *6*, 672-679. (c) Jonsson, K.O.; Holt, S.; Fowler, C.J. The endocannabinoid system: Current pharmacological research and therapeutic opportunities. *Basic. Clin. Pharmacol. Toxicol.* **2006**, *98*, 124-134. (d) Koutek, B. *et al.* Inhibitors of arachidonyl ethanolamide hydrolysis. *J. Biol. Chem.* **1994**, *269*, 22937-22940.
- ⁵¹ (a) Long J.Z. *et al.* Selective blockade of 2-arachidonoylglycerol hydrolysis produces cannabinoid behavioral effects. *Nat. Chem. Biol.* **2009**, *5*, 37-44. (b) Russo, R.; Loverme, J.; La Rana, G.; Compton, T.R.; Parrott, J.; Duranti, A.; Tontini, A.; Mor, M.; Tarzia, G.; Calignano, A.; Piomelli, D. The fatty acid amide hydrolase inhibitor URB597 (cyclohexylcarbamic acid 3'-carbamoylbiphenyl-3-yl ester) reduces neuropathic pain after oral administration in mice. *J. Pharmacol. Exp. Ther.* **2007**, *322*, 236.

Chapter

2 The monoacylglycerol lipase (MGL)

The endocannabinoid system is involved in processes as diverse as control of appetite, perception of pain and the limitation of cancer cell growth and invasion (see Chapter 1). The enzymes responsible for endocannabinoids breakdown are attractive pharmacological targets, and fatty acid amide hydrolase inhibitors, which potentiate the levels of AEA, are now undergoing pharmaceutical development. “Druggable” selective inhibitors of monoacylglycerol lipase, the key enzyme regulating the levels of the other main endocannabinoid, 2-AG, were however not identified until very recently. Their availability has resulted in a large expansion of the knowledge concerning the pharmacological consequences of monoacylglycerol lipase inhibition (MGL) and hence the role(s) played by the enzyme in the body. In this chapter, the pharmacology of MGL will be discussed, together with an analysis of the state of knowledge about MGL inhibitors and the therapeutic potential of this key enzyme of the endocannabinoid system¹.

2.1 Characterization of MGL

2.1.1 Structure of MGL

MGL was purified in 1975 for the first time from rat-adipocyte tissue, and its molecular weight was estimated to be 32.9 kDa². Some 20 years later, MGL was cloned for the

first time from a mouse-adipocyte cDNA library, and it was determined to be composed of 302 amino acids, in accord with a molecular weight of ca. 33 kDa³. The primary sequence of MGL was found to contain two lipase motifs: an active-site serine GX SXG sequence and the HG dipeptide. MGL has also been cloned from human adipocytes and rat brain, and found to contain 303 amino acids^{4,5}. MGL shares a high degree of homology in mouse-, rat-, and human-MGL amino acid sequence. Thus, at the amino acid level, human and mouse MGL are 84% identical, and mouse and rat MGL are 92% identical. The three-dimensional structure of MGL has been recently elucidated by X-ray crystallography, and the enzyme has been shown to be a dimeric molecule with amphitropic properties that can exist both in a soluble form and associated with the membrane lipid bilayers⁶. MGL belongs to the α/β hydrolase fold family. The α/β hydrolase fold is organized as a core domain constituted of a β -sheet made from 8 β -strands (one of which is antiparallel to the others) and surrounded by a series of α helices. This central domain contains the Ser122/His269/Asp239 catalytic triad, whose structural organization is well conserved. The nucleophilic serine is located at the top of the core in a typical sharp turn between α 3 helix and β 5 strand. This core domain is overhung by a much more variable domain termed cap, made of several α helices and loops that mediate structural information to provide the huge amount of α/β hydrolases family members with their specificity in both function and substrate profile.

MGL structure reveals several key features of the enzyme, which are essential to explain its biological activity. It has been speculated that the cap domain in MGL serves as a lid domain that, once the proteins come into contact with lipid droplets or membranes containing 2-AG, allows the enzyme to unveil its otherwise unreachable hydrophobic active site (interfacial activation). This process should allow the enzyme to exist in two main conformation, a "closed" and an "open" form. Moreover, it has been suggested that the hydrophobic and flexible α 4 helix of MGL cap domain may help the soluble cytosolic form of MGL either to get in close contact with or to anchor in the cytoplasmic membrane, in order to reach its lipophilic substrates. Despite this could explain why MGL was sometimes considered a cytosolic enzyme and sometimes a membrane-associated one,^{7,8} no interfacial activation has been described for MGL.

Beneath the MGL cap domain, a highly hydrophobic pocket connecting the MGL surface to its catalytic site, deeply buried in the protein, has been recognized. This cavity (25 Å in length and 8 Å in width) becomes wider as one moves away from the catalytic triad environment towards the surface of the protein and seems suitable for recognition and accommodation of the long and flexible chain of MGL substrates during their catalyzed hydrolysis process. Another narrow cavity (about 5 Å of diameter) was recognized to connect the active site to the outside of the protein. The architecture formed by loops connecting $\alpha 4$ to $\alpha 5$ and $\alpha 5$ to $\alpha 6$ helices, and the last portion of the $\alpha 5$ helix, is responsible of the formation of this narrow hole. This small channel lies perpendicularly to the trajectory that leads from the catalytic pocket to the membrane-binding site and might act as putative exit door for the glycerol moiety, released after 2-AG hydrolysis (**Figure 2.1**).

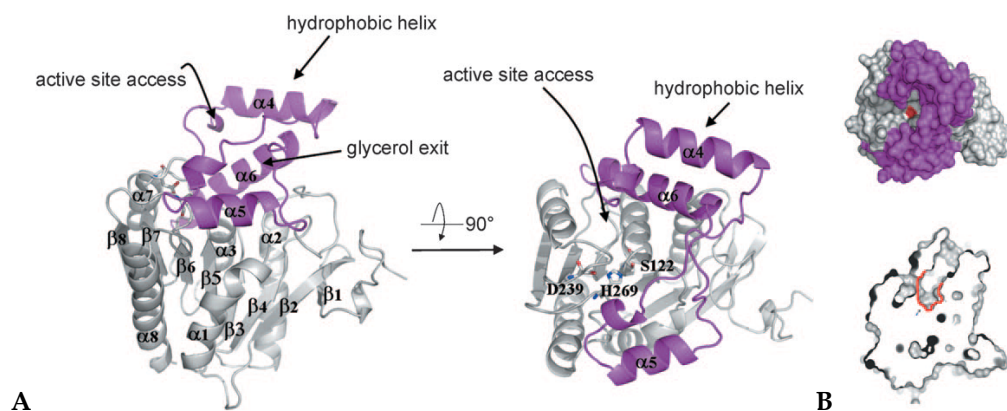


Figure 2.1 Overall structure of hMGL monomer with catalytic triad

represented as sticks, and cap domain colored magenta. (A) Side view (left) and top view (90° rotation), ribbons representation. (B) Top view, surface representation (nucleophilic Serine 122 colored in red) on top and transverse section highlighting the near environment of the nucleophilic serine lined in red (on bottom)

Several studies have revealed that three cysteines (Cys201, Cys208, Cys242, short isoform numbering), which are conserved between the human, rat and mouse orthologs, can interfere with MGL catalytic activity⁹. Cys242 is located within the active site of MGL with its sulfur atom very closely positioned to catalytic Ser122 whereas Cys201 and Cys208 were found quite far away from the catalytic serine. Cys201 and Cys208 were found solvent-exposed and located at the lipophilic tunnel's wide entrance or in the vicinity of the putative glycerol exit hole, respectively (**Figure**

2.2). While their functional role is still not fully understood, it is known from mass-spectroscopy experiments that these residues are not involved in disulfide bridge formation¹⁰. On the other hand, in the first study mentioning the characterization of purified MGL, Tornqvist and Belfrage² reported a more rapid loss of activity when the protein was incubated in absence of a reducing agent. Thus, there is a possibility that one or more of the cysteines play(s) a structural role in the stabilization of MGL active conformation in a redox-dependent manner. The role of these residues on the regulation of the enzyme activity will be further discussed in this chapter (see paragraph 2.3).

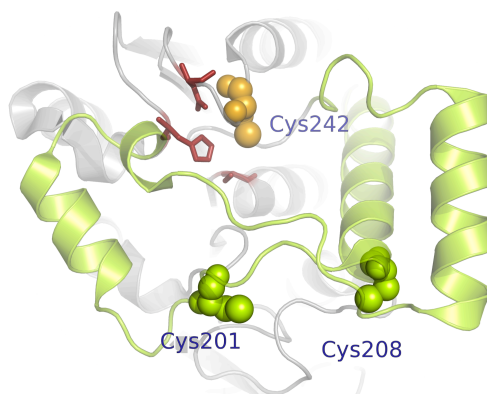


Figure 2.2 Disposition of critical cysteines. Cys242 (orange) is located close to the catalytic triad (red labeled) while Cys201 and Cys208 (green) are solvent-exposed located on the lid domain (from PDB: 3HJU)

2.1.2 Substrate selectivity

MGL is unable to cleave either diacylglycerols or triacylglycerols. Moreover, it is inactive on cholesterol esters and prostaglandinglycerol esters, and despite its known homology with viral and bacterial lysophospholipases, the enzyme does not display any lysophospholipase activity for lysophosphatidylcholine²¹¹. Several authors have studied the impact of the length and the degree of unsaturation of the substrate acyl chain, by measuring either the rate of hydrolysis or the inhibitory potency of the compounds towards the hydrolysis of a known substrate (thus recording more the affinity for the enzyme than its capability to act as a substrate). MGL hydrolyzes efficiently substrates with various number of double bonds (C18:1, C18:2; C20:4) and

acyl chain length (from C8:0 to C18:0)¹². However, the degree of unsaturation was reported to have a certain impact, with MGL displaying a preference for arachidonoylglycerol compared to palmitoylglycerol and, generally speaking, for unsaturated compared to saturated substrates (C16:0, C20:0)^{12b,13}. By measuring the inhibitory potency of a series of trifluoromethylketone derivatives on the 2-AG hydrolase activity from a rat cerebellar cytosolic fraction, Ghafouri and colleagues also observed a marked preference for the arachidonyltrifluoromethylketone and oleoyltrifluoromethylketone compared to the palmitoyl analogue. It is noteworthy to mention that, in several of these studies, data analysis might have been complicated by the fact that protein homogenates are used as the source of enzyme activity, raising concerns about the exact identity of the enzyme whose activity is measured.

2.1.3 Tissue localization of MGL

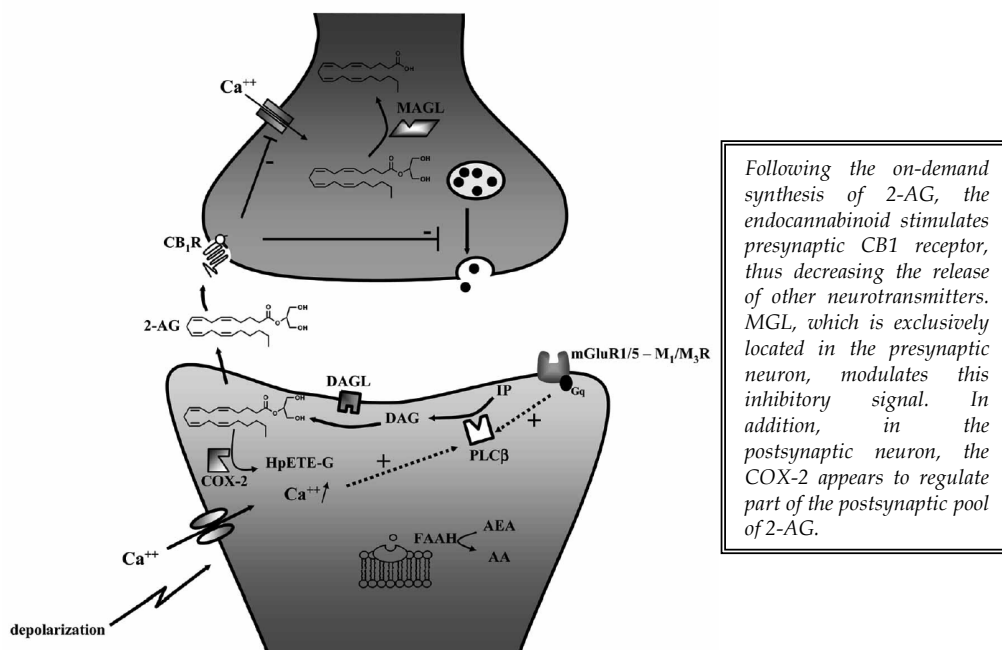
Since its first identification in the adipose tissue^{12a}, MGL localization has extended to many other tissues and is now known to constitute an ubiquitously expressed enzyme. In the rat, high levels of MGL mRNA are found in the adipose tissue, kidney and testis. Other organs include adrenal gland, brain, heart, lung, skeletal muscle, liver, ovary and spleen, in decreasing order of MGL mRNA abundance². In the brain, MGL transcript is also present ubiquitously (cortex, hippocampus, cerebellum, thalamus, striatum) despite lower mRNA levels are found in the brainstem and hypothalamus⁴. In the adipocyte, MGL was found in large lipid-containing aggregates. Besides this, a concomitant distribution in membranes as well as in the cytosol has been reported. In fact, adenovirus-mediated MGL expression in HeLa cells led to immunoreactivity and lipase activity localized in both the cytosolic and plasma membranes/particulate fractions of the cells. Second, in the hippocampus, the ultra-structural distribution of the enzyme is homogenous and no compartmental preference is reported¹⁴. Third, using ABPP-MudPIT (Activity-Based Proteome Profiling with Multidimensional Protein Identification Technology), Blankman and colleagues identified MGL both in membrane and cytosolic mouse brain proteomes⁷. This dual MGL cellular localization may either suggest the intrinsic amphitropic nature of MGL or reflect putative post-transcriptional/post-translational events regulating MGL expression and activity.

2.2 *In vivo* relevance of MGL: biochemical and physiological roles

MGL completes the hydrolysis of triacylglycerols in the adipocyte. It behaves as a selective 2-monoacylglycerol hydrolase, devoid of activity on other lipids. This observation turned out to be of utmost importance in the middle of the nineties, when the endocannabinoid system was brought to light. Indeed, besides its original role in the mobilization of fat in the adipocyte, which led to its discovery in the early sixties, the discovery of 2-arachidonoylglycerol as a key messenger of the endocannabinoid system marked a turning point in the study of MGL. Understanding of the metabolic and (patho)physiological roles of MGL, initially boosted by the selective inhibitor URB602,¹⁵ has been accelerated in recent years due to the synthesis of highly potent and selective *in vivo* efficacious inhibitors such as JZL184 (see below), as well as the development of MGL-deficient (-/-) mice.

Pharmacological or genetic inactivation of MGL lowers 2-AG hydrolytic activity by > 80% in most tissues, including the brain. The remaining 20% of 2-AG hydrolytic activity in brain arises from the serine hydrolases α/β hydrolase domain 6 (ABHD6) and ABHD12.¹⁶ Although ABHD6 and ABHD12 may have roles in 2-AG hydrolysis in certain settings, both genetic inactivation and pharmacological inactivation of MGL lead to dramatic elevations in both bulk levels and depolarization-induced interstitial levels of 2-AG in the brain, confirming that MGL is indeed the primary enzyme involved in degrading 2-AG *in vivo*.^{17,18} MGL blockade resulted in a ~90% inhibition of 2-AG hydrolysis, with the brain showing the most dramatic elevations in 2-AG and peripheral tissues often showing greater changes in other monoacylglycerols, consistent with the lipolytic role of MGL as the final step of triglyceride hydrolysis in peripheral tissues¹⁹.

One of the essential functions of cannabinoid receptors and endocannabinoids is to be involved in synaptic plasticity, as they modulate the signaling mediated by other transmitters²⁰. Depolarization of the postsynaptic neuron, as well as the activation of G_q protein-coupled receptors, results in the activation of endocannabinoid biosynthesis pathways in the postsynaptic neuron.



Following the on-demand synthesis of 2-AG, the endocannabinoid stimulates presynaptic CB_1 receptor, thus decreasing the release of other neurotransmitters. MGL, which is exclusively located in the presynaptic neuron, modulates this inhibitory signal. In addition, in the postsynaptic neuron, the COX-2 appears to regulate part of the postsynaptic pool of 2-AG.

Figure 2.3 The MGL modulates the 2-AG-dependent retrograde signaling in the presynaptic neuron.

The newly synthesized endocannabinoid travels backward, crossing the synaptic space to bind presynaptic CB_1 receptors, inhibiting calcium influx and decreasing the probability of presynaptic vesicle release. Overall, this chain of events leads to a temporary or more persistent dimming of inhibitory or excitatory currents at GABAergic and glutamatergic synapses²¹, respectively (**Figure 2.3**).

The subtlety of this modulation is further strengthened by the intervention of endocannabinoid catabolic pathways, and indeed growing evidence has emerged to assign a key role to MGL in the endocannabinoid-mediated retrograde signaling. In general, retrograde signaling can be investigated electro-physiologically in tissue slices by measurement of processes such as depolarization-induced suppression of excitation (DSE) or inhibition (DSI), with the EC component being demonstrated by the loss of the response in the presence of a CB_1 receptor antagonist such as Rimonabant²². What was not initially clear, however, was whether AEA and 2-AG played separate roles in retrograde signaling pathways in different brain regions, or whether they acted simply as alternative signaling molecules within the same system. Histochemical studies in the rat hippocampus, cerebellum and amygdala indicated that MGL was mainly

presynaptically localized, whereas FAAH was post-synaptic¹⁴ and a presynaptic localization of MGL in the human hippocampus has also been reported²³. A presynaptic localization is more logical in terms of termination of the retrograde signaling molecule, and initial evidence favoring 2-AG over AEA was the finding that the selective FAAH inhibitor URB597 did not affect DSI in the hippocampus. By demonstrating that the selective MGL inhibitor JZL184 extends the duration of DSE in cerebellar neurons and DSE/DSI in hippocampal pyramidal neurons, Straiker and Pan recently provided additional and convincing evidence for the predominance of the 2-AG/MGL pathway over that involving AEA/FAAH in the DSI/DSE process²⁴. MGL^{-/-} mice have also been used to confirm 2-AG involvement in hippocampal DSI and cerebellar DSE²⁵, although the down-regulation of CB₁ receptors seen in these animals is a complicating factor, as is the ability of cyclooxygenase-2 to contribute to the metabolism of ECs in preparations used in electrophysiological experiments.

2.3 Regulatory cysteines of MGL

The evidence for a critical role of cysteines residues inside MGL, able to regulate the activity of the enzyme, came forty years ago when the first MGL inhibitors were described: among them several sulfhydryl-reacting compounds, such as *p*-chloromercuribenzoate (pCMB), mercurichloride (HgCl₂) and *N*-ethylmaleimide (NEM), are comprised^{2,26}. Several studies were aimed at the identification of this regulatory cysteines and the elucidation of their role in the catalytic activity of MGL.

There are six cysteine residues in rat and mouse MGL, four of which are conserved in their human ortholog. A homology model of MGL constructed using as a template the crystal structure of chloroperoxidase L from *S. lividans* (**Figure 2.4**) positioned Cys242 in close proximity of a histidine residue that is part of the catalytic triad. Residues Cys201 and Cys208 were located within the lid domain, wherefrom they might be able to extend their sulfhydryl groups towards the substrate-binding site, while residues Cys32 and Cys55 were positioned in regions that could hardly interact with the catalytic site. While this computational model provided a first tentative explanation of the roles exerted by the three “regulatory” cysteines (Cys201, Cys208 and Cys242) on

MGL activity, the actual position of Cys201 and Cys208 within the lid domain was later revealed by crystal structures of human MGL.

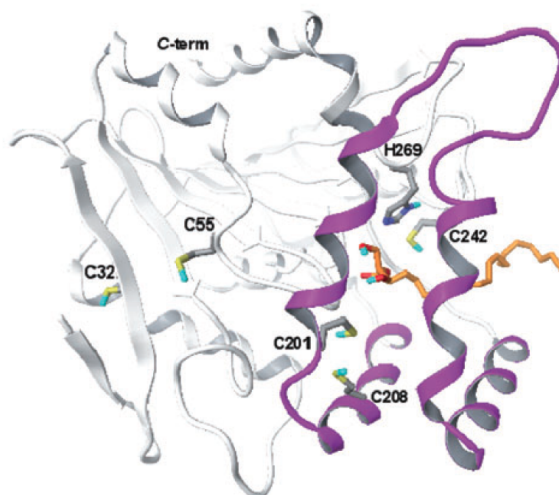


Figure 2.4 Computational three-dimensional model of rat MGL. The α/β core structure of the enzyme, shown in white, contains the catalytic triad. 2-AG is shown in orange. The lid domain is in magenta

The role of Cys242 was further elucidated by the work of Saario *et al.*⁹, investigating maleimides as MGL inhibitors. This class of compounds revealed to be covalent inhibitors able to alkylate the enzyme through a Michael addition reaction (for detail see paragraph 2.4.2). Zvonok *et al.*²⁷ through a ligand-assisted MS-based approach demonstrated that MGL inhibition by maleimides involves covalent Michael addition to Cys208 and Cys242, while the adduct fragments with Cys32 or Cys201 were not found in human MGL. On the other hand, studies with mutants of rat MGL²⁸ indicate that Cys201 could also be involved in the interaction with maleimides: the exact identity of cysteine residues targeted by this compounds is still debated. In the same studies, conducted by King and colleagues in 2009,²⁸ a series of rat MGL mutants in which individual cysteines were replaced with glycines was generated to evaluate the impact of mutation on MGL activity. Wild-type (WT) and mutant proteins displayed comparable levels of heterologous expression. Nevertheless, the Cys242G mutation produced a striking reduction in MGL activity (**Figure 2.5A**), which was due to a decrease in maximal reaction velocity rather than a change in Michaelis constant, confirming the critical role of Cys242 on MGL activity.

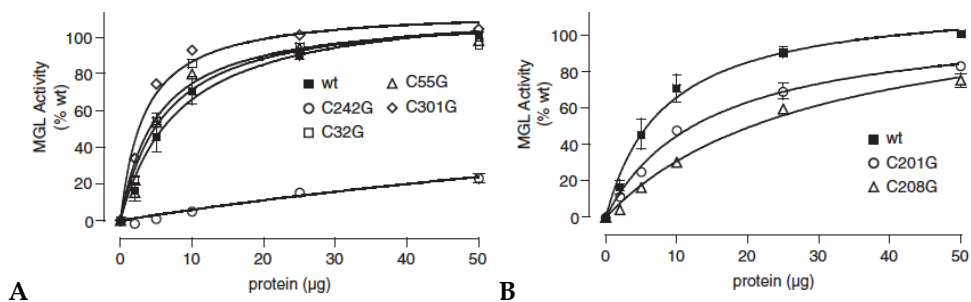


Figure 2.5 Effects of cysteine mutations (to glycine) on MGL activity. **(A)** MGL activity in MGL mutants C242G, C32G, C55G and C301G. **(B)** MGL activity in MGL mutants C201G and C208G.

Results are expressed in percentage of wild-type (WT) activity (50 mg protein) (mean \pm SEM, n = 3)

Mutations affecting Cys201 and Cys208 also caused significant decreases in enzyme activity, albeit smaller than that produced by Cys242G (**Figure 2.5B**). By contrast, mutations to cysteines located distal to the active site of MGL (Cys32G, Cys55G and Cys301G) had no effect on MGL activity. These results highlight the important functional role of cysteine residues proximal to the MGL active site, as previously suggested by computational and structural studies.

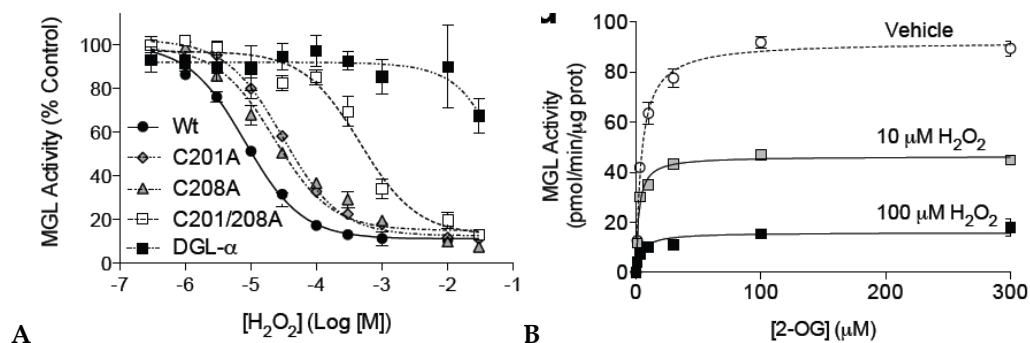
2.3.1 Sensitivity of MGL to oxidizing agents

Several studies have revealed the role of cysteines as redox-sensitive regulatory switches caused by the generation of reactive oxygen species (ROS) and the presence of oxidized thiols²⁹. Oxidation of such cysteines is converted into signals that control cell regulatory pathways and induction of gene expression. A variety of proteins, including transcription factors, molecular chaperones and protein tyrosine phosphatases, are regulated via redox processes. Common mechanisms underlie the sensitivity of cysteines to redox, such as proximity to polar and charged groups, and signal transduction is exerted via conformational changes that are conferred by the formation of disulfide and cyclic sulfenamide covalent bonds, and sulfinic, sulfenic and sulfonic acids.

Nitric oxide (NO) is recognized as one of the most important ROS and many enzymes with a reactive sulfhydryl group have been shown to be inhibited by NO reactive

species³⁰. Saario and colleagues⁹ determined the activity of MGL in the presence of NO donors *S*-nitrosoglutathione (GSNO), *S*-nitrosocysteine (CysNO), and sodium nitroprusside (SNP). However, no significant changes in the enzyme activity were shown by any of these NO species. This result suggests that MGL-like activity is not under NO regulation, a finding in agreement with the observation that inhibition of nitric oxide synthase by nitro L-arginine methyl ester and L-methylarginine has no effect on MGL activity in syn-aptoneurosomes³¹.

Intensive research about the action of the second messenger hydrogen peroxide (H₂O₂)³² on MGL have been recently conducted by Piomelli's research group (University of Irvine, California) in collaboration with the research group where I spent my PhD period at the University of Parma. Data reported in this paragraph are strictly confidential and have been recently submitted for publication. H₂O₂ modifies protein function through reversible oxidation of cysteine thiol groups to sulfenic acid (-SOH)³³. To test the idea that peroxide-dependent cysteine sulfenylation might regulate MGL activity and 2-AG signaling, MGL was exposed to concentrations of H₂O₂ that modify protein function without causing irreversible oxidative damage³⁴. H₂O₂ inhibited MGL with an IC₅₀ of 11.6±0.8 μM (Figure 2.6A). The inhibition displayed non-competitive kinetics (Figure 2.6B), and was reversible upon enzyme dilution (Figure 2.6D). Site-directed mutagenesis was helpful to determine whether regulatory cysteines contribute to peroxide-dependent MGL inhibition. Replacing either Cys201 or Cys208 with alanine caused a rightward shift in H₂O₂ potency (Figure 2.6A). An even more pronounced shift was observed when both C201 and C208 were mutated, whereas replacing Cys242 with alanine or serine had no effect (Figure 2.6C).



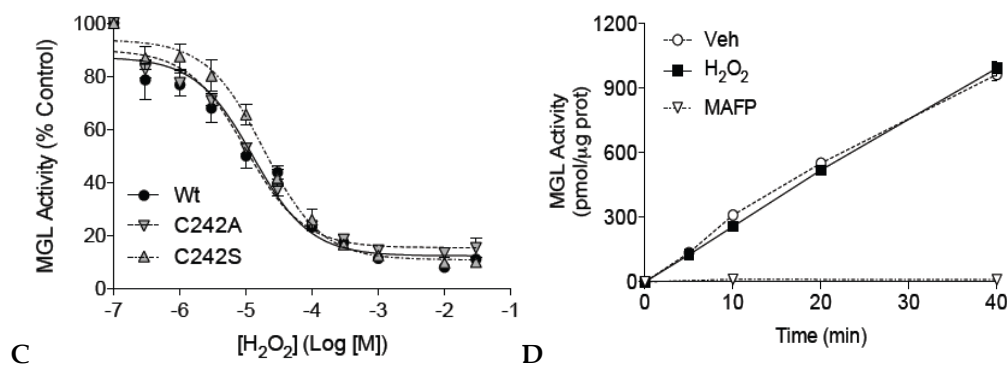


Figure 2.6 Hydrogen peroxide inhibits MGL. (A) Effects of H₂O₂ on wild-type MGL (circles), MGL mutants C201A (diamonds), C208A (triangles) or C201/208A (empty squares) and DGL-α (full squares).

(B) Michaelis-Menten kinetics of MGL inhibition by H₂O₂ (vehicle: open squares). (C) Effects of H₂O₂ on MGL (circles) or DGL-α (squares) activity. (D) Rapid dilution of MGL incubated with vehicle (circles), H₂O₂ (squares; 10 μM final), or irreversible inhibitor methylarachidonylfluorophosphonate (triangles, 23 nM final)

These findings suggest that H₂O₂ inhibits MGL through an allosteric reversible mechanism involving Cys201 and Cys208. To determine whether MGL is a substrate for sulfenylation, purified enzyme was incubated with H₂O₂ in the presence of dimedone, which reacts with short-lived sulfenic acid groups forming stable thioethers (**Figure 2.7**). Dimedone was exclusively bound to peptides containing Cys201 or Cys208 (after trypsin digestion and LC/MS analysis) identifying cysteines 201 and 208 in MGL as targets for peroxide-dependent sulfenylation.

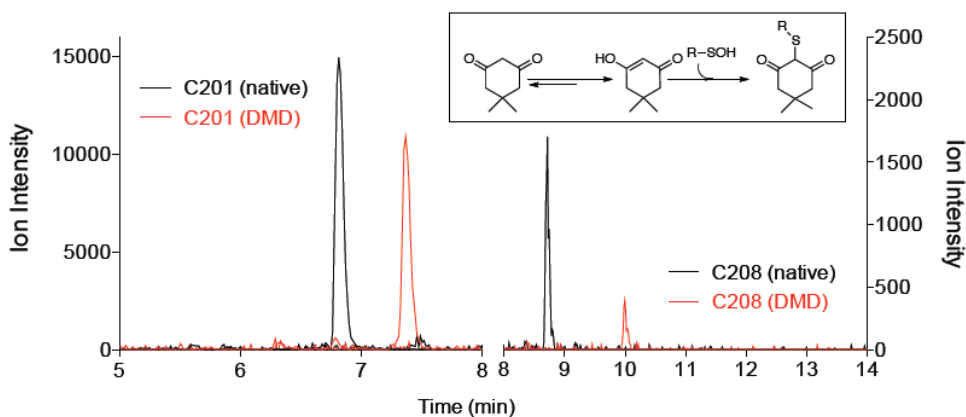


Figure 2.7 Hydrogen peroxide sulfenylates MGL. Extracted-ion currents of native (black) and dimedone (DMD)-containing (red) peptides obtained by digestion of rat MGL exposed to H₂O₂ (10 μM, 1h)

Piomelli and coworkers performed experiments on rat cortical neurons to capture transient sulfenylation-dependent changes on MGL activity. Addition of H_2O_2 resulted in a decrease of MGL activity (**Figure 2.8A**) and in an elevation of 2-AG levels (**Figure 2.8B**). Additional evidence that redox status affects MGL activity was obtained by blocking glutathione biosynthesis with L-buthionine sulfoximine (BSO). Exposing cortical neurons to BSO depleted intracellular glutathione (**Figure 2.8C**), lowered MGL activity (**Figure 2.8D**) and increased 2-AG content (**Figure 2.8E**).

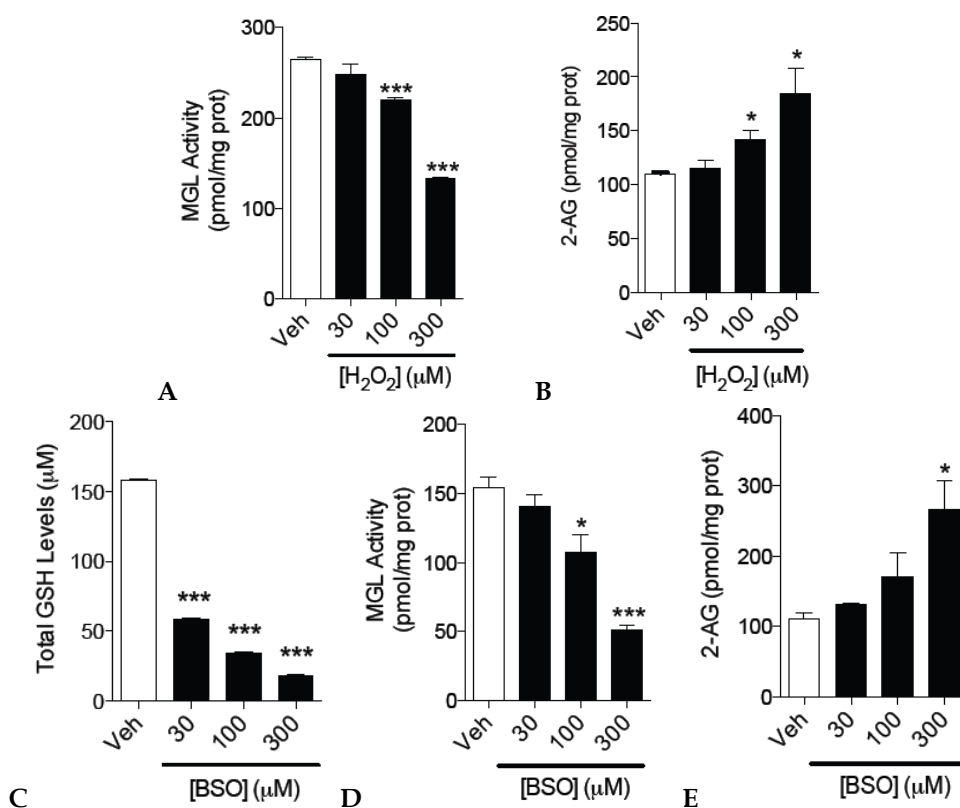


Figure 2.8 Effects of H_2O_2 (filled bars) or vehicle (open bars) on (A) MGL activity, (B) 2-AG levels. Effects of BSO (filled bars) or vehicle (open bars) on (C) GSH levels, (D) MGL activity and (E) 2-AG levels in neurons.

These evidences suggest that MGL activity is finely regulated by the redox status of the cell: the blockade of MGL catalysis results in an enhancement of 2-AG levels that could exert a neuroprotective action in response to oxidizing stress events. Further evidences confirmed this hypothesis displaying that MGL sulfenylation impairs 2-AG

degradation and also enhance 2-AG signaling. Neuro-2a cells were incubated with high levels of H₂O₂ and evaluation of cellular damage using LDH was assessed (**Figure 2.9**). The toxic effect of hydrogen peroxide was heightened by MGL overexpression (**Figure 2.9** - entry 2) and reduced by treatment with the MGL inhibitor JZL184 (**Figure 2.9** - entry 4) able to elevate 2-AG levels. Moreover H₂O₂ toxicity was enhanced by CB₁ blockade using the selective antagonist Rimonabant, only when MGL was not overexpressed (**Figure 2.9** - entry 3, Mock) or when it was inhibited by JZL184 (**Figure 2.9** - entry 6), but not by CB₂ blockade (antagonist AM630). These observations suggest that peroxide-dependent MGL deactivation enhances CB₁-mediated 2-AG signaling and the possible neuroprotective role of 2-AG.

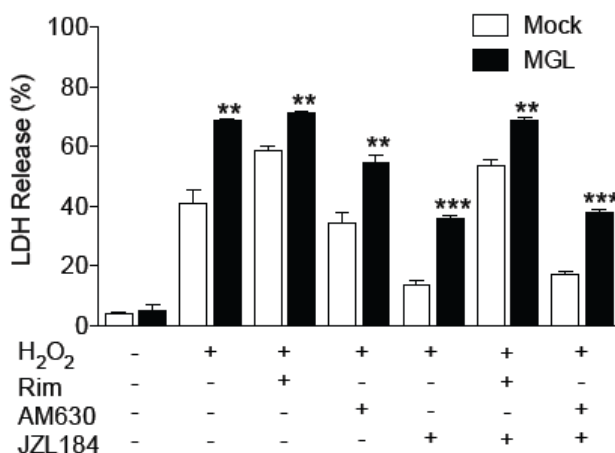


Figure 2.9 Hydrogen peroxide enhances neuronal 2-AG signaling.

Effects of H₂O₂ (300 μM), alone or combined with CB₁ antagonist Rimonabant, CB₂ antagonist AM630 or MGL inhibitor JZL-184 (1 μM), on LDH release

In conclusion, three residues of cysteine are fundamental in the regulation of MGL activity. Cys242 influence directly the hydrolyzing activity of the enzyme by interacting with the catalytic triad. Cys201 and Cys208 instead, can be considered molecular switches that finely tune MGL catalytic activity by undergoing oxidation or reduction in response to the redox status of the cell.

2.4 MGL inhibition strategies

The role of MGL as the key hydrolyzing enzyme of 2-AG in the endocannabinoid system has only recently been recognized. Therefore, the design and development of potent, selective MGL inhibitors is still in its infancy. Knowledge about the catalytic mechanism and substrate specificity are important factors to be taken into consideration, when designing new enzyme inhibitors.

While the first selective inhibitors of MGL were derivatives of the carbamate URB602,^{15,35} the most recent MGL inhibitors can be classified into three categories based on their mechanism of action:

1. compounds targeting the catalytic serine: covalent modifiers able to interact with Ser122 within the active site;
2. compounds targeting the critical cysteines: covalent modifiers able to interact with critical Cys242/Cys201/Cys208. These include iso- and benzisothiazolinones;
3. triterpenoids: non-covalent binders of MGL able to interact with Cys201 and Cys208.

To date, most MGL inhibitors are covalent binders able to generate an adduct with one of the nucleophilic residues of the target. Among them is it possible to identify miscellaneous reactive "warheads", from carbamoylating to disulfide-forming reactive fragments. A classification of available covalent MGL inhibitors can be carried out considering the reversibility of established inhibitor-enzyme interaction that mainly depend from the chemical and biological stability of established covalent interactions. In this way, among described inhibitors, alkylating agents form the most stable covalent interaction and can be considered as irreversible inhibitors. Carbamoylating agents bind MGL forming middle-range stable covalent bonds and provide MGL inhibition that range from irreversible (at least from a pharmacological point of view) to partially reversible. Finally, despite disulfide bond forming agents and acylating agents should form the most easily breakable covalent interactions, the reversibility of their action can easily range from irreversible to completely reversible, depending on the macro- or micro-environment in which their respective covalent interactions take place.

Triterpenoids are way ahead from the rest of MGL inhibitors because their mechanism of action is exerted by formation of non covalent interaction involving lid domain cysteines and they represents therefore the first-class of non covalent modifiers of the enzyme. In the next paragraphs I will provide an exhaustive description of available MGL inhibitors.

2.4.1 Targeting the catalytic serine

This class of MGL inhibitors is represented by compounds able to covalently bind MGL catalytic Ser122, directly disrupting the MGL hydrolytic activity. Among them, despite these compounds provide the most effective MGL inhibition, only few derivatives have shown high selectivity for the desired target.

For instance, highly reactive serine-binding fluorophosphonates or fluorosulphonates are able to block MGL activity³⁶ with high potency but are also able to inhibit other serine-dependent enzyme inside and outside the endocannabinoid system with comparable efficiency: compounds including trifluoromethylketones (arachidonoyltrifluoromethylketone, ATFMK; oleoyltrifluoromethylketone; palmitoyltrifluoromethylketone) and the irreversible inhibitor methylarachidonylfluorophosphate (MAFP) (**Figure 2.10**) were identified as MGL inhibitors. Despite the fact that the voluminous and lipophilic arachidonyl chain would be likely to provide MAFP and ATFMK an improved selectivity profile versus proteins belonging to other systems, these compounds also display several off-targets. MAFP was first reported as a phospholipase A2 inhibitor and inhibits FAAH and MGL with similar potencies, while ATFMK acts on MGL, FAAH and CB₁ cannabinoid receptor³⁷. This produces an undesirable complex pharmacological response from which is difficult to selectively define the 2-AG contribution to the observed biological effects. Furthermore, the ability of these fluorophosphonate derivatives to inhibit multiple serine-dependent enzymes is often responsible to high off-target toxicity, sometimes so severe to kill the treated subject. Despite the low target selectivity shown by these labeling compounds does not allow their use as drugs and limit their use as pharmacological tools, their impressive MGL inhibitory potency have induced many scientists to develop more druggable and specific serine-trapping agents.

Nithipathikom developed a series of trifluoromethylketones with a β -thioether moiety³⁸. A subset of these compounds, among which octylthiotrifluoropropan-2-one (OTFP) (**Figure 2.10**), increased 2-AG levels in prostate cancer cell lines revealing the anti-invasive effect of 2-AG. However, their inhibitory potency was only tested in crude cytosolic and membrane homogenates, and it is likely that these compounds unselectively target other esterases and probably the FAAH, since it is known that trifluoromethylketone scaffold constitutes a good template for FAAH inhibition³⁹.

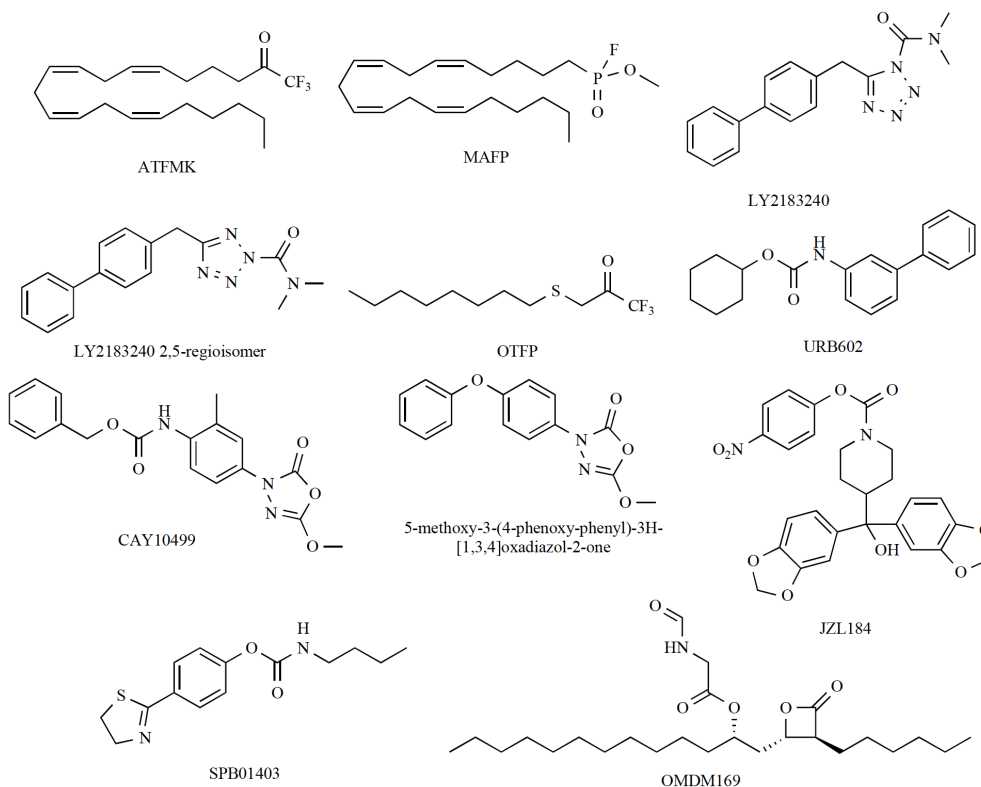


Figure 2.10 Several MGL inhibitors targeting the nucleophilic serine (Ser122)

Recently a series of carbamoyl tetrazoles and carbamates have been reported that have shown to covalently inhibit hMGL with high potency and with enhanced selectivity. Carbamoyl tetrazole LY2183240 (**Figure 2.10**) was first described as an inhibitor of anandamide transporter ($IC_{50}^{uptake} = 15 \text{ nM}$)⁴⁰. However, it has been subsequently reported that this property could result from its ability to potently and irreversibly inhibit FAAH as an off-target ($IC_{50}^{FAAH} = 21 \text{ nM}$). LY2183240 was also shown to inhibit

other lipases such as MGL ($IC_{50}^{MGL} = 5.3 \text{ nM}$)⁴¹. Indeed, as pointed out by Ortar and colleagues, the compound studied by Alexander and Cravatt likely represents a mixture of the 1,5- and 2,5-regioisomers of LY2183240⁴². The authors thus synthesized and purified both isomers and other tetrazole derivatives, and measured their inhibitory potency on the MGL and the FAAH, as well as on the anandamide transport process. On the one hand, the 1,5-regioisomer only slightly inhibits MGL, whilst being a much more potent inhibitor of anandamide degradation and transport ($IC_{50}^{FAAH} = 2.1 \text{ nM}$; $IC_{50}^{uptake} = 15 \text{ nM}$; $IC_{50}^{MGL} = 8100 \text{ nM}$). On the other hand, the 2,5- isomer interacts with a much higher affinity with MGL, but unfortunately lacks selectivity versus FAAH ($IC_{50}^{FAAH} = 33 \text{ nM}$; $IC_{50}^{uptake} = 998 \text{ nM}$; $IC_{50}^{MGL} = 20 \text{ nM}$). In a mass spectrometry analysis, the binding mode of the 2,5-regioisomer to recombinant human MGL was investigated.

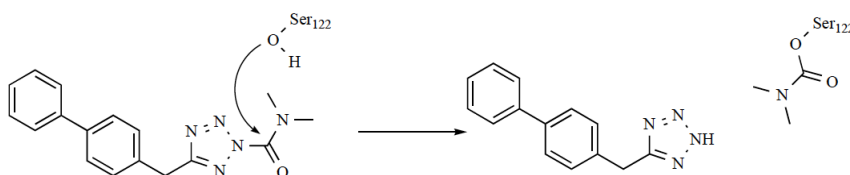


Figure 2.11 Mechanism of MGL inhibition exerted by LY2183240 2,5-regioisomer

Inhibition occurs through the attack of the Ser122 hydroxyl group (**Figure 2.11**), which leads to the formation of a carbamoylation product containing the inhibitor dimethylamino group, as demonstrated by the +71 mass increment of the tryptic fragment containing this residue. The biphenylmethyl tetrazole moiety thus constitutes the leaving group during this reaction²⁷.

Following the success associated with the use of carbamates in the development of FAAH inhibitors, Hohmann and colleagues screened a library of *O*-biphenyl and *N*-biphenyl carbamates and reported the development of URB602 (**Figure 2.10**) as the first selective inhibitor of 2-AG degradation, although its potency remained limited ($IC_{50} = 28 \text{ }\mu\text{M}$ and $223 \text{ }\mu\text{M}$ on rat brain and pure recombinant rat MGL, respectively)⁴³. Despite the fact that it was reported to inhibit FAAH and MGL with similar potencies *in vitro*,⁴⁴ it was shown to lead to the selective accumulation of 2-AG (not AEA) in rat hippocampal slices or after injection in the periaqueductal gray.⁴³ Nevertheless, URB602 was used to demonstrate the implication of the endocannabinoid system in

stress-induced analgesia, it exhibited CB₂-dependent analgesic and anti-inflammatory properties in a model of inflammation⁴⁵ and it showed significant protection from the long-term consequences of neonatal hypoxic-ischemic brain injury in rats.⁴⁶ Other carbamates that led to MGL inhibition include SPB01403 (IC₅₀ = 31 μM on rat cerebellar membranes)⁴⁷, CAY10499 (IC₅₀ = 0.5 μM to 20 nM on the pure human MGL, depending on the preincubation time)⁴⁸, and 5-methoxy-3-(4-phenoxyphenyl)-3H-[1,3,4]oxadiazol-2-one (IC₅₀ = 78 nM)⁴⁹ (**Figure 2.10**). However, SPB01403 also inactivates FAAH with a higher affinity (IC₅₀ = 0.52 μM on rat brain homogenates), and the two latter compounds lack selectivity over FAAH and, at least for CAY10499, the hormone sensitive lipase.

One of the most promising breakthroughs in the quest for selective MGL inhibitors came from the screening of a carbamate library and the development of a series of derivatives of this scaffold by Cravatt's team^{17,50}.

This resulted in the low nanomolar inhibitor JZL184 (**Figure 2.10**), which exhibits a comfortable selectivity versus FAAH *in vitro* (IC₅₀ = 6 nM and 4 μM for recombinant MGL and FAAH expressed in COS7 cells, respectively). The inhibition mechanism involves the carbamoylation of the Ser122, with *p*-nitrophenol as the leaving group (**Figure 2.12**).

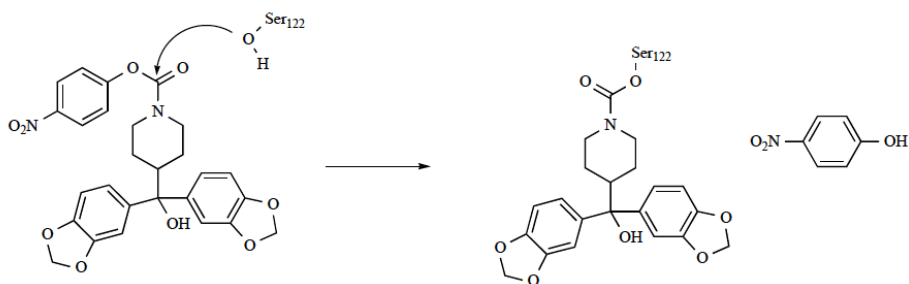


Figure 2.12 Mechanism of MGL inhibition exerted by JZL184

Enzymatic assays performed on brain membrane proteome from JZL184-treated mice confirmed the nearly complete and rather selective inhibition of MGL and 2-AG hydrolysis (75% inhibition at 4 mg/kg). Note that, depending on the dose, FAAH was inhibited as well *in vivo* although incompletely and to a lesser extent than MGL. The compound displays an interesting interspecies selectivity, being ten times more potent on human and mouse MGL than on the rat ortholog. As expected, JZL184

administration resulted in a dramatic concentration-dependent increase of brain 2-AG levels. Accumulation of *N*-acylethanolamines (in particular AEA) did not occur, unless at the highest dose (40 mg/kg). Using microdialysis, the authors also measured the signaling-competent concentrations of endocannabinoids and found that JZL184 enhances 2-AG pools in the synapsis, while leaving AEA levels unchanged.

The accumulation of 2-AG *in vivo* is accompanied by a strong CB₁-dependent analgesic effect in different models of nociception (tail immersion, phase I and II of the formalin test, as well as acetic acid-induced tail writhing). Another key finding of this study is the observation that JZL184 administration results in a subset of effects belonging to the classical “tetrad”, i.e. a CB₁ dependent hypothermia and hypomotility (but not catalepsy), thus sharing common properties with direct cannabinoid agonists, and above all rising crucial question regarding the clinical use of MGL inhibitors.

Di Marzo's team reported the development of the micromolar inhibitor OMDM169⁵¹ (**Figure 2.10**). Unlike several of the above-mentioned compounds, OMDM169 displays a good selectivity for 2-AG versus AEA degradation (IC₅₀= 0.13-0.34 μM on 2-AG hydrolysis in rat brain and rat cerebellum preparations; IC₅₀ = 3.0 μM on rat FAAH). Interestingly, OMDM169 is reversible and its inhibitory potency varies depending on the enzyme source and the species, as the compound inactivates 2-AG hydrolysis about ten times more strongly in rat than in mouse tissues (IC₅₀ = 0.92 to 7.53 μM in mouse). Considering the multiple pathways that inactivate 2-AG *in vitro*, the authors also measured the ability of OMDM169 to inhibit pure recombinant human MGL (IC₅₀ = 0.89 μM). Despite the fact that the whole spectrum of off-targets has not yet been fully investigated, several enzymes may already be pointed out. Apart from these issues, OMDM169 was tested *in vivo* for its antinociceptive properties. In the formalin test, the compound (2.5-5 mg/kg, i.p.) promoted analgesia in the second phase of nociception. This effect was accompanied by an increase in 2-AG levels in the ipsilateral paw that received formalin injection. Consistently, OMDM169 failed to elevate 2-AG level in untreated N18TG2 neuroblastoma in culture but increased its concentration when endocannabinoid biosynthesis was induced by ionomycin. This observation therefore supports the idea that inhibitors of endocannabinoid degradation could help to gain time or spatial selectivity over direct cannabinoid receptors agonists and avoid the central side effects associated with the use of the latter compounds. Unexpectedly enough given its *in vivo* pharmacological effects,

OMDM169 failed to produce a significant inhibition of 2-AG hydrolase activity in brain and paw skin from treated mice, reasons for this remaining unclear.

2.4.2 Targeting critical cysteines

The role of critical cysteines on MGL activity has been elucidated in this chapter (see paragraph 2.3). Several inhibitors affect MGL activity by interacting with these residues.

As discussed before, Saario and colleagues⁹ synthesized a series of maleimide derivatives. *N*-arachidonylmaleimide (NAM) (**Figure 2.13**) was the most potent compound of the set, with an IC₅₀ value of 0.14 μM on rat cerebellar membranes. The mechanism of inhibition exerted by NAM involves a Michael addition on one or more sulfhydryl residue(s) with a preference for Cys242 (**Figure 2.14**). Using ABPP, Blankman and colleagues confirmed the relative NAM selectivity for MGL, although a partial inhibition of FAAH and ABHD12 was also observed at higher doses. Hence, the compound was used as a pharmacological tool to unveil the consequences of a disruption of MGL activity and to elucidate the respective effects of 2-AG versus AEA⁵². However, given the fact that *in vivo*, NAM is likely to result in the covalent modification of a huge number of proteins, not necessarily in the active site, there is little chance that this compound would be a good candidate for drug development.

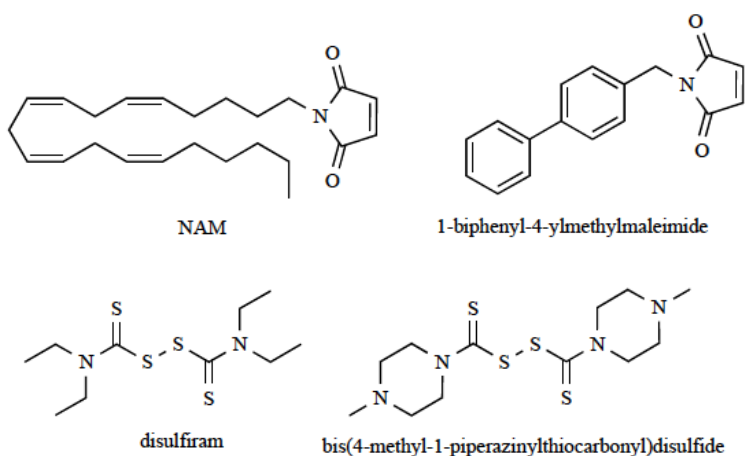


Figure 2.13 Most representative examples of inhibitors targeting one or several cysteine residue(s)

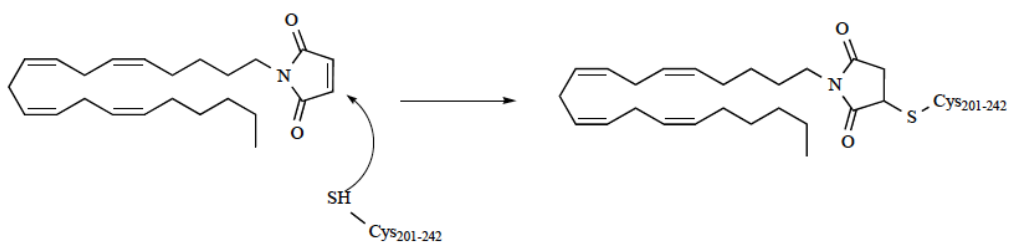


Figure 2.14 Mechanism of MGL inhibition by NAM

Noteworthy, other groups subsequently reported higher IC_{50} values for this class of compounds. Matuzsak *et al.* reported the synthesis of a series of maleimides⁵³: among them 1-biphenyl-4-ylmethylmaleimide (**Figure 2.13**) inhibits pure human MGL with an IC_{50} of 790 nM, whilst being 2 orders of magnitude less potent on the FAAH. Disulfiram (**Figure 2.13**), a well known aldehyde dehydrogenase inhibitor used since decades to treat alcoholism, was reported to inhibit human MGL with micromolar affinity⁵⁴. Recently, Kapanda and colleagues⁵⁵ also reported the development of a series of MGL inhibitors based on this template. The most potent representative, bis(4-methyl-1-piperazinylthiocarbonyl) disulfide (**Figure 2.13**), displayed an IC_{50} of 110 nM on the pure enzyme, and a more than 1000 selectivity ratio for MGL compared to FAAH. Using dithiothreitol and site-directed mutagenesis, the inhibition was shown to occur through an interaction with Cys242 and Cys208.

While investigating a series of sulfhydryl-reactive agents, King and colleagues²⁸ have reported the ability of iso- and benzisothiazolinones derivatives to inhibit rat MGL. Because of the central role of these two classes of MGL inhibitors in this PhD research project, they deserve a detailed statement provided in the next paragraph.

2.4.3 Iso and Benzisothiazolinones as MGL inhibitors

This inhibitor class, recently discovered by King and coworkers, is populated by disulfide-bond forming compounds such as isothiazol-3(2*H*)-one (ITZ) and benzo[*d*]isothiazol-3(2*H*)-one (BTZ) derivatives. These compounds were discovered as “hit compounds” during the screening of a short panel of cysteine trapping derivatives toward recombinant rat MGL. 2-octylisothiazolin-3-(2*H*)one (octhilonone) (**Figure 2.15**) was potent in inhibiting rat MGL, that is, IC_{50} in nM range (88 nM). Preliminary SAR

studies, which investigated the effects of select chemical modifications of octhilinone on MGL inhibition, revealed that substitution of the *n*-octyl group with a methyl group (2-methylisothiazol-3(2*H*)-one) resulted in a three-fold decrease in potency compared with the parent compound ($IC_{50} = 249$ nM). By contrast, introduction of a larger and more lipophilic oleoyl group at the same site ((*Z*)-2-(octadec-9-en-1-yl)isothiazol-3(2*H*)-one) resulted in a two fold increase in potency ($IC_{50} = 43$ nM). Replacement of the isothiazolinone moiety with a benzisothiazolinone group (2-octylbenzo[*d*]isothiazol-3(2*H*)-one) also yielded a potent inhibitor ($IC_{50} = 59$ nM) (**Figure 2.15**).

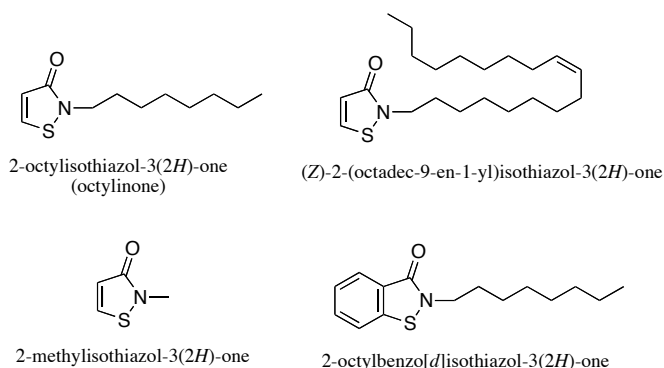


Figure 2.15 Iso and benzisothiazolinones as MGL inhibitors

Rapid dilution assay was performed to assess whether octhilinone inhibits MGL through a reversible or irreversible mechanism. As shown in **Figure 2.16A**, the dilution produced a partial recovery of enzyme activity. The partial reversibility of the effect of octhilinone is not consistent with the chemical reactivity of a Michael addition product, suggesting that octhilinone may form instead a disulfide bond with a cysteine residue in MGL (**Figure 2.16B**). Two findings support this possibility. First, the benzisothiazolinone, which cannot undergo Michael addition, was as potent as octhilinone at inhibiting MGL activity. Second, adding the reducing agent DTT (10 mM) to the incubation mixture produced a 47-fold decrease in the inhibitory potency of octhilinone (**Figure 2.16C**) without affecting basal MGL activity. A glycine-based site-direct mutagenesis scanning revealed that octhilinone interacts with Cys208 (**Figure 2.17A**) without interfering with other critical cysteines (**Figure 2.17B**). The interest for this chemical family was highlighted by the work of Matuszak and colleagues on human MGL⁵⁶. They confirmed the mechanism of action, proposed by

King *et al.*, on human MGL: after inhibition exerted by octhilinone or 2-octylbenzo[*d*]isothiazol-3(2*H*)-one (**Figure 2.15**) the activity of the enzyme was restored with increasing DTT concentrations, confirming a redox-based mechanism of inhibition.

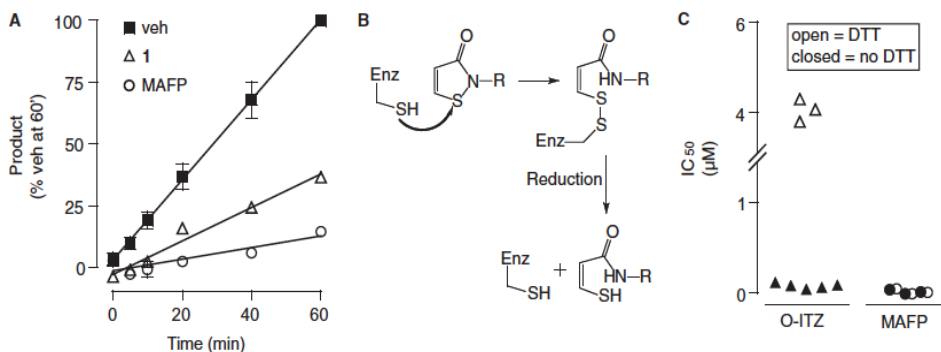


Figure 2.16 Reversibility of (MGL) inhibition by octhilinone. (A) Rapid dilution assays of purified MGL in the presence of vehicle (squares), octhilinone (triangles) or MAFP (circles). (B) Scheme illustrating the formation of a disulfide adduct between octhilinone and cysteine. (C) Effects of dithiothreitol (DTT, 10 mM) on inhibitory potency of octhilinone and MAFP towards purified MGL

They confirmed the previous observations as the inhibitory potency of octhilinone was reduced when Cys208 was mutated to alanine, compared to wild-type MGL. Additionally, its potency was also reduced in the same fashion when Cys242 was mutated. For compound 2-octylbenzo[*d*]isothiazol-3(2*H*)-one (**Figure 2.15**) both Cys201 and Cys242 mutations reduced its potency while the mutation of Cys208 did not seem to affect its inhibition properties. This results point out the classes of ITZ and BTZ as promising new partially-reversible, disulfide-forming inhibitors of MGL.

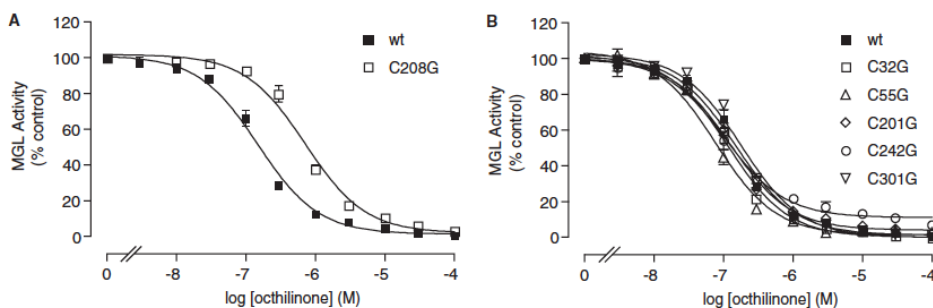


Figure 2.17 Effect of cysteine mutations on MGL inhibition by octhilinone

2.4.4 Triterpenes as MGL inhibitors

Triterpenoids are structurally diverse organic compounds, characterized by a basic backbone modified in multiple ways, allowing the formation of more than 20000 naturally occurring triterpenoid varieties. Several triterpenoids, including ursolic and oleanolic acid, betulinic acid, celastrol, pristimerin, lupeol, euphol and avicins possess antitumor and anti-inflammatory properties. Among them, pristimerin and euphol (**Figure 2.18A**) have recently gained interest as new promising MGL inhibitors⁵⁷.

Pristimerin, a natural triterpenoid, elicits cellular responses closely resembling those elicited by proteasome inhibitors, such as the rapid induction of heat shock proteins (HSPs), activating transcription factor 3 (ATF3), and C/EBP homologous protein (CHOP). Pristimerin also inhibits NF- κ B activation suppressing the activation of constitutive NF- κ B in myeloma cells. Consistent with this, pristimerin has been shown to be potently and selectively lethal to primary myeloma cells ($IC_{50} < 100$ nM) and to inhibit xenografted plasmacytoma tumors in mice⁵⁸. Pristimerin is also known as an antifungal, antimicrobial, and anti-inflammatory plant compound with an effect on the iNOS system in macrophages⁵⁹.

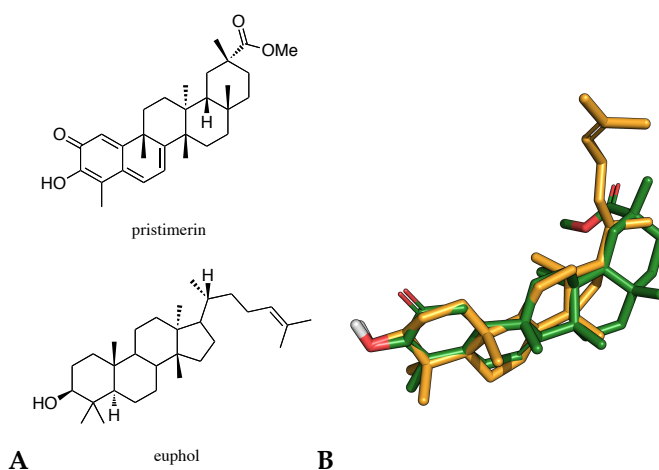


Figure 2.18 (A) Chemical structure of pristimerin and euphol. (B) Three dimensional superposition of euphol (gold) and pristimerin (green)

The tetracyclic triterpene alcohol, euphol, is the main constituent in the sap of *Euphorbia tirucalli*. Previous studies have demonstrated that euphol exerts anti-inflammatory effects associated with the inhibition of the activation of nuclear factor-

κB^{60} , the down-regulation of tumor necrosis factor- α and cyclooxygenase-2⁶¹. In addition to antiviral and anti-inflammatory effects, antitumor effects of euphol have also been observed⁶². Furthermore, recent studies also indicate that euphol has a systemic, spinal and supraspinal antinociception action: the antinociceptive effect of euphol depends largely on its ability to interact with cannabinoid system via both CB₁ and CB₂ dependent mechanism⁶³.

From the screening of a chemical library, pristimerin emerged as inhibitor of purified MGL with a median effective concentration (IC₅₀) of 93 nM. Enzyme assays showed that also euphol, having a 3D structure similar to that of pristimerin (**Figure 2.18B**), inhibits purified MGL with an IC₅₀ of 315 nM. Rapid dilution assays of the MGL-pristimerin and the MGL-euphol mixtures resulted in a virtually complete recovery of catalytic activity of the enzyme, with a reduction of V_{MAX}, which is suggestive of a reversible non-competitive inhibition exerted by both compounds (**Figure 2.19**).

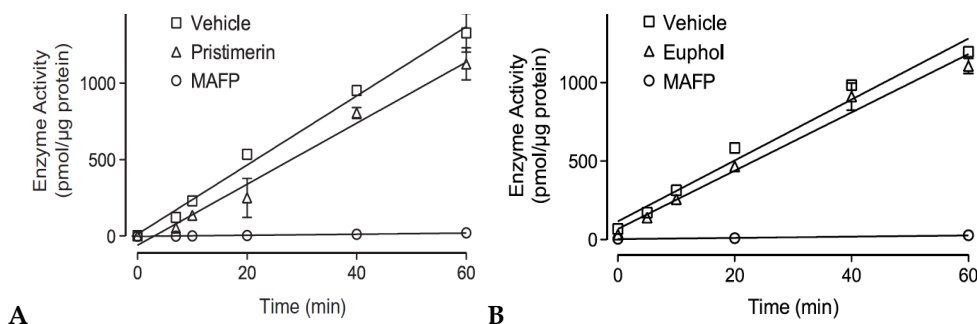


Figure 2.19 Rapid dilution assays of HeLa-MGL in the presence of vehicle (squares, DMSO, final concentration 2%), pristimerin (**A**), euphol (**B**) or MAFP (circles)

A glycine-based mutagenesis scanning revealed that the replacement of Cys208 caused a marked rightward shift in the concentration-response curve for pristimerin, whereas it had no effect on euphol (**Figure 2.20**). Conversely, a mutation affecting Cys201 significantly reduced the inhibitory potency of euphol without affecting the potency of pristimerin. The structural and mechanistic similarities between pristimerin and euphol suggest that they could occupy a common hydrophobic pocket within the lid domain of MGL. Computational studies revealed the possibility of each inhibitor to engage interactions with adjacent cysteine residues, Cys201 and Cys208, which flank

this pocket. The limited overlap of the region occupied by pristimerin and euphol with the presumptive active site of MGL is consistent with the non-competitive kinetic behavior displayed by these inhibitors. However, there are other possible explanations for such behavior, including stabilization of a conformation of MGL that is inaccessible to the substrate.

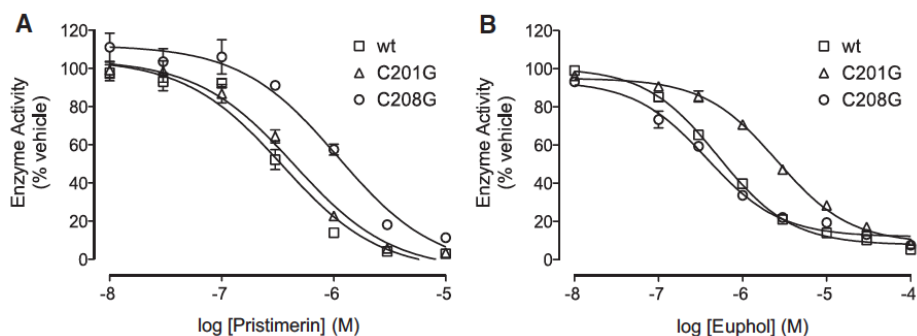


Figure 2.20 Effects of mutating Cys201 or Cys208 on MGL inhibition by pristimerin (A) and euphol (B)

2.5 Therapeutic potential of MGL inhibition

Given the roles of the endocannabinoid system in the regulation of many processes including pain, neuroprotection, appetite and even cancer diseases, enzymes involved in the endocannabinoid catabolism are potentially important targets for pharmaceutical development. Currently, the main focus has been upon fatty acid amide hydrolase (FAAH), which primarily hydrolyses AEA and related *N*-acylethanolamines to their corresponding fatty acids. FAAH inhibitors are in pharmaceutical development, with pain as a major indication. MGL inhibitors have lagged behind, but have a potential advantage over FAAH inhibitors in terms of substrate specificity, given that the *N*-acylethanolamines are a class of compounds with multiple biological actions, and for the multiple possibilities of targeting, allowed by the complex regulation of MGL activity.

A concern with the development of molecules affecting endocannabinoid metabolism is that they might produce cannabis-like effects, which would limit their usefulness. This concern was greatly reduced when the first selective FAAH inhibitor, URB597,

was found not to produce catalepsy, hypothermia or hyperphagia, responses that are seen with compounds activating central CB₁ receptors⁶⁴, and not to produce reinforcing effects in monkeys trained to self-administer Δ^9 -THC⁶⁵. With respect to MGL inhibition, JZL184 was found to produce Rimonabant-sensitive thermal hypoalgesia and hypolocomotion in mice, but it did not produce any motor impairments and catalepsy, suggesting that the full gamut of behavioral responses that characterize a general activation of brain CB₁ receptors is not seen^{17,19}.

Consistent with the role of MGL in modulating 2-AG-mediated endocannabinoid signaling, acute pharmacological blockade of MGL exerts CB₁-dependent antinociceptive effects in mouse models of noxious chemical, inflammatory, thermal, and neuropathic pain⁶⁶. MGL blockade reduces mechanical and acetone-induced cold allodynia in mice subjected to chronic constriction injury of the sciatic nerve. Recent studies have also shown that MGL blockade is protective in a mouse model of inflammatory bowel disease. MGL blockade by JZL184 reduces macroscopic and histological colon alterations and pro-inflammatory cytokines in a trinitrobenzene sulfonic acid-induced colitis model, and restores integrity of the intestinal barrier function resulting in reduced endotoxemia and peripheral and brain inflammation in a CB₁ or CB₂-dependent manner⁶⁷.

Genetic and pharmacological blockades of MGL also exhibit anti-inflammatory effects in the brain and neuroprotective effects in mouse models of Parkinson's disease and Alzheimer's disease (AD)¹⁸. Consistent with this anti-inflammatory effect, MGL blockade with JZL184 or MGL deficiency significantly protects against dopaminergic neurodegeneration and dopamine loss in an MPTP model of Parkinson's disease, concordant with suppression in pro-inflammatory eicosanoids. MGL inactivation lowers the pro-inflammatory eicosanoid levels in the AD mouse model, concordant with suppression of astrocyte and microglial activation and attenuation of pro-inflammatory cytokines, leading to a substantial reduction in amyloid plaques. Collectively, MGL inhibitors exhibit antinociceptive and anti-inflammatory effects through simultaneously enhancing endocannabinoid and suppressing eicosanoid levels in the brain. These findings identify MGL as a distinct metabolic node that couples endocannabinoid to prostaglandin signaling networks in the nervous system and suggest that inhibition of this enzyme may be a new and potentially safer way to suppress the pro-inflammatory cascades that underlie neurodegenerative disorders.

MGL have a central role also in anxiety events. Multiple studies have shown that MGL blockade by JZL184 or URB602 also exert anxiolytic responses. In a marble burying model of repetitive and compulsive behavior inherent to anxiety disorders, MGL blockade reduced marble burying at doses that did not affect motility, on-par with the activity observed with FAAH inhibitor or tetrahydrocannabinol administration, in a CB₁-dependent manner⁶⁸. MGL blockade also exerts anxiolytic effects in an elevated plus maze paradigm for anxiety, showing increased percentage open arm time and number of open arm entries under high, but not low, levels of environmental aversiveness⁶⁹. Sumislawski *et al.* showed that chronic MGL blockade prevented chronic stress-induced anxiety-like behavior and emergence of long-term depression of GABAergic transmission, indicating that enhanced endocannabinoid signaling prevents behavioral and synaptic adaptations to chronic stress that underlies the development and worsening of affective disorders⁷⁰. Collectively, MGL inhibitors show promise, much like FAAH inhibitors or direct cannabinoid agonists, in reducing anxiety.

Recently, the implication of the MGL in cancer pathogenesis has been demonstrated, raising new hopes for the development of original anticancer therapeutics based on MGL inhibition⁷¹. In their study, Nomura and colleagues found elevated MGL expression levels in aggressive versus non-aggressive human cancer cell lines. MGL overexpression increased the aggressiveness of non-aggressive cancer cell lines. On the other hand, genetic knockdown of MGL expression by interfering RNAs, as well as inhibition of the enzyme activity with an JZL184, affected the migration, invasion, cell survival and tumor growth in aggressive cancers. Importantly, exogenous fatty acids restored the loss of pathogenicity. Overall, it was shown that, in cancer cells, a panel of fatty acids and other lipids are produced following the stimulation of MGL activity to promote cell proliferation and cancer malignancy.

In just a few years, the availability of selective MGL inhibitors has allowed for the identification of the roles played by 2-AG in the body, and provided preclinical data supporting potential indications for this class of compounds. Within the pain field, issues of tolerance and “cannabis-like” effects may present obstacles to drug development, but hopefully *in vivo* data with reversible inhibitors will be forthcoming to address these issues. Within the cancer field, it is early days and *in vivo* data with genetic and orthotopic cancer models would be most useful, as would combination

studies with standard drug regimes. Nonetheless, when it is remembered that prior to 2005, no selective and “druggable” MGL inhibitors were available, the rapid progress in the field is impressive, and gives hope that the therapeutic potential of MGL as a target for drug development will be translated into a clinical reality.

References

- ¹ (a) Labar, G.; Wouters, J.; Lambert, D.M. A Review on the Monoacylglycerol Lipase: At the Interface Between Fat and Endocannabinoid Signalling *Current Medicinal Chemistry* **2010**, *17*, 2588-2607. (b) Fowler, C.J. Monoacylglycerol lipase – a target for drug development? *Br. J. Pharmacol.* **2012**; *166*, 1568-1585. (c) Mulvihill, M.M.; Nomura, D.K. Therapeutic potential of monoacylglycerol lipase inhibitors **2013**, *92*, 492-497. (d) Saario, S.M.; Laitinen, J.T. Monoglyceride Lipase as an Enzyme Hydrolyzing 2-Arachidonoylglycerol **2007**, *4*, 1903-1913.
- ² Tornqvist, H.; Belfrage, P. Purification and some properties of a monoacylglycerol-hydrolysing enzyme of rat adipose tissue. *J. Biol. Chem.* **1976**, *251*, 813-819.
- ³ Karlsson, M.; Contreras, J.A.; Hellman, U.; Tornqvist, H.; Holm, C. cDNA cloning, tissue distribution, and identification of the catalytic triad of monoglyceride lipase. Evolutionary relationship to esterases, lysophospholipases, and haloperoxidases *J. Biol. Chem.* **1997**, *272*(43), 27218-23.
- ⁴ Dinh, T.P.; Carpenter, D.; Leslie, F.M.; Freund, T.F.; Katona, I.; Sensi, S.L.; Kathuria, S.; Piomelli, D. Brain monoglyceride lipase participating in endocannabinoid inactivation *Proc. Natl. Acad. Sci. USA* **2002**, *99*(16), 10819-24.
- ⁵ Karlsson, M.; Reue, K.; Xia, Y.R.; Lusi, A.J.; Langin, D.; Tornqvist, H.; Holm, C. Exon-intron organization and chromosomal localization of the mouse monoglyceride lipase gene *Gene* **2001**, *272*(1-2), 11-8.
- ⁶ (a) Bertrand, T.; Augé, F.; Houtmann, J.; Rak, A.; Vallée, F.; Mikol, V.; Berne, P.F.; Michot, N.; Cheuret, D.; Hoornaert, C.; Mathieu, M. Structural basis for human monoglyceride lipase inhibition *J. Mol. Biol.* **2010**, *396*(3), 663-73. (b) Labar, G.; Bauvois, C.; Borel, F.; Ferrer, J.L.; Wouters, J.; Lambert, D.M. Crystal structure of the human monoacylglycerol lipase, a key actor in endocannabinoid signaling *Chembiochem.* **2010**, *11*(2), 218.
- ⁷ Blankman, J.L.; Simon, G.M.; Cravatt, B.F. A comprehensive profile of brain enzymes that hydrolyze the endocannabinoid 2-arachidonoylglycerol *Chem Biol.* **2007**, *14*(12), 1347-56.
- ⁸ Sakurada, T. *et al* *J. Biochem.* **1981**, *90*, 1413-1419.
- ⁹ Saario, S. M.; Salo, O. M.; Nevalainen, T.; Poso, A.; Laitinen, J.T.; Jarvinen, T.; Niemi, R. Characterization of the sulfhydrylsensitive site in the enzyme responsible for hydrolysis of 2-arachidonoyl-glycerol in rat cerebellar membranes *Chem. Biol.* **2005**, *12*, 649-56.
- ¹⁰ Zvonok, N.; Williams, J.; Johnston, M.; Pandarinathan, L.; Janero, D. R.; Li, J.; Krishnan, S. C.; Makriyannis, A. Full mass spectrometric characterization of human monoacylglycerol lipase generated by large-scale expression and single-step purification *J. Proteome. Res.* **2008**, *7*, 2158-64.
- ¹¹ (a) Karlsson, M.; Tornqvist, H.; Holm, C. Expression, purification, and characterization of histidine-tagged mouse monoglyceride lipase from baculovirus-infected insect cells. *Protein Expr. Purif.* **2000**, *18*, 286-92. (b) Vila, A.; Rosengarth, A.; Piomelli, D.; Cravatt, B.; Marnett, L. J. Hydrolysis of prostaglandin glycerol esters by the endocannabinoid-hydrolyzing enzymes, monoacylglycerol lipase and fatty acid amide hydrolase *Biochemistry* **2007**, *46*, 9578-85.
- ¹² (a) Kupiecki, F. P. Partial purification of monoglyceride lipase from adipose tissue. *J. Lipid Res.* **1966**, *7*, 230-5. (b) Rindlisbacher, B.; Reist, M.; Zahler, P. Diacylglycerol breakdown in plasma membranes of bovine chromaffin cells is a two-step mechanism mediated by a diacylglycerol lipase and a monoacylglycerol lipase. *Biochim. Biophys. Acta*, **1987**, *905*, 349-57.

- ¹³ Ghafouri, N.; Tiger, G.; Razdan, R. K.; Mahadevan, A.; Pertwee, R. G.; Martin, B. R.; Fowler, C. J. Inhibition of monoacylglycerol lipase and fatty acid amide hydrolase by analogues of 2- arachidonoylglycerol. *Br. J. Pharmacol.*, **2004**, *143*, 774-84.
- ¹⁴ Gulyas, A.I.; Cravatt, B.F.; Bracey, M.H.; Dinh, T.P.; Piomelli, D.; Boscia, F.; Freund, T.F. Segregation of two endocannabinoid hydrolyzing enzymes into pre- and postsynaptic compartments in the rat hippocampus, cerebellum and amygdala. *Eur. J. Neurosci.* **2004**, *20*, 441-58.
- ¹⁵ (a) Hohmann, A. G.; Suplita, R. L.; Bolton, N. M.; Neely, M. H.; Fegley, D.; Mangieri, R.; Krey, J. F.; Walker, J. M.; Holmes, P. V.; Crystal, J. D.; Duranti, A.; Tontini, A.; Mor, M.; Tarzia, G.; Piomelli, D. An endocannabinoid mechanism for stress-induced analgesia. *Nature* **2005**, *435*, 1108-12.. (b) Makara, J. K.; Mor, M.; Fegley, D.; Szabo, S. I.; Kathuria, S.; Astarita, G.; Duranti, A.; Tontini, A.; Tarzia, G.; Rivara, S.; Freund, T. F.; Piomelli, D. Selective inhibition of 2-AG hydrolysis enhances endocannabinoid signaling in hippocampus. *Nat. Neurosci.* **2005**, *8*, 1139-41.
- ¹⁶ Dinh, T.P.; Kathuria, S.; Piomelli D. RNA interference suggests a primary role for monoacylglycerol lipase in the degradation of the endocannabinoid 2-arachidonoylglycerol *Mol Pharmacol* **2004**, *66*, 1260-1264.
- ¹⁷ Long, J. Z.; Li, W.; Booker, L.; Burston, J. J.; Kinsey, S. G.; Schlosburg, J. E.; Pavon, F. J.; Serrano, A. M.; Selley, D. E.; Parsons, L. H.; Lichtman, A. H.; Cravatt, B. F. Selective blockade of 2-arachidonoylglycerol hydrolysis produces cannabinoid behavioral effects *Nat. Chem. Biol.* **2009**, *5*, 37-44.
- ¹⁸ Nomura, D.K.; Morrison, B.E.; Blankman, J.L.; Long, J.Z.; Kinsey, S.G.; Marcondes, M.C. *et al.* Endocannabinoid hydrolysis generates brain prostaglandins that promote neuroinflammation *Science* **2011**, *334*, 809-813.
- ¹⁹ Long, J. Z.; Nomura, D. K.; Cravatt, B. F. Characterization of monoacylglycerol lipase inhibition reveals differences in central and peripheral endocannabinoid metabolism. *Chem. Biol.*, **2009**, *16*, 744-53.
- ²⁰ Kano, M.; Ohno-Shosaku, T.; Hashimoto-dani, Y.; Uchigashima, M.; Watanabe, M. Endocannabinoid-mediated control of synaptic transmission *Physiol. Rev.* **2009**, *89*, 309-80.
- ²¹ Katona, I.; Freund, T.F. Endocannabinoid signaling as a synaptic circuit breaker in neurological disease. *Nat Med.* **2008**, *14*, 923-930.
- ²² Wilson, R.; Nicoll, R. Endogenous cannabinoids mediate retrograde signalling at hippocampal synapses. *Nature* **2001**, *410*, 588-592.
- ²³ Ludányi, A.; Hu, SS-J.; Yamazaki, M.; Tanimura, A.; Piomelli, D.; Watanabe, M.; *et al.* Complementary synaptic distribution of enzymes responsible for synthesis and inactivation of the endocannabinoid 2-arachidonoylglycerol in the human hippocampus. *Neuroscience* **2011**, *174*, 50-63.
- ²⁴ (a) Pan, B.; Wang, W.; Long, J. Z.; Sun, D.; Hillard, C. J.; Cravatt, B. F.; Liu, Q. S. Blockade of 2-arachidonoylglycerol hydrolysis by selective monoacylglycerol lipase inhibitor 4-nitrophenyl 4-(dibenzo[d][1,3]dioxol-5-yl(hydroxy)methyl)piperidine-1-carboxylate (JZL184) Enhances retrograde endocannabinoid signaling. *J. Pharmacol. Exp. Ther.* **2009**, *331*, 591-7. (b) Straiker, A.; Hu, S. S.; Long, J. Z.; Arnold, A.; Wager-Miller, J.; Cravatt, B. F.; Mackie, K. Monoacylglycerol lipase limits the duration of endocannabinoid-mediated depolarization-induced suppression of excitation in autaptic hippocampal neurons. *Mol. Pharmacol.* **2009**, *76*, 1220-7.
- ²⁵ (a) Pan, B.; Wang, W.; Zhong, P.; Blankman, J.L.; Cravatt, B.F.; Liu, Q.S. Alterations of endocannabinoid signaling, synaptic plasticity, learning, and memory in monoacylglycerol lipase knock-out mice. *J Neurosci.*

- 2011**, 31, 13420–13430. (b) Zhong, P.; Pan, B.; Gao, X.; Blankman, J.L.; Cravatt, B.F.; Liu, Q.S. Genetic deletion of monoacylglycerol lipase alters endocannabinoid-mediated retrograde synaptic depression in the cerebellum. *J Physiol.* **2011**, 589, 4847–4855.
- ²⁶ Kupiecki, F. P. Partial purification of monoglyceride lipase from adipose tissue. *J. Lipid Res.*, **1966**, 7, 230-5.
- ²⁷ Zvonok, N.; Pandarinathan, L.; Williams, J.; Johnston, M.; Karageorgos, I.; Janero, D. R.; Krishnan, S. C.; Makriyannis, A. Covalent inhibitors of human monoacylglycerol lipase: ligand-assisted characterization of the catalytic site by mass spectrometry and mutational analysis. *Chem. Biol.* **2008**, 15, 854-62.
- ²⁸ King, A. R.; Lodola, A.; Carmi, C.; Fu, J.; Mor, M.; Piomelli, D. A critical cysteine residue in monoacylglycerol lipase is targeted by a new class of isothiazolinone-based enzyme inhibitors. *Br. J. Pharmacol.*, **2009**, 157, 974-83.
- ²⁹ Barford, D. The role of cysteine residues as redox-sensitive regulatory switches. *Curr. Opin. Struct. Biol.* **2004**, 14(6), 679-86.
- ³⁰ Stamler, J.S.; Lamas, S.; Fang, F.C. Nitrosylation: the prototypic redox-based signaling mechanism. *Cell* **2001**, 106, 675–683.
- ³¹ Farooqui, A.A.; and Horrocks, L.A. Nitric oxide synthase inhibitors do not attenuate diacylglycerol or monoacylglycerol lipase activities in synaptoneurosomes. *Neurochem. Res.* **1997**, 22, 1265–1269.
- ³² Patel, J.C.; Rice, M.E. Classification of H₂O₂ as a neuromodulator that regulates striatal dopamine release on a subsecond time scale *Chem. Neurosci.* **2012**, 3(12), 991-1001.
- ³³ Lo Conte, M.; Carroll, K.S. The redox biochemistry of protein sulfenylation and sulfinylation. *J. Biol. Chem.* **2013**, 288(37), 26480-8.
- ³⁴ Rice, M.E. H₂O₂: a dynamic neuromodulator. *Neuroscientist* **2011**, 17, 389-406.
- ³⁵ Szabo, M.; Agostino, M.; Malone, D.T.; Yuriev, E.; Capuano, B. The design, synthesis and biological evaluation of novel URB602 analogues as potential monoacylglycerol lipase inhibitors. *Bioorg. Med. Chem. Lett.* **2011**, 21(22), 6782-7.
- ³⁶ Goparaju, S.; Ueda, N.; Taniguchi, K.; Yamamoto, S. Enzymes of porcine brain hydrolyzing 2-arachidonoylglycerol, an endogenous ligand of cannabinoid receptors. *Biochem. Pharmacol.* **2000**, 57(4), 417.
- ³⁷ Martin, B. R.; Beletskaya, I.; Patrick, G.; Jefferson, R.; Winckler, R.; Deutsch, D. G.; Di Marzo, V.; Dasse, O.; Mahadevan, A.; Razdan, R. K. Cannabinoid properties of methylfluorophosphonate analogs. *Journal of Pharmacology and Experimental Therapeutics* **2000**, 294(3), 1209-1218.
- ³⁸ Nithipatikom, K.; Endsley, M. P.; Isbell, M. A.; Falck, J. R.; Iwamoto, Y.; Hillard, C. J.; Campbell, W. B. 2-arachidonoylglycerol: a novel inhibitor of androgen-independent prostate cancer cell invasion. *Cancer Res.* **2004**, 64, 8826-30. (b) Nithipatikom, K.; Endsley, M. P.; Isbell, M. A.; Wheelock, C. E.; Hammock, B. D.; Campbell, W. B. A new class of inhibitors of 2- arachidonoylglycerol hydrolysis and invasion of prostate cancer cells. *Biochem. Biophys. Res. Commun.* **2005**, 332, 1028-33.
- ³⁹ Boger, D. L.; Sato, H.; Lerner, A. E.; Austin, B. J.; Patterson, J. E.; Patricelli, M. P.; Cravatt, B. F. Trifluoromethyl ketone inhibitors of fatty acid amide hydrolase: a probe of structural and conformational features contributing to inhibition. *Bioorg. Med. Chem. Lett.*, **1999**, 9, 265-70.
- ⁴⁰ Moore, S. A.; Nomikos, G. G.; Dickason-Chesterfield, A. K.; Schober, D. A.; Schaus, J. M.; Ying, B. P.; Xu, Y. C.; Phebus, L.; Simmons, R. M.; Li, D.; Iyengar, S.; Felder, C. C. Identification of a high-affinity binding site involved in the transport of endocannabinoids *Proc. Natl. Acad. Sci. U.S.A.* **2005**, 102, 17852-7.

- ⁴¹ (a) Alexander, J. P.; Cravatt, B. F. The putative endocannabinoid transport blocker LY2183240 is a potent inhibitor of FAAH and several other brain serine hydrolases. *J. Am. Chem. Soc.* **2006**, *128*, 9699-704. (b) Maione, S.; Morera, E.; Marabese, I.; Ligresti, A.; Luongo, L.; Ortar, G.; Di Marzo, V. Antinociceptive effects of tetrazole inhibitors of endocannabinoid inactivation: cannabinoid and noncannabinoid receptor-mediated mechanisms. *Br. J. Pharmacol.*, **2008**, *155*, 775-82.
- ⁴² Ortar, G.; Cascio, M. G.; Moriello, A. S.; Camalli, M.; Morera, E.; Nalli, M.; Di Marzo, V. Carbamoyl tetrazoles as inhibitors of endocannabinoid inactivation: a critical revisitation. *Eur. J. Med. Chem.* **2008**, *43*, 62.
- ⁴³ King, A. R.; Duranti, A.; Tontini, A.; Rivara, S.; Rosengarth, A.; Clapper, J. R.; Astarita, G.; Geaga, J. A.; Luecke, H.; Mor, M.; Tarzia, G.; Piomelli, D. URB602 inhibits monoacylglycerol lipase and selectively blocks 2-arachidonoylglycerol degradation in intact brain slices. *Chem. Biol.*, **2007**, *14*, 1357-65.
- ⁴⁴ Vandevoorde, S.; Jonsson, K. O.; Labar, G.; Persson, E.; Lambert, D. M.; Fowler, C. J. Lack of selectivity of URB602 for 2-oleoylglycerol compared to anandamide hydrolysis *in vitro*. *Br. J. Pharmacol.* **2007**, *150*, 186-91.
- ⁴⁵ Comelli, F.; Giagnoni, G.; Bettoni, I.; Colleoni, M.; Costa, B. The inhibition of monoacylglycerol lipase by URB602 showed an antiinflammatory and anti-nociceptive effect in a murine model of acute inflammation. *Br. J. Pharmacol.* **2007**, *152*, 787-94.
- ⁴⁶ Carloni, S.; Alonso-Alconada, D.; Girelli, S.; Duranti, A.; Tontini, A.; Piomelli, D.; Hilario, E.; Alvarez, A.; Balduini, W. Pretreatment with the monoacylglycerol lipase inhibitor URB602 protects from the long-term consequences of neonatal hypoxic-ischemic brain injury in rats. *Pediatr Res.* **2012**, *72*(4), 400-6.
- ⁴⁷ Saario, S. M.; Poso, A.; Juvonen, R. O.; Jarvinen, T.; Salo-Ahen, O. M. Fatty acid amide hydrolase inhibitors from virtual screening of the endocannabinoid system. *J. Med. Chem.*, **2006**, *49*, 4650-6.
- ⁴⁸ Muccioli, G. G.; Labar, G.; Lambert, D. M. CAY10499, a novel monoglyceride lipase inhibitor evidenced by an expeditious MGL assay *Chembiochem* **2008**, *9*, 2704-10.
- ⁴⁹ Minkkila, A.; Savinainen, J. R.; Kasnanen, H.; Xhaard, H.; Nevalainen, T.; Laitinen, J. T.; Poso, A.; Leppanen, J.; Saario, S. M. Screening of various hormone-sensitive lipase inhibitors as endocannabinoid-hydrolyzing enzyme inhibitors. *ChemMedChem* **2009**, *4*, 1253-9.
- ⁵⁰ Li, W.; Blankman, J. L.; Cravatt, B. F. A functional proteomic strategy to discover inhibitors for uncharacterized hydrolases. *J. Am. Chem. Soc.* **2007**, *129*, 9594-5.
- ⁵¹ Bisogno, T.; Ortar, G.; Petrosino, S.; Morera, E.; Palazzo, E.; Nalli, M.; Maione, S.; Di Marzo, V. Development of a potent inhibitor of 2-arachidonoylglycerol hydrolysis with antinociceptive activity *in vivo*. *Biochim. Biophys. Acta* **2009**, *1791*, 53-60.
- ⁵² Burstson, J. J.; Sim-Selley, L. J.; Harloe, J. P.; Mahadevan, A.; Razdan, R. K.; Selley, D. E.; Wiley, J. L. N-arachidonyl maleimide potentiates the pharmacological and biochemical effects of the endocannabinoid 2-arachidonoylglycerol through inhibition of monoacylglycerol lipase. *J. Pharmacol. Exp. Ther.* **2008**, *327*, 546-53.
- ⁵³ Matuszak, N.; Muccioli, G. G.; Labar, G.; Lambert, D. M. Synthesis and *in vitro* evaluation of N-substituted maleimide derivatives as selective monoglyceride lipase inhibitors. *J. Med. Chem.* **2009**, *52*, 7410-20.
- ⁵⁴ Labar, G.; Bauvois, C.; Muccioli, G. G.; Wouters, J.; Lambert, D.M. Disulfiram is an inhibitor of human purified monoacylglycerol lipase, the enzyme regulating 2-arachidonoylglycerol signaling. *Chembiochem.* **2007**, *8*, 1293-7.

- ⁵⁵ Kapanda, C. N.; Muccioli, G. G.; Labar, G.; Poupaert, J. H.; Lambert, D. M. Bis(dialkylaminethiocarbonyl)disulfides as potent and selective monoglyceride lipase inhibitors. *J. Med. Chem.* **2009**, *52*, 7310-4.
- ⁵⁶ Matuszak, N.; Es Saadi, B.; Labar, G.; Marchand-Brynaert, J.; Lambert, D. M. Benzisothiazolinone as a useful template for the design of new monoacylglycerol lipase inhibitors: investigation of the target residues and comparison with octhilinone. *Bioorg. Med. Chem. Lett.* **2011**, *21*(24), 7321-7324.
- ⁵⁷ King, A. R.; Dotsey, E. Y.; Lodola, A.; Jung, K. M.; Ghomian, A.; Qiu, Y.; Fu, J.; Mor, M.; Piomelli, D. Discovery of potent and reversible monoacylglycerol lipase inhibitors. *Chem. Biol.* **2009**, *16*, 1045-52.
- ⁵⁸ Tiedemann, R.E.; Schmidt, J.; Keats, J.J.; Shi, C.X.; Zhu, Y.X.; Palmer, S.E.; Mao, X.; Schimmer, A.D.; Stewart, A.K. Identification of a potent natural triterpenoid inhibitor of proteasome chymotrypsin-like activity and NF-kappaB with antimyeloma activity in vitro and in vivo. *Blood* **2009**, *113*, 4027-4037.
- ⁵⁹ Dirsch, V.M.; Kiemer, A.K.; Wagner, H.; Vollmar, A.M. The triterpenoid quinonemethide pristimerin inhibits induction of inducible nitric oxide synthase in murine macrophages. *Eur. J. Pharmacol.* **1997**, *336*(2-3), 211-7.
- ⁶⁰ Dutra, R.C.; Claudino, R.F.; Bento, A.F.; Marcon, R.; Schmidt, E.C.; Bouzon, Z.L.; Pianowski, L.F. Calixto, J.B. Preventive and therapeutic euphol treatment attenuates experimental colitis in mice. *PLoS One.* **2011**, *6*, e271222011.
- ⁶¹ Dutra, R.C.; de Souza, P.R.; Bento, A.F.; Marcon, R.; Bicca, M.A.; Pianowski, L.F. Calixto, J.B. Euphol prevents experimental autoimmune encephalomyelitis in mice: evidence for the underlying mechanisms. *Biochem Pharmacol.* **2012**, *83*, 531-542.
- ⁶² Wang, L.; Wang, G.; Yang, D.; Guo, X.; Xu, Y.; Feng, B.; Kang, J. Euphol arrests breast cancer cells at the G1 phase through the modulation of cyclin D1, p21 and p27 expression. *Mol. Med. Rep.* **2013**, *8*(4), 1279-85.
- ⁶³ Dutra, R.C.; Bortolini Simao da Silva, K.A.; Bento, A.F.; Marcon, R.; Paszcuk, A.F.; Meotti, F.C.; Pianowski, L.F. Calixto, J.B. Euphol, a tetracyclic triterpene produces antinociceptive effects in inflammatory and neuropathic pain: The involvement of cannabinoid system *Neuropharmacology* **2012**, *63*, 593-605.
- ⁶⁴ Kathuria, S.; Gaetani, S.; Fegley, D.; Valiño, F.; Duranti, A.; Tontini, A.; Mor, M.; Tarzia, G.; La Rana, G.; Calignano, A.; Giustino, A.; Tattoli, M.; Palmery, M.; Cuomo, V.; Piomelli, D. Modulation of anxiety through blockade of anandamide hydrolysis. *Nat Med.* **2003**, *9*(1), 76-81.
- ⁶⁵ Justinova, Z.; Mangieri, R.; Bortolato, M.; Chefer, S.; Mukhin, A.; Clapper, J.; *et al.* Fatty acid amide hydrolase inhibition heightens anandamide signaling without producing reinforcing effects in primates. *Biol Psychiat.* **2008**, *64*, 930-937.
- ⁶⁶ Guindon, J.; Guijarro, A.; Piomelli, D.; Hohmann, A.G. Peripheral antinociceptive effects of inhibitors of monoacylglycerol lipase in a rat model of inflammatory pain *Br. J. Pharmacol.* **2011**, *163*, 1464-1478.
- ⁶⁷ Alhouayek, M.; Lambert, D.M.; Delzenne, N.M.; Cani, P.D.; Muccioli, G.G. Increasing endogenous 2-arachidonoylglycerol levels counteracts colitis and related systemic inflammation *FASEB J.* **2011**, *25*, 2711-2721.
- ⁶⁸ Kinsey, S.G.; O'Neal, S.T.; Long, J.Z.; Cravatt, B.F.; Lichtman A.H. Inhibition of endocannabinoid catabolic enzymes elicits anxiolytic-like effects in the marble burying assay *Pharmacol. Biochem. Behav.* **2011**, *98*, 21-27.

⁶⁹ Sciolino, N.R.; Zhou, W.; Hohmann, A.G. Enhancement of endocannabinoid signaling with JZL184, an inhibitor of the 2-arachidonoylglycerol hydrolyzing enzyme monoacylglycerol lipase, produces anxiolytic effects under conditions of high environmental aversiveness in rats. *Pharmacol. Res.* **2011**, *64*, 226–234.

⁷⁰ Sumislawski, J.J.; Ramikie, T.S.; Patel S. Reversible gating of endocannabinoid plasticity in the amygdala by chronic stress: a potential role for monoacylglycerol lipase inhibition in the prevention of stress-induced behavioral adaptation *Neuropsychopharmacology* **2011**, *36*, 2750–2761.

⁷¹ Nomura, D. K.; Long, J. Z.; Niessen, S.; Hoover, H. S.; Ng, S. W.; Cravatt, B. F. Monoacylglycerol lipase regulates a fatty acid network that promotes cancer pathogenesis. *Cell* **2010**, *140*, 49-61

Chapter

3 MGL inhibitors: results and discussion

Monoacylglycerol lipase (MGL), as seen in the previous chapters, plays a key role in the inactivation of the stimulatory signal exerted by 2-AG, the main “on-demand” released endocannabinoid ligand for CB₁ receptors. The role of MGL as new attractive therapeutic target for treatment of pain, neurodegenerative diseases, anxiety and cancer has been elucidated from several pharmacological studies (see Chapter 2). Targeting the enzyme involved to the catabolism of the major endocannabinoid is a promising approach to avoid side effects derived by direct stimulation of cannabinoid receptors. Molecular and crystallographic studies have provided a framework for the understanding of the structure and the mechanism of action of this enzyme: these informations led to the discovery of the first generation of selective MGL inhibitors. They revealed to be fundamental tools for a deep investigation of the physiological and therapeutic functions of MGL. The lack of potency, selectivity or the total disruption of the catalytic activity showed by these “early” inhibitors confined their development as potential drugs.

The discovery of isothiazol-3(2*H*)-one (ITZ), benzo[*d*]isothiazol-3(2*H*)-one (BTZ) and triterpene derivatives as hit compounds for MGL inhibition has provided the fundamentals for the development of new potent MGL inhibitors with a novel mechanism. Therefore, there is a widespread interest of the scientific community in the development of allosteric inhibitors able to interact with the modulatory cysteines of MGL external to the active site, i.e. Cys201 and Cys208. The modulation of these critical residues is the access point for the comprehension of oxidation-dependent inactivation of the enzyme (see Chapter 2). The design of redox-reversible inhibitors

targeting regulatory cysteines is a modern and powerful strategy to increase in a “physiological” way 2-AG signaling, avoiding side effects of a total and irreversible inhibition exerted by covalent modifiers of the catalytic triad. The major challenge of uncouple benefic and side effects of the endocannabinoid system stimulation requires the development of allosteric inhibitors of MGL.

The research work discussed in this PhD thesis takes place within this overall picture. My work was aimed to the investigation of structure-activity relationships (SAR) of partially-reversible allosteric inhibitors of MGL, i.e. BTZ and triterpene derivatives, to increase the knowledge in a field still in its infancy.

The results reported in this chapter are the outcome of an interdisciplinary research work involving different research area and groups. A comprehensive discussion of the role of BTZ and triterpenes derivatives as MGL inhibitors and the understanding of the workflow beyond the research process requires describing results not directly obtained from my own investigations.

My work has been focused on the organic synthesis of BTZ and triterpene derivatives. Moreover, I performed reactivity studies on BTZ by means of NMR spectroscopy. Computational studies and reactivity analysis on BTZ by means of HPLC-UV and HPLC-ESI-MS have been performed from the computational and the bio-analytic part of the group where I spent my PhD period, respectively. Biological evaluation of the synthesized compounds on MGL was carried out by the research group of Prof. Piomelli (University of Irvine, California).

3.1 BTZs as MGL inhibitors: results and discussion

BTZs are characterized by the presence of a sulfenamide-based sulfhydryl-reactive warhead (red labeled) and driver groups R, R' (blue labeled) necessary for a proper drug-target recognition and positioning and for the modulation of the warhead reactivity (**Figure 3.1**). The five-membered sulfenamide core is labile in a variety of ways. The sulfur atom tends to be the more electrophilic center of the S-N bond. Nucleophilic attack on sulfur can be taken by amines, by thiols, and by alkyl-

magnesium halides, which leads to either new sulfenamide derivatives or compounds such as sulfides and disulfides.

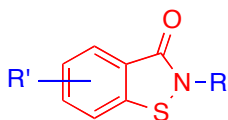
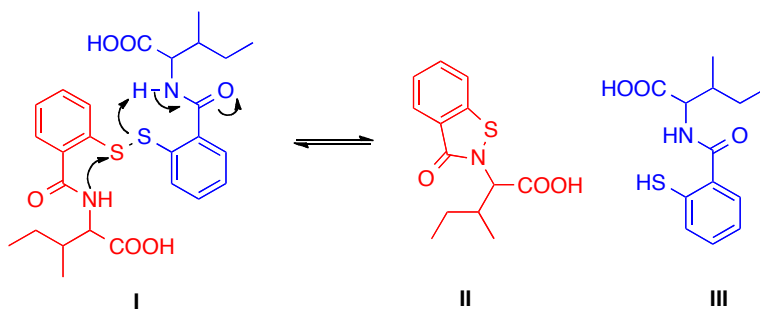


Figure 3.1 BTZ general structure: warhead portion (red labeled) and driver portion (blue labeled)

Sanchez¹ reported the synthesis of a series of unsymmetrical disulfides through a reaction involving a ring opening nucleophilic attack of a thiol on BTZs, confirming the high reactivity of these compounds toward sulfur-based nucleophiles. The reactivity of the sulfur atom to nucleophilic additions leading to a disulfide bond is, as seen in the previous chapter, at the base of the mechanism of inhibition on MGL. Moreover, BTZ are very sensitive to reducing agents: the S-N bond can be easily disrupted from common reducing agents (H₂, hydrides) leading to the formation of the ring-opened sulfhydryl derivative. The sulfhydryl form is very susceptible to oxidation: air oxygen is sufficient to generate the symmetric disulfide.



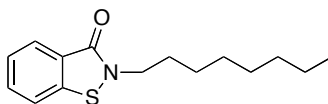
Scheme 3.1 Proposed route of degradation of **I** in aqueous solution, leading to formation of benzisothiazolinone **II** and sulfhydryl **III**

Phillips *et al.*² reported an interesting degradation reaction occurring in aqueous media for 2,2'-dithiobis[*N*-isoleucylbenzamide] **I** (**Scheme 3.1**), which can dismutate into its sulfhydryl monomer **III** and benzisothiazolinone **II**. BTZs, in aqueous environment, can be generated from disproportionation of disulfides and they establish a dynamic equilibrium as outlined in **Scheme 3.1**.

Several methods have been reported for the synthesis of the BTZ scaffold³. Most of these methods are based on an oxidative cyclization in the presence of chlorine, chlorinating agents or iodine with a nucleophilic attack exerted from the nitrogen atom on the activated sulfur atom.

BTZs are compounds well known as additives in cosmetic preparations, paints and glues and as industrial biocides⁴. The biological properties of this class have been deeply investigated. BTZs showed antibacterial, antifungal, antimicrobial and genotoxic activities⁵. *N*-phenylbenzothiazolones have been investigated as inhibitors of the tautomerase activity of the proinflammatory cytokine MIF (macrophage migration inhibitory factor): several BTZ-based compounds were found to possess antagonist activity in the low micromolar range⁶. BTZs were recently reported as promising caspase-3⁷, histone acetyltransferase⁸ and blood platelet aggregation inhibitors⁹. In a recent study conducted by Dahl and coworkers¹⁰ on the properties of a series of BTZs as inhibitors of the phosphomannose isomerase, the most promising compounds were profiled for bioavailability parameters, including metabolic stability, plasma stability, and permeability. The pharmacokinetic profile of a representative of this series was also assessed demonstrating the potential of these compounds for *in vivo* efficacy when dosed orally in disease models.

The high inhibitory potency of BTZ compound **1** (Figure 3.2) on MGL showing a IC_{50} of 59 nM, reported in the milestone work of King and colleagues¹¹, represented a promising starting point to set up a structure-activity relationships (SAR) study.



1

Figure 3.2 Structure of 2-octylbenzo[*d*]isothiazol-3(2*H*)-one

The establishment of a covalent bond between MGL and BTZs allows to freely expand the diversity of decorating groups around the warhead core with reduced risk of binding loss. However, the driver portion of BTZ should be designed to assure a good basal affinity for MGL. This portion is also designed to modulate the reactivity of

sulfenamidic warhead through a differential contribution to its electronic distribution. The possibility of a double modulation of the driver portion by insertion of substituents at nitrogen (R) and modulatory groups on the benzene ring (R') (**Figure 3.1**) was a crucial criteria for the choice of BTZ over ITZ core as lead structure.

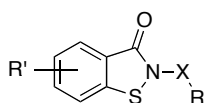
The diversity of decorating group around the BTZ warhead was expanded in order to:

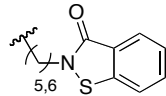
1. explore the pharmacophoric space around the targeted Cys201/Cys208 in order to get crucial information about the drug-target interaction;
2. modulate the reactivity of the sulfenamidic warhead to optimize their druggability;
3. achieve a better activity-stability balance;

Beside the biological evaluation of the newly synthesized BTZ derivatives on MGL, the modifications performed were aimed to increase the knowledge about the reactivity of this chemical class toward biological thiols in order to define a structure-reactivity landscape for BTZs.

To accomplish these purposes 3 clusters of BTZs have been synthesized, as outlined in **Table 3.1**.

Table 3.1. Overview of scaffold modifications around the BTZ core



Cluster 1			Cluster 2			Cluster 3		
X	R	R'	X	R	R'	X	R	R'
CH ₂	H Alkyl Alkylaryl	H	CH ₂	Benzyl	Nitro Hydroxy Alkyloxy Alkyl	N-H N- Me	Alkylaryl 	H

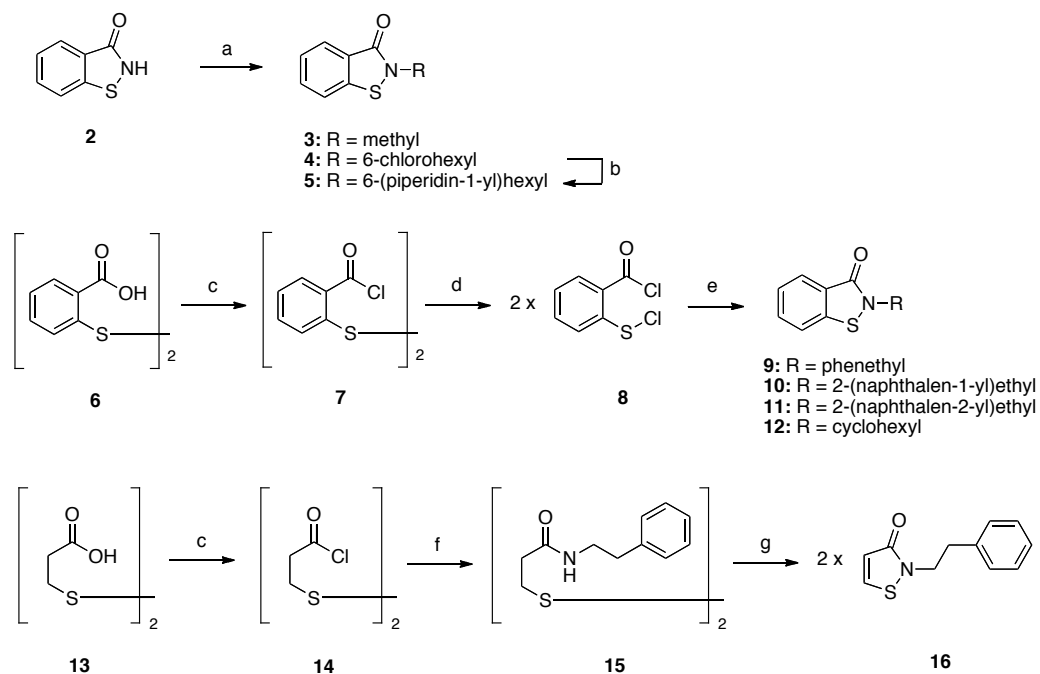
Compounds variously substituted on the sulfenamidic nitrogen with alkyl or alkylaryl substituents populate Cluster 1. Starting from the reference compound **1**, the influence of lipophilicity, shape and steric hindrance of the lateral chain were explored.

Compounds belonging to Cluster 2 were synthesized to evaluate the influence of substituents with different electronic and steric properties on the benzene ring of BTZ

warhead. We tried to achieve a modulation of inhibitory potency on MGL by affecting the reactivity of the sulfenamidic warhead. Cluster 3 is populated by 2-aminoalkylaryl derivatives and bidentate ligands.

3.1.1 Chemistry

For the synthesis of compounds belonging to Cluster 1, outlined in **Scheme 3.2**, different strategies were applied. Final products **3** and **5** were obtained *via* nucleophilic substitution from commercially available compounds **2**, treated with potassium carbonate and a proper electrophilic side chain. This reaction was carried out activating the benzo[*d*]isothiazol-3(2*H*)-one **2** in basic conditions to obtain *in situ* the activated nucleophilic benzo[*d*]isothiazol-3-olate salt.

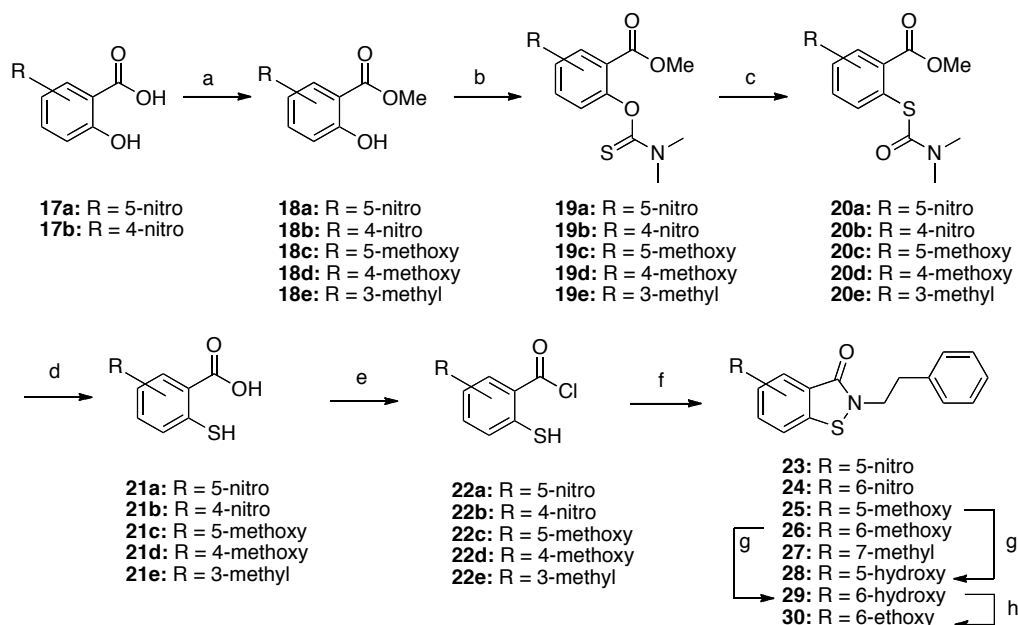


Scheme 3.2 Synthesis of BTZs and ITZ belonging to Cluster 1. *Reagents and conditions*: a) K_2CO_3 , alkyl halide, MeCN, r.t., 16h; b) K_2CO_3 , KI, MeCN, 60° C, 16h; c) $SOCl_2$, reflux, 6h; d) Cl_2 , CCl_4 , r.t., 2h; e) amine, dry TEA, r.t., 16h f) 2-phenylethanamine, dry TEA, dry DCE, r.t., 2h; g) SO_2Cl_2 , dry DCE, 0° C, 2h.

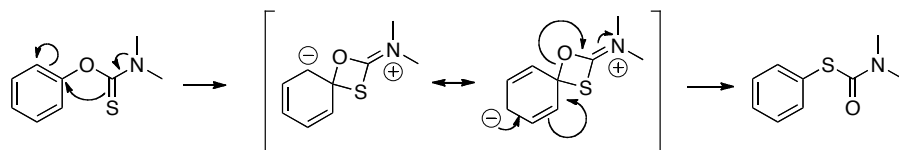
Compound **4**, an intermediate with a terminal chlorine atom in the side chain, was converted to final product **5** by a simple displacement of the chlorine using piperidine as nucleophilic species. Since a basic environment is required to deprotonate the nitrogen of benzo[*d*]isothiazol-3(2*H*)-one, the occurrence of elimination side reactions made this synthetic strategy not suitable to obtain final compounds in which aliphatic side chains were joined to the heterocyclic warhead by a secondary carbon. In order to move around to this side reactions occurrence and to achieve a good synthetic methodology for the preparation of *N*-alkylaryl and *N*-alkyl derivatives, other synthetic routes were carried out. Compounds **9-12** were synthesized in a 3-step sequence starting from dithiosalicylic acid **6** converted into the corresponding acyl chloride by reaction with SOCl₂ and oxidized in presence of bubbling gaseous chlorine to generate intermediate **8** that, after reaction with the proper amine, led to the formation of compounds **9-12** in modest to good yields. To Cluster 1 belongs also the isothiazolinone **16** that was synthesized with a similar procedure: acyl chloride **14** was firstly reacted with 2-phenethylamine and the isolated amide **15** was then subjected to oxidative cyclization exerted by SO₂Cl₂.

Phenyl-substituted BTZs **23-30** belonging to Cluster 2 were synthesized with a common procedure as outlined in **Scheme 3.3**. The strategy used for synthesis of Cluster 1-BTZs was not exploitable due to the lack of commercially available properly substituted dithiosalicylic derivatives. The key step of the synthetic procedure employed is the insertion of the sulfur atom on the phenyl ring that was accomplished through the Newman-Kwart rearrangement (NKR). The NKR allows access to thiophenols from phenols, as *O*-thiocarbamates are readily prepared and hydrolysis of *S*-thiocarbamates can readily be achieved. Indeed, intramolecular aryl migration of *O*-thiocarbamates (**19a-e**) at high temperatures led to *S*-thiocarbamates (**20a-e**). As the NKR requires elevated temperatures, several side reactions can occur, and these can be catalyzed by trace impurities. The use of *N,N*-dimethylthiocarbamates has a major advantage in that these compounds tend to crystallize more easily and can therefore be easily purified. The accepted mechanism for the NKR, confirmed by kinetics experiments, is depicted in **Scheme 3.4**. The reaction exhibits the first-order kinetics typical for intramolecular reactions together with a large and negative entropy of activation. The driving force is the thermodynamically favorable conversion of a C=S into a C=O bond ($\Delta H \sim 13 \text{ kcal mol}^{-1}$). Typically for aromatic nucleophilic substitution

reactions, electron-withdrawing groups in the *para*- and *ortho*-positions show a substantial activating effect.



Scheme 3.3 Synthesis of BTZs belonging to Cluster 2. *Reagents and conditions:* a) conc. H_2SO_4 , super-dry MeOH, reflux; b) DABCO or NaH, *N,N*-dithiocarbamoylchloride, dry DMF; c) MW, diphenylether; d) NaOH, MeOH/ H_2O 2:1, reflux; e) SOCl_2 , reflux, 6h; f) 2-phenylethanamine, dry TEA then I_2 , dry THF, 0°C to r.t., 20h; g) BBr_3 , dry benzene 0°C to reflux, 3h; h) K_2CO_3 , EtBr, dry MeCN, 0°C to 30°C , 25h



Scheme 3.4 Mechanism of NKR

The use of a pressure-proof microwave oven allowed discarding the classical heating conditions that led to destruction of the substrate and to formation of side products on prolonged contact with the hot reaction vessel walls. The microwave-assisted procedure provided a significant reduction of the reaction times and a slightly increase in yields.

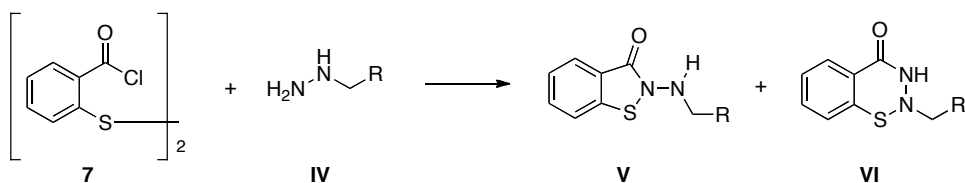
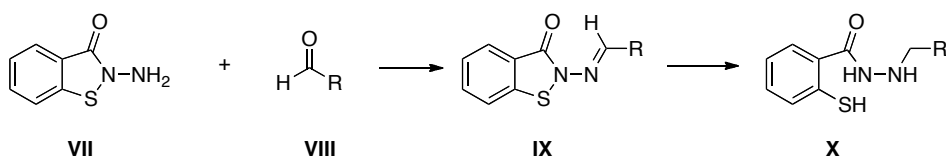
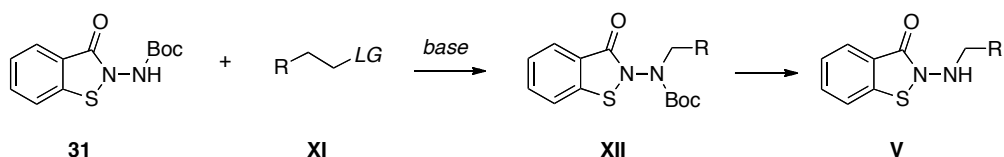
The properly substituted 2-hydroxy methylbenzoate **18a-e** was reacted with *N,N*-dithiocarbamoyl chloride in presence of a base in dimethylformamide (DMF). The

choice of the base was influenced by the acidity of the hydroxyl group. The basic catalysis exerted by 1,4-diazabicyclo[2.2.2]octane (DABCO) was sufficient to obtain compounds **18a-b** in good yield while resulted ineffective for compounds **18c-e**. The latters required the use a stronger base such as sodium hydride (NaH) to reach appreciable conversions. After the NKR, *S*-thiocarmates **20a-e** were hydrolyzed by exposure to NaOH, leading to the formation of 2-mercaptobenzoic acids **21a-e**. Hydrolytic conditions were not effective for compound **20e**, indeed, product **21e** was not isolated, while the product of hydrolysis of **20e** showed the intact thiocarbate moiety; this intermediate (methyl 2-((dimethylcarbamoyl)thio)-3-methylbenzoate) was used for the next reaction step exploiting the thiocarbate moiety as leaving group. Substituted benzoic acids **21a-d** and the aforementioned product of **20e** hydrolysis were then treated with SOCl₂ to generate acyl chlorides **22a-e** that were isolated and used without any further purification. The highly reactive acyl chlorides were finally subjected to a one-pot oxidative cyclization with 2-phenethylamine in anhydrous THF in presence of iodine, to generate final products **23-27** in good yields. Compounds **25** and **26** were used to synthesize final products **28** and **29**, respectively, through a demethylation reaction exerted by boron tribromide in benzene. Compound **30** was synthesized from product **29** *via* nucleophilic substitution with ethyl bromide in presence of potassium carbonate.

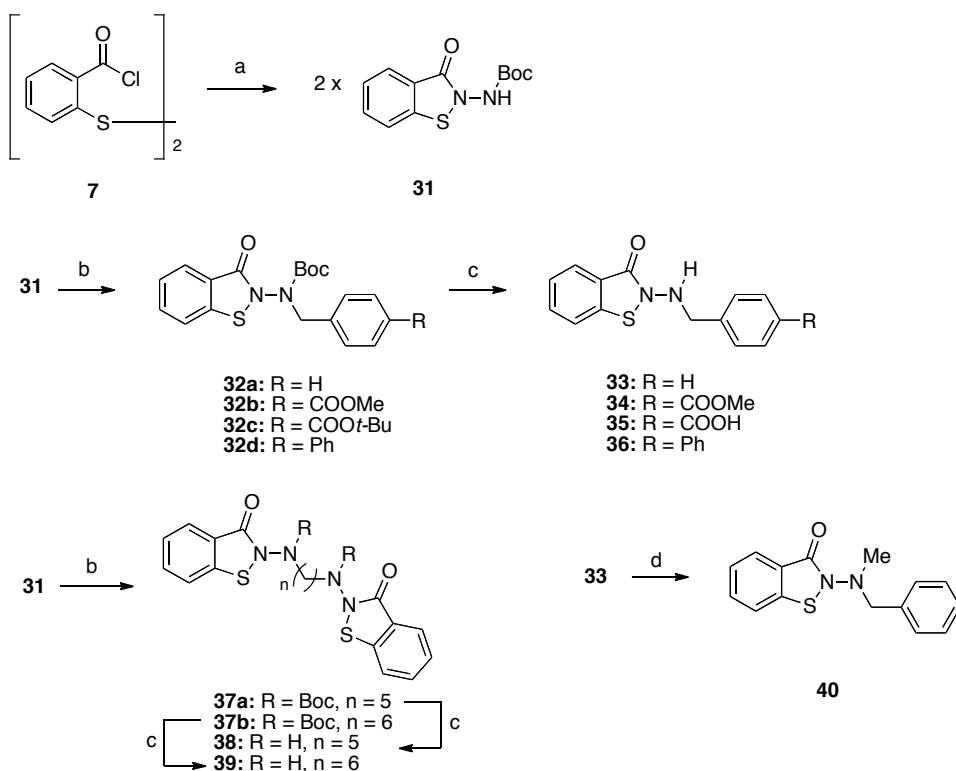
The synthesis of BTZs belonging to Cluster 3 required the investigation of various synthetic pathways, outlined in **Scheme 3.5**. Strategy A was centered on the oxidative cyclization between dithiosalicylic chloride **7** and the preformed hydrazine **IV**. Results were not fully satisfactory due to the formation of a mixture of the 5-membered desired product **V** and the undesired 6-membered derivative **VI**.

Strategy B was based on a classical reductive amination. BTZ **VII** was reacted with the proper aldehyde and after isolation of the imine derivative **IX** the reduction step was performed. As expected, classical imine reduction conditions (H₂, Pd/C or NaBCNH₃) led to ring opening of the BTZ core confirming the instability of the sulfenamidic moiety to reductive conditions.

Synthesis of BTZs belonging to Cluster 3 was accomplished following Strategy C. Boc-protected BTZ **31** was reacted, in presence of a base, with the proper lateral chain fragment **XI** functionalized with a leaving group (halide), following a S_N2 mechanism. The subsequent cleavage of the protecting group allowed obtaining desired product **V**.

A Oxidative cyclization**B Reductive amination****C $\text{S}_{\text{N}}2$ and deprotection****Scheme 3.5** Overview of synthetic strategies applied for the synthesis of BTZs belonging to Cluster 3

This strategy revealed to be solid and versatile and was applied for the synthesis of a wide range of compounds. The choice of the proper base was fundamental to avoid elimination side-reactions and to increase the yield of the process. Potassium bis(trimethylsilyl)amide (KHMDs), a very hindered base, was chosen for its high basic properties and its low nucleophilic character thus avoiding the formation of undesired side-products. Intermediate **31** (**Scheme 3.6**) was generated, through the consolidated oxidative cyclization exerted by iodine, from compound **7** and *tert*-butyl hydrazinecarboxylate and was used as starting material for the synthesis of the final products. Compound **31**, in a two-step reaction process according to Strategy C, was firstly treated with KHMDs and the proper alkyl halide and subsequently oxidized by means of iodine to generate intermediates **32a-d** and **37a-b**. In the second step, acidic cleavage of the Boc group by exposure to an equivolume mixture of trifluoroacetic acid and dichloromethane, afforded final products **33-36**, **38** and **39**. Compound **40** was obtained by methylation of final product **33** with methyl iodide and a nucleophilic weak base such as imidazole.

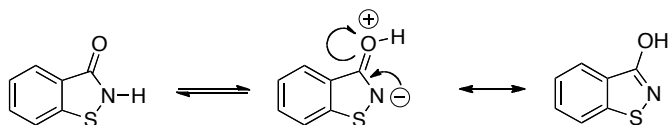


Scheme 3.6 Synthesis of BTZs belonging to Cluster 3. *Reagents and conditions:* a) *tert*-butyl hydrazinecarboxylate, dry TEA dry THF, 0°C to r.t., 16h then I₂, r.t., 4h; b) KHMDS, alkyl halide, dry DMF, 0° C to r.t., 16h; c) TFA, DCM, 0° C to r.t., 4h; d) MeI, imidazole, r.t., 16h

3.1.2 Biological evaluation of BTZ derivatives on MGL

The synthesized BTZ compounds were evaluated for their ability to inhibit recombinant purified rat MGL overexpressed in *E. Coli*. At first we investigated the influence of substituents on the nitrogen atom of the warhead core evaluating the role of lipophilicity and steric hindrance of the lateral chain. The IC₅₀ values for BTZs belonging to Cluster 1 are reported in **Table 3.2** along with that of the reference compound **1**. Replacing the *n*-octyl group with an hydrogen atom (**2**) resulted in a significant decrease of the inhibitory potency (IC₅₀ = 306.5 nM), which was recovered with the introduction of a methyl substituent on the nitrogen atom (**3** - IC₅₀ = 59.5 nM). The lack of a *N*-substituent probably decreases the activity of compound **2** on MGL because of the existence of a prototropic equilibrium between the nitrogen and the

oxygen atoms of non-substituted isothiazol-3-one¹². This hydrogen transfer induces the isothiazol-3-onic system aromatization and produces a fully aromatized 3-hydroxybenzisothiazole (**Scheme 3.7**).



Scheme 3.7 Prototropic equilibrium of compound 2

In this form, the sulfenamidic system is not present, precluding any reactivity toward nucleophiles. Indeed, the S-N bond cleavage induced by a nucleophilic attack on 3-hydroxybenzisothiazole sulfur atom is unfavored because it should lead to the disruption of heterocyclic system aromaticity.

Table 3.2 Inhibition of purified recombinant rat MGL by BTZs and ITZ belonging to Cluster 1.

Compound	R	IC ₅₀ (nM) ^a
1	<i>n</i> -octyl	59 ± 7
2	H	306.5 ± 32.7
3	Me	59.5 ± 5.8
12		55.5 ± 7.4
4		195.2 ± 12.3
9		34.1 ± 2.0
10		21.8 ± 5.2
11		54.2 ± 15.7
Compound	Structure	IC ₅₀ (nM) ^a
16		758.6 ± 49.8

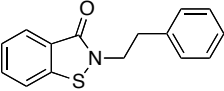
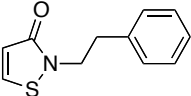
^a Reported are Means ± SEM (n = 3-4)

The similar activity of compounds **1** (ClogP: 5.2) and **3** (ClogP: 1.5) suggests that the enzyme can tolerate broad modification of the *N*-side chain both in term of steric bulk and lipophilicity. This also suggests that an increase in lipophilicity does not bring to a parallel increase of potency in the BTZ series, differently to what had been observed for the less lipophilic isothiazolinone series (Chapter 2) The first hypothesis was confirmed by compound **12**, bearing a cyclohexyl side chain that have intermediate properties in terms of ClogP (ClogP: 3.5) but a significant difference in terms of shape compared to the *n*-octyl group of reference compound **1**. This shape variance, however, had no impact on potency, indeed, compounds **1** and **12** showed comparable IC₅₀ values. The introduction of a side chain with a basic terminal piperidine (**4**) brought a significant decrease of activity (IC₅₀ = 195.2 nM) suggesting that protonation of the side chain could be detrimental because a certain level of lipophilicity is required to achieve good inhibitory potency on MGL.

Compound **9**, bearing a 2-phenethyl group that confers a lipophilicity within the “allowed” range (ClogP: 3.6), showed a slightly increment in the inhibitory potency (IC₅₀ = 34.1 nM), revealing the profitable insertion of an aromatic portion in the side chain. With compounds **10** and **11** we explored the possibility to increase the aromatic portion with an α - and β -naphthyle group, respectively. Both these compounds showed high inhibitory potency on MGL with IC₅₀ in the low nanomolar range appointing *N*-alkylaryl BTZ as the most promising hits. The slightly drop of potency of compound **11** compared to **10** suggests that the bent shape of the α -naphthyle group is better tolerated. Eventually, we synthesized for comparison the homologous ITZ **16** of leading compound **9** that showed a IC₅₀ of 758.6 nM on MGL.

Despite this result seems to point out BTZs as a more potent class of MGL inhibitors, is not appropriate to compare the inhibitory potency of BTZs and ITZs. This because the two classes have different SAR, indeed, previous studies on the ITZ othililone, revealed that increasing lipophilicity of the *N*-side chain enhanced activity on MGL¹¹, while this finding is not found for the BTZ class. Moreover, site-direct mutagenesis studies in which individual regulatory Cys201 and Cys208 were replaced with alanines and the mutants were expressed in HeLa cells, had indicated different preferential target cysteines for the two classes. We examined how cysteine mutations influence the ability of compounds **9** and **16** to inhibit MGL.

Table 3.3 Inhibition of purified recombinant rat MGL by compounds **9** and **16** with selective mutation of Cys201 and Cys208

Cpd	Structure	IC ₅₀ (nM) ^a				Cys Index (C201-208A/Wt)
		Wt	C201A	C208A	C201-208A	
9		34.1	242.9	72.6	604.7	17.7
		± 2.0	± 18.0	± 30.3	± 10.2	
16		758.6	461.5	1239.9	1968.9	2.6
		± 49.8	± 59.5	± 20.4	± 59.6	

^a Reported are Means ± SEM (n = 3-4)

As outlined in **Table 3.3**, IC₅₀ of compound **9** dropped to 242.9 nM when Cys201 was converted to alanine and to 72.6 nM on Cys208A MGL mutant. Conversely, compound **16** showed a higher, yet limited, loss of potency when Cys208 was muted to alanine (IC₅₀ = 1239.9), compared to wild-type MGL. These outcomes, in agreement with previous studies performed by Matuszak *et al.* on human MGL¹³, display the preferential interaction of BTZs with Cys201 while Cys208 seems to be the favorite target residue for ITZs. Evaluation of activity of compounds **9** and **16** on double mutants (C201/208A) MGL resulted in a significant decrease of inhibitory potency with IC₅₀ of 604.7 nM and 1968.9 nM, respectively. This additive effect observed on the double mutant enzyme suggests that both Cys201 and Cys208 may be involved in the inhibition process exerted by BTZs and ITZs. A Cys index, calculated as the ratio between IC₅₀ values on double mutant and wild type MGL, expresses the specificity of thiol-reactive inhibitors for the two cysteines Cys201 and Cys208. A high Cys index, as observed for compound **9**, means that the inhibitor is much less potent in inhibiting MGL lacking both the cysteines on the lid domain, so it is probably acting at one of these (or both). A small Cys index suggests that the inhibitor has other mechanisms, that could be, e.g., interaction with Cys242.

We next conducted a deep study about the mechanism of action of lead compound **9** and its MGL inhibitory effect on 2-AG signaling. We utilized a rapid dilution assay to assess whether compound **9** inhibits MGL through a reversible or irreversible mechanism. Purified MGL was first preincubated with a concentration of compound **9**

that was 10-fold higher than its IC_{50} value, and then diluted 100-fold (to 10% of its IC_{50} value). As shown in **Figure 3.3B**, the dilution produced a total recovery of enzyme activity. By contrast, when MGL was incubated with the irreversible serine-reacting probe MAFP, MGL activity did not recover after dilution. The restoration of the catalytic activity of the enzyme upon dilution revealed the reversible inhibitory mechanism of compound **9**, consolidating previous findings reported for this class of compounds^{11,13}.

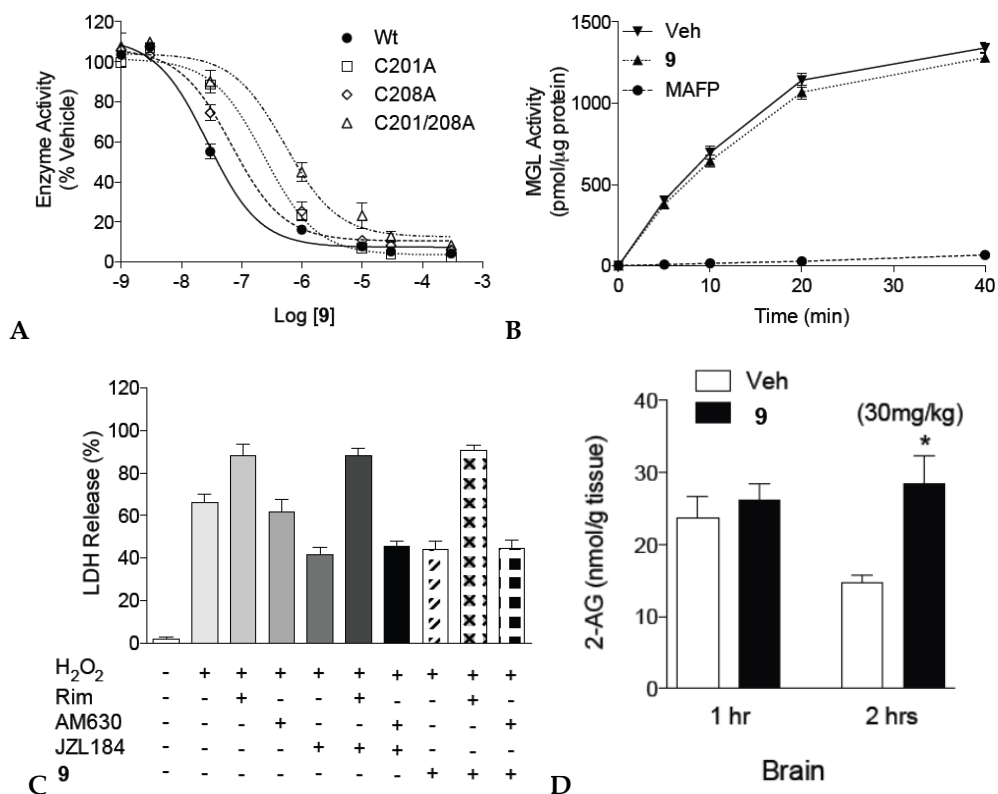


Figure 3.3 (A) Effects of compound **9** on wild-type MGL (circles), MGL mutants C201A, C208A or C201/208A. (B). Rapid dilution of MGL incubated with vehicle, compound **9** (10 μ M final), or MAFP (23 nM final) (C) Effects of H₂O₂ (300 μ M), alone or combined with CB₁ antagonist Rimonabant, CB₂ antagonist AM630, MGL inhibitor JZL-184 (1 μ M) or compound **9** (1 μ M), on LDH release. (D) Effect of compound **9** (30 mg/Kg i.p.) on 2-AG levels in rat brain

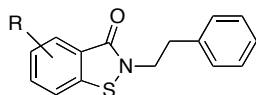
Mutagenesis studies (**Table 3.3**, **Figure 3.3A**) and rapid dilution assay showed an H₂O₂-like behavior of compound **9** on MGL (see Chapter 2). To evaluate the ability of our compound to modulate 2-AG levels, *in vitro* and *in vivo* experiments were

performed. Neuro-2a cells were incubated with high levels of H₂O₂ and evaluation of cellular damage using LDH was assessed (**Figure 3.3C**). The toxic effect of hydrogen peroxide (**Figure 3.3C** - entry 2) was heightened by CB₁ blockade using the selective antagonist Rimonabant (**Figure 3.3C** - entry 3) but not by CB₂ blockade (antagonist AM630, **Figure 3.3C** - entry 4). Conversely, LDH release was reduced by treatment with the irreversible MGL inhibitor JZL184 (**Figure 3.3C** - entry 5). Administration of compound **9** combined with H₂O₂ resulted in a reduction of cellular damage (**Figure 3.3C** - entry 6) comparable with that of JZL184. These results display that blockade of MGL activity, and the consequent increase of 2-AG levels, reduces cellular damage elucidating the CB₁-mediated neuroprotective role of 2-AG, and that compound **9** has the same ability as JZL184 to exert this blockade on Neuro-2a cells, when added at the same concentration. Moreover, administration of compound **9** in animal models with a dose of 30 mg/kg resulted in an increase of 2-AG levels in rat brain after 2 hours (**Figure 3.3D**). These outcomes display the ability of tested BTZ **9** to selective inhibit MGL catalytic activity and to modulate 2-AG signaling both *in vitro* and *in vivo*.

The structure-activity relationships for BTZs belonging to Cluster 1 revealed the role of the side chain lipophilicity and the good tolerance of the enzyme to steric modification of the *N*-substituents, possibly due to the surface-exposed position of Cys201 and Cys208 that allows diversified accommodations of the lateral chain. We next investigated, through the introduction on the benzene ring in positions conjugated to the sulfur atom or to the carbonyl moiety, the effect of substituents with different electronic properties on the inhibitory potency of BTZs. We also evaluated the influence of a steric hindering group inserted close to the reactive sulfur atom. These scaffold modifications were aimed at modulating the reactivity of the sulfenamidic warhead. We synthesized compounds **23-30** (Cluster 2) keeping fixed the 2-phenethyl side chain of the lead compound **9**. We inserted a polar electron-withdrawing group such as -nitro (**23**, **24**), hydrophilic (-hydroxy **28**, **29**) and lipophilic (-methoxy and -ethoxy **25**, **26**, **30**) electron-donor groups at position 5 and 6 of the benzene ring. Evaluation of potency of Cluster 2-BTZs on rat MGL was assessed and the results, outlined in **Table 3.4**, revealed a general loss of potency. The most considerable decrease of potency was registered for compounds **29** and **27** with IC₅₀ of 2.5 and 13.1

μM , respectively. No clear influence of the electronic effects on inhibitory potency emerged from BTZs belonging to this set.

Table 3.4 Inhibition of purified recombinant rat MGL by BTZs belonging to Cluster 2



Compound	R	IC ₅₀ (nM) ^a
9	H	34.1 ± 2.0
23	5-NO ₂	163.4 ± 2.8
28	5-OH	135.0 ± 3.8
25	5-OMe	568.0 ± 55.3
24	6- NO ₂	237.9 ± 10.3
29	6-OH	2547.0 ± 879.7
26	6-OMe	512.2 ± 64.4
30	6-OEt	208.4 ± 10.6
27	7-Me	13069.5 ± 523.9

^a Reported are Means ± SEM (n = 3-4)

On the other hand, the role of steric hindrance was evidenced with compound **27** (IC₅₀ = 13069.5 nM), which displayed the negative influence of a bulky group in position 7 close to the reactive core of the molecule. The steric hindrance of the methyl group could reduce the reactivity of the warhead hampering the sulfur atom and reducing the rate of the nucleophilic attack by the thiol group of the targeted cysteine.

The results obtained suggest that insertion of substituents on the benzene ring of BTZ is poorly tolerated and forced us to continue our SAR investigation focusing on the lateral chain that appeared to be the only fragment of the molecule susceptible to profitable modifications. To design new compounds for further SAR exploration, computational studies were performed. In order to evaluate the conformations of BTZ derivatives covalently bound to Cys201, as suggested by mutagenesis studies, the crystal structure of human MGL 3HJU was selected as model structure and it was used for covalent docking studies. Binding modes obtained for compounds **9** are represented in **Figure 3.4A** (orange carbons). The covalent adduct of compound **9** showed a polar interaction between the sulfenamidic nitrogen and the backbone

oxygen of Pro198, which can stabilize the binding mode. Compound **33**, bearing a nitrogen atom at the α -position of the sulfenamidic core, assumed a comparable conformation, but the polar interaction with the backbone carbonyl was taken by the peripheral (formerly exocyclic) NH group as depicted in **Figure 3.4A** (deep-teal carbons). Notably, the exocyclic nitrogen could enhance the water solubility of this derivative. It could be protonated under acidic conditions, thus increasing the electron-withdrawal effect of the exocyclic nitrogen on sulfenamidic system.

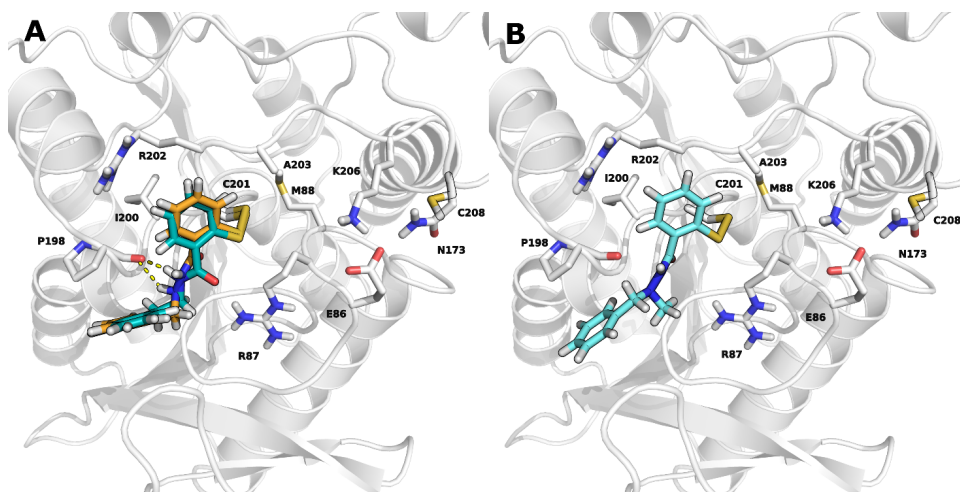


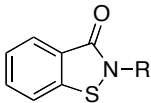
Figure 3.4 (A) Covalently bound compounds **9** (orange carbons) and **33** (deep-teal carbons) assume a very similar binding mode, which is strengthened by the formation of hydrogen bonds (yellow dashes) with the backbone oxygen of Pro198. (B) The introduction of the *N*-methyl group in compound **40** (light cyan carbons) prevents the formation of polar contacts between the ligand and the protein

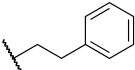
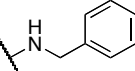
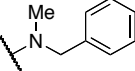
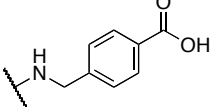
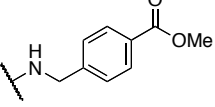
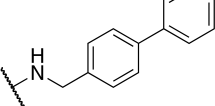
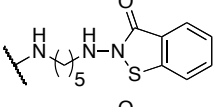
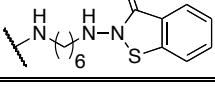
Compound **33** showed a high inhibitory potency on MGL with a IC_{50} of 19.5 nM (**Table 3.5**), supporting our model. This encouraging result led us to explore SAR for this new cluster, populated by 2-amino derivatives.

Compound **33**, the most potent BTZ synthesized, was subjected to detailed studies on mutant enzymes. The results, outlined in **Table 3.6**, showed comparable potency on single mutants with a IC_{50} of 54.4 nM on C201A mutant and 44.9 nM on C208A MGL. This data revealed a different behavior from compound **9** with a loss of selectivity for Cys201. The additive effect of double mutation on inhibitory potency of compound **33** was observed with a IC_{50} on C201-208A mutant of 782.0 nM.

The introduction of a methyl substituent on the exocyclic nitrogen yielded to compound **40**. The results of binding modes obtained for compound **40**, showing the influence of the methyl group that hamper the formation of any polar interaction (**Figure 3.4B**), were reflected by the 10-fold loss of activity observed for this compound ($IC_{50} = 189.4$ nM).

Table 3.5 Inhibition of purified recombinant rat MGL by BTZs belonging to Cluster 3



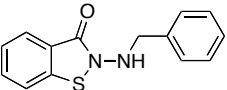
Compound	Structure	IC_{50} (nM) ^a
9		34.1 ± 2.0
33		19.5 ± 0.8
40		189.4 ± 39.7
35		277.7 ± 1.9
34		93.9 ± 5.5
36		322.1 ± 18.7
38		22.3 ± 3.7
39		21.0 ± 0.3

^a Reported are Means \pm SEM (n = 3-4)

The introduction of an acid group (**35**) in position 4 of the benzylamino side chain was devised to allow the formation of hydrogen bonds with Lys206 and Glu86, which were involved in an intramolecular saline bond in the crystal structure of the enzyme.

Hypothetical covalent adducts of MGL with compounds **35** and **34** are represented in **Figure 3.5**.

Table 3.6 Inhibition of purified recombinant rat MGL by compound **33**
with selective mutation of Cys201 and Cys208

Cpd	Structure	IC ₅₀ (nM) ^a				Cys Index (C201-208A/Wt)
		Wt	C201A	C208A	C201-208A	
33		19.5 ± 0.8	54.4 ± 4.1	44.9 ± 8.7	782.0 ± 77.5	40.1

^a Reported are Means ± SEM (n = 3-4)

These possible interactions, hypothesized by docking studies, are not sufficient to generate a specific *in vitro* enhancement of inhibitory potency, indeed, IC₅₀ of compounds **35** and **34** on purified MGL are 277.7 nM and 93.9 nM, respectively. The introduction of a second phenyl ring in position 4 of the benzylamino side chain resulted in a loss of activity as well, with a IC₅₀ for compound **36** of 322.1 nM.

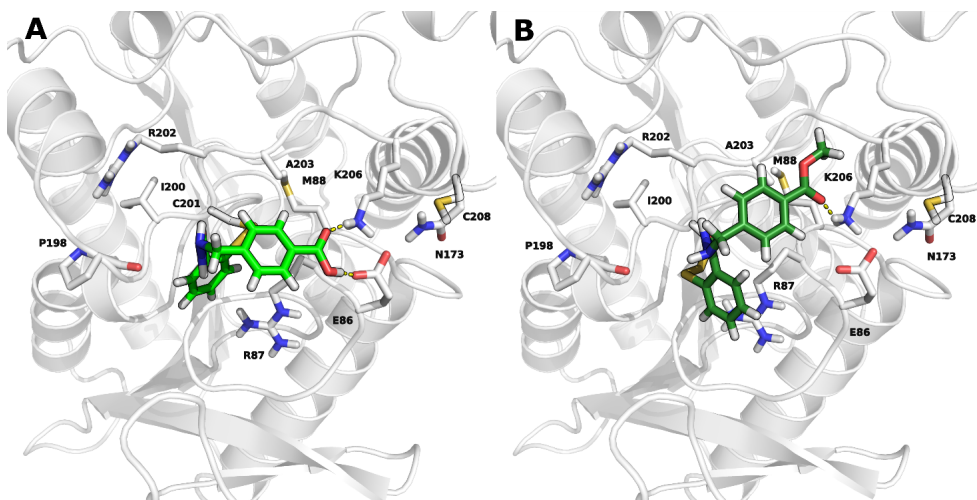


Figure 3.5 (A) Binding modes for compound **35** show the interaction of the acid group with Lys206 and Glu86. (B) Docking results for compound **34** gave binding modes comparable to that obtained for **35** showing polar interactions with Lys206

As the modulation of the lateral chain of compound **33** always led to less active compounds, we next focused our attention on the investigation of bidentate ligands. Mutagenesis studies revealed that mutating both Cys201 and Cys208 to alanine reduced the inhibitory potency of BTZs, compared to WT MGL, supporting the design of compounds able to concurrently interact with both cysteines generating a synergistic inhibitory effect. To test this hypothesis an Induced Fit Docking study was performed in order to evaluate the binding mode of symmetric ligands, based on compound **33** scaffold, looking for the optimal linker length to reach both Cys201 and Cys208. The results of the Induced Fit Docking Study are represented in **Figure 3.6**.

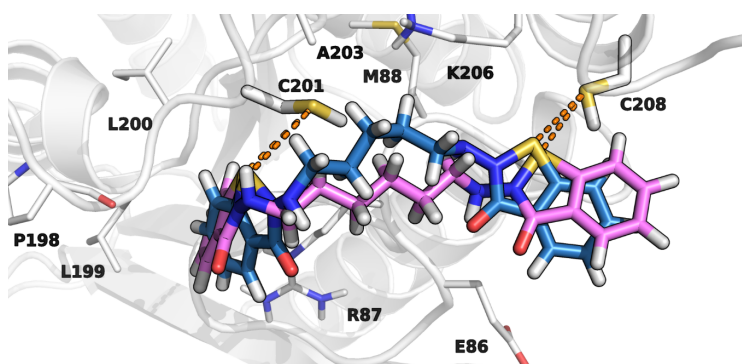
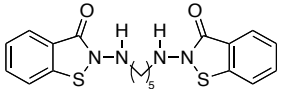
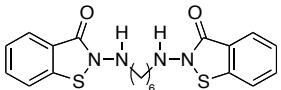


Figure 3.6 Both compounds **38** (blue carbons) and **39** (pink carbons) occupy the region separating CYS201 from CYS208; orange dashes indicate the distance between the cysteines thiol groups and the benzo[*d*]isothiazol-3(2*H*)-one moieties of the symmetric compounds

The flexible alkyl chain of both compounds **38** and **39** occupy the region situated between Cys201 and Cys208, while the sulfur atoms of the BTZ groups reside nearby the cysteines thiol groups, suggesting that both the pentyl and the hexyl linker represent suitable spacers. Compounds **38** and **39** showed IC_{50} of 11.6 and 16.8 nM, respectively, on purified rat MGL. To evaluate if these results are ascribable to a simultaneous interaction with both cysteines, compounds **38** and **39** were tested on mutant MGL. As reported in **Table 3.7** compound **38** showed a 20-fold decrease in potency on both C201A and C208A single mutant. This result is consistent with a inhibitory mechanism that involves the simultaneous covalent reaction with both cysteines. This hypothesis is supported by the high values of IC_{50} on double mutant MGL (1460.7) and Cys Index. Compound **39** showed a minor loss of potency on single mutants, especially on C208A MGL (IC_{50} = 82.7 nM), and a 120-fold decrease of

inhibitory potency on double mutant with a Cys Index comparable to that of compound **39**.

Table 3.7 Inhibition of purified recombinant rat MGL by compound **38** and **39** with selective mutation of Cys201 and Cys208

Cpd	Structure	IC ₅₀ (nM) ^a				Cys Index (C201-208A/Wt)
		Wt	C201A	C208A	C201-208A	
38		11.5	229.8	219.8	1460.7	127.0
		± 1.5	± 69.0	± 33.9	± 465.0	
39		16.8	114.3	82.7	2079.6	129.3
		± 0.4	± 8.9	± 11.6	± 40.0	

^a Reported are Means ± SEM (n = 3-4)

3.1.3 Reactivity studies on BTZ derivatives

To better understand the chemical properties of BTZ class and to evaluate the behavior of these compounds in presence of thiols of biological relevance, we performed detailed studies on their reactivity. The experimental reactivity of BTZs in the presence of thiols was studied by means of HPLC-UV and HPLC-ESI-MS analysis, monitoring the decreasing concentration of BTZ and the formation of new species as the reaction proceeded. Reactions were performed mimicking physiological conditions (PBS buffer, pH 7.4, 37° C) and choosing as reactive counterpart of BTZ the most abundant thiol in cells, glutathione (GSH). To minimize the potential interference of atmospheric oxygen on this elaborate ox-redox system, we performed reactions under argon atmosphere with degassed solvents. The first attempts were conducted using equimolar concentrations of BTZ and GSH, trying to measure the rate of the nucleophilic substitution of GSH on the sulfur atom of BTZs. However, reaction occurred in seconds and rate was impossible to be measured, as, for the majority of tested BTZs, at the first time point (i.e. t ~ 30 s) BTZ had almost totally reacted with GSH. Moreover, the HPLC chromatogram revealed the formation of different reaction species, whose relative amounts were not reproducible from one experiment to another (data not

shown). Therefore, we decided to investigate the reactions of BTZ in presence of two equivalents of GSH and to monitor the time-course of reaction species in solution. We observed that at two different reaction time-points, $t=60$ and $t=120$ min, a condition of pseudo-equilibrium among reaction species was reached. $t = 60$ min was therefore chosen as appropriate reaction time to investigate the identity of unknown species in solution by HPLC-ESI-MS/MS analysis.

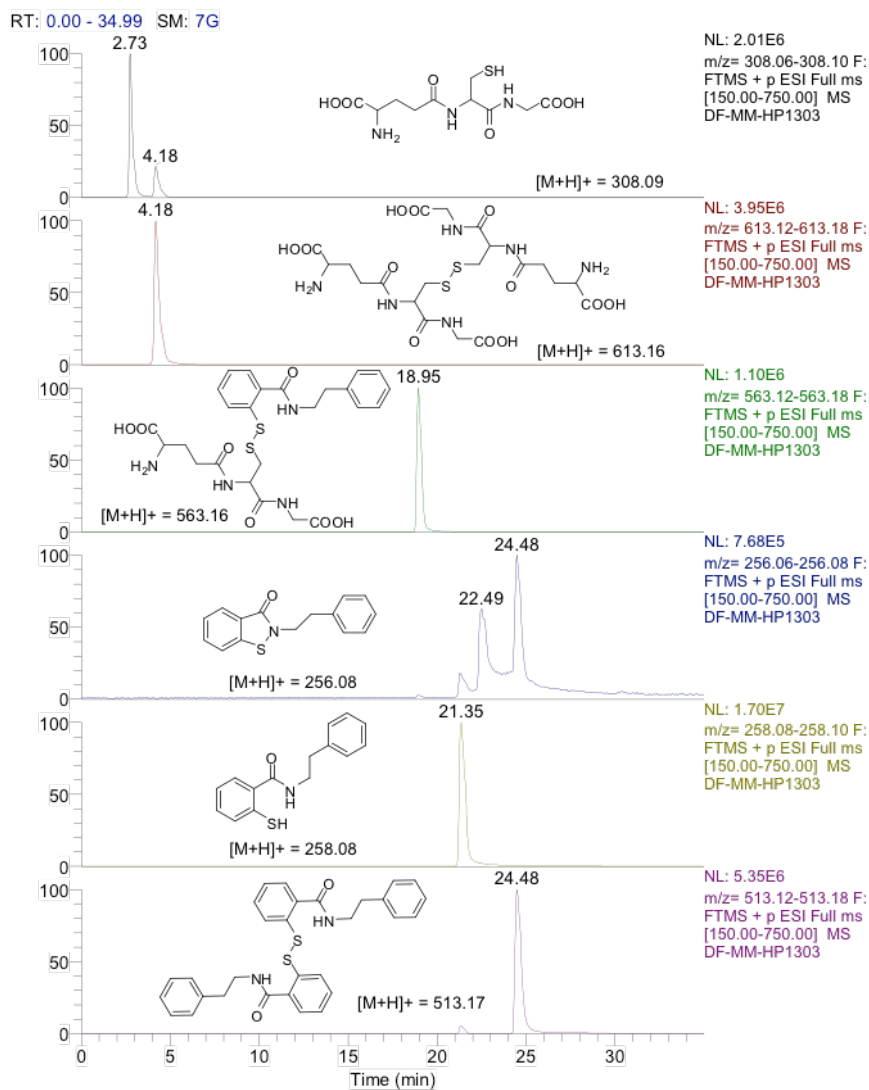
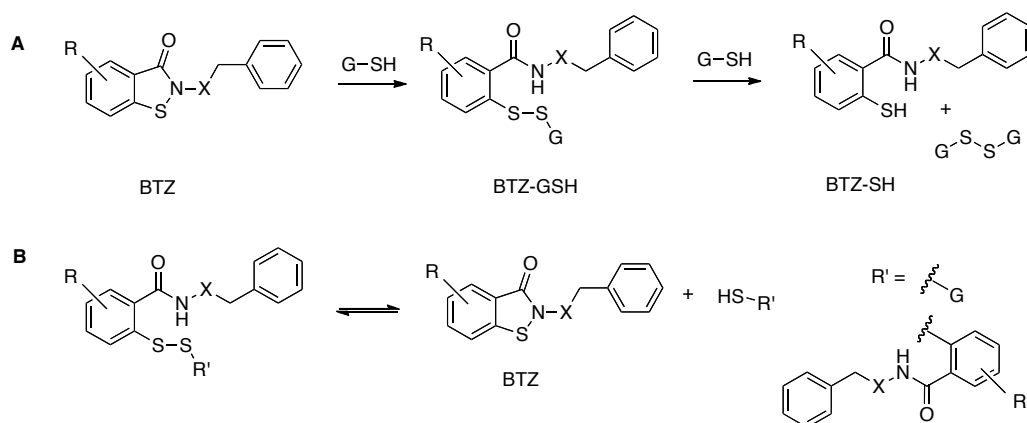


Figure 3.7 HPLC-MS extracted ion chromatograms showing reaction species identified after a 60 min incubation of BTZ with two equivalents of GSH.

In **Figure 3.7**, the extracted ion chromatograms from a HR-MS full scan analysis ($m/z = 150\text{--}750$ amu) in positive ion mode of a 60-min incubation of BTZ **9** with GSH are presented. At $m/z = 308.09$, Retention Time (RT) = 2.73 min a peak of monoprotonated molecular ion $[M+H]^+$ corresponding to unreacted GSH was present (See LC/MS Trace #1). At $m/z = 256.08$ and RT = 22.49 min a small peak of unreacted BTZ is present (Trace #4). The other peak at RT = 24.48 min is the product ion from another species, the symmetric disulfide of BTZ, in solution (see below).

At RT = 18.95 min, and at $m/z = 563.16$ (Trace 3) a peak was present, which corresponded to the BTZ conjugate with GSH. This conjugate BTZ-GSH was formed by a 1:1 reaction of BTZ with GSH (**Scheme 3.8A**).



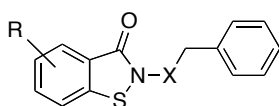
Scheme 3.8 **A** Reaction pathway of BTZ in presence of 2-fold excess of GSH **B** Disproportionation of mixed and symmetric disulfides in aqueous media leading to formation of the native BTZ and the corresponding sulfhydryl monomer

In presence of another equivalent of GSH, the BTZ-GSH conjugate was prone to further react generating a substituted thiosalicylamide BTZ-SH ($m/z = 258.08$, RT = 21.35 min, Trace #5) and oxidized glutathione (GSSG, $m/z = 613.16$, RT = 4.18 min, Trace #2). Thiosalicylamide could react as a thiolic nucleophile able to attack both native BTZ and BTZ-GSH conjugate in order to generate symmetric disulfide ($m/z = 513.17$, RT = 24.48 min, Trace #6), which in turn is susceptible of a new nucleophilic attack by GSH. On the other hand, the disproportionation reaction of disulfides in aqueous media leading to restoration of BTZ and to the corresponding sulfhydryl compound (BTZ-SH or GSH) is well known in literature² (**Scheme 3.8B**).

In our attempt to build a reactivity scale among the selected set of BTZs, we focused our attention on the measurement of the concentrations of unreacted GSH, of oxidized glutathione disulfide (GSSG) and on the formation of the mixed disulfide BTZ-GSH. Moreover, we monitored the concentration of BTZ still present under pseudo-equilibrium conditions that could reveal the capability of BTZ to be regenerated in the ox-redox process and, therefore, to be available for further reactions with nucleophiles. As already stated, we aimed to modulate the reactivity of the BTZ nucleus *vs.* thiol nucleophiles by different substitution at positions 5 and 6 of the BTZ ring with groups endowed with opposite electronic properties. Substitution at position 7 was explored with the aim to evaluate the effect of an increased steric hindrance at this position on BTZ reactivity. In **Table 3.8** are reported the results obtained for our set of BTZs after a 60-min incubation time during which 200 μM GSH reacted with 100 μM BTZ. Due to the absence of an adequate calibration standard, we couldn't quantify the BTZ-GSH conjugate present and we therefore reported in **Table 3.8** the difference between initial concentration of GSH (200 μM) and the sum of final GSH + 2*GSSG concentrations. Peak areas derived from HPLC/UV runs were lower than the detection limits for compounds **24** and **27**. The same was observed for compound **23**, for which the estimated BTZ-GSH concentration was close to the standard deviation of the GSH concentrations measured. For the reference compound **9** no intact BTZ was detected, with a small amount of mixed disulfide, while GSH and GSSG were approximately equimolar. For the nitro derivatives **23** and **24** no BTZ nor BTZ-GSH were detected, which allows to simplify the complex scheme of reactions traced above to two half-cell reactions, consisting of GSH oxidation and BTZ reduction to a mixture of salicylamide and symmetrical dithiosalicylate. This is probably due to the fact that the electron withdrawing effect on the benzene rings destabilizes the mixed disulfide BTZ-GSH. In this context, the 5-nitro derivative **23** resulted a stronger oxidant than the 6-nitro, giving a significantly higher ratio GSSG/GSH, which is consistent with its conjugation to the sulfur atom. Compounds substituted with the electron-donating methoxy group gave significant residual concentrations of the mixed disulfide, more evident for the 5-methoxy derivative **25**, which also showed a small, yet detectable concentration of intact BTZ. Compared to the reference compound **9**, the pseudo-equilibrium concentrations of reduced GSH did not show highly significant differences, pointing out a limited effect of this substituent on redox potential. The hydroxyl substituent

also caused a stabilization of the mixed disulfides BTZ-GSH, as evidenced by mass balance calculation and the highest peak areas observed by UV-HPLC (not shown). As all compounds **23-29** were less potent than **9** as MGL inhibitors, the relevance of electronic properties on this activity is not clear. On the other hand, this study clearly indicated that a substitution hindering the free access to the ring sulfur, as in the 7-methyl derivative **27**, strongly reduces the ability of the BTZ to react with the thiol group of free GSH. In parallel, compound **27** was much less potent than other compounds as a MGL inhibitor.

Table 3.8 Reactivity of substituted BTZs with glutathione in PBS at pH 7.4. Concentrations of reaction species under equilibrium conditions (t = 60 min)



Cpd	R	X	[GSH] (μM) ^a	[GSSG] (μM) ^a	[BTZ] (μM) ^a	Estimated [BTZ-GSH] (μM) ^a
9	H	CH ₂	73.4 ± 4.7	59.3 ± 1.1	< LOD	8.0
23	5-NO ₂	CH ₂	32.1 ± 9.5	78.3 ± 4.8	< LOD	11.3
24	6-NO ₂	CH ₂	105.1 ± 7.5	46.9 ± 1.3	< LOD	1.1
25	5-OMe	CH ₂	80.9 ± 3.8	40.7 ± 2.5	1.2 ± 0.5	37.7
26	6-OMe	CH ₂	66.1 ± 4.2	58.4 ± 3.5	< LOD	17.1
28	5-OH	CH ₂	83.1 ± 2.3	53.4 ± 0.7	< LOD	10.1
29	6-OH	CH ₂	30.7 ± 10.9	69.9 ± 4.1	1.3 ± 0.4	29.5
27	7-Me	CH ₂	186.6 ± 4.5	7.6 ± 0.2	99.3 ± 5.4	0.0
33	H	NH	23.8 ± 1.0	64.2 ± 7.8	2.5 ± 0.3	47.8

^a Reported are Means ± SD (n = 3); ^b LOD = limit of detection

In principle, a good cysteine-addressed inhibitor should be able to react with target cysteines forming a stable disulfide adduct. From this point of view, benzisothiazolinone is a highly reactive warhead, and a significant reduction of its reactivity leads to a loss of potency. On the other hand, its ability to maintain (or regenerate at equilibrium) a significant concentration of intact warhead in the presence of high concentrations of competing thiols (e.g. reduced GSH within a cell) could be useful for in vitro and in vivo activity. Interestingly, the 2-amino derivative **33** showed

both the ability to react with GSH, forming a rather stable mixed disulfide, and the highest concentration of intact BTZ after 1 hour.

While these experiments gave indications on the behavior of BTZs at longer times, to get information about the kinetics of this warhead with thiols we setup a new series of experiments based on $^1\text{H-NMR}$ spectroscopy.

As the reactive counterpart of BTZs we chose *N*-acetyl cysteine (NAC) in order to have a structural accessible thiol easy to be monitored by NMR spectroscopy. Equimolar concentration of BTZ and NAC were dissolved separately in a deuterated solvent with a final concentration of 80 mM and they were rapidly mixed in a NMR tube at 25° C. The first monodimensional proton spectra was recorded after 4 minutes (technical time necessary to set up the experiment) and then spectra were collected every 2 minutes until reaction was complete. We monitored the variation of signals intensity corresponding to BTZ and NAC and the appearance of new resonance peaks belonging to new species generated after the reaction between the substrates. The choice of the proper deuterated solvent was fundamental for the success of the experiments. First attempts were conducted in PBS-deuterated water (PBS- D_2O) in order to mimic physiological conditions and to obtain results that could be compared to reactivity studies with GSH. The lack of sensitivity of NMR methodology forced us to use high concentration of the reactive partners, which generated solubility problems. Moreover, the reaction in PBS- D_2O was complete at first checkpoint ($t = 4$ min) with formation of different species that generated complex spectra, confirming results obtained during the reactivity studies with GSH. The use of deuterated methanol (MeOD) solved solubility problems and decreased the rate of reaction allowing monitoring the time-course of the first step of the reaction.

Nucleophilic attack of thiol group of NAC on sulfenamidic sulfur of BTZ leads to the formation of an adduct BTZ-NAC, that in these conditions is stable and not susceptible to side reaction or disproportion events, generating readable spectra in which is possible to easily identify BTZ, NAC and the adduct signals. In particular, in the $^1\text{H-NMR}$ spectra of the reaction mixture, we monitored the singlet corresponding to the acetyl group of NAC (2.0 ppm) and the one belonging to BTZ-NAC adduct that is shifted at higher magnetic fields (~ 1.9 ppm). Other significant signals are the methylenic hydrogens of NAC in α position to the sulfhydryl group, which generate a

double quartet at 2.9 ppm. In the BTZ-NAC adduct the two methylenic protons become diastereotopic generating an AB system with two distinct doublet of doublets at ~ 3.0 and ~ 3.2 ppm.

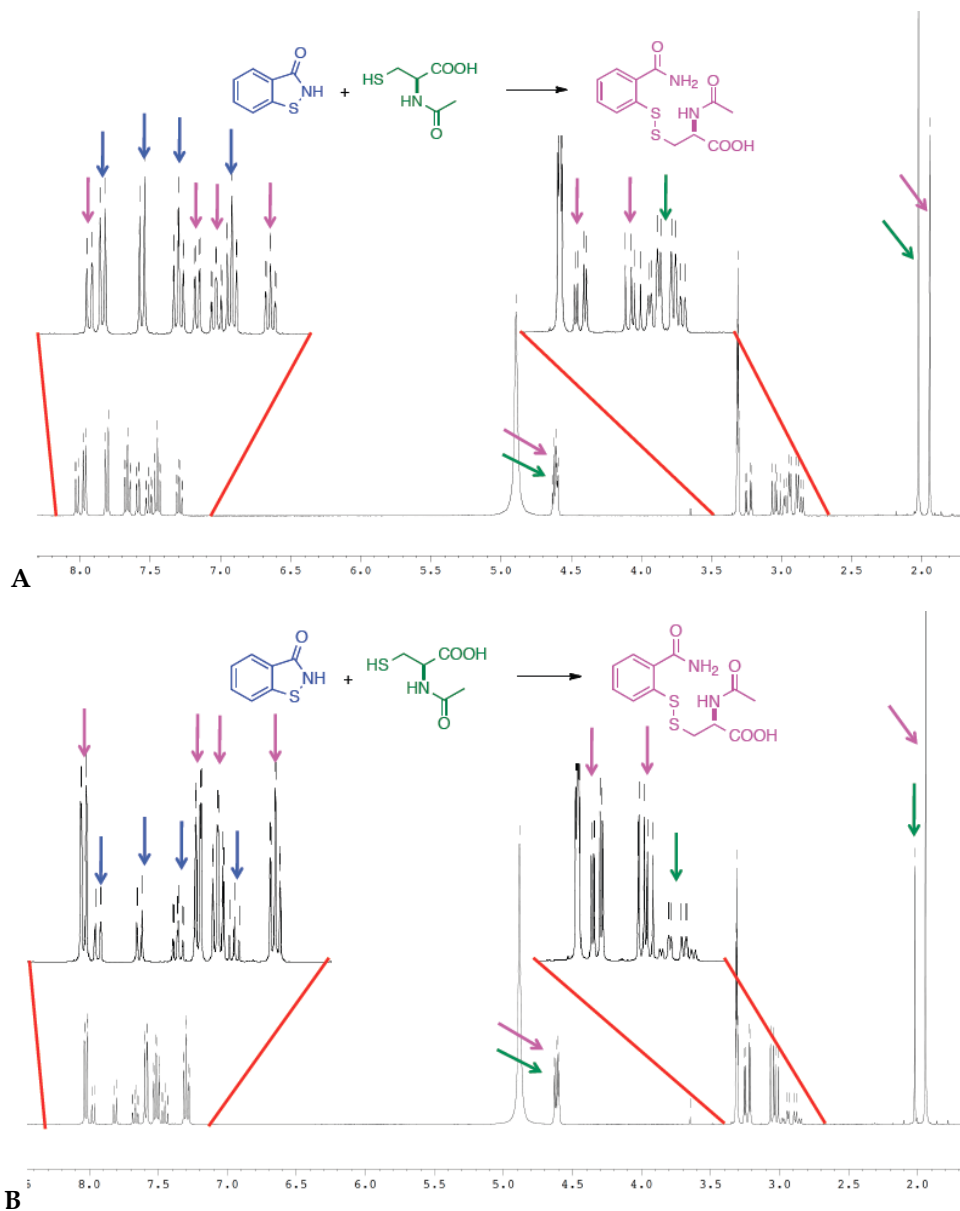


Figure 3.8 $^1\text{H-NMR}$ of reaction between compound 2 and NAC.

Spectra registered at 4 min (A) and 40 min (B).

In **Figure 3.8** are reported, as an example, NMR spectra of compound **2** reacting with NAC. The two spectra registered at 4 min (**A**) and 40 min (**B**) reveal clearly the time course of reaction with decrease of BTZ and NAC peaks (blue and green respectively) and the concomitant proportional appearance of BTZ-NAC signals (magenta).

Quantification of reaction species in solution was afforded through integration of significant peaks, proportional to the relative concentrations. Kinetic traces of reaction between BTZ and NAC were obtained plotting concentrations, expressed as molar fraction (X_i), over time. In **Figure 3.9A** is reported as example the time course of reaction between compound **2** and NAC showing the progressive disappearance of NAC (red trace) and the proportional appearance of the BTZ-NAC adduct (light blue trace).

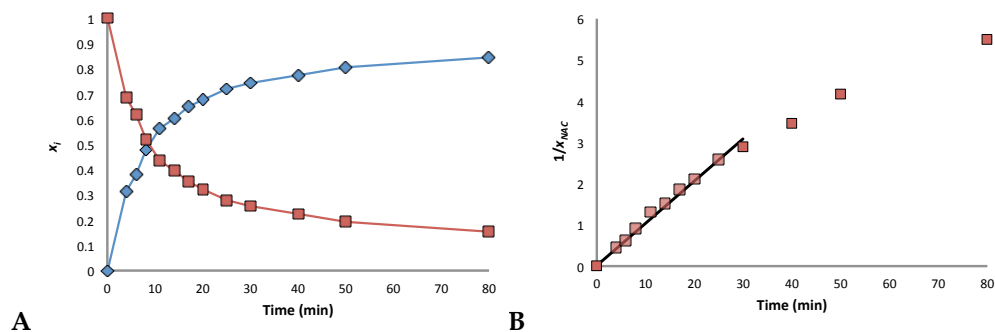
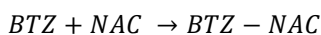


Figure 3.9 Kinetic traces for the reaction of compound **2** with NAC. Concentrations were determined by $^1\text{H-NMR}$. (**A**) The disappearance of NAC (red trace) and the appearance of BTZ-NAC adduct (light blue trace) *vs.* time. (**B**) Plot of $1/X_{\text{NAC}}$ *vs.* time shows a linear trend up to 70% of conversion (second-order reaction)

The determination of the reaction order was fundamental to calculate parameter such as the rate constant (κ) and the half-life ($t_{1/2}$) of species involved and, therefore, to obtain crucial information about the rate of the transformation. Interaction between BTZ and NAC (eq. 1) gives a second-order reaction with a rate law described by eq. 2. The integrated rate law (eq. 3) shows that the plot of reciprocal of NAC concentration *vs.* time should be a straight line. In **Figure 3.9B** we report the plot on $1/X_{\text{NAC}}$ *vs.* time for compound **2**.

eq. 1:



eq. 2:

$$v = - \frac{d [NAC]}{[NAC]} = \kappa [NAC]^2$$

eq. 3:

$$\frac{1}{[NAC]_t} - \frac{1}{[NAC]_0} = \kappa t$$

Reaction of **2** with NAC follows a second order rate law (linear plot) between 0 and 30 min corresponding to 70% of NAC reacted, while it deviates from a linear trend in last part of the interaction. This behavior could be ascribed to diffusion problems that reduced the rate of reaction when the concentration of the reactants decreased. Therefore, we proceeded to calculate the rate constant of reaction (κ) for the liner part of the plot, represented by the slope of the straight line and, through eq. 4, the $t_{1/2}$ of NAC resulting in 9.95 min (**Table 3.9**).

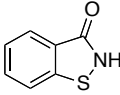
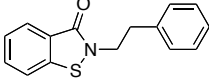
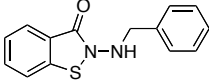
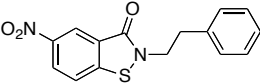
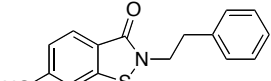
eq. 4:

$$t_{1/2} = \frac{1}{\kappa [NAC]_0}$$

We next tested compounds **9**, **33**, **23**, **29** in the same experimental conditions. The results are outlined in **Table 3.9**. Compounds **9** and **29** showed the same behavior of compound **2**: up to 70% of conversion, data were fitted by a linear trend according to a second-order reaction. For these compounds, it was possible to calculate NAC half-time, that was of 3.56 minutes for **9** and 10.78 minutes for **29**. Reaction of compounds **33** and **23** was complete at first checkpoint ($t = 4$ min) and was impossible to determine NAC half-time, that was, therefore, lower than 2 minutes. The results obtained by this kinetic investigation can be correlated to the *in vitro* potency of BTZ. Compounds showing the highest NAC half-live values (**2** and **29**) are the less potent on MGL, conversely compounds **9** and **33** that show a fast rate of reaction with NAC are very potent on the enzyme confirming the hypothesis that inhibition exerted by BTZ on MGL is strictly dependent from their inner warhead reactivity toward thiol nucleophiles. Comparing the last data with those obtained with GSH in water, it can be speculated that more different requirements must be fulfilled to have a potent MGL inhibitor addressing exposed cysteines. Thus, while compound **29** had shown

favorable features in the first test (formation of stable disulfide adduct, presence of a small quote of intact BTZ), its lower reaction rate is probably the reason of low inhibitory potency. On the other hand, the nitro-derivative **23** has a good reaction rate, but its lack of ability to form stable adducts can explain its lower potency, compared to compound **33**.

Table 3.9 Calculation of NAC half-time by $^1\text{H-NMR}$

Compound	Structure	NAC $t_{1/2}$ (min) ^a
2		9.95 ± 0.28
9		3.56 ± 0.49
33		$<2^b$
23		$<2^b$
29		10.78 ± 0.57

^a Reported are Means \pm SD (n = 3); ^b Reaction complete at first checkpoint (t = 4 min)

3.2 Triterpenes as MGL inhibitors: results and discussion

As anticipated in Chapter 2, from the screening of a chemical library, King and coworkers¹⁴ reported pristimerin **42** (**Figure 3.10**) as a potent inhibitor of purified MGL with a median effective concentration (IC_{50}) of 93 nM. Enzyme assays showed that also euphol, a bioisoster of pristimerin, inhibits purified MGL with an IC_{50} of 315 nM.

SAR studies were conducted by King and colleagues on friedelane-based pentacyclic triterpenoids including celastrol **41**, dihydrocelastrol **43** and pristimerol **44** (**Figure 3.10**). The inhibitory potencies of these compounds appeared to be particularly sensitive to chemical modifications at the two opposite ends of their rigid terpenoid scaffold: the esterification of the carboxyl group at carbon 29, which increased

inhibitory activity, and the reduction of the quinone methide ring, which decreased such activity. During my PhD research I investigated SAR for this class of terpenoids. The crystal structure of human MGL 3HJU was selected as model structure and it was used for docking studies. Binding modes obtained for pristimerin showed the triterpene can be placed at the entrance of the substrate cavity, thus affecting lid domain flexibility and the access of the substrate to the catalytic pocket (**Figure 3.11A**).

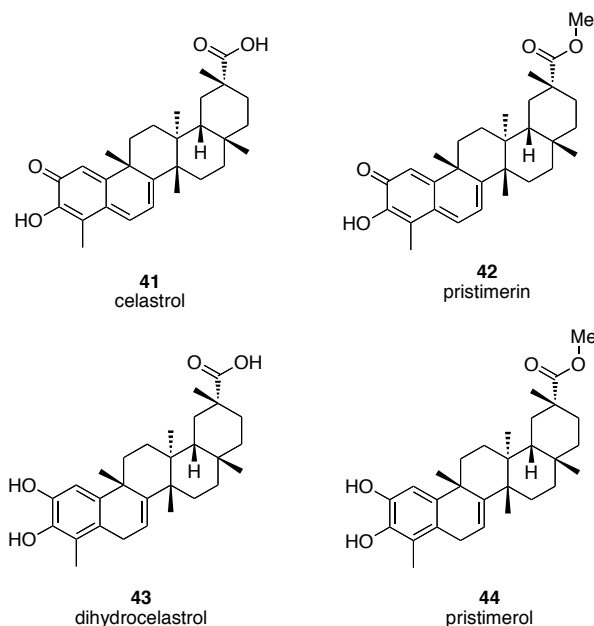


Figure 3.10 Structures of friedelane-based pentacyclic triterpenoids

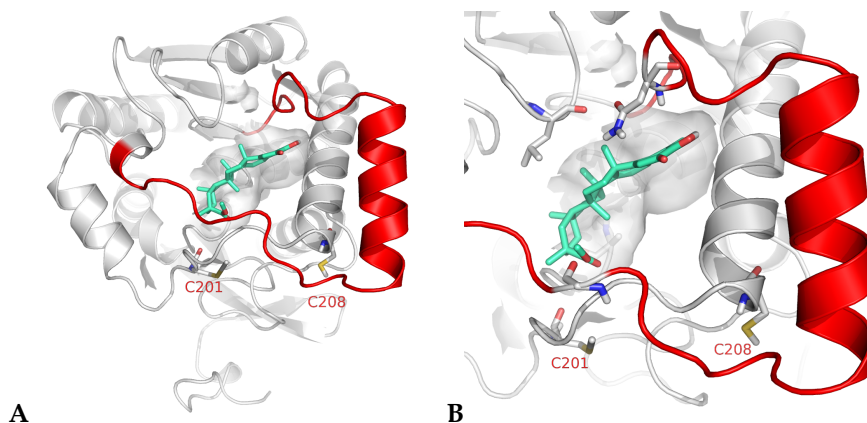
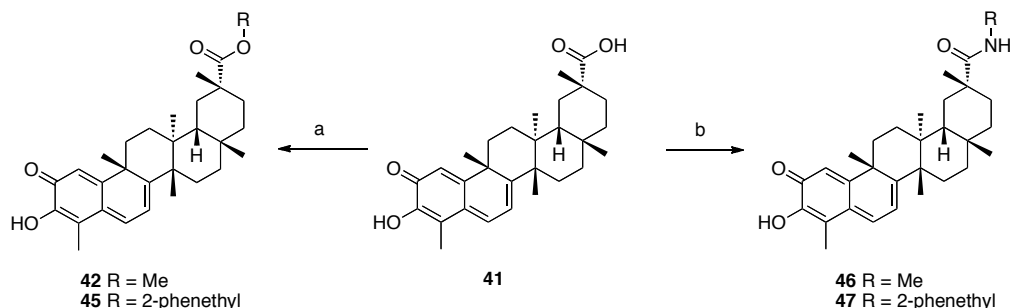


Figure 3.11 **A** Binding modes for pristimerin **42** show the blockade of the lid domain (red) and the occupancy of the substrate cavity. **B** Detail of the interaction with a backbone carbonyl

In the docked pose, the ester group of pristimerin pointed toward a backbone carbonyl of MGL (**Figure 3.11B**). This model can explain the loss of potency of celastrol **41** observed by King *et al.* ($IC_{50} = 1.6 \mu\text{M}$), ascribing it to electrostatic repulsion between the carboxylate anion of celastrol and the backbone carbonyl. In the same docking pose, the methyl group linked to the pristimerin ester lined a loop of the lid domain, taking hydrophobic interactions. This loop is just above the region of the lid domain that includes Cys201 and Cys208. We tested this hypothesis by increasing the lipophilicity of the ester group to assess possible hydrophobic interactions with the lid domain. Furthermore, the ester moiety was replaced with an amide group to test the possibility of an hydrogen bond interaction with a backbone carbonyl.

3.2.1 Chemistry

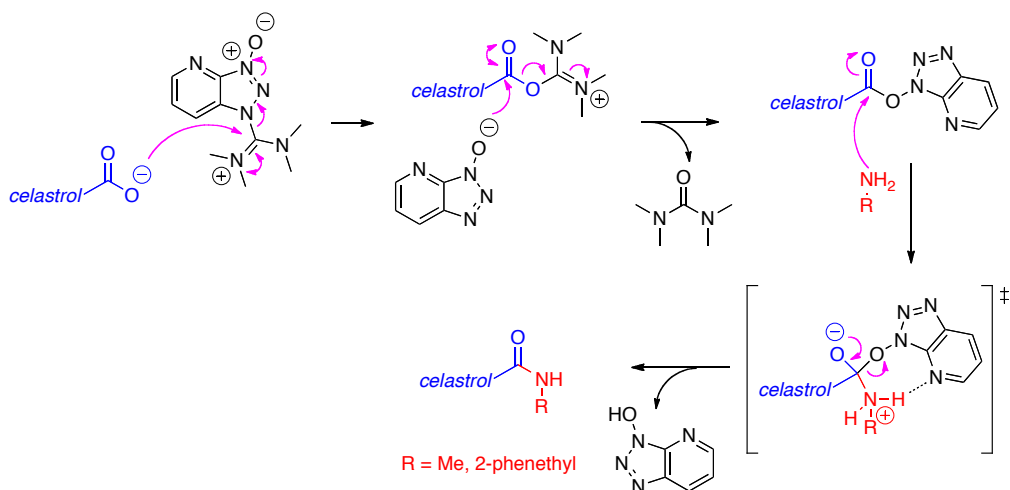
Synthesis of triterpenoids derivatives was accomplished starting from the commercially available carboxylic acid **41** (celastrol) as outlined in **Scheme 3.9**. Ester derivatives **42** and **45** were synthesized by treatment of celastrol **41** with a mild base such as NaHCO_3 in order to ensure deprotonation of the acidic group without interfering with the quinone-methide hydroxyl group. Subsequent substitution reaction of the preformed celastrol carboxylate on methyl iodide or 2-bromoethyl benzene afforded the desired products **42** and **45** in high yields.



Scheme 3.9 Synthesis of celastrol derivatives. *Reagents and conditions:* a) NaHCO_3 , MeI or 2-bromoethyl benzene, dry DMF, r.t., 20h; b) HATU, DIPEA, methylamine or 2-phenylethanamine, dry DMF 0°C to r.t., 20h.

The synthesis of the amide derivatives of celastrol **46** and **47** was successfully achieved through the use of the coupling agent 1-[Bis(dimethylamino)methylene]-1H-1,2,3-triazolo[4,5-b]pyridinium 3-oxid hexafluorophosphate (HATU).

In the first step (**Scheme 3.10**) the carboxylate anion, formed by deprotonation exerted by the Hunig's base DIPEA, attacks HATU to form the unstable *O*-acyl(tetramethyl)isouronium salt. The generated anion rapidly attacks the isouronium salt, affording the activated ester and giving a stoichiometric quantity of tetramethylurea. Addition of the nucleophilic amine, methylamine or 2-phenylethanamine, to the activated ester resulted in the acylation of the carboxylic moiety leading to formation of final compounds **46** and **47**.



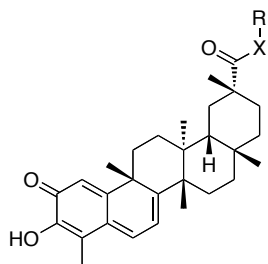
Scheme 3.10 Mechanism of action of coupling agent HATU

3.2.2 Biological evaluation of celastrol derivatives on MGL

Synthesized triterpenes were incubated with non-purified rat MGL (cell lysates of MGL-transfected HeLa cells) to evaluate their inhibitory potency and the results are outlined in **Table 3.10**. Re-synthesized pristimerin **42** was re-tested on MGL and revealed a IC_{50} of 568 nM. The difference with previous data that reported a IC_{50} of 93 nM can be ascribed to a dissimilarity in the protocol used during the *in vitro* test (purified *vs.* non-purified MGL). The replacement of the methyl group of the ester functionality (compound **42**) with a more bulky and lipophilic substituent such as the

2-phenethyl group (compound **45**) didn't result in enhancement of potency as expected from computational studies. However, only a small increase of IC_{50} (796 nM, 1.5x) was observed, which suggests that hindered lipophilic groups are tolerated. In spite of the lack of additional hydrophobic interactions, this is not in open contrast with the proposed docking pose, where solvent, instead of lining the hydrophobic lid domain, could also surround the phenethyl group.

Table 3.10 Inhibition of non-purified rat MGL by triterpenes derivatives



Compound	X	R	IC_{50} (nM)
42	O	Me	568
45	O		796
46	NH	Me	1478
47	NH		1437

On the other hand, the amide-based compounds **46** and **47** showed a marked decrease of inhibitory potency on MGL, which is inconsistent with the possibility to take an attractive polar interaction with the backbone carbonyl pointed out by the docking study. These controversial results could be due to the fact that lid-domain flexibility has a negative impact on the predictivity of static docking models. However, the present results, although based on limited exploration of the chemical space, discourage the aim of improving the MGL-inhibitor potency of pristimerin derivatives through simple modifications at the ester functionality.

3.3 Conclusions

The role of MGL as key enzyme of the ECS has been thoroughly discussed in this PhD dissertation. The discovery of partially-reversible modulators (ITZs and BTZs) of this enzyme has been an extraordinary step forward in the field of MGL inhibitors. This class regulates the activity of the enzyme through an allosteric modulation of the cysteines 201 and 208, preserving the integrity of the catalytic site. This approach has some potential advantages, or at least differences, with respect to known active-site directed (ASD) covalent inhibitors: (i) although non-competitive, MGL inhibition by cysteine-trapping agents is reversible, avoiding both competition with high concentrations of substrate (which would reduce activity) and prolonged inhibition of MGL function; (ii) the analogy between their effect on wild type and Cys-mutated MGL and that of hydrogen peroxide suggests that, while MGL inhibition could be a way for the cell to stimulate antioxidant defenses in the presence of increasing levels of ROS, BTZs could mimic the same stimulation while avoiding the damages due to oxidation; (iii) MGL inhibition by these compounds is redox-sensitive: this could lead to selective activation of the endocannabinoid system, possibly avoiding the cannabinoid-like effects observed for active site inhibitors. While these potential advantages still need to be confirmed by *in vivo* studies, structural optimization of BTZ inhibitors, comprehension of the role of their interaction with thiols and SAR exploration was a prerequisite for these studies.

During my PhD research a deep SAR study for BTZs as MGL inhibitors has been performed. As a result of the SAR investigation, we identified promising lead compounds **9** and **33** with IC_{50} of 34 and 19 nM and bidentate ligands **38** and **39** with IC_{50} of 11 and 16 nM on the purified enzyme, respectively, improving the potency of reference compound **1**.

SAR gathered for BTZ derivatives point out how the recognition portion, able to establish non-covalent interaction with the target enzyme, plays a marginal role in the inhibition process exerted by BTZs suggesting that their relatively high inhibitory potency on MGL is likely due to the reactivity of the sulfenamidic fragment toward thiol-based nucleophiles.

Kinetic experiments and reactivity studies performed in presence of biological thiols supports this finding. Indeed, kinetic experiment with NAC outlined a significant

correlation between the *in vitro* potency of BTZ and their experimental reactivity, i.e. the compounds revealing the highest reaction rates are the ones most potent on MGL. Moreover, reactivity studies with GSH revealed the complex behavior of the BTZ class if exposed to biological thiols in physiological conditions. BTZs instantly react with GSH establishing a pseudo-equilibrium condition among different oxidized species. The modulation of the BTZ core reactivity by introduction of electronically diversified substituents, didn't afford valuable results. Only with the introduction of a bulky group close to reactive sulfur atom, a decrease of reactivity can be achieved resulting, unfortunately, in an undesired loss of potency. Although BTZs can be depleted by intracellular GSH, the discovery of compounds able to be restored during the ox-redox process is a promising outcome.

The recent findings about the sensitivity of MGL to oxidation stimuli are an important breakthrough in the knowledge of the biological relevance of this enzyme. These studies, developed from collaboration between the research group where I spent my PhD period and the research group of Professor Piomelli (University of Irvine, California) revealed the inhibitory effect of hydrogen peroxide exerted through oxidative sulfenylation of critical cysteines 201 and 208.

The major achievement of our research work was to characterize the mechanism of action and SAR of a class of MGL inhibitors, BTZs, able to mimic the physiological inactivation exerted by H₂O₂. We speculate that BTZs mimic the oxidative action of hydrogen peroxide acting on key cysteine residues 201 and 208 of MGL, uncoupling the damage suffered from all cellular compartments after oxidative stress from the physiological "protective" inactivation of MGL. This hypothesis is corroborated by the *in vitro* and *in vivo* studies performed on compound **9** showing that blockade of MGL activity reduces cellular damage exerted by hydrogen peroxide and increase 2-AG content in rats brain. Compound **9** revealed to be a valuable tool for elucidating the neuroprotective role of 2-AG in response to oxidative stress events. These findings appoint BTZs as promising inhibitors with a potential application as neuroprotective agents.

However, the molecular mechanism at the basis of the inhibition exerted by H₂O₂ and BTZs still need to be elucidated. Our hypothesis is centered around the flexibility of the lid domain, that can generate an "open" or a "closed" conformation of MGL, as supported by crystallographic data, allowing or blocking the access of the substrate to

the catalytic site. Hydrogen peroxide and BTZs, acting on the peroxidatic cysteines located on the lid domain, could induce and/or stabilize the structural “closed” conformation associated with a low catalytic activity of MGL. Metadynamics and molecular modeling studies have been performed to explore the conformational space of MGL with particular focus on the lid domain flexibility. Preliminary evidences, which need to be further validated, showed that metadynamics of MGL modeled from the crystal structure assume a stable “open” conformation corresponding to a free energy minimum (**Figure 3.12A**). When models simulating oxidation of Cys201 by sulfenylation (mimicking the hydrogen peroxide action) or by formation of a disulfide bond (mimicking the inhibition of BTZs) were explored, a switch from the “open” to the “closed” conformation, thus blocking the recruitment of the substrate, was observed (**Figure 3.12B,C**).

The understanding of the molecular mechanism of inhibitions exerted by BTZs is a fundamental tool to proceed the investigation of these promising inhibitors.

The SAR investigation performed on celastrol-based triterpenes reveal the troublesome development of this class of compounds as exploitable MGL inhibitors. The rigid scaffold of the molecule allows few structural modification: the exploration of the quinone methide ring and the carboxyl group at carbon 29 have been reported in the present and in previous studies leading always to less active compounds compared to the reference inhibitor pristimerin. While this is not sufficient to rule out the possibility that MGL-inhibitor potency of triterpenes could be improved by chemical modification, at the moment we conclude that, among the classes of compounds interacting with the regulatory function of cysteines within the lid domain, BTZ derivatives appear more promising for further chemical development.

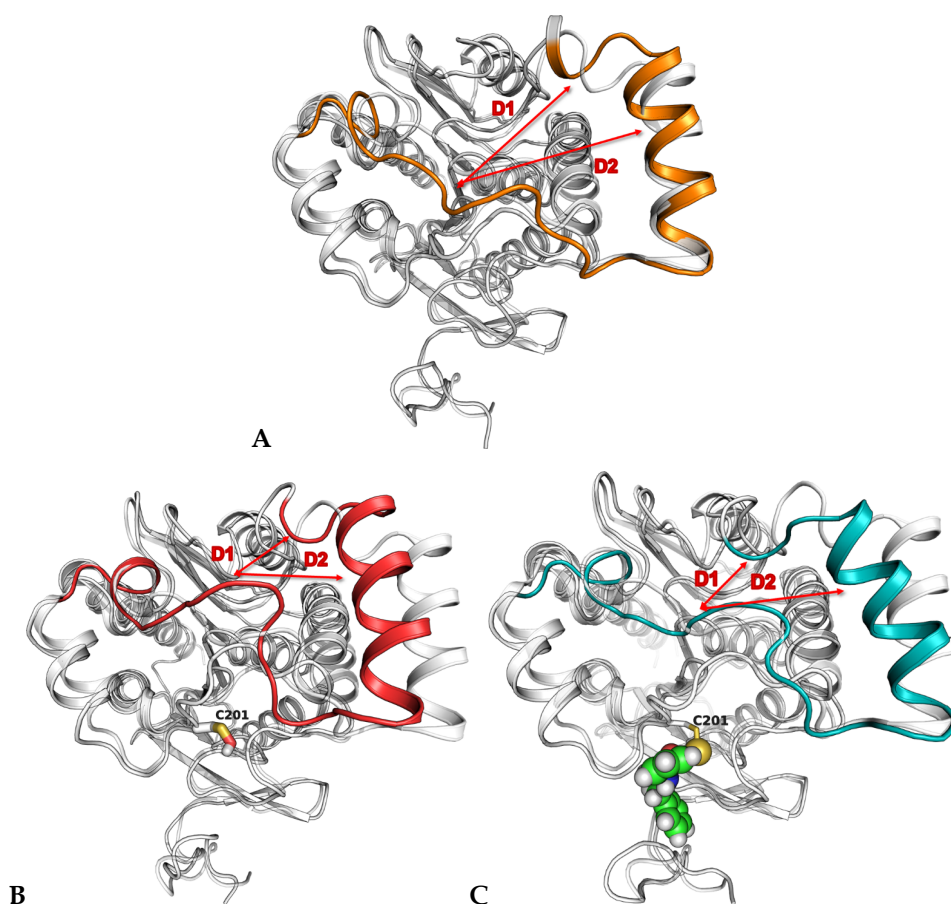


Figure 3.12 Well-tempered Metadynamics on MGL. The distances between CA of selected residues (D1 and D2, red arrows) on the lid domain rims have been used as collective variables describing the lid domain motions. (A) Metadynamics simulation of MGL modeled from the crystal structure (grey cartoon) shows an energy minimum corresponding to an “open” conformation of the lid domain (orange cartoon). (B, C) Metadynamics simulations of MGL modeled with C201 oxidized to sulfenic acid (red cartoon) and MGL modeled with compound **9** covalently bound to C201 (green cartoon) show free energy minima corresponding to “closed” conformations of the lid domain.

References

- ¹ Sanchez, J.P. A ring opening reaction of benzisothiazolones. A new route to unsymmetrical disulfide *J. Heteroc.Chem.* **1997**, *34*, 1463.
- ² Phillips, L. R; Malspeis L.; Tubbs, E. K.; Supko, J. G. Characterization of a novel degradation product of 2,2,7-dithiobis[N-isoleucylbenzamide], an inhibitor of HIV nucleocapsid protein zinc finger *J. Pharm. Biomed. Anal.* **2000**, *23*, 395–402.
- ³ (a) Bordi, F.; Catellani, P.L.; Morini, G.; Plazzi, P.V.; Silva, C.; Barocelli, E; Chiavarini, M. 4-(3-Oxo-1,2-benzisothiazolin-2-yl)alkanoic, phenyl and phenoxyalkanoic acids: synthesis and anti-inflammatory, analgesic, and antipyretic properties. *Farmaco* **1989**, *44*(9), 795-807. (b) Zlotin, S.G.; Kislitsin, P.G.; Podgursky, A.I.; Samet, A.V.; Semenov, V.V.; Buchanan, III A.C.; Gakh, A.A. Synthetic utilization of polynitroaromatic compounds. 2. Synthesis Of 4,6-dinitro-1,2-benzisothiazol-3-ones and 4,6-dinitro-1,2-benzisothiazoles from 2-benzylthio-4,6-dinitrobenzamides. *J. Org. Chem.* **2000**, *65*(25), 8439-43.
- ⁴ Russel, A.D.; Hugo, W.B.; Ayliffe, G.A.J. Disinfection, preservation and sterilization, *Blackwell Scientific Publications, 2nd edition, Oxford* **1992**, 65.
- ⁵ (a) Zani F. Antimicrobial and genotoxic activities of N-substituted 2,2'-dicarboxamidodiphenyldisulfides. *Farmaco* **1992**, *47*(2), 219-28. (b) Massimo, G.; Zani, F.; Coghi, E.; Bellotti, A.; Mazza, P. Biological studies on 1,2-benzisothiazole derivatives. III. Evaluation of antibacterial, antifungal and DNA-damaging activities of 1,2-benzisothiazolin-3-ones. (c) Dou, D.; Alex, D.; Du, B.; Tiew, K.C.; Aravapalli, S.; Mandadapu, S.R.; Calderone, R.; Groutas, W.C. Antifungal activity of a series of 1,2-benzisothiazol-3(2H)-one derivatives. *Bioorg. Med. Chem.* **2011**, *19*(19), 5782-7. *Farmaco* **1990**, *45*(4), 439-46. (c) Mor, M.; Zani, F.; Mazza, P.; Silva, C.; Bordi, F.; Morini, G.; Plazzi, P.V. Biological studies on 1,2-benzisothiazole derivatives V. Antimicrobial properties of N-alkanoic, N-aryllalkanoic and N-aryloxyalkanoic derivatives of 1,2-benzisothiazolin-3-one: QSAR study and genotoxicity evaluation. *Farmaco* **1996**, *51*(7), 493-501.
- ⁶ Jorgensen, W.L.; Trofimov, A.; Du, X.; Hare, A.A.; Leng, L.; Bucala, R. Benzisothiazolones as modulators of macrophage migration inhibitory factor. *Bioorg. Med. Chem. Lett.* **2011**, *21*(15), 4545-9.
- ⁷ Liu, D.; Tian, Z.; Yan, Z.; Wu, L.; Ma, Y.; Wang, Q.; Liu, W.; Zhou, H.; Yang, C. Design, synthesis and evaluation of 1,2-benzisothiazol-3-one derivatives as potent caspase-3 inhibitors. *Bioorg. Med. Chem.* **2013**, *21*(11), 2960-7.
- ⁸ Furdas, S.D.; Shekfeh, S.; Bissinger, E.M.; Wagner, J.M.; Schlimme, S.; Valkov, V.; Hendzel, M.; Jung, M.; Sippl, W. Synthesis and biological testing of novel pyridoisothiazolones as histone acetyltransferase inhibitors. *Bioorg. Med. Chem.* **2011**, *19*(12), 3678-89.
- ⁹ Baggaley, K.H.; English, P.D.; Jennings, L.J.; Morgan, B.; Nunn, B.; Tyrrell, A.W. Inhibitors of Blood Platelet Aggregation. Effects of Some 1,2-benzisothiazol-3-ones on Platelet Responsiveness to Adenosine Diphosphate and Collagen *J. Med. Chem.* **1985**, *28*, 1661–1667.
- ¹⁰ Dahl, R.; Bravo, Y.; Sharma, V.; Ichikawa, M.; Dhanya, R.P.; Hedrick, M.; Brown, B.; Rascon, J.; Vicchiarelli, M.; Mangravita-Novo, A.; Yang, L.; Stonich, D.; Su, Y.; Smith, L.H.; Sergienko, E.; Freeze, H.H.; Costford,

N.D. Potent, Selective, and Orally Available Benzoisothiazolone Phosphomannose Isomerase Inhibitors as Probes for Congenital Disorder of Glycosylation Ia *J. Med. Chem.* **2011**, *54*, 3661–3668.

¹¹ King, A. R.; Lodola, A.; Carmi, C.; Fu, J.; Mor, M.; Piomelli, D. A critical cysteine residue in monoacylglycerol lipase is targeted by a new class of isothiazolinone-based enzyme inhibitors. *Br. J. Pharmacol.* **2009**, *157*, 974-983

¹² Katritzky, A.R. *et al.*; in “Advance in Heterocyclic Chemistry” - supplement 1: “The tautomerism of Heterocycles”, (Eds. Katritzky A.R and Boulton A.J.), Academic Press, **1976**, Sec. 2E, 312-313.

¹³ Matuszak, N.; Muccioli, G. G.; Labar, G.; Lambert, D. M. Synthesis and in vitro evaluation of N-substituted maleimide derivative as selective monoglyceride lipase inhibitors. *J. Med. Chem.* **2009**, *52*, 7410-7420.

¹⁴ King, A. R.; Dotsey, E. Y.; Lodola, A.; Jung, K. M.; Ghomian, A.; Qiu, Y.; Fu, J.; Mor, M.; Piomelli, D. Discovery of potent and reversible monoacylglycerol lipase inhibitors. *Chem. Biol.* **2009**, *16*, 1045-52.

Chapter

4 Synthesis of NSC172285: a stereochemistry issue

4.1 Introduction

Fibroblast growth factor-2 (FGF2) is a member of a large family of structurally related proteins that affect the growth, differentiation, migration and survival of a wide variety of cell types¹. FGF2 and other members of the FGF family bind to heparin and heparan sulfate, linear sulfated polysaccharides known as glycosaminoglycans². The binding of FGF2 to heparan sulfate has been demonstrated to reflect a complex biochemical regulatory mechanism for this growth factor. The interaction of FGF2 with heparin protects FGF2 against heat or acid denaturation and protease cleavage. While heparin is only synthesized by connective tissue mast cells, heparan sulfate is widely distributed throughout all mammalian tissues and organs attached to core proteins as heparan sulfate proteoglycans (HSPG). HSPGs are a functionally diverse class of molecules found on cell surfaces and in the extracellular matrix where they have been demonstrated to interact with FGF2 and modulate its distribution and function³. FGF2 interacts with specific cell surface receptor proteins derived from four separate genes (FGFR1-4)⁴. A number of splice variants exist for each receptor type resulting in differing ligand binding domains. The splice variants confer specificity in signaling in response to the various FGF family members. FGF2 has been proposed to have two separate receptor binding sites, which might allow a single FGF2 to bind to two receptors or to interact with a single receptor in two separate positions⁵. HSPGs can increase the affinity of FGF2 for its receptors⁶ and potentially act as a bridge to

facilitate the dimerization of receptors leading to the formation of productive HSPG/FGF2/FGFR ternary complexes⁷ (**Figure 4.1**).

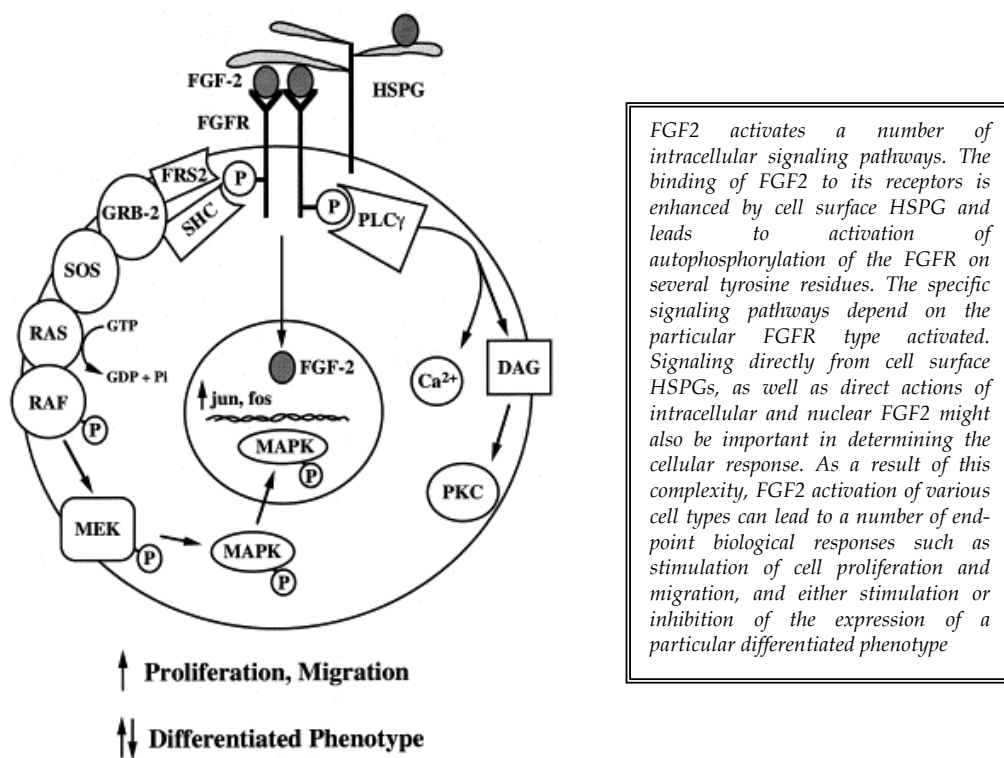


Figure 4.1 Schematic of FGF2 signaling pathways

FGF2 plays key roles in development, remodeling and disease states in almost every organ system¹. One of the best characterized activities of FGF2 is its ability to regulate the growth, chemotaxis and function of vascular cells such as endothelial and smooth muscle cells⁸. *In vivo*, FGF2 shows angiogenic activity in different experimental models⁹ and modulates neovascularization during wound healing, inflammation, atherosclerosis and tumor growth¹⁰, thus representing a possible target for anti-angiogenic therapies¹¹.

Natural and synthetic molecules able to interfere with HSPG/FGF2/FGFR interaction may act as angiogenesis inhibitors. To this respect, structural analysis of FGFR ligands and screening of random phage epitope libraries have led to the design of synthetic peptides able to target FGFRs and compete for ligand binding, thus inhibiting the

biological activity of FGF2¹². Similarly, FGF2-binding peptides have been identified as *in vitro* and/or *in vivo* FGF2 antagonists.

Presta and coworkers at the University of Brescia have recently discovered from a virtual screening campaign of a National Cancer Institute (NCI) library, a promising new inhibitor of the FGF2-FGFR interaction. The steroid-based compound NSC172285 emerged from this screening was found to bind the FGF2 portion involved in the interaction with FGFR thus blocking the formation of the ternary complex HSPG/FGF2/FGFR necessary for the correct signaling pathway. NSC172285 was tested *in vitro* on multiple human myeloma cells and revealed to inhibit cell proliferation with a IC_{50} of 3.6 μ M (**Figure 4.2A**). Moreover, in addition to the antiproliferative activity it showed a promising cytotoxic effect on myeloma cells: at 6 μ M cell death for apoptosis was found to be almost 80% while at 10 μ M cell death was 100% (**Figure 4.2B**). This preliminary *in vitro* studies displayed promising antiproliferative and cytotoxic properties of this FGF2 inhibitor. Therefore further analyses were required to evaluate its therapeutic properties.

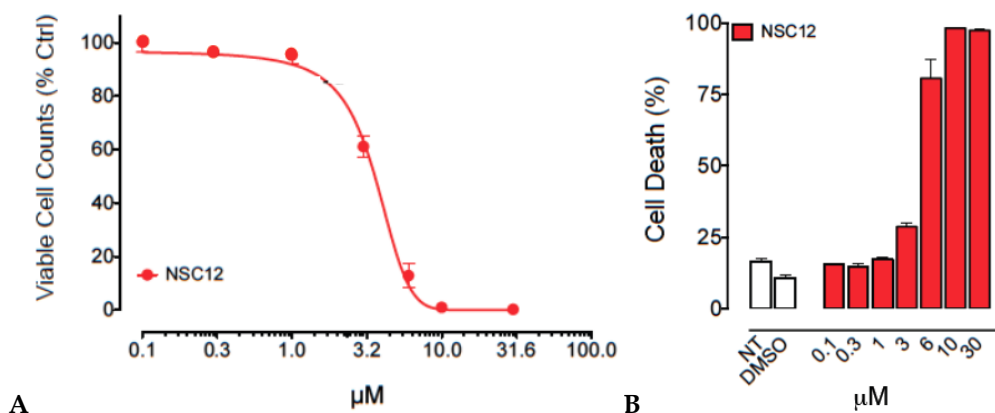


Figure 4.2 NSC172285 effects *in vitro*. (A) *In vitro* anti-proliferative effect on KMS11 human multiple myeloma cells treated with increasing doses of NSC172285 (IC_{50} : \sim 3.6). (B) Induction of cell death (reported as percent of PI⁺ cells) was assessed in KMS11 cells treated with increasing concentrations of NSC172285.

Compound NSC172285 was furnished to the research group of Prof. Presta from the NCI Chemotherapeutic Agents Repository in milligrams amounts, inadequate for a complete and deep investigation of its inhibitory properties. The collaboration between

the research group of Prof. Presta and Prof. Mor, where I spent my PhD period, resulted in a joint effort to pursue the investigation on NSC172285 as FGF2-FGFR inhibitor. The first step to be made was for sure the re-synthesis of the NCI compound with an eye turned to future modification of the scaffold in order to explore structure activity-relationships (SAR). Therefore, during my PhD research I designed and performed the synthesis of NSC172285.

4.2 Retrosynthetic approach and preliminary considerations

The synthesis of compound NSC172285 was not reported in literature. Unexpectedly, the first challenge we faced was the decoding of the unclear structure furnished by the NCI (**Figure 4.3A**) and a printout of an sdf file from the Presta group (**Figure 4.3B**). Two major inconsistencies were immediately individuated:

1. the stereochemistry of the junction between cycles B and C in the sdf file was not consistent with a classical steroidal scaffold;
2. the stereochemistry of C20 was not defined in the NCI formula.

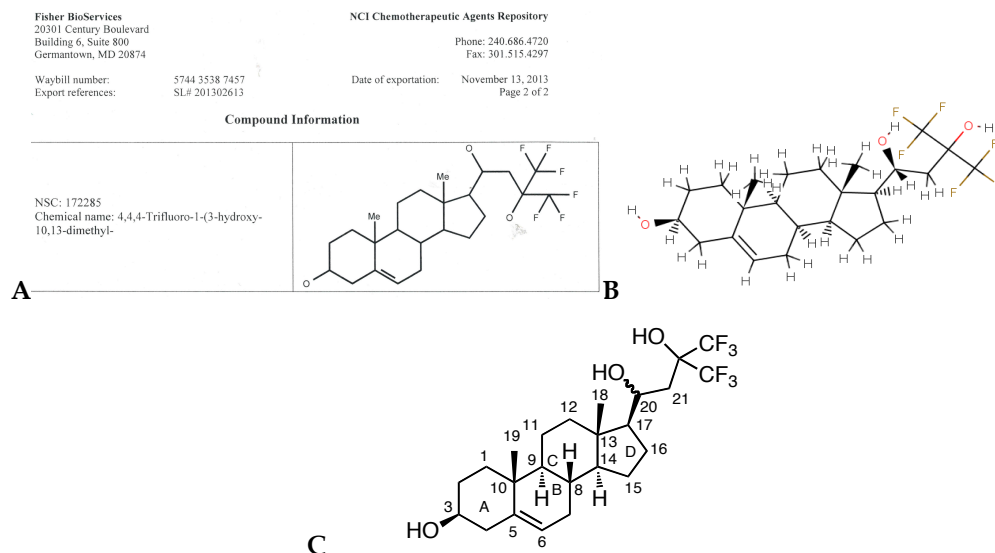
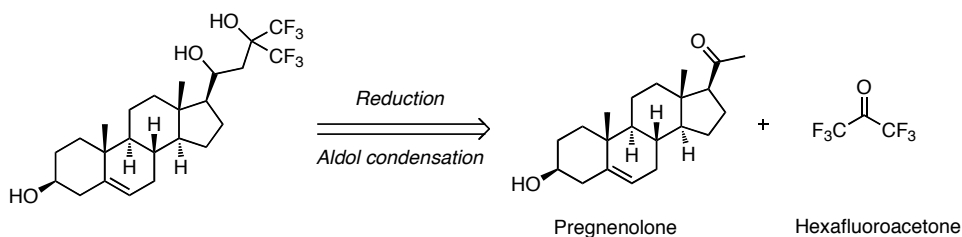


Figure 4.3 (A-B) Structural characterization of compound NSC172285 furnished by NCI. **(C)** Correct structure of the target molecule with proper atom numbering and ring lettering.

In the structure of NSC172285 is clearly recognizable a steroidal scaffold. We speculate that in the chemical formula present in the printout of the sdf file, presumably automatically generated by a software, the *cis*-junction between cycles B and C was the outcome of a genuine mistake.

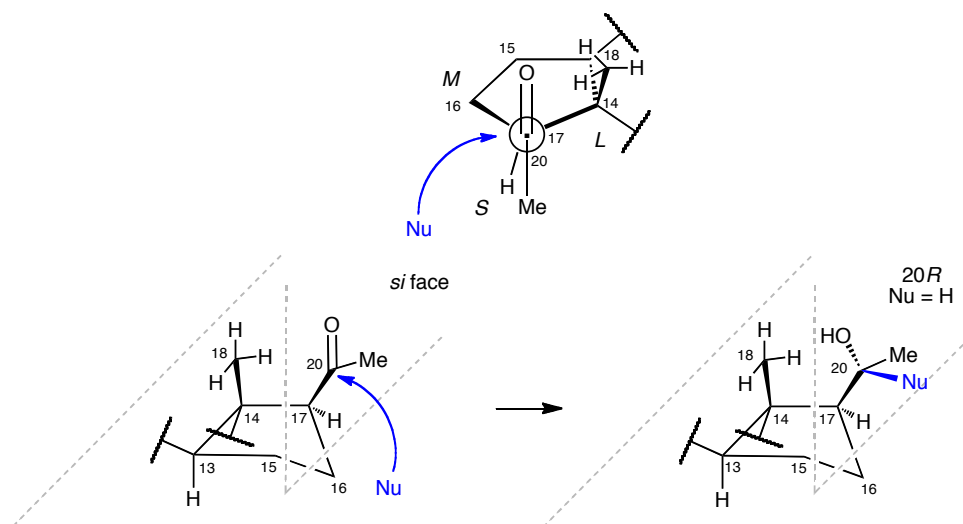
Our hypothesis was supported by the lack of reports in the literature about steroidal skeletons with *cis*-junctions between the B and C rings. In the target molecule a 3,3-di(trifluoromethyl)propane-1,3-diol motif is also identifiable. 1,3-diols can be prepared by, *inter alia*, the reaction between an alkene and formaldehyde (the Prins reaction). A common strategy to obtain substituted 1,3-diols is the aldol reaction between ketones and either aldehydes (to obtain β -keto secondary alcohols) or another ketone (to obtain β -keto tertiary alcohols). Subsequent reduction of the carbonyl moiety leads to the formation of the 1,3-diol. The retrosynthetic rationalization (**Scheme 4.1**) applied to our target molecule involved the reduction of the aforementioned β -keto tertiary alcohol, in turn obtained from the aldol reaction between the steroid-based methyl ketone and hexafluoroacetone (HFA). We anticipated condensing in an aldol fashion a pregnenolone derivative (3 β -hydroxypregn-5-en-20-one), a steroid hormone.



Scheme 4.1 Retrosynthetic approach for NSC172285.

The reduction step is crucial because of the formation of a new stereogenic center at C20. The trigonal planar sp^2 -hybridized carbonyl is converted to a sp^3 -hybridized chiral center upon addition to the *re* or *si* face of the keto group. The influence of neighboring chiral centers, as well as the nature of the reducing agent employed in the reaction could in principle affect the stereochemistry of the newly generated stereocenter. It is worth remembering the lack of a clear stereochemistry attribution for C20 of NSC172285. As a first hypothesis, we assumed that the compound in the NCI library could have been generated under conditions favoring the product in line with several literature precedents.

Midland and Kwon¹³ deeply investigated the reduction of pregnenolone. Typical nucleophilic reducing agents such as NaBH₄ and LiAlH₄ provided the 20*R* product, and hindered trialkylborohydrides provided nearly 99% epimeric purity. Borane-based reducing agents such as borane-dimethyl sulfide (BMS) or 9-BBN were reported to give the 20*R* alcohol as well. The stereochemistry of nucleophilic addition to ketones has been postulated by Ahn to occur from a conformation that places the entering group in an antiperiplanar arrangement with the largest group at the adjacent chiral center. The trajectory of nucleophilic addition to pregnenolone C20 carbonyl then brings the nucleophile over the smallest group as depicted in **Scheme 4.2**.



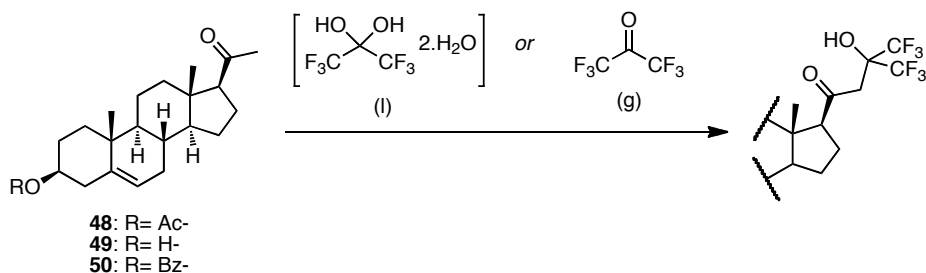
Scheme 4.2 Mechanistic rationalization for the attack of a generic nucleophile Nu (blue) on the C20 of pregnenolone. Felkin-Ahn model (on top) reveal the preference for a nucleophilic attack on the *si* face

Felkin-Ahn model shows the disposition of smallest *S* (H), medium *M* and large *L* groups (5-membered D ring of the steroid) and the favored attack on the *si* face of the ketone leading to the formation of the Cram product. A decisive contribution to the nucleophile trajectory is exerted by the steric hindrance of the methyl group which hampers the attack on the *re* face. If the entering group is a low priority substituent (as in the case of a reduction reaction where Nu = H) the attack on the *si* face leads therefore to the formation of the *R* diastereoisomer.

4.3 Results and discussion

4.3.1 Chemistry

According to our retrosynthetic analysis (**Scheme 4.1**) the first step required the aldol reaction between pregnenolone and HFA. HFA comes in the form of a colorless, hygroscopic, non-flammable, highly reactive gas characterized by a musty odor. It is known to react with metal enolates derived from a variety of carbonyl compounds and to obtain aldols and related derivatives¹⁴. Moreover, HFA reacts with silyl enol ethers in presence of a Lewis acid and the product can be easily dehydrated under very mild conditions¹⁵. Although these encouraging reported applications of HFA in aldol condensations, the main disadvantage we had to overcome was the lack of suppliers of gaseous HFA. The commercially available form of this substance is hexafluoroacetone trihydrate (3.0 H₂O), in which one molecule of water is incorporated in the form of a geminal diol. Most aldol condensation protocols requires strictly anhydrous reaction conditions due to air and moisture sensitivity of the reactive partners involved; therefore, the direct use of hydrate HFA is strongly discouraged, as only one sixth of the enolate reagent could engage in the aldol process, the rest being destroyed by water. On the other hand, organocatalytic¹⁶ and Mukaiyama-type¹⁷ aldol reactions have been recently developed to work efficiently even in aqueous solvent systems. We therefore pursued this route and planned to perform the aldol reaction using HFA trihydrate in a water-tolerant methodology. Pregnenolone was purchased in the form of its cheap precursor pregnenolone acetate **48**, with the protection of the hydroxyl functionality at C3 as an acetate ester already coming with the commercially available material. This was considered to avoid side reactions during the synthetic pathway. The first attempts were performed following an organocatalytic protocol. Entry 1 and entry 2 (**Table 4.1**) show the results obtained with pyrrolidine and L-proline as catalysts respectively, using as reactive partners pregnenolone acetate **48** and trihydrate HFA. In both cases conversion of starting material into the desired product was not observed and compound **48** was fully recovered after work-up. Given the unsatisfactory results we desisted from the organocatalytic methodology and we applied a canonical aldol reaction.

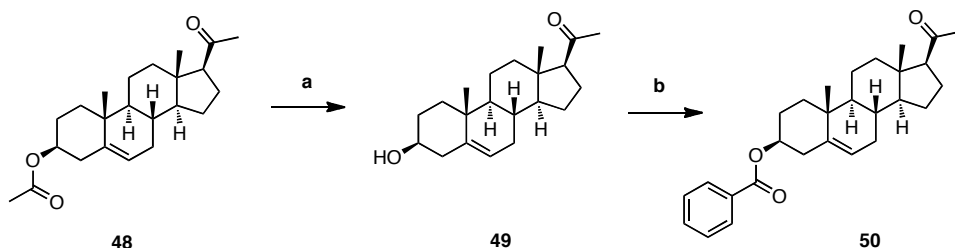
Table 4.1 Screening results for the aldol reaction between pregnenolone **49** or derivatives **48**, **50** and HFA

Entry	Reactive partners	Conditions	Yield ^a (%)	Comments
1	48 + HFA (l)	Pyrrolidine, DMF, r.t.	-	no conversion
2	48 + HFA (l)	L-proline, DMSO, r.t.	-	no conversion
3	48 + HFA (l)	KOH ^c , TBAC, DCE/H ₂ O, r.t.	-	deacetylation product
4	49 + HFA (l)	1. TIPS-OTf ^d , TEA, DCM 2. TMS-OTf, DCE/H ₂ O	-	undesired product
5	50 + HFA (g)	BuLi, DIPEA, dry THF, -78°C	20	LDA impurities
6	50 + HFA (g)	KHMDS, dry THF, -78°C work-up: NH ₄ Cl sat. solution	30	partially dehydration of desired product
7	50 + HFA (g)	KHMDS, dry THF, -78°C work-up: NH ₄ Cl 5% sol.	48	
8	50 + HFA (g)	KHMDS, dry THF, -78°C work-up: Acetic acid 5% sol.	67	

^a isolated yield^c 3.0 eq. of KOH were used^d 2.2 eq of TIPS-OTf were used

A first attempt (**Table 4.1** - entry 3) was carried out with KOH as base in a solvent mixture of dichloroethane (DCE) and water using tetrabutylammonium chloride (TBAC) as phase transfer catalyst. An excess of KOH (3 eq.) was employed in order to assure the enolization of the α -carbonyl position. Conversion of the starting material was incomplete and the formed product revealed to be the undesired deacetylated product i.e. pregnenolone **49**. We next tried to apply a Mukaiyama methodology (**Table 4.1** - entry 4). A manipulation of the hydroxyl protecting group was at this point required: we removed the acetyl group by exposure to KOH (**Scheme 4.3**) to

obtain pregnenolone **49** that was reacted with triisopropylsilyl trifluoromethanesulfonate (TIPS-OTf) in presence of triethylamine (TEA).



Scheme 4.3 Protecting groups manipulation. *Reagents and conditions:* (a) KOH, MeOH/DCM, r.t., 2h; (b) Benzoyl chloride, DMAP, pyridine, 0° C to r.t., 24h

The use of 2.2 eq. of TIPS-OTf allowed the simultaneous silylation of C3 hydroxyl and the generation of the silyl enol ether that was isolated and reacted with trihydrate HFA in presence of trimethylsilyl trifluoromethanesulfonate (TMS-OTf) as Lewis acid. The reaction led to the formation of an undesired product, whose structure could not be attributed unequivocally by NMR and MS. All these unsuccessful outcomes forced us to reconsider the use of hydrate HFA in the aldol reaction. We therefore investigated the possibility of generating *in situ* gaseous HFA. The lack of literature about a productive dehydration technique for HFA with a common laboratory set-up was partially filled by industrial patents reporting the dehydration of HFA exerted by strong acids, such as concentrated HCl or HF. The generation of gaseous HFA was accomplished by dropping trihydrate HFA in concentrated sulfuric acid warmed at 50° C: we observed the saturation of the flask by a white mist, allegedly the HFA gas. This could be delivered directly, with the aid of a stream of nitrogen, into the reaction vessel containing the enolate partner. With this technique in hands, we could optimize the choice of conditions for the aldol reaction. We firstly replaced the acetate ester-protecting group on the C3 hydroxyl with a benzoate (**50**) to avoid the potential double enolization of the starting material. The lithium enolate of compound **50** was generated by treatment with butyl lithium in presence of diisopropyl amine, to generate LDA (lithium diisopropylamide) in anhydrous THF at -78°C (**Table 4.1** - entry 5). After the enolate was formed, we delivered through a cannula the generated gaseous HFA to the enolate solution. The set up of the reaction is depicted in **Figure 4.4**.

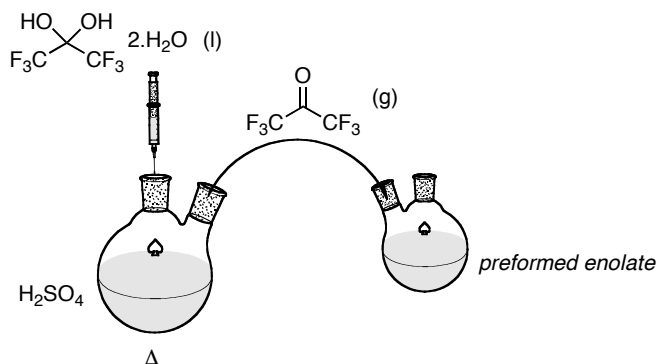
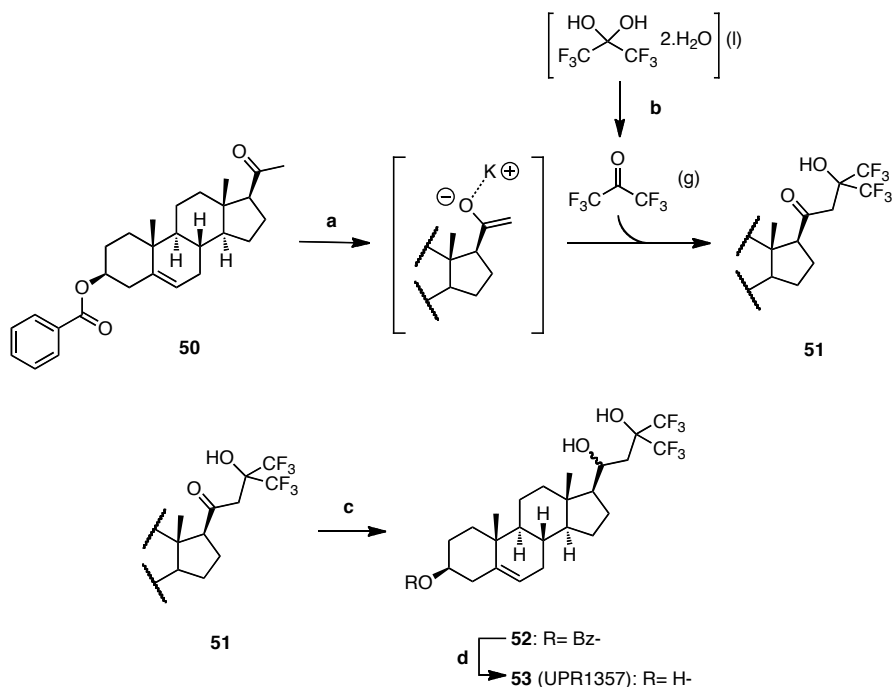


Figure 4.4 Schematic set up for the aldol reaction with *in situ* generation of gaseous HFA

This optimized procedure allowed the isolation of the desired product in modest yield (20%). The main drawback of this protocol was the presence of an impurity consistent with 2,2,2-trifluoro-*N,N*-diisopropylacetamide derived from the attack of LDA on HFA. The purification of desired product resulted to be troublesome; we decided therefore to change the reaction conditions. We envisioned the use of potassium bis(trimethylsilyl)amide (KHMDs) (**Table 4.1** - entry 6), to shut down the nucleophilicity of the spent base. Conversion of the starting material, evaluated by TLC analysis, was appreciable but not complete; after working-up the reaction with a saturated aqueous solution of ammonium chloride, a second spot appeared. Analysis by means of NMR and MS of the isolated side-product showed it to be the dehydrated aldol product (α - β unsaturated ketone). The desired molecule could nevertheless be isolated with a relieving yield of 30%.

We speculated the dehydrated product to arise from the basic conditions employed during the work up. Switching to a 5% aqueous solution of ammonium chloride reduced the dehydration of the product and the yield of the process increased to 47% (**Table 4.1** - entry 7). The best result was finally obtained with a 5% solution of acetic acid in water. The yield of the process was assessed to be a satisfactory 67% (**Table 4.1** - entry 8). At this point, with a robust synthesis in hands, we could tackle the reduction of the carbonyl function to the corresponding alcohol. This was straightforwardly accomplished by treatment of compound **51** with NaBH_4 in a mixture of methanol and THF. Eventually, the reduced molecule was obtained by direct saponification of the benzoate ester to liberate the C3 hydroxyl group. The synthetic pathway for the

synthesis of compound **53**, tagged as UPR1357 is summarized in **Scheme 4.4**. The molecule synthesized was then tested *in vitro* to evaluate its inhibitory activity.



Scheme 4.4 Synthetic pathway for molecule **53** (UPR1357). *Reagents and conditions:* (a) KHMDS, dry THF, -78° C, 30 min; (b) H_2SO_4 , 50° C; (c) NaBH_4 , MeOH/THF, r.t., 2h; (d) MeONa, MeOH/THF, r.t., 1 h.

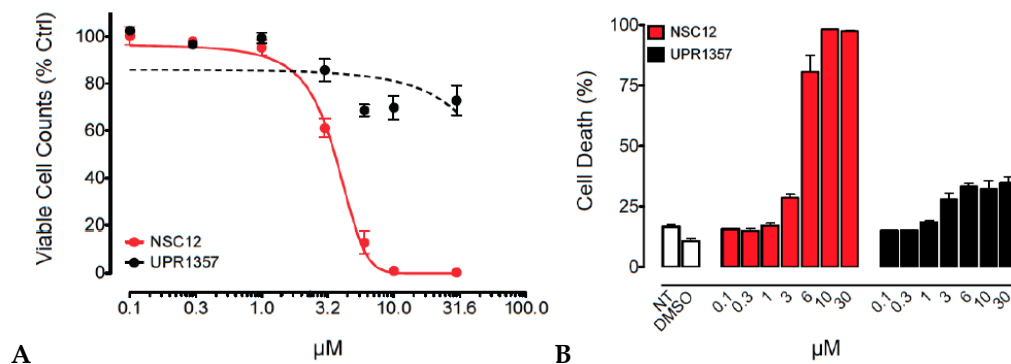


Figure 4.5 (A) *In vitro* anti-proliferative effect on KMS11 human multiple myeloma cells treated with increasing doses of NSC172285 (red) and UPR1357 (black) compounds. No relevant inhibitory effect was observed when UPR1357 compound was tested. **(B)** Induction of cell death was assessed in KMS11 cells treated with increasing concentrations of NSC172285 (red) and UPR1357 (black).

Surprisingly, as shown in **Figure 4.5**, no relevant inhibitory effects were observed when UPR1357 was tested. Puzzled by these findings, we speculated the two molecules being different diastereoisomers and decided to make a deep investigation on the structure of the two molecules. ESI-MS spectra of both compounds was recorded and showed the same mass peak ($m/z = 483.3$ $[M+H]^+$) and the same molecular fragmentations (**Figure 4.6A,B**). Co-injection of the two compounds in HPLC-MS revealed two different peaks with different retention times, thereby confirming that the molecule synthesized UPR1357 was not chemically equivalent to NCS172285.

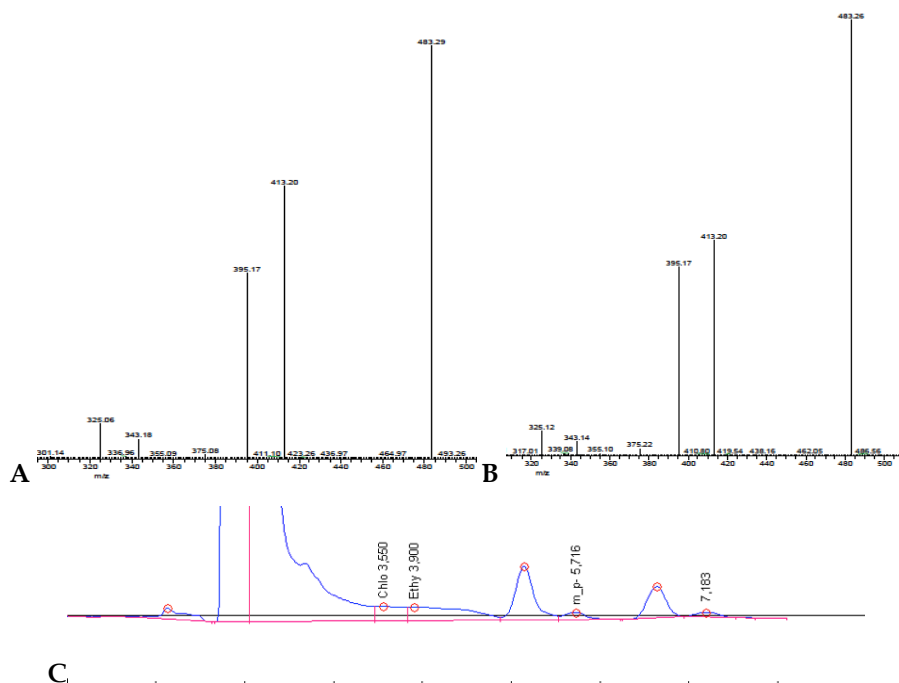


Figure 4.6 Mass spectra for compounds NSC172285 (**A**) and UPR1357 (**B**) revealed the same molecular fragmentation. (**C**) Co-injection in HPLC-MS of a mixture of compounds NSC172285 (peak 1) and UPR1357 (peak 2)

$^1\text{H-NMR}$ spectra displayed subtle, but remarkable differences between the compounds: as shown in **Figure 4.7**, from the superposition of the spectra was clearly identifiable a different shift for the singlet signals belonging to H18, a different pattern of the aliphatic resonance peaks (1.0-2.1 ppm) and a slight shift of the triplet signal corresponding to H20. We came to the conclusion that UPR1357 and NSC172285 were

two different chemical species and we speculated they could be epimers at C20. This hypothesis was consistent with the structural evidences recorded (same mass spectrum, different NMR spectra). Indeed, the absolute configuration of C20 was not univocally defined in the structure of NCS172285, and we concluded that being the only new stereogenic center generated during the synthesis, the *diastereomeric* nature of the two compounds could only derive from an *epimeric* relationship at C20.

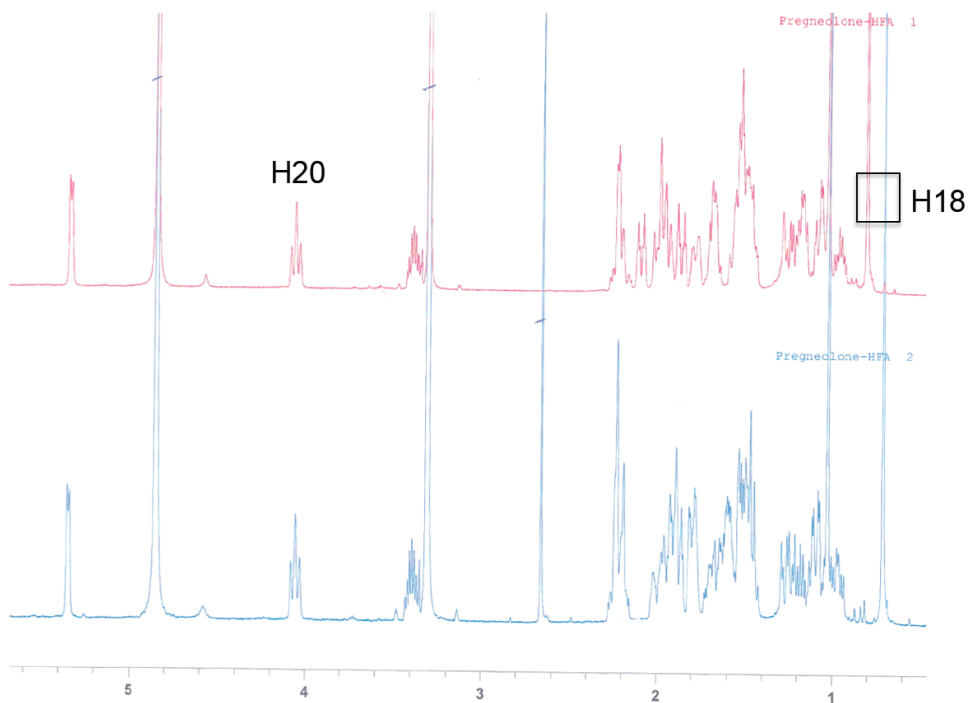


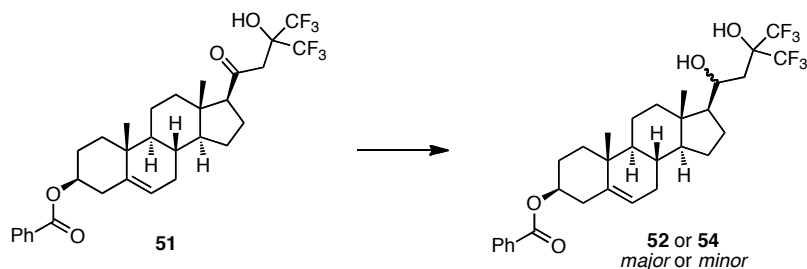
Figure 4.7 Superposition of NCS172285 (blue) and UPR1357 (red) ^1H -NMR spectra.

To test our hypothesis we reviewed our synthetic procedure in order to establish a protocol for the reduction of ketone **51** that could generate the C20 epimer of compound **52**. The results of this screening effort are outlined in **Table 4.2**.

Employing aluminum-based reducing agents such as lithium aluminium hydride (LiAlH_4) (**Table 4.2** - entry 2) and the hindered diisobutylaluminium hydride (DIBAL-H) (**Table 4.2** - entry 3) led to the exclusive formation of the C20 epimer **52** as already obtained with the precedent protocol (**Table 4.2** - entry 1). The first encouraging results were obtained using sodium triacetoxyborohydride (**Table 4.2** - entry 4). Owing to the steric and electronic effects of the acetoxy groups, sodium

triacetoxyborohydride is a milder reducing agent than sodium borohydride or even sodium cyanoborohydride and it is especially suitable for reductive aminations of aldehydes and ketones¹⁸.

Table 4.2 Screening results for the reduction of compound **51** generating C20 epimers **52** (*major*) or **54** (*minor*)^a



Entry	Reducing agent	Solvent	Temperature	<i>d^r</i> <i>major:minor</i>
1	NaBH ₄	MeOH/THF	r.t.	>99:1 ^c
2	LiAlH ₄	THF	0° C	>99:1 ^c
3	DIBAL-H	THF	0° C	>99:1 ^c
4	Na(OAc) ₃ BH ^{d,e}	THF	0° C to r.t.	87:13
5	NaBH ₄ /CeCl ₃ ·7H ₂ O	MeOH/THF	r.t.	>99:1 ^c
6	BMS/D-prolinol ^e	THF	r.t.	93:7
7	BMS/L-prolinol ^e	THF	r.t.	>99:1 ^c

^a reaction conditions: 1.0 eq. (0.03 mmol) of **51**, 1.2/1.3 eq. of reducing agent

^b determined by ¹H-NMR analysis of the crude reaction mixture

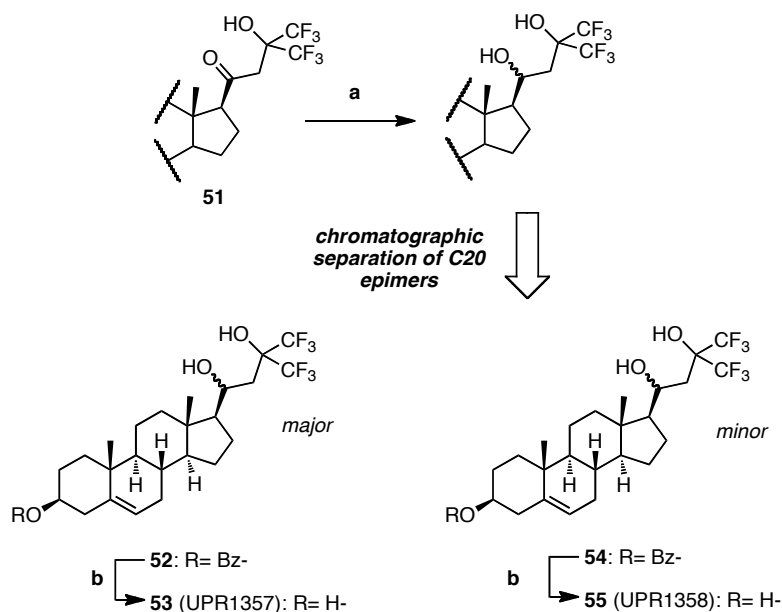
^c exclusively formation of *major* C20 epimer was observed

^d 6.0 eq. of Na(OAc)₃BH were used

^e conversion of the starting material not complete

Evans and coworkers deeply investigated the use of Na(OAc)₃BH in reduction of β-hydroxy ketones¹⁹. These reductions proceed by an apparent rate-determining exchange of the substrate hydroxyl group for an acetate of the triacetoxyborohydride which precedes the reduction step, which proceeds by intramolecular hydride delivery. This led us to assume that the intramolecular hydride transfer, opposite to the classical intermolecular reduction, might result in a reverse stereochemical course of the process, leading to the formation of *minor* C20 epimer. The reaction of substrate

51 with $\text{Na}(\text{AcO})_3\text{BH}$ was indeed very slow and a large excess of reductant was necessary to obtain an appreciable conversion of the starting material. The diastereomeric ratio (*dr*), determined by means of $^1\text{H-NMR}$ spectroscopy on crude reaction mixture, was 87:13 in favor of *major 52* epimer. Reduction of a series of keto steroids, including pregnenolone, under Luche's conditions ($\text{NaBH}_4/\text{CeCl}_3 \cdot 7\text{H}_2\text{O}$) was investigated by Št'astná and coworkers²⁰. They reported, for pregnenolone, an increase of the *minor* 20S alcohol when the reduction was performed with sodium borohydride in presence of cerium (III) chloride heptahydrate. Application of Luche's reduction conditions to our substrate **51** didn't provide the desired effect: exclusive formation of the *major* C20 epimer was again observed (**Table 4.2** – entry 5). Borane reductions with chiral ligands were reported for pregnenolone. Göndös *et al.*²¹ demonstrated that the use of borane methyl sulfide (BMS) in presence of prolinol-based chiral ligands reversed the stereochemistry affording the 20S alcohol as major product. The protocol developed by Göndös and colleagues was applied to our starting material **51**. The use of D-prolinol in combination with BMS afforded a mixture of *major 52* and *minor 54* products with a *dr* of 93:7 while L-prolinol afforded exclusively diol **52**.



Scheme 4.5 Synthetic pathway for compound **55** (UPR1358). Reagents and conditions: (a) $\text{Na}(\text{AcO})_3\text{BH}$, THF, 0°C to r.t., 6h; (b) MeONa , MeOH/THF , r.t., 1 h.

Among the screened procedures the best results were obtained with $\text{Na}(\text{AcO})_3\text{BH}$ as reducing agents. The reduction using sodium triacetoxyborohydride was repeated on a larger scale in order to obtain, after a troublesome chromatographic separation performed with the aid of an automated medium pressure column chromatography, compound **54** in sufficient amount. The benzoate ester group was removed by transesterification with catalytic MeONa in MeOH to afford product **55** tagged as UPR1358. The synthesis of this compound is summarized in **Scheme 4.5**.

We performed ^1H -NMR and ^{13}C -NMR analysis on UPR1358 **55** to verify its chemical identity with NSC172285. The perfect superposition of ^1H -NMR spectra revealed the correctness of the epimeric assumption for the two compounds (**Figure 4.8**). As expected, by testing *in vitro* UPR1358 and NSC172285, the two compounds showed the same antiproliferative and cytotoxic profile (**Figure 4.9**).

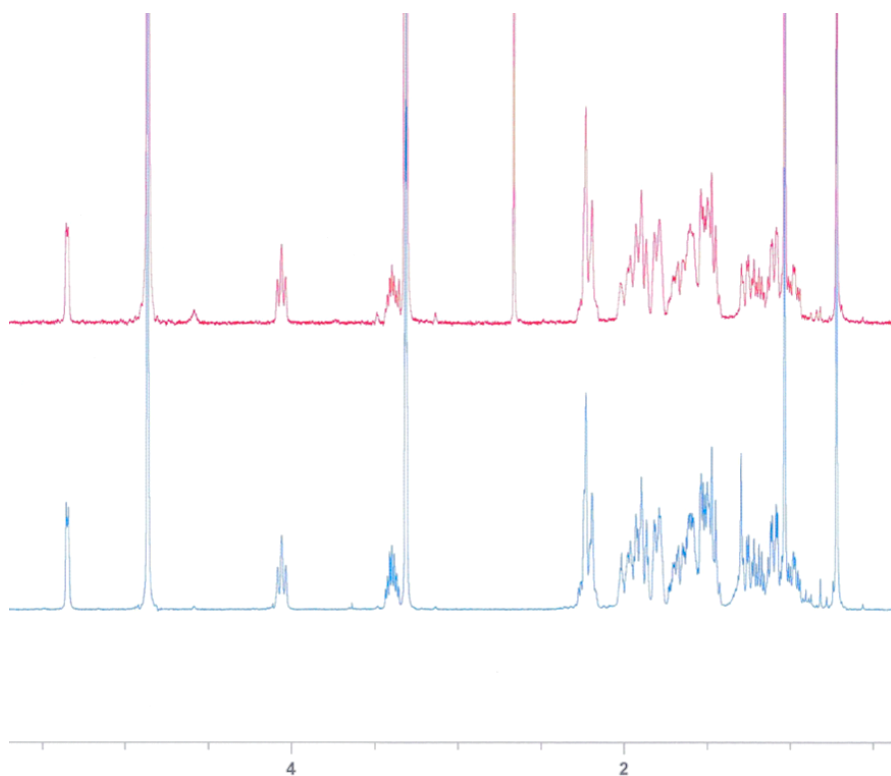


Figure 4.8 Superposition of NSC172285 (red) and UPR1358 (**55**) (blue) ^1H -NMR spectra.

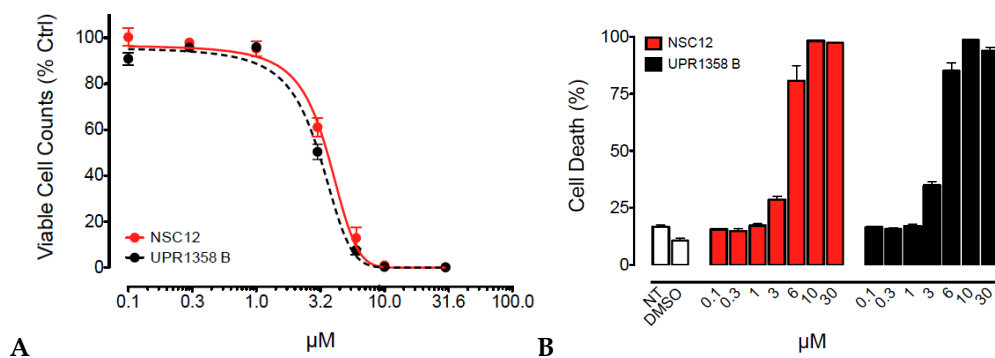


Figure 4.9 (A) In vitro anti-proliferative effect on KMS11 human multiple myeloma cells treated with increasing doses of NSC172285 (red) and UPR1358 (black) compounds. (B) Induction of cell death (reported as percent of PI⁺ cells) was assessed in KMS11 cells treated with increasing concentrations of NSC172285 (red) and UPR1358 (black).

4.3.2 Stereochemistry attribution

After having accomplished the design and the synthesis of the two diastereoisomers UPR1357 **53** and UPR1358 **55**, a complete characterization of this novel compounds was required. We finally had to face the elusive question that we postponed for a later moment at the beginning of our synthesis, about the absolute configuration at C20. The challenge resided in the univocal attribution of the absolute stereochemistry of the newly generated stereocenter of the reduction step by means of NMR spectroscopy. As previously said (see paragraph 4.1), literature evidences let us to speculate that the *major* and *minor* products of the reduction step (compound **52** and compound **54**), were the 20*R* the 20*S* respectively, and therefore corresponding final products **53** and **55** would have the same absolute configuration.

Interpretation of the NMR spectra started from the observation of the peculiar multiplicity of the resonance peak corresponding to H20. In both compounds **53** and **55** the signal observed for H20 is a triplet with identical coupling constants (*J*) of 10.3 Hz. As shown in **Figure 4.10**, H20 possesses 3 vicinal protons (H17, H21a, H21b) and its signal could, in principle, be split into up to eight lines: a doublets of doublets of doublets (ddd).

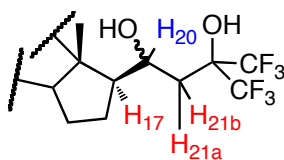


Figure 4.10 H20 proton (blue labeled) is coupled with vicinal protons H17, H21a and H21b (red labeled)

The unexpected H20 low multiplicity can be attributed to two reasons: 1) two coupling constants are equal and 2) the magnitude of coupling with one of the vicinal proton is null. ^1H -TOCSY experiment with selective band center irradiation on the H20 signal allowed isolating, from the crowded aliphatic portion of the spectra, the signals belonging to the same spin system (**Figure 4.11**).

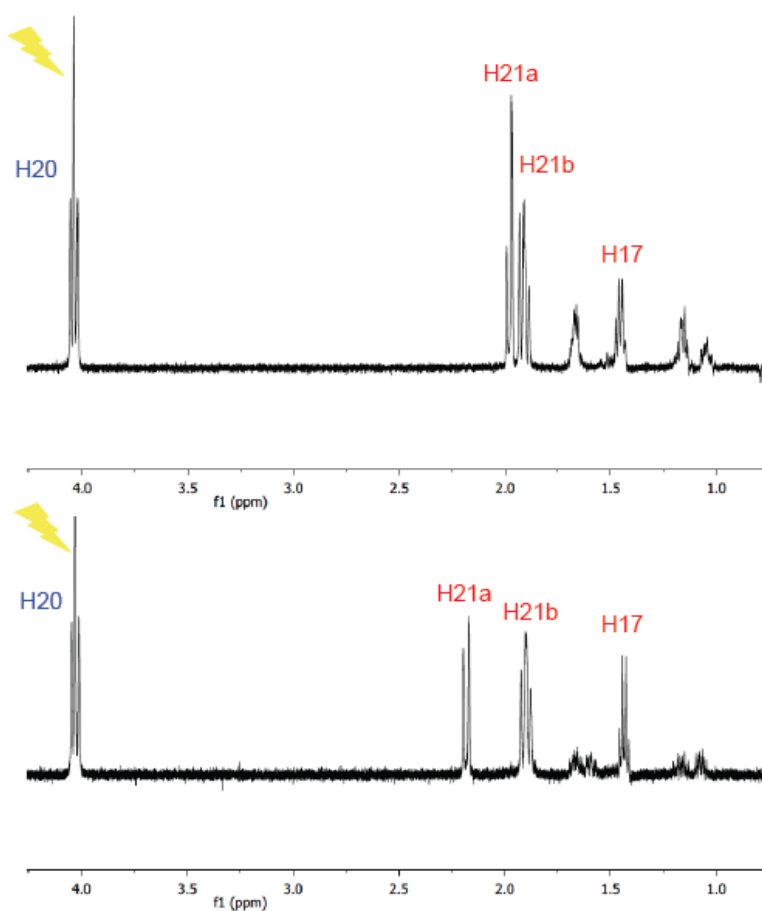


Figure 4.11 ^1H -TOCSY spectra for compounds **53** (on top) and **54** (on bottom)

The peaks corresponding to H21a and H21b, directly coupled with H20, could be easily identified, as they possess the highest intensity. The doublet at 1.98 ppm for compound **53** and at 2.18 ppm for compound **55** was assigned to the hydrogen marked as H21a; in both molecules this proton has only one geminal (2J) coupling with H21b ($J = 15.0$ and 15.1 Hz, respectively). The signal at 1.91 ppm for compound **53** and at 1.88 ppm for compound **55** was assigned to the hydrogen marked as H21b. The multiplicity of this proton is poorly resolved: the overlapping of a doublet of doublets resonance lines generate a triplet-like signal in which is possible, however, to identify two coupling constants. H21b have one geminal (2J_1) coupling with H21a ($J_1 = 15.0$ and 15.1 Hz for compounds **53** and **55**, respectively) and a vicinal (3J_2) coupling with H20 ($J_2 = 11.1$ and 11.3 Hz for compounds **53** and **55**, respectively). Thus, H21a was found to have null coupling with H20. According to Karplus' equation, the dihedral angle between these protons should be close to 90° . Moreover the value of the coupling constants between H17-H20 and H20-H21b is consistent with a diaxial 3J coupling suggesting an *anti*-conformation. We speculated a conformationally locked, six-membered arrangement induced by an intramolecular hydrogen-bond involving the hydroxyls of the 1,3 diol portion. (Figure 4.12A).

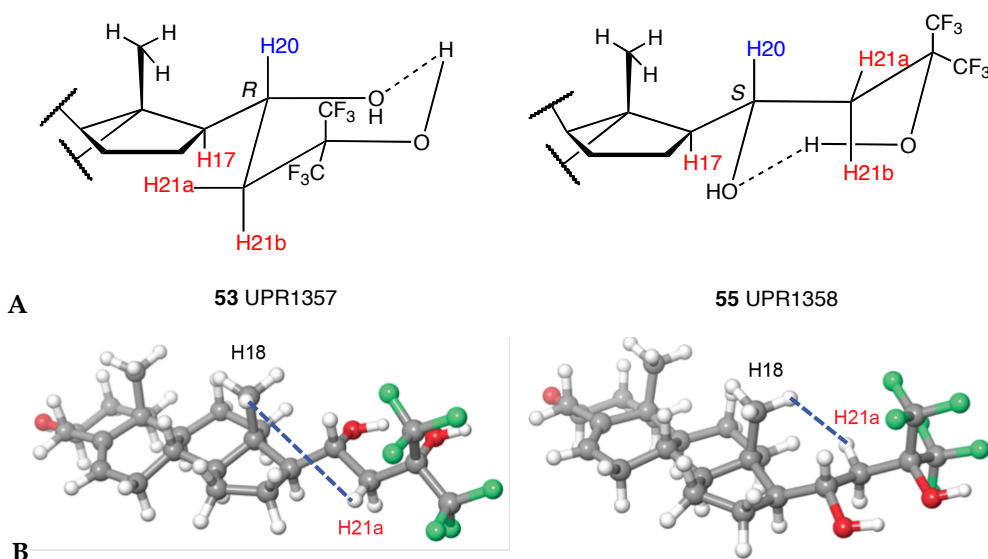


Figure 4.12 (A) Preferred conformations for compounds **53** and **55**.

(B) Geometries of compounds **53** and **55**. See experimental section for details.

With the minimum-energy geometries represented in **Figure 4.12B**, the coupling constants calculated by the software Schrodinger Maestro 9.7 for H20 were consistent with the observed triplets. In particular, the calculated values for H20-H17, H20-H21b and H20-H21a were 9.9, 11.0 and 1.0 Hz for **53** and 9.7, 11.3 and 1.5 for **55**, respectively. From the minimized geometries of the final compounds with 20*R* and 20*S* stereochemistry (tentatively assigned for **53** and **55**, respectively) it is possible to see the enantiomorphic arrangement of the diol motif (**Figure 4.12B**), where a remarkable difference in the distance between the C18 methyl group and the C21 methylene suggested the use of Nuclear Overhauser Enhancement (NOE) monodimensional NMR experiments to discriminate the two epimers. In particular for compound **55**, 20*S* diastereoisomer, the proximity of H21a to H18, in the conformer of minimum energy, is sufficient to result in a NOE contact. Reversely for diastereoisomer **53**, 20*R* alcohol, the distance between H21a and H18, when adopting the same conformation, is not sufficient for a nuclear transfer spin polarization between the nuclei.

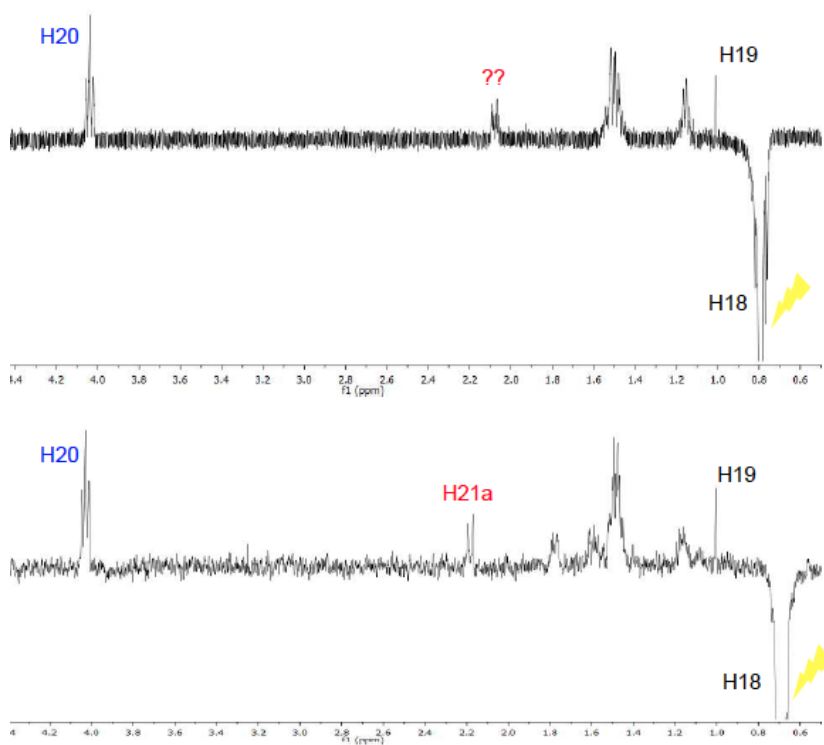
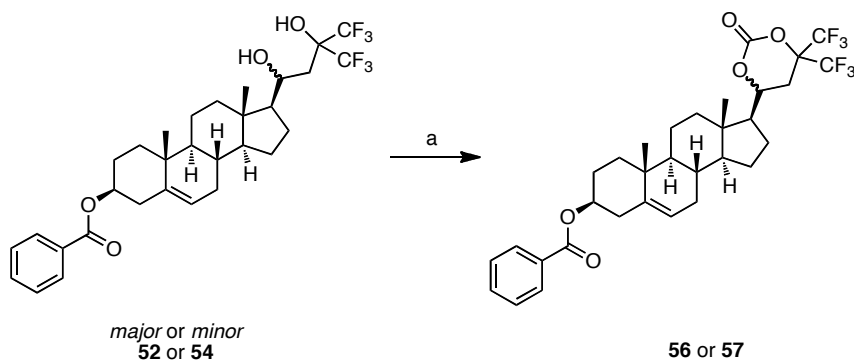


Figure 4.13 1D NOE-NMR spectra of compounds **53** (on top) and **55** (on bottom) with selective band center irradiation on H18

The results of 1D NOE experiment with selective band center irradiation on the H18 protons of the methyl group are reported in **Figure 4.13**. The NOE-NMR spectra of both compounds show a clear NOE contact between H18 and H20, indicating an identical relative distance, as well as for the relative intensity of H18 and H19 (proton on $-\text{CH}_3$ C19). While compound **55** shows NOEs between H18 and a proton at 2.18 ppm that is unequivocally assigned to H21a, compound **53** shows significant NOEs with protons at 2.05, 1.50 and 1.15 ppm; these signals, however, could not be unequivocally identified by the use of 2D-COSY and HSQC-NMR experiments. In particular, the NOE contact at 2.05 is close to the signal attributed to H21a (1.98 ppm) and the lack of an unambiguous attribution for this signal did not allow drawing final conclusions. Additionally, the poor signal/noise ratio proved detrimental to the success of these NOE experiments.

We thus decided to functionalize final products blocking the diol conformation by engaging the C20 and C22 hydroxyls in a 6-membered ring. At the same time, we looked for a functionalization that could shift some of the critical signals at lower magnetic fields, to avoid overlapping and simplify the attribution of the key peaks. We accomplished these purposes by synthesizing the corresponding cyclic carbonate derivatives **56** and **57** by treatment of benzoylated precursors **52** and **54**, respectively, with triphosgene (**Scheme 4.6**): the electrophilic properties of the carbonyl moiety clarified the spectra of the aliphatic portion by altering the chemical shift of several protons.



Scheme 4.6 Synthesis of compounds **56** and **57**. *Reagents and conditions:* (a) triphosgene, pyridine, DCM, -50°C to r.t., 2h.

In particular critical H21a, that assumes a (pseudo-) equatorial arrangement in the 6-membered ring (H21eq), resonates at 2.42 ppm for compound **56** and at 2.55 ppm for compound **57**, in a region of the spectra free of other resonance peaks.

The energy-minimized geometries (**Figure 4.14**) allowed the calculation of the distance between H21eq and H18, found to be 4.33 and 2.46 Å for compounds **56** and **57**, respectively. As previously described for compounds **53**, the distance between H18 and H21eq of compound **56**, is not sufficient for a significant NOE contact while the distance of 2.46 Å between H18 and H21eq in compound **57** can result in a NOE contact, analogously to the parent compound **55**.

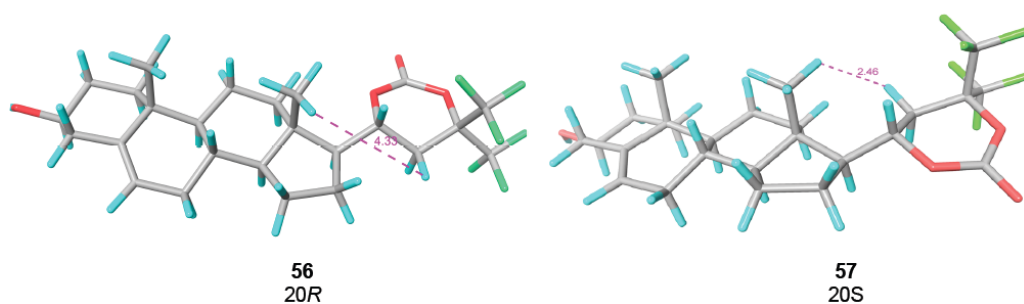


Figure 4.14 Geometries of compounds **56** and **57**

The results of NOE investigations are outlined in **Figure 4.15**. H18 of compound **56** shows NOE contacts with H19 ($d = 2.95$ Å), H16 ($d = 2.43$ Å), H11ax ($d = 2.18$ Å), H8 ($d = 2.17$ Å), H12eq ($d = 2.53$ Å) and H20 ($d = 2.35$ Å); the unequivocal assignment of these signals was accomplished by 2D-COSY and HSQC-NMR experiments and these results are consistent with the proposed conformation (see **Figure 4.14**). As expected, no contact was observed between H21eq (2.42 ppm) and H18 of compound **56**. On the contrary, H18 of **57** shows NOE contacts with H19 ($d = 2.96$ Å), H8 ($d = 2.17$ Å), H21eq ($d = 2.46$ Å) and H20 ($d = 2.41$ Å).

The results collected were sufficient to confirm the initial hypothesis of the stereochemistry of the compounds: the NOE contact between H18 and H12eq of compound **57** is consistent with a 20S absolute configuration while the absence of this contact in compound **56** reveal a *R* configuration for C20. The complete structures of the final compounds **53** (UPR1357) and **55** (UPR1358) with explicit absolute configuration of C20 are reported in **Figure 4.16**.

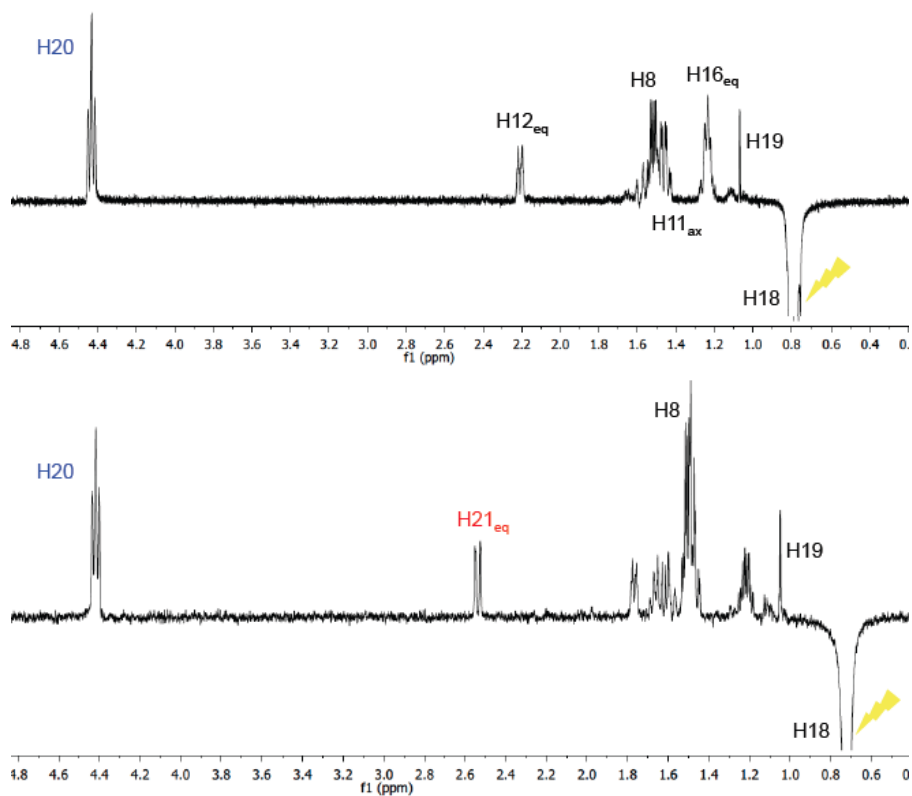


Figure 4.15 1D NOE-NMR spectra of compounds 56 (on top) and 57 (on bottom) with selective band center irradiation on H18

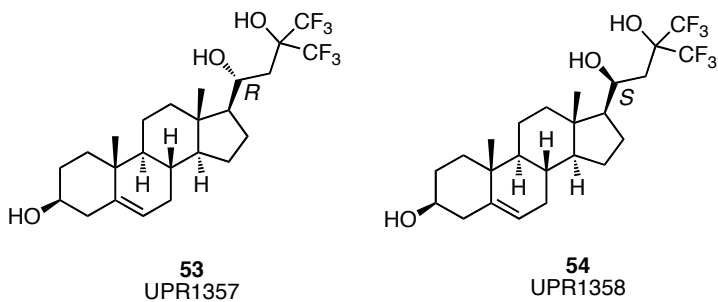


Figure 4.16 Structure of final compounds 53 (UPR1357) and 55 (UPR1358)

4.4 Conclusions

In this Chapter the synthesis of NSC172285 is reported. The major challenge associated was the necessity of planning the synthesis on the base of a poorly described structure. A synthetic pathway for NSC172285, not reported in the literature before, was setup and an efficient method for using HFA trihydrate as electrophilic partner in an aldol reaction, with standard laboratory equipment was developed. The hurdle of the reduction step relied in the formation of one or two products, with the *minor* 20S compound **55** (UPR1358 - NCS172285) possessing the highest inhibitory potency on FGF2-FGFR interaction. In the stereochemistry of C20 resides the first SAR evidence for this class of compounds.

Eventually, the unequivocal attribution of the stereochemistry at C20 was carried out through a simple derivatization, leading to a compound that could be thoroughly analyzed by means of NOE experiments, confirming the preliminary observations made on final compounds **53** and **55**.

Future directions point to the investigation of SAR starting from the C20 as crucial site for biological activity.

References

- ¹ Bikfalvi, A.; Klein, S.; Pintucci, G.; Rifkin, D.B. Biological roles of fibroblast growth factor-2 *Endocr. Rev.*, **1997**, *18*, 26–45.
- ² Conrad, H.E. Heparin-binding Proteins *Academic Press*, San Diego **1998**
- ³ (a) Iozzo, R.V. Matrix proteoglycans: from molecular design to cellular function *Annu. Rev. Biochem.* **1998**, *67*, 609–652. (b) Schlessinger, J.; Lax, I.; Lemmon, M. Regulation of growth factor activation by proteoglycans: what is the role of the low affinity receptors? *Cell.* **1995**, *83*, 357–60. (c) Rusnati, M.; Presta, M.; Interaction of angiogenic basic fibroblast growth factor with endothelial cell heparan sulfate proteoglycans. Biological implications in neovascularization. *Int. J. Clin. Lab. Res.* **1996**, *26*, 15–23.
- ⁴ Klint, P.; Claesson-Welsh, L. Signal transduction by fibroblast growth factor receptors. *Front Biosci.* **1999**, *4*, D165–77.
- ⁵ Kan, M.; Wang, F.; Xu, J.; Crabb, J.W.; Hou, J.; McKeehan, W.L. An essential heparin-binding domain in the fibroblast growth factor receptor kinase *Science* **1993**, *259* (26), 1918–1921.
- ⁶ Yayon, A.; Klagsbrun, M.; Esko, J.D.; Leder, P.; Ornitz, D.M. Cell surface, heparin-like molecules are required for binding basic fibroblast growth factor to its high affinity receptor *Cell* **1991**, *64*, 841–848.
- ⁷ Schlessinger, J.; Plotnikov, A.N.; Ibrahimi, O.A. *et al.* Crystal structure of a ternary FGF-FGFR-heparin complex reveals a dual role for heparin in FGFR binding and dimerization. *Mol. Cell.* **2000**, *6*, 743–50.
- ⁸ Presta, M.; Dell’Era, P.; Mitola, S. *et al.* Fibroblast growth factor/fibroblast growth factor receptor system in angiogenesis. *Cytokine Growth Factor Rev.* **2005**, *16*, 159–78.
- ⁹ Folkman, J.; Klagsbrun, M. Angiogenic factors *Science* **1987**, *235*, 442–7.
- ¹⁰ Nugent, M.A.; Iozzo, R.V. Fibroblast growth factor-2. *Int. J. Biochem. Cell Biol.* **2000**, *32*, 115–20.
- ¹¹ (a) Gerwins, P.; Skoldenberg, E.; Claesson-Welsh, L. Function of fibroblast growth factors and vascular endothelial growth factors and their receptors in angiogenesis. *Crit. Rev. Oncol. Hematol.* **2000**, *34*, 185–94. (b) Rusnati, M.; Presta, M. Fibroblast growth factors/fibroblast growth factor receptors as targets for the development of anti-angiogenesis strategies. *Curr. Pharm. Des.* **2007**, *13*, 2025–44.
- ¹² (a) Ray, J.; Baird, A.; Gage, F.H. A 10-amino acid sequence of fibroblast growth factor 2 is sufficient for its mitogenic activity on neural progenitor cells. *Proc. Natl. Acad. Sci. USA.* **1997**, *94*, 7047–52. (b) Rusnati, M.; Camozzi, M.; Moroni, E. *et al.* Selective recognition of fibroblast growth factor-2 by the long pentraxin PTX3 inhibits angiogenesis. *Blood* **2004**, *104*, 92–9.
- ¹³ Midland, M.M.; Kwon, Y.C. Stereochemistry of hydroboration of α -chiral olefins and reduction of α -chiral ketones. An unusual anti-Cram selectivity with dialkylboranes *J. Am. Chem. Soc.* **1983**, *105*, 3725–3727.
- ¹⁴ (a) Krespan, C.G.; Middleton, W.J. *Fluorine chem. Rev.* **1967**, *1*, 145. (b) Hudlicky, M. *Chemistry of Organic Fluorine Compounds 2nd ed.*, John Wiley, New York **1976**. (c) Chambers, R.D. *Fluorine in Organic Chemistry*, John Wiley, New York **1973**
- ¹⁵ Ishihara, T.; Shinjo, H.; Inoue, Y.; Ando, T. Regiospecific α -hexafluoroisopropylideneation of ketones using hexafluoroacetone *J. Fluor. Chem.* **1983**, *22*, 1–19

- ¹⁶ Mlynarski, J.; Paradowska, J. Catalytic asymmetric aldol reactions in aqueous media *Chem. Soc. Rev.* **2008**, *37*, 1502-1511
- ¹⁷ Kitano, T.; Kobayashi, S. Mukaiyama Aldol Reactions in Aqueous Media. *Adv. Synth. Catal.* **2013**, *355*(16), 3095-3118
- ¹⁸ Abdel-Magid, A. F.; Mehrman, S. J. A Review on the Use of Sodium Triacetoxyborohydride in the Reductive Amination of Ketones and Aldehydes *Organic Process Research & Development* **2006**, *10*(5), 971.
- ¹⁹ Evans, D.A.; Chapman, K.T.; Carreira, E. M. Direct reduction of β -hydroxy ketones employing tetramethylammonium triacetoxyborohydride *J. Am. Chem. Soc.* **1988**, *110*, 3560-3578.
- ²⁰ Štátná, E.; Černý, I.; Pouzar, V.; Chodounská, H. Stereoselectivity of sodium borohydride reduction of saturated steroidal ketones utilizing conditions of Luche reduction *Steroids*, **2010**, *75*, 721-725
- ²¹ Göndös, G.; Dombi, G.; Orr, J. C.; A new chiral director for the highly diastereoselective borane reduction of steroid-20-ones *Monatshefte für Chemie* **2000**, *131*, 1055-1059

Chapter

5

Experimental section

5.1 Chapter 3

5.1.1 Chemistry

All chemicals were used as received unless stated otherwise. All reactions were performed under a steady overpressure of nitrogen delivered through a balloon. Tetrahydrofuran was distilled over sodium/benzophenone prior to use. Anhydrous solvents such as dichloromethane, *N,N*-dimethylformamide, toluene and acetonitrile were directly purchased from an appropriate vendor, and were supplied stored over 3 Å molecular sieves and packed under Ar. They were subsequently manipulated by syringe under a steady pressure of nitrogen. Column chromatography was performed on silica gel 60 (0.040-0.063 mm) under forced flow of the appropriate solvent mixtures. TLC analysis was conducted on HPTLC aluminum sheets (Sigma-Aldrich, silica gel 60, F₂₅₄), compounds were visualized by UV absorption (245 nm) and/or by dipping in a solution of (NH₄)₆Mo₇O₂₄ · 4 H₂O 25 g/l and (NH₄)₄Ce(SO₄)₄ · 2 H₂O 10 g/l, in 1 L of 10% aqueous H₂SO₄. Microwave reactions were conducted using a CEM Discover synthesis unit (CEM Corp., Matthews, NC). Melting points were not corrected and were determined with a Gallenkamp melting point apparatus. ¹H- and ¹³C-NMR spectra were recorded with a Bruker AV 300, 400. Chemical shifts (δ scale) are reported in parts per million (ppm) relative to the central peak of the solvent. ¹H-NMR spectra are reported in the following order: multiplicity, number of protons and approximate coupling constant (*J* value) in hertz (Hz); signals were characterized as s (singlet), d (doublet), dd (doublet of doublets), t (triplet), dt (doublet of triplets), q (quartet), m (multiplet), bs (broad siglet). Mass Spectra were recorded on a Applied Biosystem API-150 EX system spectrometer with an ESI or an APCI interface. Final compound **2** was purchased from Sigma-Aldrich whereas compound **1** was synthesized according to literature methods¹. Purity of final compounds were analyzed on ThermoQuest (Italia) FlashEA1112 Elemental Analyzer for C, H, and N (analyses were within 0.4% of theoretical values) or by HPLC with UV detection at λ = 254 or 220. Purity of compounds was determined by analytical high performance liquid chromatography (HPLC) employing a Shimadzu HPLC gradient system (Shimadzu Corp., Kyoto, Japan) equipped with two LC-10AD solvent delivery modules, a Rheodyne 7125 sample injector and a SPD-10A UV-VIS detector. Prior to analysis, samples were prepared in MeOH at a final concentration of 0.1 mg/mL. Chromatographic

separation occurred on a Supelco Discovery C₁₈ column (150 X 4.6 mm, 5 mm particle size) by gradient elution. Flow rate was 1 mL/min and injected volume was 10 mL. Solvent A was methanol and Solvent B was water both added of 0.1% v/v formic acid. Gradient conditions A were employed for all BTZs compounds: t(0 min): 55% A: 45% B; t(15 min): 95% A: 5% B; t(17 min): 95% A: 5% B; returning to initial conditions after 1 min. Isocratic conditions B were employed for all triterpenes compounds: 90% A: 10% B t(13 min). Purity results are presented as t_R (min) and relative chemical purity (%). All tested compounds were >95% pure.

2-Methylbenzo[d]isothiazol-3(2H)-one 3: To a RT stirring solution of benzo[d]isothiazol-3(2H)-one **2** (61 mg, 0.393 mmol) in MeCN (2 ml) anhydrous K₂CO₃ (54 mg, 0.393 mmol) and KI (88 mg, 166.00 mmol) is added. The resulting white suspension is refluxed for 30 min and then cooled back to r.t.. Iodomethane (25 μ l, 0.393 mmol) is added and the reaction mixture stirred at r.t. for 20h under nitrogen atmosphere. The solvent is evaporated under reduced pressure and the crude is purified by FC (SiO₂, DCM100% then DCM/Et₂O 95:5) furnishing 287 mg of pure 2-methylbenzo[d]isothiazol-3(2H)-one **3** as white waxy solid (65%); ¹H-NMR (300 MHz, CDCl₃) δ : 8.00 (d, 1H, *J* = 7.11 Hz); 7.59-7.49 (m, 2H); 7.36 (m, 1H); 3.41 (s, 3H). MS-APCI: Calc. for C₈H₇NOS: 166.0, Found: 165.8 [M+H⁺]. Anal. Calc. for C₁₅H₁₂N₂O₃S: C, 58.15; H, 4.27; N, 8.48; Found: 58.43; H, 4.35; N, 8.19. Melting point = 54° C.

2-(6-Chlorohexyl)benzo[d]isothiazol-3(2H)-one 4: To a RT stirring solution of benzo[d]isothiazol-3(2H)-one **2** (100 mg 0.66 mmol) in MeCN (2 ml), K₂CO₃ (91.41 mg, 0.66 mmol) is added and the resulting suspension is stirred for 10 min under nitrogen atmosphere. 1-chloro-6-iodohexane (1.0 ml, 6.6 mmol) is dropwise added over 5 min and the resulting mixture is stirred for 18 h and then refluxed for 1h. The solvent is removed by distillation under reduced pressure and the crude is purified by FC (SiO₂, EtOAc/Hex 50:50) to give 66 mg of the expected product **4** as colorless oil (37%). ¹H-NMR (300 MHz, CDCl₃) δ : 8.03 (d, 1H, *J* = 7.9 Hz); 7.63-7.54 (m, 12H); 7.40 (td, 1H, *J* = 8.0, 1.3 Hz); 3.90 (t, 2H, *J* = 7.1 Hz); 3.52 (t, 2H, *J* = 6.6 Hz); 1.78 (m, 4H); 1.51 (m, 4H).

2-(6-(Piperidin-1-yl)hexyl)benzo[d]isothiazol-3(2H)-one 5: Piperidine (29 μ l, 0.29 mmol) is dropwise added to a r.t. stirring solution of K₂CO₃ (169.0 mg, 1.22 mmol), KI (8.13 mg, 0.049 mmol) and 2-(6-chlorohexyl)benzo[d]isothiazol-3(2H)-one **4** (66 mg, 0.25 mmol) in dry DMF (1 ml). The resulting suspension is heated to 60° C and stirred under nitrogen atmosphere. After 18h the reaction further piperidine (29 μ l, 0.29 mmol) and DMF (1 ml) are added and the reaction is carried out by microwave irradiation (Power = 200 W, Temperature = 110° C, Pressure = 100 psi, Time = 5 min). DMF is removed by distillation under reduced pressure and EtOAc is added. After filtration, the crude is purified by FC (SiO₂, DCM/MeOH 95:5) giving 33 mg of expected product as colorless oil (yield = 41%); ¹H-NMR (300 MHz, CDCl₃) δ : 8.00 (d, 1H, *J* = 7.9 Hz); 7.61-7.52 (m, 2H); 7.38 (m, 1H); 3.87 (t, 2H, *J* = 7.3 Hz); 2.35 (bs, 4H); 2.27 (t, 2H, *J* = 7.8 Hz); 1.75 (quintet, 2H, *J* = 7.1 Hz); 1.61-1.32 (m, 12H). MS-APCI: Calc. for C₁₈H₂₆N₂OS: 319.2, Found: 319.5 [M+H⁺]. Anal. Calc. for C₁₈H₂₆N₂OS x 1/2 H₂O: C, 66.01; H, 8.31; N, 8.55; Found: C, 66.33; H, 8.15; N, 8.42.

2,2'-Disulfanediyldibenzoyl chloride 7: A r.t. stirring suspension of 2,2'-Dithiosalicylic acid **6** (600 mg 1.96 mmol) in SOCl₂ (19.6 ml, 268.4 mmol) is refluxed until it became a solution and then for further 3h. The

solution is cooled to RT and exceeding SOCl_2 is distilled away under reduced pressure. The obtained dark-red residue is stripped with anhydrous toluol (twice) and used, without any further purification.

2-(Chlorocarbonyl)phenyl hypochlorothioite 8: The crude 2,2'-disulfanediyldibenzoyl chloride is suspended in dry CCl_4 at r.t. and an anhydrous flux of Cl_2 is bubbled through the suspension until the suspended solid residue is completely dissolved. The reaction vessel was tightly closed and the bubbling is stopped so to leave the reaction mixture under a Cl_2 saturated atmosphere for an additional 1 h. The reaction mixture is rapidly filtered and the solvent is distilled away under reduced pressure giving a yellow oil used without any further purification.

General method A: cyclization. To a 0°C stirring suspension of the proper amine (1.5 eq.) and dry TEA (4.8 eq.) in dry DCM, a solution of 2-(chlorocarbonyl)phenyl hypochlorothioite **8** in dry DCM is dropwise added over 2 min. The reaction mixture is stirred at r.t. under nitrogen atmosphere for 16 h. The solvent is distilled away under reduced pressure from the reaction mixture, the residue is taken up with EtOAc and the resulting mixture is washed with Na_2CO_3 saturated aqueous solution, 0.1M HCl aqueous solution and brine. The organic phase is dried over Na_2SO_4 and the solvent removed under reduced pressure affording the crude product that is subjected to flash column chromatography with an appropriate eluent mixture and to crystallization to furnish the purified product.

2-Phenethylbenzo[d]isothiazol-3(2H)-one 9: Starting from a 0.392M solution (1.0 ml, 0.39 mmol) of 2-(chlorocarbonyl)phenyl hypochlorothioite **8** according to method A, after purification by FC (SiO_2 Hex/EtOAc 70:30) and crystallization from *n*-hexane, final product (16 mg, 11%) is obtained as pale yellow crystals. $^1\text{H-NMR}$ (300 MHz, CDCl_3) δ : 8.04 (dd, 1H, $J = 7.9, 0.7$ Hz); 7.60 (td, 1H, $J = 8.2, 1.2$ Hz); 7.53 (d, 1H, $J = 7.4$ Hz); 7.40 (td, $J = 7.9, 1.0$ Hz); 7.24-7.35 (m, 5H); 4.15 (d, 2H, $J = 7.4$ Hz); 3.09 (t, 2H, $J = 7.7$ Hz). MS-APCI: Calc. for $\text{C}_{15}\text{H}_{13}\text{NOS}$: 256.1, Found: 256.2 $[\text{M}+\text{H}^+]$. Anal. Calc. for $\text{C}_{15}\text{H}_{13}\text{NOS}$: C, 70.56; H, 5.13; N, 5.49; Found: C, 70.58; H, 5.10; N, 5.39. Melting point = $90\text{-}92^\circ\text{C}$.

2-(2-(Naphthalen-1-yl)ethyl)benzo[d]isothiazol-3(2H)-one 10: Starting from a 0.392M solution (2.6 ml, 1.02 mmol) of 2-(chlorocarbonyl)phenyl hypochlorothioite **8** according to method A, after purification by FC (SiO_2 DCM 100%) and crystallization from *n*-hexane, final product (25 mg, 14%) is obtained as pale yellow crystals. $^1\text{H-NMR}$ (300 MHz, CDCl_3) δ : 8.25 (d, 1H, $J = 8.4$ Hz); 8.07 (d, 1H, $J = 7.8$ Hz); 7.88 (d, 1H, $J = 7.8$ Hz); 7.78 (t 1H, $J = 4.5$ Hz); 7.63-7.39 (m, 7H); 4.22 (t, 2H, $J = 7.8$ Hz); 3.54 (t, 2H, $J = 7.8$ Hz). MS-APCI: Calc. for $\text{C}_{19}\text{H}_{15}\text{NOS}$: 306.1, Found: 306.2 $[\text{M}+\text{H}^+]$. Anal. Calc. for $\text{C}_{19}\text{H}_{15}\text{NOS}$: C, 74.72; H, 4.95; N, 4.59. Found: C, 74.66; H, 4.98; N, 4.61. Melting point = $101\text{-}102^\circ\text{C}$.

2-(2-(Naphthalen-2-yl)ethyl)benzo[d]isothiazol-3(2H)-one 11: Starting from a 0.392M solution (2.6 ml, 1.02 mmol) of 2-(chlorocarbonyl)phenyl hypochlorothioite **8** according to method A, after purification by FC (SiO_2 DCM 100%) and crystallization from *n*-hexane, final product (28 mg, 15%) is obtained as yellow crystals. $^1\text{H-NMR}$ (300 MHz, CDCl_3) δ : $^1\text{H-NMR}$ (300 MHz, CDCl_3) δ : 8.04 (d, 1H, $J = 7.8$ Hz); 7.76-7.83 (m, 3H); 7.71 (s, 1H); 7.58 (td, 1H, $J = 8.2, 1.2$ Hz); 7.36-7.50 (m, 5H); 4.23 (t, 2H, $J = 7.2$ Hz); 3.24 (t, 2H, $J = 7.5$ Hz).

MS-APCI: Calc. for C₁₉H₁₅NOS: 306.1, Found: 306.3 [M+H⁺]. Anal. Calc. for C₁₉H₁₅NOS * 1/10 H₂O: C, 74.28; H, 4.99; N, 4.56; Found: C, 74.21; H, 4.97; N, 4.58. Melting point = 114-115° C.

Cyclohexylbenzo[d]isothiazol-3(2H)-one 12: Starting from a 0.22M solution (11.90 ml, 2.62 mmol) of 2-(chlorocarbonyl)phenyl hypochlorothioite **8** according to method A, after purification by FC (SiO₂ Hex/Et₂O 65:35) and vacuum distillation, final product (312 mg, 30%) is obtained as a white solid. ¹H-NMR (300 MHz, CDCl₃) δ: 8.05 (d, 1H, J = 7.89 Hz); 7.63-7.55 (m, 2H); 7.39 (m, 1H); 4.65-4.58 (m, 1H); 2.06 (d, 2H, J = 10.32 Hz); 1.89 (d, 2H, J = 11.97 Hz); 1.74 (bd, 1H, J = 13.08 Hz); 1.60-1.42 (m, 4H); 1.30-1.20 (m, 1H). MS-APCI: Calc. for C₁₅H₁₇NOS: 234.1, Found: 234.0 [M+H⁺]. Anal. Calc. for C₁₅H₁₇NOS: C, 66.92; H, 6.48; N, 6.00; Found: C, 66.68; H, 6.58; N, 5.82. Melting point = 84-85° C.

3,3'-Dithiopropionyl chloride 14: A stirring suspension of 3,3'- Dithiopropionic acid **13** (1200 mg 5.7 mmol) in SOCl₂ (6 ml) is refluxed until complete dissolution of the solid starting material (30 min). The solvent is evaporated under reduced pressure giving a brown oil used without any further purifications.

3,3'-Disulfanediyibis(N-phenethylpropanamide) 15: To a 0° C stirring solution of 2-phenylethanamine (1370 μl, 10.88 mmol) and dry TEA (987 μl, 7.04 mmol) in dry 1,2-dichloroethane (17 ml) a 1.18 M solution (2.7 ml, 3.2 mmol) of 2,2'-dithiopropionyl chloride **14** in dry DCM is dropwise added over 2 min maintaining the temperature of reaction mixture below 15° C. The resulting suspension is allowed to reach r.t. and was stirred for 2 h. The crude is diluted with DCM (30 ml), washed with pH = 4.75 acetate buffer (10 ml, 2 times) and water (10 ml, 1 time). The organic layer is dried over anhydrous Na₂SO₄, filtered and the solvent is evaporated under reduced pressure giving 2.020 g of pale yellow solid. The obtained solid is washed with Et₂O giving 1.389 g of desired product as a white solid (85%). ¹H-NMR (300 MHz, CDCl₃) δ: 7.35-7.21 (m, 10H); 5.93 (bs, 2H); 3.55 (q, 4H, J = 6.87 Hz); 2.95 (t, 4H, J = 7.01 Hz) 2.84 (t, 4H, J = 7.02 Hz); 2.53 (t, 4H, J = 6.99 Hz).

2-Phenethylisothiazol-3(2H)-one 16: A 0.75M solution of SO₂Cl₂ in dry 1,2-dichloroethane (4,8 ml, 3.6 mmol) is dropwise added to a 0° C stirring suspension of 3,3'-disulfanediyibis(N-phenethylpropanamide) **15** (500 mg, 1.2 mmol) in dry 1,2-dichloroethane (7 ml) over 2h. The solvent is evaporated under reduced pressure and the yellow oily residue is taken up with DCM. The resulting mixture is washed with H₂O (10 ml, 2 times), dried over anhydrous Na₂SO₄, filtered and concentrated under reduced pressure giving 697 mg of yellow oil. The crude is purified by FC (SiO₂, DCM/Et₂O 98:2 then 90:10) and crystalized from *n*-hexane giving 194 mg of desired product as a pale yellow powder (39%). ¹H NMR (300 MHz, CDCl₃) δ: 8.00 (d, 1H, J = 6.24 Hz); 7.35-7.22 (m, 5H); 6.27 (d, 1H, J = 6.24 Hz); 4.05 (t, 2H, J = 7.14 Hz); 3.04 (t, 2H, J = 7.44 Hz). MS-APCI: Calc. for C₁₁H₁₁NOS: 206.1, Found: 206.2 [M+H⁺]. Anal. Calc. for C₁₁H₁₁NOS: C, 64.36; H, 5.40; N, 6.82; Found: C, 64.48; H, 5.42; N, 6.84. Melting point = 78-79° C.

General method B: synthesis of intermediates 18a-b. To a stirring suspension of the corresponding 2-hydroxynitrobenzoic acid in super-dry MeOH is added conc. H₂SO₄ (0.3 eq.) and the resulting mixture is refluxed for 96 hours. The solution is cooled to r.t. and MeOH is removed under reduced pressure. The residue is dissolved in EtOAc and washed twice with water. The organic phase is dried over Na₂SO₄ and the

solvent removed under reduced pressure to afford the desired product used without any further purification.

Methyl 2-hydroxy-5-nitrobenzoate (18a): Starting from 2-hydroxy-5-nitrobenzoic acid **17a** (2 g, 10.92 mmol) the desired product is obtained as a light yellow powder (2.90g, yield 97%), according to method B. ¹H-NMR (300 MHz, CDCl₃) δ: 8.78 (d, 1H, *J* = 2.8 Hz); 8.32 (dd, 1H, *J* = 9.2, 2.8 Hz); 7.06 (d, 1H, *J* = 9.2 Hz); 4.01 (s, 3H)

Methyl 2-hydroxy-4-nitrobenzoate (18b): Starting from 2-hydroxy-4-nitrobenzoic acid **17b** (2 g, 10.92 mmol) the desired product is obtained as a light yellow powder (1.73 g, yield 81%), according to method B. ¹H-NMR (300 MHz, MeOD) δ: 8.12 (d, 1H, *J* = 8.7 Hz); 7.78 (m, 2H); 4.04 (s, 3H)

General method C: synthesis of intermediates 19a-e. To a solution of intermediate **18a-e** and DABCO or NaH (from 1.2 to 2.2 eq.) in dry DMF is quickly added under N₂ atmosphere, *N,N*-dithiocarbamoylchloride (1.5 eq.). The reaction is stirred at different temperatures until completion (see below for details). DMF is removed under reduced pressure and the residue is dissolved in EtOAc and washed twice with H₂O, HCl 1% and NaHCO₃. The organic phases are collected, dried over Na₂SO₄ and the solvent removed under reduced pressure. The crude product is subjected to flash column chromatography with an appropriate eluent mixture to furnish the purified product.

Methyl 2-((dimethylcarbamothioyl)oxy)-5-nitrobenzoate 19a: Starting from methyl 2-hydroxy-5-nitrobenzoate **18a** (500 mg, 2.536 mmol) and DABCO (341 mg, 3.04 mmol), reaction is stirred at r.t. for 1.5 hours. The residue is purified by FC (SiO₂ Hex/EtOAc 80:20) giving 500 mg of desired product as a yellow powder (yield = 68%), according to method C. ¹H-NMR (300 MHz, CDCl₃) δ: 8.86 (d, 1H, *J* = 2.8 Hz); 8.41 (d, 1H, *J* = 8.9, 2.9 Hz); 7.29 (d, 1H, *J* = 8.9 Hz); 3.90 (s, 3H); 3.46 (s, 3H); 3.42 (s, 3H).

Methyl 2-((dimethylcarbamothioyl)oxy)-4-nitrobenzoate 19b: Starting from methyl 2-hydroxy-4-nitrobenzoate **18b** (600 mg, 3.05 mmol) and DABCO (681 mg, 6.09 mmol), reaction is stirred at r.t. for 16 hours. The residue is purified by FC (SiO₂ Hex/EtOAc 75:25) giving 396 mg of desired product as a yellow powder (yield = 40%), according to method C. ¹H-NMR (300 MHz, CDCl₃) δ: 8.15 (m, 2H); 8.00 (s, 1H); 3.90 (s, 3H); 3.47 (s, 3H); 3.43 (s, 3H).

Methyl 2-((dimethylcarbamothioyl)oxy)-5-methoxybenzoate 19c: Starting from methyl 2-hydroxy-5-methoxybenzoate **18c** (2.0 g, 10.9 mmol) and NaH (526 mg, 13.2 mmol) reaction is stirred at r.t. for 16 hours. The residue is triturated in DEE giving 1.83 g of desired product as a white powder (yield = 65%), according to method C. ¹H-NMR (400 MHz, CDCl₃) δ: 7.51 (d, 1H, *J* = 3.0 Hz); 7.11 (dd, 1H, *J* = 8.8, 3.0 Hz); 7.05 (d, 1H, *J* = 8.8 Hz); 3.86 (s, 6H); 3.49 (s, 3H); 3.41 (s, 3H). ¹³C-NMR (100 MHz, CDCl₃) δ: 188.1; 164.7; 157.0; 147.4; 125.9; 124.3; 119.5; 115.5; 55.8; 52.3; 43.4; 38.9.

Methyl 2-((dimethylcarbamothioyl)oxy)-4-methoxybenzoate 19d: Starting from methyl 2-hydroxy-4-methoxybenzoate **18d** (2.0 g, 10.9 mmol) and NaH (526 mg, 13.2 mmol) reaction is stirred at r.t. for 16 hours and additional 6 hours at 50° C. The residue is triturated in DEE giving 1.7 g of desired product as a white

powder (yield = 60%), according to method C. ¹H-NMR (300 MHz, CDCl₃) δ: 7.96 (d, 1H, *J* = 8.8 Hz); 6.82 (dd, 1H, *J* = 8.8, 2.6 Hz); 6.62 (d, 1H, *J* = 2.5 Hz); 3.85 (s, 3H); 3.80 (s, 3H); 3.47 (s, 3H); 3.39 (s, 3H). ¹³C-NMR (75 MHz, CDCl₃) δ: 187.3; 164.6; 163.7; 155.5; 133.0; 116.2; 111.9; 110.5; 55.8; 51.9; 43.4; 39.0.

Methyl 2-((dimethylcarbamothioyl)oxy)-3-methylbenzoate 19e: Starting from methyl 2-hydroxy-3-methylbenzoate **18d** (2.0 g, 10.9 mmol) and NaH (526 mg, 13.2 mmol) reaction is stirred for 16 hours at 50° C. The residue is purified by FC (SiO₂ Hex/EtOAc 90:10) giving 711 mg of desired product as a yellow powder (yield = 55%), according to method C. ¹H-NMR (300 MHz, CDCl₃) δ: 7.80 (dd, 1H, *J* = 7.8, 1.3 Hz); 7.38 (dd, 1H, *J* = 6.9, 1.0); 7.16 (t, 1H, *J* = 7.7) 3.78 (s, 3H); 3.42 (s, 3H); 3.35 (s, 3H); 2.21 (s, 3H).

General method D: synthesis of intermediates 20a-e. Corresponding intermediate **19a-e** is suspended in diphenylether and the reaction is performed in a microwave reactor: 300W, 250°C, 0 PSI (open vessel) for different times (see below for details). When the starting material disappeared the solvent was removed by filtration on silica pad and the crude product is subjected to flash column chromatography with an appropriate eluent mixture to furnish the purified product.

Methyl 2-((dimethylcarbamoyl)thio)-5-nitrobenzoate 20a: Compound **19a** (640 mg, 2.25 mmol) is reacted for 1 min and purified by FC (SiO₂ Hex/EtOAc 60:40) giving 500 mg of desired product as a yellow solid (yield = 78%), according to method D. ¹H-NMR (300 MHz, CDCl₃) δ: 8.73 (d, 1H, *J* = 2.6 Hz); 8.28 (dd, 1H, *J* = 8.7, 2.6 Hz); 7.84 (d, 1H, *J* = 8.7 Hz); 3.95 (s, 3H); 3.15 (bs, 3H); 3.05 (bs, 3H).

Methyl 2-((dimethylcarbamoyl)thio)-4-nitrobenzoate 20b: Compound **19b** (396 mg, 1.39 mmol) is reacted for 20 min and purified by FC (SiO₂ Hex/EtOAc 70:30) giving 319 mg of desired product as a yellow solid (yield = 80%), according to method D. ¹H-NMR (300 MHz, CDCl₃) δ: 8.46 (d, 1H, *J* = 2.1 Hz); 8.23 (dd, 1H, *J* = 8.6, 2.2 Hz); 8.00 (d, 1H, *J* = 8.6 Hz) 3.93 (s, 3H); 3.15 (s, 3H); 3.04 (s, 3H).

Methyl 2-((dimethylcarbamoyl)thio)-5-methoxybenzoate 20c: Compound **19c** (200 mg, 0.7 mmol) is reacted for 20 min and purified by FC (SiO₂ Hex/EtOAc 60:40) giving 190 mg of desired product as a yellow oil (yield = 95%), according to method D. ¹H-NMR (300 MHz, CDCl₃) δ: 7.40 (d, 1H, *J* = 8.6 Hz); 7.32 (d, 1H, *J* = 2.9 Hz); 6.93 (dd, 1H, *J* = 8.8, 2.9 Hz); 3.79 (s, 3H); 3.74 (s, 3H); 2.96 (bs, 6H). ¹³C-NMR (75 MHz, CDCl₃) δ: 166.6; 166.5; 159.8; 138.9; 136.4; 119.7; 117.1; 115.8; 55.3; 52.1; 36.7.

Methyl 2-((dimethylcarbamoyl)thio)-4-methoxybenzoate 20d: Compound **19d** (200 mg, 0.7 mmol) is reacted for 10 min and purified by FC (SiO₂ Hex/EtOAc 80:20) giving 190 mg of desired product as a yellow oil (yield = 95%), according to method D. ¹H-NMR (400 MHz, CDCl₃) δ: 7.78 (d, 1H, *J* = 8.7 Hz); 7.03 (d, 1H, *J* = 2.5 Hz); 6.76 (dd, 1H, *J* = 8.7, 2.5 Hz); 3.69 (s, 3H); 3.66 (s, 3H); 2.94 (bs, 3H); 3.87(bs, 3H). ¹³C-NMR (100 MHz, CDCl₃) δ: 165.8; 165.5; 161.2; 132.3; 131.8; 125.8; 122.2; 113.6; 55.1; 51.5; 36.5.

Methyl 2-((dimethylcarbamoyl)thio)-3-methylbenzoate 20e: Compound **19e** (825 mg, 3.2 mmol) is reacted for 30 min and purified by FC (SiO₂ Hex/EtOAc 80:20) giving 735 mg of desired product as a yellow oil

(yield = 89%), according to method D. ¹H-NMR: (300 MHz, CDCl₃) δ: 7.54 (dd, 1H, *J* = 7.5, 1.6 Hz); 8.28 (dd, 1H *J* = 7.6, 1.1 Hz); 7.29 (d, 1H, *J* = 7.6 Hz) 3.83 (s, 3H); 3.09 (bs, 3H); 2.97 (bs, 3H); 2.43 (s, 3H).

General method E: synthesis of intermediates 21a-e. The intermediate **20a-e** is suspended in a 2:1 MeOH/H₂O mixture, NaOH is added and the reaction is refluxed for 16 hours. MeOH is removed under reduced pressure and the mixture is cooled by adding ice water (temperature below 15°C). To the solution is added 1% HCl until a white precipitate appeared. The precipitate is filtered off and dried to afford the desired compound used without any further purification.

2-Mercapto-5-nitrobenzoic acid 21a: Starting from methyl 2-((dimethylcarbamoyl)thio)-5-nitrobenzoate **20a** (500 mg, 1.75 mmol), the desired product (255 mg, 73%) is obtained as a yellow powder, according to method E. ¹H-NMR (300 MHz, DMSO) δ: 8.69 (s, 1H); 8.34 (m, 1H); 8.13 (m, 1H).

2-Mercapto-4-nitrobenzoic acid 21b: Starting from methyl 2-((dimethylcarbamoyl)thio)-4-nitrobenzoate **20b** (319 mg, 1.12 mmol), the desired product (172 mg, 77%) is obtained as a yellow powder, according to method E. ¹H-NMR (300 MHz, MeOD) δ: 8.57 (s, 1H); 8.34 (d, 1H, *J* = 8.5 Hz); 8.13 (d, 1H, *J* = 8.6 Hz).

2-Mercapto-5-methoxybenzoic acid 21c: Starting from methyl 2-((dimethylcarbamoyl)thio)-5-methoxybenzoate **20c** (1.7 g, 6.5 mmol), the desired product (600 mg, 50%) is obtained as a white powder, according to method E.

2-Mercapto-4-methoxybenzoic acid 21d: Starting from methyl 2-((dimethylcarbamoyl)thio)-4-methoxybenzoate **20d** (1.6 g, 6.1 mmol), the desired product (1.4 g, 92%) is obtained as a white powder, according to method E.

2-((Dimethylcarbamoyl)thio)-3-methylbenzoic acid 21e: Starting from methyl 2-((dimethylcarbamoyl)thio)-3-methylbenzoate **20e** (735 mg, 2.9 mmol), product **21e** (293 mg, 60%) is obtained as a white powder, according to method E. ¹H-NMR (300 MHz, D₂O) δ: 7.38 (m, 3H); 3.04 (bs, 3H); 3.04 (bs, 3H); 2.84 (bs, 3H); 2.28 (s, 3H).

General method F: synthesis of intermediates 22a-e. Compound **21a-e** is suspended in SOCl₂ (50-100 eq.) and refluxed for 6h. The reaction turned to a deep brown color and became clear. SOCl₂ is removed under reduced pressure and the residue is stripped twice with dry toluene. The brown oil (quantitative yield) obtained is dried, stored under nitrogen and used for the next step without any further purification.

General method G: oxidative cyclization using iodine. In a dried, two-neck flask the proper amine (1.25 eq.) is dissolved in dry THF under nitrogen atmosphere at 0°C. Dry TEA (3 eq.) is added to the mixture before a solution of preformed acyl chloride (1 eq.), dissolved in dry THF, is added. The reaction is gently warmed to r.t. and stirred for 16 hours. A solution of I₂ (1.25 eq.) dissolved in dry THF is then added and the resulting mixture is stirred for further 4 h. The solvent is removed under reduced pressure and the residue is dissolved in EtOAc and washed twice with a PH=7 buffer phosphate. The organic phase is dried over

Na₂SO₄ and the solvent removed under reduced pressure affording the crude product that is subjected to flash column chromatography with an appropriate eluent mixture and/or to crystallization to furnish the purified product.

5-Nitro-2-phenethylbenzo[d]isothiazol-3(2H)-one 23: Starting from compound **22a** (280 mg, 1.29 mmol) and 2-phenethylamine, the desired product is obtained, according to method G, as yellow crystals (230 mg, 60%) after purification by FC (SiO₂ Hex/EtOAc 80:20) and crystallization from DCM/*n*-hexane. ¹H-NMR (300 MHz, CDCl₃) δ: 8.86 (d, 1H, *J* = 2.1 Hz); 8.41 (dd, 1H, *J* = 8.8, 2.3 Hz); 7.62 (d, 1H, *J* = 8.8 Hz); 7.25 (m 4H); 4.15 (t, 2H, *J* = 7.1 Hz); 3.07 (t, 2H, *J* = 7.3 Hz). MS-APCI: Calc. for C₁₅H₁₂N₂O₃S: 301.1, Found: 301.3 [M+H⁺]. ¹³C-NMR (75 MHz, CDCl₃) δ: 164.0; 146.3; 146.2; 137.3; 128.9; 128.8; 127.2; 126.2; 125.2; 122.7; 121.3; 45.9; 35.6. HPLC purity: *t*R 8.45 min - 99.2%. Melting point = 140° C.

6-Nitro-2-phenethylbenzo[d]isothiazol-3(2H)-one 24: Starting from compound **22b** (163 mg, 0.75 mmol) and 2-phenethylamine, the desired product is obtained, according to method G, as yellow crystals (19 mg, 30%), after purification by FC (SiO₂ Hex/EtOAc 65:35) and crystallization from DCM/*n*-hexane. ¹H-NMR (300 MHz, CDCl₃) δ: 8.45 (d, 1H, *J* = 1.38 Hz); 8.23 (dd, 1H, *J* = 8.61, 1.77 Hz); 8.18 (d, 1 H, *J* = 8.58 Hz); 7.31 (m 4H); 4.20 (t, 2H, *J* = 7.14, Hz); 3.11 (t, 2H, *J* = 7.32 Hz). MS-APCI: Calc. for C₁₅H₁₂N₂O₃S: 301.1, Found: 301.1 [M+H⁺]. Anal. Calc. for C₁₅H₁₂N₂O₃S: C, 59.99; H, 4.03; N, 9.33; Found: C, 59.94; H, 3.94; N, 9.06.

5-Methoxy-2-phenethylbenzo[d]isothiazol-3(2H)-one 25: Starting from compound **22c** (668 mg, 3.3 mmol) and 2-phenethylamine, the desired product is obtained, according to method G, as brown crystals (500 mg, 55%), after purification by FC (SiO₂ Hex/EtOAc 80:20) and crystallization from DCM/*n*-hexane. ¹H-NMR (300 MHz, CDCl₃) δ: 7.45 (d, 1H, *J* = 2.5 Hz); 7.35 (d, 1H, *J* = 8.8 Hz); 7.30-7.16 (m, 6H); 4.09 (t, 2H, *J* = 7.3 Hz); 3.84 (s, 3H); 3.03 (t, 2H *J* = 7.7 Hz). ¹³C-NMR (75 MHz, CDCl₃) δ: 165.4; 158.4; 137.9; 132.1; 129.0; 128.7; 126.9; 125.7; 122.5; 121.3; 107.8; 55.8; 45.6; 35.7. MS-APCI: Calc. for C₁₅H₁₂N₂O₃S: 286.1, Found: 286.2 [M+H⁺]. HPLC purity: *t*R 13.03 min - 98.5%

6-Methoxy-2-phenethylbenzo[d]isothiazol-3(2H)-one 26: Starting from compound **22d** (1.2 g, 5.7 mmol) and 2-phenethylamine, the desired product is obtained, according to method G, as brown crystals (678 mg, 42%), after purification by FC (SiO₂ Hex/EtOAc 70:30) and crystallization from DCM/*n*-hexane. ¹H-NMR (400 MHz, CDCl₃) δ: 7.93 (d, 1H, *J* = 8.6 Hz); 7.32-7.26 (m, 5H); 6.98-6.94 (m, 2H); 4.11 (t, 2H, *J* = 7.3 Hz); 3.90 (s, 3H); 3.07 (t, 2H, *J* = 7.3 Hz). ¹³C-NMR (100 MHz, CDCl₃) δ: 165.2; 162.9; 142.5; 138.0; 129.0; 128.7; 127.8; 126.8; 117.9; 114.7; 103.1; 55.8; 45.4; 35.8. MS-APCI: Calc. for C₁₅H₁₂N₂O₃S: 286.1, Found: 286.1 [M+H⁺]. HPLC purity: *t*R 9.1 min - 99.9%

7-Methyl-2-phenethylbenzo[d]isothiazol-3(2H)-one 27: Starting from compound **22e** (309 mg, 1.2 mmol) and 2-phenethylamine, the desired product is obtained, according to method G, as a brown solid (40 mg, 19%), after purification by FC (SiO₂ Hex/EtOAc 70:30 and Hex/EtOAc 50:50). ¹H-NMR (300 MHz, CDCl₃) δ: 7.88 (dd, 1H, *J* = 7.1, 1.0 Hz); 7.37-7.22 (m, 8H); 4.15 (t, 2H, *J* = 7.5 Hz); 3.09 (t, 2H, *J* = 7.29 Hz); 2.34 (s, 3H). ¹³C-NMR: (75 MHz, CDCl₃) δ: 165.9; 140.4; 137.8; 131.9; 129.9; 128.9; 128.7; 126.8; 126.0; 124.5; 124.1; 45.5; 36.8; 18.7. MS-ESI: Calc. for C₁₆H₁₅NOS: 270.1, Found: 270.2 [M+H⁺]. HPLC purity: *t*R 11.2 min - 97.8%

General method H: synthesis of final product 28-29. Compound **25-26** is dissolved under nitrogen atmosphere in dry benzene at 0°C. BBr₃ (2.1 eq.) is dropwise carefully added and the reaction turned deep brown. The mixture is warmed to r.t. and refluxed for 1 hour; finally is cooled to r.t. and stirred for an additional hour. The reaction is quenched with water and EtOAc is added. The organic and the aqueous phases are separated, the organic layer is washed with water and the aqueous layer is washed several times with EtOAc. The organic phases are collected, dried over Na₂SO₄ and the solvent is removed under reduced pressure. The crude product is subjected to flash column chromatography with an appropriate eluent mixture and to crystallization to furnish the purified product.

5-Hydroxy-2-phenethylbenzo[d]isothiazol-3(2H)-one 28: Starting from 5-methoxy-2-phenethylbenzo[d]isothiazol-3(2H)-one **25** (99 mg, 0.35 mmol) after purification by FC (SiO₂ Hex/EtOAc 50:50) and crystallization from EtOH/H₂O final product (33 mg, 35%) is obtained as a light yellow powder, according to method H. ¹H-NMR (300 MHz, CDCl₃) δ: 7.70 (d, 1H, *J* = 2.37 Hz); 7.40 (d, 1H, *J* = 8.67, Hz); 7.28 (m, 6H); 4.14 (t, 2H, *J* = 7.35 Hz); 3.08 (t, 2H, *J* = 7.68 Hz). MS-APCI: Calc. for C₁₅H₁₃NO₂S: 272.1, Found: 272.3 [M+H⁺]. Anal. Calc. for C₁₅H₁₃NO₂S: C, 66.40; H, 4.83; N, 5.16; Found: C, 66.70; H, 4.97; N, 4.94.

6-Hydroxy-2-phenethylbenzo[d]isothiazol-3(2H)-one 29: Starting from 6-methoxy-2-phenethylbenzo[d]isothiazol-3(2H)-one **26** (200 mg, 0.70 mmol) after purification by FC (SiO₂ Hex/EtOAc 50:50) final product (47 mg, 25%) is obtained as a light yellow powder, according to method H. ¹H-NMR (300 MHz, MeOD) δ: 7.74 (d, 1H, *J* = 8.64 Hz); 7.26-7.18 (m, 5H); 7.02 (d, 1H, *J* = 2.01 Hz); 6.87 (dd, 1H, *J* = 2.01, 8.64 Hz); 4.07 (t, 2H, *J* = 7.35 Hz); 3.03 (t, 2H, *J* = 7.68 Hz). MS-APCI: Calc. for C₁₅H₁₃NO₂S: 272.1, Found: 272.3 [M+H⁺]. HPLC purity: *t*R 7.0 min - 99.3%. Melting point = 172°C.

6-Ethoxy-2-phenethylbenzo[d]isothiazol-3(2H)-one 30: To a 0°C suspension of compound **29** (125 mg, 0.52 mmol) in dry MeCN (7ml), K₂CO₃ (71 mg, 0.62 mmol) is slowly added. After few minutes to the solution is added EtBr (40 μl, 0.62 mmol). The mixture is gradually warmed to 30°C and stirred overnight. Once the reaction is complete the solvent is removed under reduced pressure. The residue is portioned between water and DCM (15 ml) and the organic phase is washed with water (3 * 15 ml), dried over Na₂SO₄, filtered and the solvent evaporated under reduced pressure affording 135mg of a brown oil. The residue is purified by FC (SiO₂ Hex/EtOAc 70:30) to give 114 mg of pure product (yield = 74%). The product was crystallized from *n*-hexane giving 77 mg of white crystals (yield after crystallization = 50%). ¹H-NMR (300 MHz, CDCl₃) δ: 7.92 (d, 1H, *J* = 8.64 Hz); 7.30 (m, 5H); 6.94 (m, 5H); 4.15 (m, 4H); 3.06 (t, 2H, *J* = 7.68 Hz); 1.47 (t, 3H, *J* = 6.96 Hz). MS-APCI: Calc. for C₁₇H₁₇NO₂S: 300.1, Found: 300.2 [M+H⁺]. HPLC purity: *t*R 11.1 min - 96.0%. Melting point = 107°C.

***Tert*-butyl (3-oxobenzo[d]isothiazol-2(3H)-yl)carbamate 31:** Starting from *tert*-butyl hydrazinecarboxylate and 2,2'-disulfanediyldibenzoyl chloride **7** (620 mg, 1.80 mmol), according to method G, the desired product is obtained after purification by FC (SiO₂ Hex/EtOAc 60:40) as a pale yellow solid (865 mg, 90%). ¹H-NMR (300 MHz, CDCl₃) δ: 8.07 (d, 1H, *J* = 7.9 Hz), 7.67 (t, 1H, *J* = 8.2 Hz); 7.51 (d, 1H, *J* = 8.1 Hz); 7.41 (t, 1H, *J* = 7.3 Hz); 7.06 (bs, 1H); 1.51 (s, 9H); Melting point = 170° C

General method I: Synthesis of intermediates 32-d, 37a-b To a 0°C solution of compound **31** in dry DMF is portionwise added KHMDS (1.2 eq.). The reaction is stirred under nitrogen atmosphere for 10 minutes before a solution of the corresponding alkyl halide in dry DMF is added. The solution is gradually warmed to r.t. and stirred for 16 hours. The solvent is removed under reduced pressure and to the residue is added a PH 7 phosphate buffer and extracted 3 times with EtOAc. The organic phase is dried over Na₂SO₄, filtered and the solvent evaporated under reduced pressure affording the crude product that is subjected to flash column chromatography with an appropriate eluent mixture to furnish the purified product.

Tert-butyl benzyl(3-oxobenzo[*d*]isothiazol-2(3*H*)-yl)carbamate 32a: Starting from compound **31** (700 mg, 2.62 mmol) and benzylbromide (0.38 ml, 3.15 mmol) product **32a** (586 mg, 62%) is obtained as a white solid after purification by FC (SiO₂ Hex/EtOAc 80:20), according to method I. ¹H-NMR (300 MHz, CDCl₃) δ: 8.04 (d, 1H, *J* = 8.5 Hz); 7.57 (d, 1H, *J* = 8.3 Hz); 7.27 (m, 7H); 5.28 (d, 1H, *J* = 14.7 Hz); 4.49 (d, 1H, *J* = 14.8 Hz); 1.41 (bs, 9H).

Methyl 4-(((tert-butoxycarbonyl)(3-oxobenzo[*d*]isothiazol-2(3*H*)-yl)amino)methyl)benzoate 32b: Starting from compound **31** (213 mg, 0.80 mmol) and methyl 4-(bromomethyl)benzoate after purification by FC (SiO₂ Hex/EtOAc 80:20), product **32b** (237 mg, 71%) is obtained as a yellow oil, according to method I. ¹H-NMR (400 MHz, CDCl₃) δ: 8.01 (m, 3H), 7.58 (t, 1H, *J* = 7.2 Hz); 7.43 (d, 2H, *J* = 8.0 Hz); 7.34 (m, 2H); 5.25 (bd, 1H, *J* = 17.5 Hz); 4.56 (bd, 1H, *J* = 15.0 Hz); 3.89 (s, 3H); 1.41 (bs, 9H). ¹³C-NMR (100 MHz, CDCl₃) δ: 166.8; 141.0; 140.8, 132.9, 130.0, 129.9; 129.8; 128.8; 127.3; 125.5; 121.8; 120.5; 51.2; 28.1.

Tert-butyl 4-(((tert-butoxycarbonyl)(3-oxobenzo[*d*]isothiazol-2(3*H*)-yl)amino)methyl)benzoate 32c: Starting from compound **31** (163 mg, 0.6 mmol) and *tert*-butyl 4-(bromomethyl)benzoate after purification by FC (SiO₂ Hex/EtOAc 90:10), product **32c** (150 mg, 54%) is obtained as a yellow oil, according to method I. ¹H-NMR (300 MHz, CDCl₃) δ: 8.01 (d, 1H, *J* = 7.8 Hz); 8.94 (d, 2H, *J* = 8.2 Hz); 7.57 (t, 1H, *J* = 7.3 Hz); 7.41-7.31 (m, 4H); 5.25 (bd, 1H, *J* = 14.0 Hz); 4.55 (bd, 1H, *J* = 15.0 Hz); 1.56 (s, 9H); 1.40 (bs, 9H).

Tert-butyl ([1,1'-biphenyl]-4-ylmethyl)(3-oxobenzo[*d*]isothiazol-2(3*H*)-yl)carbamate 32d: Starting from compound **31** (179 mg, 0.7 mmol) and 4-(bromomethyl)-1,1'-biphenyl after purification by FC (SiO₂ Hex/EtOAc 90:10), product **32d** (220 mg, 76%) is obtained as a white solid, according to method I. ¹H-NMR (300 MHz, CDCl₃) δ: 8.04 (d, 1H, *J* = 7.4); 7.60-7.55 (m, 5H); 7.45-7.25 (m, 7H); 5.30 (bd, 1H, *J* = 16.1 Hz); 4.53 (bd, 1H, *J* = 14.9); 1.45 (bs, 9H).

Di-*tert*-butyl pentane-1,5-diylbis((3-oxobenzo[*d*]isothiazol-2(3*H*)-yl)carbamate) 37a: Starting from compound **31** (500 mg, 1.9 mmol) and 1,5-diiodopentane (167 μl, 1.1 mmol) after purification by FC (SiO₂ Hex/EtOAc 70:30), product **37a** (294 mg, 52%) is obtained as a light yellow solid, according to method I. ¹H-NMR (400 MHz, CDCl₃) δ: 8.00 (d, 2H, *J* = 7.8 Hz); 7.60 (t, 2H, *J* = 7.6 Hz); 7.44 (d, 2H, *J* = 8.1 Hz); 7.34 (t, 2H, *J* = 7.5 Hz); 3.75-3.60 (m, 4H); 1.69-1.35 (m, 24H).

Di-*tert*-butyl exane-1,5-diylbis((3-oxobenzo[*d*]isothiazol-2(3*H*)-yl)carbamate) 37b: Starting from compound **31** (500 mg, 1.9 mmol) and 1,6-diiodoexane after purification by FC (SiO₂ Hex/EtOAc 80:20), product **37b**

(327 mg, 57%) is obtained as a white sponge, according to method I. ¹H-NMR (400 MHz, CDCl₃) δ: 8.00 (d, 2H, *J* = 7.8 Hz); 7.60 (t, 2H, *J* = 7.3 Hz); 7.44 (d, 2H, *J* = 8.1 Hz); 7.34 (t, 2H, *J* = 7.6 Hz); 3.72 (q, 2H, *J* = 7.4 Hz); 3.57 (q, 2H, *J* = 7.4 Hz); 1.66-1.36 (m, 26H).

General method J: synthesis of final compounds 33-36, 38-39. To a solution of the corresponding precursor **32a-d**, **37a-b** in DCM is dropwise added TFA (25 eq.) at 0°C. The reaction is gently warmed to r.t. and stirred for four hours. The solvent is removed under reduced pressure and the residue is dissolved in EtOAc and washed twice with NaHCO₃ aqueous saturated solution and once with brine. The organic phase is dried over Na₂SO₄, filtered and the solvent evaporated under reduced pressure affording the crude product that is subjected to flash column chromatography with an appropriate eluent mixture to furnish the purified product.

2-(Benzylamino)benzo[*d*]isothiazol-3(2*H*)-one 33: Starting from intermediate **32a** (400 mg, 1.12 mmol) after purification by FC (SiO₂ DCM/EtOAc 97:3) and crystallization from *n*-hexane final product (200 mg, 70%) is obtained as white crystals, according to method J. ¹H-NMR (300 MHz, DMSO) δ: 7.83 (t, 2H, *J* = 8.5 Hz); 7.64 (t, 1H, *J* = 7.2 Hz); 7.32 (m, 6H); 6.76 (t, 1H, *J* = 4.1 Hz); 4.19 (d, 2H, *J* = 4.0 Hz). ¹³C-NMR (75 MHz, DMSO) δ: 168.8; 144.9; 142.8; 137.3; 134.0; 133.4; 132.6; 130.8; 130.5; 128.8; 127.0; 59.2. MS-APCI: Calc. for C₁₄H₁₂N₂O₃: 257.3, Found: 257.2 [M+H⁺]. Anal. Calc. for C₁₄H₁₂N₂O₃: C, 65.60; H, 4.72; N, 10.93; Found: C, 65.47; H, 4.71; N, 10.79. Melting point = 110°C.

Methyl 4-(((3-oxobenzo[*d*]isothiazol-2(3*H*)-yl)amino)methyl)benzoate 34: Starting from intermediate **32b** (237 mg, 0.57 mmol) after purification by FC (SiO₂ Hex/EtOAc 70:30) and crystallization from DCM/Hex final product (90 mg, 50%) is obtained as white crystals, according to method J. ¹H-NMR (300 MHz, CDCl₃) δ: 8.00 (m, 3H); 7.60 (t, 1H, *J* = 7.3 Hz); 7.50 (d, 2H, *J* = 8.2 Hz); 7.38 (m, 2H); 5.41 (bs, 1H); 4.36 (s, 1H); 3.90 (s, 3H). ¹³C-NMR (75 MHz, CDCl₃) δ: 167.0; 164.9; 141.6; 139.7; 132.3; 129.9; 129.9; 129.2; 126.6; 125.5; 123.3; 120.4; 55.0; 52.2. MS-ESI: Calc. for C₁₆H₁₄N₂O₃S: 315.3, Found: 315.2 [M+H⁺]. HPLC-UV *t*R purity: 6.6 min – 98.9%. Melting point = 174 - 176°C.

4-(((3-Oxobenzo[*d*]isothiazol-2(3*H*)-yl)amino)methyl)benzoic acid 35: Starting from intermediate **32c** (150 mg, 0.3 mmol) after purification by FC (SiO₂ Hex/EtOAc 40:60) final product (60 mg, 61%) is obtained as a white powder, according to method J. ¹H-NMR (300 MHz, CD₃COOD) δ: 8.04 (d, 3H, *J* = 8.2 Hz); 7.61 (m, 4H); 7.44 (dt, 1H, *J* = 8.0, 1.8 Hz); 4.40 (s, 2H). ¹³C-NMR (75 MHz, CD₃COOD) δ: 172.7; 167.2; 144.6; 141.6; 134.2; 131.8; 130.8; 130.5; 120.0; 127.3; 124.6; 122.1; 55.8. MS-ESI: Calc. for C₁₅H₁₂N₂O₃S: 301.1, Found: 301.3 [M+H⁺]. HPLC-UV purity: *t*R 7.1 min - 96%

2-(((1'-Biphenyl)-4-ylmethyl)amino)benzo[*d*]isothiazol-3(2*H*)-one 36: Starting from intermediate **32d** (220mg, 0.5 mmol) after purification by FC (SiO₂ Hex/EtOAc 70:30) final product (98 mg, 60%) is obtained as a white powder, according to method J. ¹H-NMR (300 MHz, CDCl₃) δ: 8.03 (d, 1H, *J* = 7.9 Hz); 7.60-7.33 (m, 12H); 5.02 (bs, 1H); 4.35 (s, 2H). ¹³C-NMR (75 MHz, CDCl₃) δ: 164.8; 140.9; 140.8; 139.7; 135.4; 132.2; 129.7; 128.8; 127.6; 127.5; 127.2; 126.6; 125.5; 120.4; 55.2; MS-APCI: Calc. for C₂₀H₁₆N₂O₃: 333.4, Found: 333.3 [M+H⁺]. HPLC-UV purity: *t*R 14.9 min – 99.9%

2,2'-(Pentane-1,5-diylbis(azanediyl))bis(benzo[*d*]isothiazol-3(2*H*)-one) 38: Starting from intermediate **37a** (294 mg, 0.5 mmol) after purification by FC (SiO₂/Hex/EtOAc 30:70) final product (146 mg, 75%) is obtained as a white solid, according to method J. ¹H-NMR (300 MHz, CDCl₃) δ: 8.00 (d, 2H, *J* = 7.8 Hz); 7.60 (t, 2H, *J* = 7.6 Hz); 7.47 (d, 1H *J* = 8.0 Hz); 7.37 (t, 2H, *J* = 7.5 Hz); 4.58 (bs, 2H); 3.15 (t, 4H, *J* = 6.6 Hz); 1.64-1.48 (m, 6H). ¹³C-NMR (75 MHz, CDCl₃) δ: 164.6; 139.4; 132.1; 126.6; 125.5; 123.7; 120.4; 51.4; 27.4; 24.3. MS-ESI: Calc. for C₁₉H₂₀N₄O₂S₂: 401.1, Found: 401.5 [M+H⁺]. HPLC purity: *t*R 5.6 min - 98.8%

2,2'-(Exane-1,5-diylbis(azanediyl))bis(benzo[*d*]isothiazol-3(2*H*)-one) 39: Starting from intermediate **37b** (327 mg, 0.5 mmol) after purification by FC (SiO₂/Hex/EtOAc 20:80) final product (103mg, 48%) is obtained as a white solid, according to method J. ¹H-NMR (400 MHz, CDCl₃) δ: 8.03 (d, 2H, *J* = 7.9 Hz); 7.62 (t, 2H, *J* = 7.6 Hz); 7.51 (d, 2H, *J* = 8.0 Hz); 7.40 (t, 2H, *J* = 7.5 Hz); 4.15 (bs, 2H); 3.17 (t, 2H, *J* = 6.6 Hz); 1.62-1.44 (m, 8H). ¹³C-NMR (100 MHz, CDCl₃) δ: 164.6; 139.5; 132.1; 126.6; 125.5; 123.7; 120.5; 51.5; 27.5; 26.8. MS-ESI: Calc. for C₂₀H₂₂N₄O₂S₂: 415.1, Found: 415.4 [M+H⁺]. HPLC purity: *t*R 7.2 min - 99.1%

2-(Benzyl(methyl)amino)benzo[*d*]isothiazol-3(2*H*)-one 40: To a solution of **33** (58 mg, 0.23 mmol) in MeI (0.7 ml, 11.18 mmol), imidazole (16 mg, 0.24 mmol) is added in one portion. The solvent is evaporated under reduced pressure and the residue is purified by FC (SiO₂/DCM/MeOH 99:1) affording 39 mg (yield = 64%) of product as a pale yellow waxy solid. ¹H-NMR (300 MHz, CDCl₃) δ: 8.00 (d, 1H, *J* = 7.9 Hz); 7.58 (td, 1H, *J* = 8.0, 1.2 Hz); 7.44 (d, 1H, *J* = 8.0 Hz); 7.25-7.35 (m, 4H); 4.24 (s, 2H); 2.95 (s, 3H). MS-APCI: Calc. for C₁₅H₁₄N₂OS: 271.1, Found: 271.3 [M+H⁺]. Anal. Calc. for C₁₅H₁₄N₂OS: C, 66.64; H, 5.22; N, 10.36; Found: C, 66.87; H, 5.46; N, 9.84. Melting point = 142°C.

(2*R*,4*a*S,6*a*S,12*b*R,14*a*S,14*b*R)-methyl 10-hydroxy-2,4*a*,6*a*,9,12*b*,14*a*-hexamethyl-11-oxo-1,2,3,4,4*a*,5,6,6*a*,11,12*b*,13,14,14*a*,14*b*-tetradecahydronicene-2-carboxylate 42:

Commercially available compound **41** (celastrol) (80 mg, 0.2 mmol) is dissolved in dry DMF at 0°C under nitrogen atmosphere. NaHCO₃ (44 mg, 0.5 mmol) and MeI (56 μl, 0.9 mmol) are added and the mixture stirred overnight under nitrogen and protected from light. To the reaction are added DEE (10 ml) and Ammonium chloride saturated solution (10 ml) and aqueous phase is washed 5 times with DEE. Organic phases are collected and washed with water (20 ml) and brine (20 ml). The organic phase is dried over Na₂SO₄ and the solvent evaporated under reduced pressure affording 102 mg of an orange oil. The residue was purified by FC (SiO₂/Hex/EtOAc 85:15) giving 61 mg of an orange solid (yield = 74%). ¹H-NMR (400 MHz, CDCl₃) δ: 7.00 (d, 1H, *J* = 7.0 Hz); 6.52 (s, 1H); 6.33 (d, 1H, *J* = 7.2 Hz); 3.54 (s, 3H); 2.40 (d, 1H, *J* = 15.7 Hz); 2.23 (s, 3H); 2.19-2.00 (m, 6H); 1.89-1.32 (m, 13H); 1.25 (s, 3H); 1.16 (s, 3H); 1.08 (s, 3H); 0.95 (d, 1H, *J* = 14 Hz); 0.52 (s, 3H). ¹³C-NMR (75 MHz, CDCl₃) δ: 178.8, 178.3, 170.3, 164.9, 146.1, 134.2, 127.5, 126.7, 119.6, 118.2, 117.3, 51.6, 45.1, 44.4, 43.0, 40.7, 40.5, 39.5, 38.3, 36.5, 34.9, 33.6, 32.8, 31.7, 30.8, 31.0, 30.6, 30.0, 29.7, 28.7, 21.7, 18.4, 10.3. APCI-MS Calc. for C₃₀H₄₀NO₄: 465.3, Found: 465.4 [M+H⁺]. HPLC-UV purity: *t*R 6.03 min - 99.9%.

2*R*,4*a*S,6*a*S,12*b*R,14*a*S,14*b*R)-phenethyl 10-hydroxy-2,4*a*,6*a*,9,12*b*,14*a*-hexamethyl-11-oxo-1,2,3,4,4*a*,5,6,6*a*,11,12*b*,13,14,14*a*,14*b*-tetradecahydronicene-2-carboxylate 45:

Commercially available compound **41** (celastrol) (50 mg, 0.1 mmol) is dissolved in dry DMF under nitrogen atmosphere. NaHCO₃ (28 mg, 0.3 mmol) and phenethylbromide (75 µl, 0.6 mmol) are added and the mixture stirred overnight under nitrogen and protected from light. To the reaction are added DEE (10 ml) and Ammonium chloride saturated solution (10 ml) and aqueous phase is washed 5 times with DEE. Organic phases are collected and washed with water (20 ml) and brine (20 ml). The organic phase is dried over Na₂SO₄ and the solvent evaporated under reduced pressure affording 200 mg of an orange oil. The residue was purified by FC (SiO₂ Hex/EtOAc 90:10) giving 54 mg of an orange solid (yield = 88%). ¹H-NMR (400 MHz, CDCl₃) δ: 7.33-7.20 (m, 5H); 7.04 (d, 1H, *J* = 7.1 Hz); 6.54 (s, 1H); 6.34 (d, 1H, *J* = 7.1 Hz); 4.25 (dt, 1H, *J* = 10.9, 6.7 Hz); 4.03 (dt, 1H, *J* = 11.0, 6.6 Hz); 2.90 (t, 2H, *J* = 6.6 Hz); 2.36 (d, 1H, *J* = 15.9 Hz); 2.23 (s, 3H); 2.20-1.83 (m, 5H); 1.71-1.25 (m, 14H); 1.15 (s, 3H); 1.10 (s, 3H); 0.94 (d, 1H, *J* = 13.9 Hz); 0.43 (s, 3H). ¹³C-NMR: (75 MHz, CDCl₃): 178.4, 170.4, 164.9, 146.1, 138.2, 134.3, 129.0, 128.6, 127.5, 126.7, 119.7, 118.2, 117.3, 65.2, 45.1, 44.4, 43.1, 40.5, 39.5, 38.4, 36.5, 34.9, 33.7, 32.8, 31.7, 30.9, 30.5, 29.9, 29.6, 28.7, 21.7, 18.5, 10.4. APCI-MS Calc. for C₃₇H₄₆NO₄: 555.3, Found: 555.4 [M+H⁺]. HPLC-UV purity: *t*R 5.27 min – 99.9%

(2R,4aS,6aS,12bR,14aS,14bR)-10-hydroxy-N,2,4a,6a,9,12b,14a-heptamethyl-11-oxo-1,2,3,4,4a,5,6,6a,11,12b,13,14,14a,14b-tetradecahydronicene-2-carboxamide 46:

Commercially available compound **41** (celastrol) (50 mg, 0.1 mmol) is dissolved in dry DMF at 0°C under nitrogen atmosphere. DIPEA (38 µl, 0.2 mmol) and HATU (42 mg, 0.1 mmol) are added and the mixture stirred for 15 min. Methylamine solution 2.0M in THF (111 µl, 0.2 mmol) is added and the reaction is stirred overnight under nitrogen and protected from light. To the reaction are added DEE (10 ml) and ammonium chloride saturated solution (10 ml) and aqueous phase is washed 5 times with DEE. Organic phases are collected and washed with water (20 ml) and brine (20 ml). The organic phase is dried over Na₂SO₄ and the solvent evaporated under reduced pressure affording 75 mg of an orange oil. The residue was purified by FC (SiO₂ Hex/EtOAc 30:70) giving 34 mg of an orange solid (yield = 66%). ¹H-NMR: (400 MHz, CDCl₃) δ: 7.01 (dd, 1H, *J* = 1.2, 7.1 Hz); 6.54 (d, 1H, *J* = 1.2 Hz); 6.34 (d, 1H, *J* = 7.2 Hz); 5.75 (d, 1H, *J* = 4.1 Hz); 2.67 (d, 3H, *J* = 4.6 Hz); 2.44 (d, 1H, *J* = 14.1 Hz); 2.20 (s, 3H); 2.16-1.48 (m, 13H); 1.43 (s, 3H); 1.25 (s, 3H); 1.14 (s, 3H); 1.12 (s, 3H); 1.01 (d, 1H, *J* = 14.0 Hz); 0.61 (s, 3H). ¹³C-NMR (100 MHz, CDCl₃) δ: 178.5, 178.2, 164.9, 146.1, 134.4, 127.5, 119.6, 118.2, 117.4, 45.2, 44.5, 43.2, 40.4, 39.5, 38.3, 36.5, 35.1, 33.7, 33.6, 31.7, 31.7, 31.4, 31.0, 30.2, 29.6, 28.8, 26.5, 21.8, 18.2, 10.4. APCI-MS Calc. for C₃₀ H₄₁NO: 464.3, Found: 464.4 [M+H⁺]. HPLC-UV purity: *t*R 3.4 min – 97.3%.

(2R,4aS,6aS,12bR,14aS,14bR)-10-hydroxy-2,4a,6a,9,12b,14a-hexamethyl-11-oxo-N-phenethyl-1,2,3,4,4a,5,6,6a,11,12b,13,14,14a,14b-tetradecahydronicene-2-carboxamide 47:

Commercially available compound **41** (celastrol) (50 mg, 0.1 mmol) is dissolved in dry DMF at 0°C under nitrogen atmosphere. DIPEA (38 µl, 0.2 mmol) and HATU (42 mg, 0.1 mmol) are added and the mixture stirred for 15 min. Phenethylamine (27 µl, 0.2 mmol) is added and the reaction is stirred overnight under nitrogen and protected from light. To the reaction are added DEE (10 ml) and Ammonium chloride saturated solution (10 ml) and aqueous phase is washed 5 times with DEE. Organic phases are collected and washed with water (20 ml) and brine (20 ml). The organic phase is dried over Na₂SO₄ and the solvent evaporated under reduced pressure affording 60 mg of an orange oil. The residue was purified by FC (SiO₂ Hex/EtOAc 65:45) giving 46 mg of an orange solid (yield = 78%). ¹H-NMR (400 MHz, CDCl₃) δ: 7.30 (m, 2H); 7.23 (m,

1H); 7.16 (d, 2H, $J = 7.0$ Hz); 7.04 (d, 1H, $J = 7.0$ Hz); 6.56 (s, 1H); 6.35 (d, 1H, $J = 7.2$ Hz); 5.71 (t, 1H, $J = 4.1$ Hz); 3.39 (q, 2H, $J = 6.7$ Hz); 2.76 (t, 2H, $J = 6.8$ Hz); 2.40 (d, 1H, $J = 14.5$ Hz); 2.23 (s, 3H); 2.12 (dd, 1H, $J = 3.9$, 13.9 Hz); 1.90-1.78 (m, 5H); 1.66-1.44 (m, 10H); 1.30-1.25 (m, 4H); 1.20 (s, 3H); 1.10 (s, 3H); 0.92 (d, 1H, $J = 7.1$ Hz); 0.55 (s, 3H). ^{13}C -NMR (75 MHz, CDCl_3) δ : 178.3, 177.7, 170.6, 164.9, 146.1, 139.0, 134.2, 128.8, 128.8, 127.5, 126.7, 119.6, 118.1, 117.2, 45.1, 44.4, 43.1, 40.7, 40.4, 39.4, 38.2, 36.4, 35.3, 35.0, 33.8, 33.6, 31.7, 31.1, 30.8, 30.2, 29.5, 28.7, 21.8, 18.4, 10.4. APCI-MS Calc. for $\text{C}_{37}\text{H}_{47}\text{NO}_3$: 554.3, Found: 554.3 $[\text{M}+\text{H}^+]$. HPLC-UV purity: t_R 4.7 min – 97.6%.

5.1.2 Pharmacology

Collected biological data were from experimentations carried out by Prof. Piomelli's research group (Departments of Anatomy and Neurobiology, Pharmacology and Biological Chemistry, University of California Irvine Irvine, CA, USA)

MGL Cloning. Rat MGL cDNA was cloned out of the pBluescript-SK vector using the following primers: 5'-CGCGGCAGCCATATGCTGAGGCAAGTTCACC (forward primer) and 5'-AGCAGCCGGATCCTCTCAGGGTAGACACCTAG (reverse primer). These primers introduced a BamHI and an NdeI endonuclease restriction site at the 5' and 3' end of the cDNA, respectively. Platinum Pfx DNA polymerase (Invitrogen, Carlsbad, CA) was used to run the polymerase chain reaction (PCR), followed by BamHI/NdeI double digest of the PCR product and the pET15b vector (Novagen, La Jolla, CA) containing an n-terminal histidine tag. The vector and the PCR product were ligated using T4 DNA ligase (Promega, Madison, WI) following the dephosphorylation of the pET15b vector DNA. The ligation setup was transformed into DH5 α E.coli cells and plated on a Luria Broth agar plate containing 50 $\mu\text{g}/\text{ml}$ ampicillin. Ten colonies were selected and their plasmid DNAs were purified according to the QIAGEN plasmid DNA miniprep Kit protocol (QIAGEN, Valencia, CA). Restriction digest analysis resulted in four positive clones, which were subjected to DNA sequencing, confirming the correct sequence.

MGL Expression and Purification. Clone 2 was expressed in Rosetta 2(DE3)pLysS E. coli cells (Novagen) at 37°C using 1 mM isopropyl-beta-D-thiogalactopyranoside (IPTG). This clone was used for all subsequent protein expression experiments. 4 L of LB + 50 $\mu\text{g}/\text{ml}$ ampicillin were inoculated with 40 ml of overnight culture of Rosetta 2(DE3)pLysS cells transformed with pET15b/MGL grown in LB + 50 $\mu\text{g}/\text{ml}$ ampicillin. Cells were grown at 37°C until the optical density (OD) at 600 nm reached 0.8. At this point, addition of IPTG to a final concentration of 1 mM induced MGL overexpression. After 4 h, the cells were harvested by centrifugation at 6,000g for 15 min and the bacterial pellet was resuspended in 100 ml of lysis buffer (50 mM HEPES pH 7.4, 300 mM NaCl, 10 mM MgCl_2 , 10 μM E-64 and 10 $\mu\text{g}/\text{ml}$ aprotinin). The cells were lysed using a French press and the cell lysate centrifuged at 3,000g for 1 h at 4°C to separate the membrane fraction from the cell debris. The supernatant (membrane fraction) was then subjected to another centrifugation at 35,000g for 1 h at 4°C. The pellet was resuspended in 50 mM HEPES pH 7.4., 300 mM NaCl, 3 mM β -mercaptoethanol, 1% Triton X-100, stirred for about 30 min, and centrifuged again at 5,000g for 1 h at 4°C. The supernatant was loaded onto a TALON column (Clontech, Mountain View, CA) equilibrated with 50 mM HEPES pH 7.4, 300 mM NaCl, 3 mM β -mercaptoethanol, 0.1% Triton X-100 (buffer A). The column was

washed with 5 volumes of buffer A, and the protein subsequently eluted from the column using a step gradient of imidazole ranging from 10 to 200 mM imidazole in buffer A (5 column volumes each). The protein eluted at about 75 mM imidazole.

MGL assay. Either 10 ng of purified MGL or 2.5–50 μ g of protein from MGL-transfected HeLa cell lysates were preincubated with inhibitors for 10 min at 37°C in assay buffer (50 mM Tris-HCL, pH 8.0, 0.5 mg mL⁻¹ bovine serum albumin, fatty acid-free). Following preincubation, 2-oleoylglycerol (2-OG) substrate (10 μ M final) was added, and samples were incubated for an additional 10 min at 37°C. Reactions were stopped with chloroform : methanol (2:1, vol : vol), containing heptadecanoic acid (5 nmol) as an internal standard. In some experiments with cell lysates, 1(3)heptadecanoylglycerol (1-HG) and heptadecenoic acid were used as substrate and internal standard respectively. Samples were subjected to centrifugation at 2000 \times g at 4°C for 10 min, and the organic layers were collected and dried under a stream of N₂. The residues were suspended in chloroform : methanol (1:3, vol : vol) and analysed by liquid chromatography/mass spectrometry (LC/MS).

LC/MS analysis. We used a reversed-phase Eclipse C18 column (30 \times 2.1 mm i.d., 1.8 μ M, Agilent Technologies, Wilmington, DE, USA) eluted with 95% of solvent A and 5% solvent B for 0.6 min at a flow rate of 0.6 mL.min⁻¹ with column temperature set at 50°C. Solvent A consisted of methanol containing 0.25% acetic acid and 5 mM ammonium acetate. Solvent B consisted of water containing 0.25% acetic acid and 5 mM ammonium acetate. Under these conditions, analytes eluted from the column at the following retention times: oleic acid, 0.34 min; heptadecanoic acid, 0.37 min; heptadecenoic acid, 0.29 min. Electrospray ionization was in the negative mode, capillary voltage was set at 4 Kv, and fragmentor voltage was 100 V. N₂ was used as drying gas at a flow rate of 13 L.min⁻¹ and a temperature of 350°C. Nebulizer pressure was set at 60 psi. For quantification purposes, we monitored the [M-H]⁻ ions of m/z = 281.3 for oleic acid, m/z = 269 for heptadecanoic acid, and m/z = 267 for heptadecenoic acid.

Rapid dilution assay. Samples containing of purified MGL (100-fold concentrated compared with standard assays) were preincubated with 10-fold the IC₅₀-equivalent concentration of octhilinone, MAFP or vehicle (dimethylsulphoxide, DMSO, final concentration 2%) for 20 min at 37°C. Samples were then diluted 100-fold with assay buffer containing substrate to initiate reactions, and the time course of product formation was measured by LC/MS.

Site direct mutagenesis. A full-length rat MGL cDNA was subcloned into the pEF6/V5-His vector (Invitrogen, San Diego, CA, USA). The MGL gene was modified by using the QwikChange II XL Site-Directed Mutagenesis Kit (Stratagene, La Jolla, CA, USA) following the manufacturer's instructions. Primers were commercially synthesized (Invitrogen). Following DNA sequencing, positive clones were identified and transfected into HeLa cells by using the Superfect transfectant reagent (Qiagen, Valencia, CA, USA), following standard protocol. Cells were resuspended in ice-cold Tris-HCL (50 mM, pH 8.0) containing 0.32 M sucrose and harvested by using a cell scraper. Lysates were sonicated on ice for 1 min followed by three rounds of freeze thawing. Samples were subjected to centrifugation at 100 000 \times g at 4°C for 30 min to separate membrane (pellet) and cytosolic (supernatant) fractions.

Protein analysis. Protein concentrations were measured by using the BCA Protein Assay kit (Pierce, Rockford, IL, USA). Samples (5 μ g) were electrophoresed on a 4–20% SDS-polyacrylamide gel (Invitrogen) and transferred to a polyvinylidene difluoride membrane (Amersham, Piscataway, NJ, USA). Membranes were blocked in 10% milk and incubated in the presence of anti-V5 monoclonal antibody (1:3000, 12 h;

Invitrogen). Immunoreactive bands were visualized by using the ECL-Plus kit (Amersham), exposed to high performance chemiluminescence film (Amersham) and developed with a Mini-Medical film processor (AFP Imaging, Elmsford, NY, USA). As a loading control, membranes were stripped for 15 min at room temperature and probed again by using an anti-actin monoclonal antibody (1:10 000, 12 h; Calbiochem, La Jolla, CA, USA).

Statistical analyses. All results are expressed as mean SEM. Non-linear regression analyses were performed by using Prism (GraphPad Software Inc., La Jolla, CA, USA). Statistical significance was assessed by the Student's t-test.

5.1.3 Computational studies

Molecular Modeling. Molecular Modeling studies were performed using the Schrödinger software suite. Ligand molecules were built in Maestro 9.2² and prepared with Ligprep 2.5³; the protein structure was refined using the Protein Preparation Wizard tool⁴. Covalent docking studies were performed using Prime 3.0⁵, while docking studies were carried out with Glide 5.7^{6,7}.

Protein Preparation. The crystal structure of human MGL (PDB 3HJU, chain A) was used as model structure for docking studies. The hydrogen atoms were added, and the hydrogen bonding network was optimized by sampling the conformation of histidine, asparagine and glutamine side chains; the orientations of thiol and hydroxyl group were optimized and the protonation state of ionizable residues were adjusted to be consistent with physiological pH. The resulting structure was subjected to a restrained minimization with the OPLS2005 force field in which only hydrogen atoms were free to move. A second minimization was performed by restraining the heavy atoms until a RMSD value of 0.3 Å.

Covalent Docking Studies. The Prime Covalent Docking facility was used to perform covalent docking studies. In order to allow the accommodation of the ligands, both the attachment residue (CYS201) and residues within 8 Å of CYS201 were allowed to adjust in the loop sampling procedure. Ligands **9**, **33**, **34**, **35** and **40** were initially prepared using Ligprep 2.5, and then minimized with MacroModel 9.9⁸, applying the OPLS2005 force field⁹ to an energy gradient of 0.05 kJ mol⁻¹ Å⁻¹. 20 poses were collected for each covalent docking run and ranked according to the Prime Energy values. The top ranked poses were selected and subjected to energy minimization to an energy gradient of 0.05 kJ mol⁻¹ Å⁻¹.

Docking studies. Docking studies were performed to evaluate the binding modes of compounds **38** and **39**. The Induced Fit Docking protocol was applied in order to account for both ligands and protein flexibility during the ligand docking procedure. As a first step, a softened-potential docking was performed by applying van der Waals radii scaling factors of 0.6 and 0.5 on the non polar-atoms of the protein and the ligands, respectively. Energy grids for this first docking run were centered on Cys201 and Cys208, with the enclosing box length in X and in Y set to 10 Å and the box length in Z set to 16 Å. Ligands **38** and **39**, which were previously prepared with Ligprep 2.5 were then flexibly docked in the standard precision mode. The resulting complexes were then subjected to the protein refinement step. In this stage residues within a distance of 6 Å from any ligand pose were refined through a side-chain conformational search and finally minimized. The final step of the IFD procedure involved a further docking run of the ligands in the protein structures generated in the previous step. The complexes were evaluated according to their IFD score and

finally minimized with MacroModel 9.9, applying the OPLS2005 force field to an energy gradient of $0.05 \text{ kJ mol}^{-1} \text{ \AA}^{-1}$.

Metadynamics studies. The Protein Data Bank code used for human MGL is 3HJU¹⁰, and the used sequence comprises residues P7-A297 of the chain A. Models of MGL with C201 and C208 oxidized to sulfenic acid and of MGL with a covalent adduct of UPR1218 at C201 were built from 3HJU using Maestro 9.6². Well-tempered Metadynamics¹¹ simulations were performed using Desmond 3.4¹². Each system comprises a portion of POPC membrane bilayer, using the coordinates provided by the Orientation of Protein in Membranes (OPM) database¹³. The protein membrane systems are solvated with spc water molecules, in a simulation box including approximately 95000 atoms. The OPLS2005 force field was used to model the system. The system was relaxed using a modified version of a membrane relaxation protocol implemented in the Desmond package. The equilibration phase was then followed by 100ns well-tempered metadynamics performed in the NPT ensemble at 300K and 1 atm, using the Langevin coupling system. Bond lengths to hydrogens were constrained using M-SHAKE; short-range electrostatic interactions were cut off at 9 \AA , while long-range electrostatic interactions were calculated using the Smooth Particle Mesh Ewald method. A RESPA integrator was used with a time-step of 2 fs, and long-range electrostatics were computed every 6 fs. The Metadynamics method allows the enhanced sampling of the conformational space by adding to the total energy of the system an external history-dependent potential, which is a function of few degrees of freedom called Collective Variables (CVs). In this work the distances between the center of mass of carbons α (CA) of specific residues on the lid domain of MGL were used as CVs. Specifically, CV1 corresponds to the distance between the centers of mass of residues 176-179 and residues 150-157 CA, while CV2 corresponds to the distance between the centers of mass of residues 176-179 and residues 158-164 CA. The width of the Gaussians was set at 0.05 \AA ; the time interval between consecutive depositions was 0.09 ps. The well-tempered implementation involves adjusting the height of the Gaussians added; in this work the initial height was set to 0.03 kcal/mol , and the potential was adjusted by using a kT of 2.4. The convergence of the simulations performed was evaluated by analyzing the free energy difference at 5 ns intervals. Once the free energy profile stopped changing, the simulations were considered as converged. Each simulation was run for 100ns and analyzed upon convergence.

5.1.4 Reactivity studies with glutathione

Stock solutions of all reagents were purged with argon and all reactions took place under argon atmosphere removing aliquots for analysis by syringe under positive argon pressure. Reactions were initiated by injection of a 10 mM DMSO stock solution of benzisothiazolone (final concentration: 100 \mu M) into a temperature equilibrated (37.0°C) vial containing a buffered reaction solution with a 2-fold molar excess of glutathione (GSH) over benzisothiazolinone (final GSH concentration: 200 \mu M). Final concentration of DMSO was 1% v/v in 10 mM phosphate buffered saline (PBS) pH 7.4. The disappearance of reacting BTZ and the formation of corresponding reaction species was monitored by HPLC/UV using a gradient elution. Column used was a Supelco Discovery C_{18} column $150 \times 4.6 \text{ mm i.d.}$, 5 \mu m particle size (Supelco, Bellefonte, PA, USA). Eluent A: water added of 0.05% v/v trifluoroacetic acid (TFA); eluent B: methanol added of 0.05% v/v TFA. Gradient was as follows: $t(0 \text{ min})$: 95% A:5% B; $t(6 \text{ min})$: 95% A:5% B; $t(26 \text{ min})$: 5% A:95%

B; t(28 min): 5% A:95% B returning to initial conditions in 0.5 min. Total gradient time was 30 min. Absorbance was monitored at the two wavelengths of 210 and 254 nm. Flow rate was 1 mL/min. Injected volume: 10 μ L.

A Shimadzu HPLC gradient system (Shimadzu Corp., Kyoto, Japan) fitted with two LC-10AD Shimadzu pumps and a Shimadzu SPD-10 variable wavelength detector was employed for analysis. Standard curves for quantification of GSH and oxidized glutathione (GSSG) were prepared in PBS buffer and showed good linearity in the 5-500 μ M concentration range. The limit of quantification (LOQ) was 5 μ M, monitoring absorbance at $\lambda = 210$ nm. Standard curves for quantification of concentrations of BTZ were prepared by spiking PBS buffer with stock solutions of test compounds in the 100 nM-100 μ M concentration range. The limit of quantification (LOQ) was 100 nM, monitoring absorbance at $\lambda = 254$ nm. The coefficients of correlation (r^2) were > 0.99 for all curves.

Identity of reaction species was confirmed by HPLC-ESI-MS/MS analysis. Column used was a Phenomenex Sinergy Fusion (100 \times 2.0mm i.d., 4 μ m particle size (Phenomenex, Bologna, Italy). Eluent A: water added of 0.1% v/v formic acid (FA); eluent B: methanol added of 0.1% v/v FA. Chosen gradient was as follows: t(0 min): 95% A:5% B; t(1 min): 95% A:5% B; t(6 min): 5% A:95% B; t(9 min): 5% A:95% B returning to initial conditions in 0.5 min. Total gradient time was 13 min. Flow rate was 350 μ L/min. Injected volume: 10 μ L. A Thermo Accela UHPLC gradient system (Thermo Italia, Milan, Italy) coupled to a Thermo TSQ Quantum triple quadrupole mass spectrometer with heated electrospray ionization (H-ESI) ion source was used for compound detection and analysis. Mass spectrometric analyses were done in positive ion mode and in full scan mode in the 150-750 amu range. H-ESI interface parameters were set as follows: probe middle (D) position; capillary temperature 270 $^{\circ}$ C; spray voltage 3.0 kV. Nitrogen was used as nebulizing gas at the following pressure: sheath gas 35 psi; auxiliary gas 15 arbitrary units (a.u.). Argon was used as the collision gas at a pressure of approximately 1.5 mtorr (1 torr = 133.3 Pa). The software Xcalibur, version 1.3, (Thermo Italia, Milan, Italy) was employed for data acquisition and processing.

5.1.5 Kinetic studies by NMR spectroscopy

NMR spectra of compounds **2**, **9**, **33**, **23** and **29** were recorded on a Bruker AV 400 MHz spectrometer at 298 K. Equimolar concentration (80 mM) of BTZ and NAC were separately dissolved in deuterated methanol and mixed together. 1 H-NMR spectra were measured at 4 minutes and then every 2 minutes until reaction was complete. 1 H chemical shifts were given on the δ scale and were calibrated to the residual solvent signal of MeOD at δ 3.31.

5.2 Chapter 4

5.2.1 Chemistry

All chemicals were used as received unless stated otherwise. All reactions were performed under a steady overpressure of nitrogen delivered through a balloon. Tetrahydrofuran was distilled over sodium/benzophenone prior to use. Anhydrous solvents such as dichloromethane, *N,N*-dimethylformamide, pyridine were directly purchased from an appropriate vendor, and were supplied stored over 3 Å molecular sieves and packed under Ar. They were subsequently manipulated by syringe under a steady pressure of nitrogen. Column chromatography was performed on silica gel 60 (0.040-0.063 mm) under forced flow of the appropriate solvent mixtures. TLC analysis was conducted on HPTLC aluminum sheets (Sigma-Aldrich, silica gel 60, F₂₅₄), compounds were visualized by UV absorption (245 nm) and/or by dipping in a solution of (NH₄)₆Mo₇O₂₄ · 4 H₂O 25 g/l and (NH₄)₄Ce(SO₄)₄ · 2 H₂O 10 g/l, in 1 L of 10% aqueous H₂SO₄. ¹H- and ¹³C-NMR spectra were recorded with a Bruker AV 300, 400 and with a Varian 600. Chemical shifts (δ scale) are reported in parts per million (ppm) relative to the central peak of the solvent. ¹H-NMR spectra are reported in the following order: multiplicity, number of protons and approximate coupling constant (*J* value) in hertz (Hz); signals were characterized as s (singlet), d (doublet), dd (doublet of doublets), t (triplet), dt (doublet of triplets), q (quartet), m (multiplet), bs (broad signal). Mass Spectra were recorded on a Applied Biosystem API-150 EX system spectrometer with an ESI or an APCI interface. Purity of final compounds were analyzed by HPLC with UV detection at λ = 220. Purity of compounds was determined by analytical high performance liquid chromatography (HPLC) employing a Shimadzu HPLC gradient system (Shimadzu Corp., Kyoto, Japan) equipped with two LC-10AD solvent delivery modules, a Rheodyne 7125 sample injector and a SPD-10A UV-VIS detector. Prior to analysis, samples were prepared in MeOH at a final concentration of 0.1 mg/mL. Chromatographic separation occurred on a Supelco Discovery C₁₈ column (150 X 4.6 mm, 5 mm particle size) by gradient elution. Flow rate was 1 mL/min and injected volume was 10 mL. Solvent A was MeCN and Solvent B was water both added of 0.1% v/v formic acid. Isocratic conditions were employed for all final compounds: 75% A: 25% B. Purity results are presented as *t*R (min) and relative chemical purity (%). All tested compounds were >95% pure.

1-((3S,8S,9S,10R,13S,14S,17S)-3-hydroxy-10,13-dimethyl-2,3,4,7,8,9,10,11,12,13,14,15,16,17-tetradecahydro-1H-cyclopenta[a]phenanthren-17-yl)ethanone 49:

Commercially available pregnenolone acetate **48** (2.0 g, 5.6 mmol) is dissolved in a mixture of MeOH/DCM 1:3 (60 ml), a solution of KOH (3.1 g, 56 mmol) in MeOH (20 ml) is added at r.t. and the reaction is stirred for two hours. Reaction mixture is neutralized with a 1M HCl solution, added of EtOAc (50 ml) and washed with 3 times with brine (30 ml). The organic phase is dried over Na₂SO₄ and the solvent evaporated under reduced pressure affording 1.7 g of a white powder used without any further purification (yield = 98%). ¹H-NMR (300 MHz, CDCl₃) δ: 5.33 (bd, 1H, *J* = 5.2 Hz); 3.50 (m, 1H); 2.51 (t, 1H, *J* = 9.0 Hz); 2.32-2.15 (m, 3H); 2.11 (s, 3H); 2.05-1.97 (m, 2H); 1.88-1.81 (m, 2H); 1.71-1.37 (m, 9H); 1.29-0.93 (m, 7H); 0.62 (s, 3H). ¹³C-NMR

(100 MHz, CDCl₃) δ: 209.7; 140.9; 121.4; 71.6; 63.7; 56.9; 50.0; 44.1; 42.3; 38.9; 37.3; 36.6; 31.9; 31.8; 31.6; 24.5; 22.8; 21.1; 19.4; 13.3. ESI-MS Calc. for C₂₁H₃₂O₂: 317.2, Found: 317.1 [M+H⁺].

(3S,8S,9S,10R,13S,14S,17S)-17-acetyl-10,13-dimethyl-2,3,4,7,8,9,10,11,12,13,14,15,16,17-tetradecahydro-1H-cyclopenta[a]phenanthren-3-yl benzoate 50:

Pregnenolone **49** (2.5 g, 8.0 mmol) is dissolved in pyridine (30 ml) at 0° C. Benzoyl chloride (1.2 ml, 10.3 mmol) and DMAP (96 mg, 0.8 mmol) are added and the reaction mixture is stirred at r.t. for 24 h. 1M HCl solution is added and the mixture is diluted with DCM (50 ml). Organic phase is washed with brine (20 ml) and HCl 1M (20 ml), dried over Na₂SO₄ and the solvent is evaporated under reduced pressure. The crude product is triturated in EtOAc affording 2.7 g of desired product as a white solid (yield = 81%). ¹H-NMR (300 MHz, CDCl₃) δ: 8.05 (d, 2H, *J* = 7.1 Hz); 7.57 (t, 1H, *J* = 7.4 Hz); 7.45 (t, 1H, *J* = 7.7 Hz); 5.44 (bd, 1H, *J* = 4.3 Hz); 4.87 (m, 1H); 2.57 (t, 1H, *J* = 9.1 Hz); 2.50 (d, 2H, *J* = 7.8 Hz); 2.26-1.92 (m, 8H); 1.83-1.48 (m, 8H); 1.30-1.19 (m, 3H); 1.14-1.05 (m, 4H); 0.66 (s, 3H). ¹³C-NMR (100 MHz, CDCl₃) δ: 209.7; 166.1; 139.8, 132.9; 130.9; 129.6; 128.4; 122.6; 74.5; 63.8; 56.9; 50.0; 44.1; 38.9; 38.2; 37.1; 36.8; 31.9; 31.9; 31.7; 27.9; 24.6; 22.9; 21.2; 19.5; 13.3. ESI-MS Calc. for C₂₈H₃₆O₂: 413.3, Found: 413.1 [M+Na⁺].

(3S,8S,9S,10R,13S,14S,17S)-10,13-dimethyl-17-(4,4,4-trifluoro-3-hydroxy-3-(trifluoromethyl)butanoyl)-2,3,4,7,8,9,10,11,12,13,14,15,16,17-tetradecahydro-1H-cyclopenta[a]phenanthren-3-yl benzoate 51:

In a two neck flask, compound **50** (150 mg, 0.4 mmol) is dissolved in dry THF under nitrogen atmosphere at -78° C. A solution of KHMDS (99 mg, 0.5 mmol) in dry THF is added and the reaction mixture is stirred at -78° C for 30 min. In a separate two neck flask conc. H₂SO₄ (10 ml) is warmed to 50° C and linked through a cannula with the enolate flask. Trihydrate HFA (large excess ≈ 3 ml) is dropped inside the H₂SO₄ and a colorless gas formation is observed. Through a positive nitrogen pressure, gaseous HFA is bubbled inside the enolate solution. The reaction mixture is then warmed to r.t.. A 5% aqueous solution of acetic acid is added and the reaction is stirred for 15 min before being diluted with EtOAc. The organic phase is then washed with H₂O (10 ml) and brine (10 ml), dried over Na₂SO₄ and the solvent is evaporated under reduced pressure affording a yellow oil (370 mg). The residue is purified by FC (SiO₂ Hex/DCM 50:50) giving 140 mg of a white solid (yield = 67%). ¹H-NMR (400 MHz, CDCl₃) δ: 8.04 (d, 2H, *J* = 7.1 Hz); 7.55 (t, 1H, *J* = 7.4 Hz); 7.43 (t, 1H, *J* = 7.8 Hz); 7.08 (s, 1H); 5.41 (bd, 1H, *J* = 4.7 Hz); 4.86 (m, 1H); 2.94 (d, 1H, *J* = 17.2 Hz); 2.80 (d, 1H, *J* = 17.2 Hz); 2.61 (t, 1H, *J* = 9.0 Hz); 2.47 (bd, 2H, *J* = 7.0 Hz); 2.18 (q, 1H, *J* = 9.3 Hz); 2.04-1.90 (m, 4H); 1.79-1.49 (m, 8H); 1.30-1.20 (m, 3H); 1.09-1.04 (m, 4H); 0.69 (s, 3H). ¹³C-NMR (100 MHz, CDCl₃) δ: 212.1; 166.1; 139.8; 132.9; 130.8; 129.6; 128.4; (127.0; 123.9; 121.1; 118.4 (CF₃)₂); 122.3; (76.8; 76.5; 76.2; 75.9 (COH(CF₃)₂); 74.4; 64.9; 57.0; 49.9; 45.3; 38.7; 38.3; 37.8; 37.1; 36.7; 32.0; 31.8; 27.9; 24.4; 22.9; 21.1; 19.5; 13.3. ESI-MS Calc. for C₃₁H₃₆F₆O₃: 387.3, Found: 387.2 [M+H⁺].

(3S,8S,9S,10R,13S,14S,17S)-10,13-dimethyl-17-((R)-4,4,4-trifluoro-1,3-dihydroxy-3-(trifluoromethyl)butyl)-2,3,4,7,8,9,10,11,12,13,14,15,16,17-tetradecahydro-1H-cyclopenta[a]phenanthren-3-yl benzoate 52:

Compound **51** (140 mg, 0.2 mmol) is dissolved in a MeOH/THF 1:1 mixture before NaBH₄ (12 mg, 0.3 mmol) is added at r.t.. Reaction is stirred 2 hours before a 1M HCl solution (5 ml) is added and stirring is continued for 15 min. Then reaction is diluted with a 2M NaOH solution and stirred for additional 2 hours. Organic phase, after addition of EtOAc (10 ml) is washed with brine (10 ml) dried over Na₂SO₄ and the solvent is

evaporated under reduced pressure affording a white solid (120 mg). The residue is purified by FC (SiO₂ Hex/DCM 30:70) giving 100 mg of a white powder (yield = 72%). ¹H-NMR (400 MHz, CDCl₃) δ: 8.03 (d, 2H, J = 7.1 Hz); 7.56 (t, 1H, J = 7.4 Hz); 7.44 (t, 1H, J = 7.8 Hz); 6.77 (s, 1H); 5.42 (bd, 1H, J = 4.8 Hz); 4.88 (m, 1H); 4.21 (q, 1H, 9.3 Hz); 2.98 (d, 1H, J = 7.7 Hz); 2.48 (m, 2H); 2.18 (q, 1H, J = 9.3 Hz); 2.09-1.92 (m, 6H); 1.81-1.35 (m, 9H); 1.26-1.15 (m, 3H); 1.09-1.040 (m, 4H); 0.84 (s, 3H). ¹³C-NMR (100 MHz, CDCl₃) δ: 166.7; 139.8; 133.2; 130.4; 129.7; 128.4; (128.0; 127.3; 125.1; 124.4; 122.3; 121.5; 119.2; 118.4; (CF₃)₂); 122.6; (77.1; 76.8; 76.5; 76.2 (COH(CF₃)₂); 56.9; 56.1; 50.0; 42.6; 39.9; 38.2; 37.2; 36.8; 33.7; 31.9; 31.7; 28.3; 27.8; 25.4; 24.5; 21.0; 19.5; 12.6. ESI-MS Calc. for C₃₁H₃₈F₆O₄: 587.3, Found: 587.2 [M-H].

(R)-4,4,4-trifluoro-1-((3S,8S,9S,10R,13S,14S,17S)-3-hydroxy-10,13-dimethyl-2,3,4,7,8,9,10,11,12,13,14,15,16,17-tetradecahydro-1H-cyclopenta[a]phenanthren-17-yl)-3-(trifluoromethyl)butane-1,3-diol 53 (UPR1357):

Compound **52** (100 mg, 0.2 mmol) is dissolved in a MeOH/THF 2:1 mixture before Na (5 mg, 0.2 mmol) is added and the reaction stirred for 1 hour. After neutralization with a 1M HCl solution, the mixture is diluted with EtOAc and the organic phase is washed with brine (5 ml) dried over Na₂SO₄ and the solvent is evaporated under reduced pressure affording a white solid (95 mg). The residue is purified by FC (SiO₂ Hex/EtOAc 70:30) giving 76 mg of a white powder (yield = 93%). ¹H-NMR (600 MHz, MeOD) δ: 5.34 (bd, 1H, J = 2.8 Hz); 4.06 (t, 1H, J = 10.3 Hz); 3.39 (heptuplet, 1H, J = 4.9 Hz); 2.21 (m, 2H); 2.10 (dt, 1H, J = 3.5, 12.8); 2.02-1.92 (m, 3H); 1.85 (dt, 1H, J = 3.54, 13.4); 1.78 (m, 1H); 1.69 (m, 2H); 1.57-1.45 (m, 6H); 1.29-1.14 (m, 4H); 1.09-1.02 (m, 4H); 0.96 (td, 1H, J = 5.2, 6.2); 0.81 (s, 3H). ¹³C NMR (100 MHz, MeOD) δ: 141.0; (128.2; 127.5; 125.4; 124.6; 122.5; 121.8; 119.7; 119.0; (CF₃)₂); 121.0; (76.9; 76.8; 76.4 (COH(CF₃)₂); 71.1; 70.9; 56.7; 56.3; 50.5; 42.4; 41.7; 39.2; 37.3; 36.4; 33.5; 31.8; 31.7; 31.0; 25.1; 24.2; 20.7; 18.6; 11.2. ESI-MS Calc. for C₂₄H₃₄F₆O₃: 483.2, Found: 483.3 [M-H]. HPLC-UV purity: tR 6.6 min - 96%.

(3S,8S,9S,10R,13S,14S,17S)-10,13-dimethyl-17-((S)-4,4,4-trifluoro-1,3-dihydroxy-3-(trifluoromethyl)butyl)-2,3,4,7,8,9,10,11,12,13,14,15,16,17-tetradecahydro-1H-cyclopenta[a]phenanthren-3-yl benzoate 54:

Compound **51** (90 mg, 0.2 mmol) is dissolved in THF before Na(OAc)₃BH (190 mg, 0.9 mmol) is added at 0° C. Reaction is warmed to r.t. and stirred for 6 hours. A 1M HCl solution (5 ml) is added and stirring is continued for 15 min. Then reaction is diluted with a 2M NaOH solution and stirred for additional 2 hours. Organic phase, after addition of EtOAc (10 ml) is washed with brine (10 ml) dried over Na₂SO₄ and the solvent is evaporated under reduced pressure affording a white solid (120 mg). The residue is purified by FC (SiO₂ Hex/EtOAc 80:20) and by means of Biotage (gradient t(0): Hex/EtOAc 98:2; t(20) Hex/EtOAc 80:20) giving 22 mg of a white powder (yield = 24%). ¹H-NMR (300 MHz, CDCl₃) δ: 8.03 (d, 2H, J = 7.2 Hz); 7.55 (t, 1H, J = 7.4 Hz); 7.43 (t, 1H, J = 7.7 Hz); 6.42 (bs, 1H); 5.42 (bd, 1H, J = 4.4 Hz); 4.85 (m, 1H); 4.21 (t, 1H, 9.6 Hz); 2.47 (d, 2H, J = 7.8 Hz); 2.23 (d, 1H, J = 15.2 Hz); 2.04-1.43 (m, 13H); 1.35-1.07 (m, 8H); 0.85 (m, 1H); 0.72 (s, 3H). ESI-MS Calc. for C₃₁H₃₈F₆O₄: 587.3, Found: 587.2 [M-H].

(S)-4,4,4-trifluoro-1-((3S,8S,9S,10R,13S,14S,17S)-3-hydroxy-10,13-dimethyl-2,3,4,7,8,9,10,11,12,13,14,15,16,17-tetradecahydro-1H-cyclopenta[a]phenanthren-17-yl)-3-(trifluoromethyl)butane-1,3-diol 55 (UPR1358):

Compound **54** (70 mg, 0.1 mmol) is dissolved in a MeOH/THF 2:1 mixture before Na (3 mg, 0.2 mmol) is added and the reaction stirred for 1 hour. After neutralization with a 1M HCl solution, the mixture is diluted with EtOAc and the organic phase is washed with brine (5 ml) dried over Na₂SO₄ and the solvent is evaporated under reduced pressure affording a white solid (66 mg). The residue is purified by FC (SiO₂ Hex/EtOAc 80:20) giving 55 mg of a white powder (yield = 96%). ¹H-NMR (600 MHz, MeOD) δ: 5.35 (bd, 1H, *J* = 5.5 Hz); 4.05 (t, 1H, *J* = 10.3 Hz); 3.39 (heptuplet, 1H, *J* = 4.6 Hz); 2.24-2.19 (m, 3H); 1.98 (m, 1H); 1.94-1.86 (m, 2H); 1.80 (m, 2H); 1.72-1.43 (m, 8H); 1.28-1.04 (m, 5H); 1.02 (s, 3H); 0.96 (td, 1H, *J* = 11.4, 4.7); 0.72 (s, 3H). ¹³C-NMR (100 MHz, MeOD) δ: 142.4; (129.6; 128.7; 126.8; 126.0; 124.0; 123.2; (CF₃)₂); 122.4; (76.9; 76.8; 76.4 (COH(CF₃)₂); 72.6; 71.8; 59.1; 58.1; 51.7; 43.1; 42.8; 40.6; 38.6; 37.8; 35.0; 33.0; 32.9; 32.4; 31.0; 26.6; 25.0; 22.1; 20.0; 12.9. ESI-MS Calc. for C₂₄H₃₄F₆O₃: 483.2, Found: 483.3 [M-H]. HPLC-UV purity: *t*R 5.2 min - 98%.

(3S,8S,9S,10R,13S,14S,17S)-10,13-dimethyl-17-((R)-2-oxo-6,6-bis(trifluoromethyl)-1,3-dioxan-4-yl)-2,3,4,7,8,9,10,11,12,13,14,15,16,17-tetradecahydro-1H-cyclopenta[a]phenanthren-3-yl benzoate 56:

Compound **52** (50 mg, 0.08 mmol) is dissolved in dry DCM (5ml) under nitrogen atmosphere before pyridine (70 µl, 0.8 mmol) is added. The mixture is cooled to -50°C and thiphosgene (25mg, 0.08 mmol) is added and stirred for 2h. Once warmed to r.t. the mixture is added of a saturated aqueous solution of NH₄Cl and a 1M HCl solution. The mixture is then diluted with EtOAc and the organic phase is washed with brine (5 ml) dried over Na₂SO₄ and the solvent is evaporated under reduced pressure affording a white solid (55 mg). The residue is purified by FC (SiO₂ Hex/DCM 50:50) giving 40 mg of a white powder (yield = 77%). ¹H-NMR (400 MHz, MeOD) δ: 8.03 (m, 2H); 7.54 (m, 1H); 7.42 (t, 1H, *J* = 7.7 Hz); 5.40 (bd, 1H, *J* = 3.9 Hz); 4.86 (m, 1H); 4.44 (t, 1H, 10.9 Hz); 2.47-2.38 (m, 3H); 2.21 (m, 2H); 2.19 (m, 3H); 2.17-1.45 (m, 9H); 1.28-1.03 (m, 8H); 0.78 (s, 3H).

(3S,8S,9S,10R,13S,14S,17S)-10,13-dimethyl-17-((R)-2-oxo-6,6-bis(trifluoromethyl)-1,3-dioxan-4-yl)-2,3,4,7,8,9,10,11,12,13,14,15,16,17-tetradecahydro-1H-cyclopenta[a]phenanthren-3-yl benzoate 57:

Compound **54** (70 mg, 0.1 mmol) is dissolved in dry DCM (5ml) under nitrogen atmosphere before pyridine (70 µl, 1.2 mmol) is added. The mixture is cooled to -50°C and thiphosgene (42mg, 0.1 mmol) is added and stirred for 2h. Once warmed to r.t. the mixture is added of a saturated aqueous solution of NH₄Cl and a 1M HCl solution. The mixture is then diluted with EtOAc and the organic phase is washed with brine (5 ml) dried over Na₂SO₄ and the solvent is evaporated under reduced pressure affording a white solid (65 mg). The residue is purified by FC (SiO₂ Hex/EtOAc 95:5) giving 50 mg of a white powder (yield = 68%). ¹H-NMR (400 MHz, MeOD) δ: 8.03 (m, 2H); 7.54 (m, 1H); 7.43 (t, 1H, *J* = 7.8 Hz); 5.42 (bd, 1H, *J* = 4.9 Hz); 4.86 (m, 1H); 4.21 (t, 1H, 9.1 Hz); 2.54 (dd, 1H, *J* = 15.2, 2.0 Hz); 2.47 (m, 1H); 2.21 (dd, 1H, *J* = 12.2, 13.8 Hz); 2.10-1.99 (m, 3H); 1.91 (dt, 1H, *J* = 3.44, 13.28); 1.82-1.43 (m, 10H); 1.34-1.01 (m, 7H); 0.72 (s, 3H).

5.2.2 Pharmacology

Collected biological data were from experimentations carried out by Prof. Presta's research group (Department of Biomedical Sciences and Biotechnology, School of Medicine, University of Brescia, Brescia, Italy).

Viable cell counting. Cells were cultured under appropriate conditions for 48 hours in the presence of increasing doses of different compounds. Propidium iodide staining (Immunostep, Salamanca, SP, EU) was used to detect PI- viable cells by flow cytometry. Absolute cell counts were obtained by the counting function of the MACSQuant® Analyzer (Miltenyi Biotec).

5.2.3 Computational studies

Geometries. Geometries of compounds **53**, **55-57** were optimized with OPLS2005 Force Field in combination with an implicit solvent model (water) using a convergence criteria for energy minimization of 0.05 Kcal mol⁻¹ Å⁻¹.

References

- ¹ King, A. R.; Lodola, A.; Carmi, C.; Fu, J.; Mor, M.; Piomelli, D. A critical cysteine residue in monoacylglycerol lipase is targeted by a new class of isothiazolinone-based enzyme inhibitors. *Br. J. Pharmacol.* **2009**, *157*, 974-983
- ² Maestro, version 9.2; Schrödinger, LLC: New York, 2011.
- ³ LigPrep, version 2.5; Schrödinger, LLC: New York, 2011.
- ⁴ Prime, version 3.0; Schrödinger, LLC: New York, 2011.
- ⁵ a) Schrödinger Suite 2011 Protein Preparation Wizard; Schrödinger, LLC: New York, 2011; (b) Epik version 2.2; Schrödinger, LLC, New York, NY, 2011; (c) Impact, version 5.7; Schrödinger, LLC: New York, 2011; (d) Prime, version 3.0; Schrödinger, LLC: New York, 2011.
- ⁶ Glide, version 6.1; Schrödinger, LLC: New York, 2011.
- ⁷ Friesner, R. A.; Banks, J. L.; Murphy, R. B.; Halgren, T. A.; Klicic, J. J.; Mainz, D. T.; Repasky, M. P.; Knoll, E. H.; Shelley, M.; Perry, J. K.; Shaw, D. E.; Francis, P.; Shenkin, P. S. Glide: a new approach for rapid, accurate docking and scoring. 1. Method and assessment of docking accuracy. *J. Med. Chem.* **2004**, *47*, 1739-1749.
- ⁸ MacroModel, version 9.9; Schrödinger, LLC: New York, 2011.
- ⁹ Jorgensen, W. L.; Maxwell, D. S.; Tirado-Rives, J. Development and testing of the OPLS all-atom force field on conformational energetics and properties of organic liquids. *J. Am. Chem. Soc.* **1996**, *118*, 11225-11236.
- ¹⁰ Labar, G.; Bauvois, C.; Borel, F.; Ferrer, J.L.; Wouters, J.; Lambert, D.M. Crystal structure of the human monoacylglycerol lipase, a key actor in endocannabinoid signaling *Chembiochem.* **2010**, *11*(2), 218.
- ¹¹ (a) Barducci, A.; Bussi, G.; Parrinello, M. *Phys. Rev. Lett.* **2008**, *100*, 020603; (b) Barducci, A.; Bonomi, M.; Parrinello, M. *Biophys. J.* **2010**, *98*, L44-6.
- ¹² Desmond Molecular Dynamics System, version 3.4, D. E. Shaw Research, New York, NY, 2013.
- ¹³ Lomize, M. A.; Lomize, A. L.; Pogozheva, I. D.; Mosberg, H. I. *Bioinformatics* **2006**, *22*, 623 – 625.